List of Contributors

Dr J. A. Chudek and Professor G. Hunter, *School of Life Sciences, Division of Inorganic and Physical Chemistry, University of Dundee, Dundee, DD1 4HN*

Dr H. Kimura, *Department of Biological Sciences, Gunma University, Kiryu, Gunma 376-8515, Japan*

Professor A. Shoji, *Department of Biological Sciences, Faculty of Engineering, Gunma University, Kiryu, Gunma 376-8515, Japan*

Dr H. Sugisawa, *NMR Applications Laboratory, Analytical Instruments Division, JEOL Ltd, Akishima, Tokyo 196-0021, Japan*

Professor A. G. Webb, *Department of Electrical and Computer Engineering, University of Illinois at Urbana-Champaign, 1406 W. Green St, Urbana IL 61801, USA*

Professor Y. Yamamoto, *Department of Chemistry, University of Tsukuba, Tsukuba 305-8571, Japan*

Preface

As with other members of this series of *Annual Reports on NMR* volume 45 consists of a collection of accounts of progress in various areas of NMR activity. The first report covers Temperature Measurements using NMR by A. G. Webb, following this is a review on Structural Studies of Amino Acids, Polypeptides and Proteins in the Solid State by ^{1}H CRAMPS NMR from A. Shoji, H. Kimura and H. Sugisawa, the next contribution from J. A. Chudek and G. Hunter is on STRAFI and SPI Magnetic Resonance Imaging, finally Y. Yamamoto reports on NMR Studies of Internal Hydrogen Bonds in Metalloproteins.

It is my pleasure to have this opportunity to express my thanks to all of these authors and to the production staff at Academic Press (London) for the timely appearance of this volume.

Royal Society of Chemistry
Burlington House
London, UK

G. A. WEBB
April 2001

Temperature Measurements using Nuclear Magnetic Resonance

A. G. WEBB

Department of Electrical and Computer Engineering, University of Illinois at Urbana-Champaign, 1406 W. Green St, Urbana IL 61801, USA

1. Introduction 1
2. Temperature-dependent NMR parameters 3
3. NMR temperature measurements in the liquid state 4
   3.1. Proton 4
   3.2. Heteronuclei 16
4. NMR temperature measurements in the solid state 29
   4.1. Phase transition calibration materials 30
   4.2. Proton chemical shifts 31
   4.3. Carbon chemical shifts 32
   4.4. Nitrogen chemical shifts 33
   4.5. Phosphorus chemical shifts 35
   4.6. Tin chemical shifts 35
   4.7. Lead chemical shifts 38
5. *In vivo* temperature mapping using magnetic resonance imaging 40
   5.1. T_1-based techniques and applications 41
   5.2. Molecular diffusion based techniques and applications 46
   5.3. Proton reference frequency methods 49
   5.4. Applications of the proton reference frequency method 52
6. Non-medical applications of temperature mapping 59
Acknowledgements 59
References 60

1. INTRODUCTION

A wide range of magnetic resonance experiments, encompassing high-resolution liquid-state nuclear magnetic resonance (NMR) spectroscopy, solid-state NMR spectroscopy and magnetic resonance imaging (MRI), requires accurate measurements of sample temperature. As an example, variable temperature NMR spectrocopy is used extensively for measurements of exchange rates, with errors in the measurement of sample temperature often

ANNUAL REPORTS ON NMR SPECTROSCOPY
VOLUME 45 ISBN 0-12-505445-9

the limiting factor in the accuracy of the final result. Although variable temperature (VT) units use heating or cooling air at a well-defined temperature, this often does not define accurately the actual temperature of the sample. This is true, for example, when high-powered homo- or heteronuclear decoupling is used, especially if the sample is lossy. Temperature gradients can also form within the sample. In high-resolution liquid-state NMR these gradients lead to broadened lineshapes for resonances which have a temperature-dependent chemical shift, and impose limits on spectral resolution. If the temperature gradient is large it can cause convection currents within the sample, in turn leading to reductions in the signal-to-noise (S/N) ratio in pulse sequences using magnetic field gradients for coherence-order selection. In solid-state NMR experiments, in which the sample is rotated at high speed, there is a complex interaction of thermal effects within the sample. These effects include frictional heating of the rotor and bearing gas, Joule-Thompson heating or cooling from the expansion of the driving and bearing gases, and induction of eddy currents within the sample. Different probe configurations may have very different thermal characteristics, such that 'identical' experiments carried out on different spectrometers with the same nominal VT reading may actually correspond to very different temperatures within the sample. In the area of MRI, non-invasive *in vivo* temperature mapping of thermal therapies, such as ultrasound and laser ablation, has developed rapidly in the past ten years. Accurate, localized thermal measurements are required to ensure that temperatures within the heated area of, for example, a tumour are sufficient to kill the diseased tissue, while temperatures in the surrounding healthy tissue remain at a level that does not cause damage.

For all of the applications outlined above, and many others besides, it is desirable to use NMR parameters which possess an intrinsic temperature dependence in order to measure directly the sample temperature. These measurements can either be performed as a pre-experiment calibration procedure using identical data acquisition parameters as for the actual experiment, or as an *in situ* measurement using the actual sample. Temperature-dependent NMR parameters include spin–lattice (T_1) and spin–spin (T_2) relaxation times, chemical shifts, dipolar and scalar couplings, molecular diffusion coefficients and net equilibrium polarization. Dependent upon the particular application, each of these parameters has been utilized as an NMR 'thermometer'.

This article is divided into three sections, comprising liquid-state NMR, solid-state NMR, and MRI, respectively. Within each section, the physical basis for the temperature dependence of the particular NMR parameter is introduced, with applications presented subsequently. Although the emphasis is placed on chemical compounds which have been used in actual temperature measurements, there are also shorter sections covering the thermal properties of compounds which may bear re-examination as temperature probes.

2. TEMPERATURE-DEPENDENT NMR PARAMETERS

This section summarizes briefly the basis for the temperature dependence of those NMR parameters most widely used for thermal measurements, and references sections in the article in which further discussion and applications are included. The parameters considered are net polarization, chemical shielding (σ), T_1 relaxation times, scalar (J) coupling and molecular diffusion coefficients.

In NMR experiments the signal intensity is proportional to the net equilibrium magnetization or polarization, M_0, given by:

$$M_0 = \frac{N\gamma^2 h^2 I(I+1)}{12\pi^2 \mu_0 kT} B_0 \tag{1}$$

where N is the number of nuclei, γ is the gyromagnetic ratio, h is Plank's constant, I is the nuclear spin angular momentum quantum number, μ_0 is the relative permitivity, k is Bolzmann's constant, and T is the absolute temperature in Kelvin (K). Higher sample temperature, therefore, results in lower equilibrium polarization and lower NMR signal. Since the temperature sensitivity is not very high (approximately 0.32% per degree at 298 K), and the value of M_0 is difficult to measure, this parameter has found relatively little use in measuring temperature directly, but is an important factor in T_1-based imaging methods described in Section 5.1.

The shielding constant (σ) of a particular nucleus can be expressed as:[1]

$$\sigma(T, \rho) = \sigma_0(T) + \sigma_1'(T)\rho_{\text{liq}}(T) + \cdots \tag{2}$$

where ρ is the density of the sample, $\sigma_0(T)$ is the temperature-dependent electronic shielding intrinsic to the molecule, i.e. a measure of the change in the nuclear shielding with rotation and vibration, and the term $\sigma_1'(T)\rho_{\text{liq}}(T)$ represents the effects of intermolecular interactions which include the temperature dependence of the sample density on the electronic shielding. For many 'light' nuclei such as ^{1}H, ^{13}C, ^{15}N and ^{19}F, intermolecular interactions are the larger factor in the temperature dependence of chemical shifts in the liquid phase. This dependence is dominated by changes in liquid density with temperature, even when the intermolecular coefficient $\sigma_1'(T)$ is only mildly temperature dependent. Since $\sigma_1'(T)$ is generally positive for these nuclei, increased shielding is measured with increasing temperature, corresponding to a shift to lower resonant frequencies and a larger value of σ. Applications of chemical shift temperature measurement techniques using these nuclei can be found in Sections 3.1.1, and 3.2.1–3.2.3. In contrast, for a transition metal that is complexed with a ligand, the intermolecular coefficient of shielding is very small since the central metal ion is surrounded by the ligands. The dominant term in Eq. (2) is now $\sigma_0(T)$, which has a negative

value, and so these metal nuclei usually show deshielding with increased temperature. Intrinsic transition metal chemical shifts are discussed in Section 3.2.4, and the indirect effect on the chemical shift of protons in the ligand are described in Section 3.1.2.

Other mechanisms can also give rise to temperature-dependent chemical shifts. A chemical species may exist in a number of tautomeric or conformational forms, or in equilibrium with a second chemical species, and the measured chemical shift is the weighted average of these different chemical forms. Since such equilibria are invariably temperature dependent, so too is the chemical shift. Examples of this phenomenon can be found in Sections 3.2.1, 3.2.5, 4.2 and 4.4.

The process of T_1 relaxation can have contributions from a number of different mechanisms, e.g. dipole–dipole, scalar coupling of the first or second kind, quadrupolar, chemical shift anisotropy (CSA) and spin-rotation. The temperature dependence of the T_1 relaxation time depends upon the relative contribution of each of these mechanisms. For example, if spin-rotation is the dominant relaxation mechanism, then the T_1 value decreases linearly with increasing temperature, whereas if dipole–dipole is dominant the T_1 value increases with increasing temperature in the extreme narrowing limit. Examples of temperature measurements using T_1 are included in Sections 3.2.5 and 5.1.

The temperature dependence of scalar couplings (Sections 3.2.2 and 3.2.4) can also arise from several different mechanisms. For example, chemical exchange processes can mediate these couplings in the same way as described earlier for temperature-dependent chemical shifts. Dipolar coupling constants are also temperature-dependent, as outlined in Section 3.1.3.

Finally, the molecular diffusion coefficient, D, in liquids is temperature dependent, as predicted by the Stokes–Einstein equation:

$$D = \frac{kT}{6\pi\eta R_D} \tag{3}$$

where η is the sample viscosity and R_D the molecular hydrodynamic radius. Relevant thermal MRI measurements are covered in Section 5.2.

3. NMR TEMPERATURE MEASUREMENTS IN THE LIQUID STATE

3.1. Proton

Exploiting the temperature dependence of proton NMR parameters has the advantages of high S/N and wide potential application. In liquid-state NMR the temperature dependence of the proton chemical shift has been the technique used almost exclusively.

3.1.1. Proton chemical shifts

The first measurements of the dependence of proton chemical shifts δ on temperature were performed[2,3] using ethanol, and observing the shift of the OH proton with respect to the methyl and methylene protons. The first extensive study[4] of hydrogen-bonding mediated chemical shifts showed that, in the gas phase at very low pressures, the chemical shift measured at a particular temperature is essentially $\sigma_0(T)$ in Eq. (2). In the liquid phase, two factors alter the chemical shift from the value measured in the gas phase. The first factor is the change in bulk susceptibility caused by the change in density. The second factor is the 'association shift', which is the difference between the calculated and measured chemical shifts. The calculated value is given by:

$$(\delta_{\text{liq}})_{\text{calc}} = \delta_{\text{gas}} + \frac{2\pi\chi_v(T)}{3} \times 10^6 \tag{4}$$

where $\chi_v(T)$ is the volume susceptibility of the compound. The association shift was found to be highly correlated with the degree of hydrogen bonding in the molecule. As can be seen from the data in Table 1, a high temperature dependence of the chemical shift was also correlated with a high association shift. This suggests that the primary contribution to the association shift is the temperature-dependent hydrogen bonding structure. For liquids exhibiting very small association shifts, the dominant term for the overall temperature dependence of the chemical shift is $\chi_v(T)$.

Further studies of the temperature dependence of compounds capable of forming hydrogen bonds were carried out in decanoic acid[5] and in acetic and benzoic acids.[6,7] Since the H $\cdots$ O hydrogen bond is much weaker than a normal valence bond, there is a low-frequency vibrational mode in which the distance between the two atoms changes.[8] Even at low temperatures, a substantial number of molecules are found in the excited states of this vibrational mode. Since this mode is anharmonic, the effective value of the distance between the atoms will depend upon the degree of excitation. The

Table 1. Proton temperature sensitivities and association shifts (adapted from ref. 4)

Compound	Range (°C)	Sensitivity (ppm °C^{-1})	Association shift (ppm)
C_2H_6	−90 to +22	−0.002	0 (−98°C)
NH_3	−77 to +22	−0.0058	1.05 (−77°C)
H_2O	+25 to +110	−0.0095	4.58 (0°C)
HCl	−90 to +22	−0.0085	2.05 (−86°C)
HBr	−75 to +22	−0.01	1.78 (−67°C)
HI	−35 to −5	−0.01	2.55 (−5°C)
HF	−70 to +22	−0.014	>6.65 (−60°C)

observed chemical shift is a weighted average of the chemical shifts of the individual vibrational states. As temperature increases, the effective length of the hydrogen bond increases, reducing the deshielding effect of the oxygen atom at the proton, and a high frequency shift results in the proton resonance frequency. Calculations[9–11] have shown that a large component of the observed temperature dependence of the proton chemical shift in hydrogen-bonded liquids results from changes in the effective length of the hydrogen bond. Similar conclusions were reached[12] in a model of NMR, thermal and dielectric data for water, based on a two-state model involving an equilibrium between a hydrogen-bonded 'icelike' fraction and a non-hydrogen-bonded 'monomer' fraction.

The two systems used most often for temperature measurements in high-resolution NMR spectroscopy and MRI are both based on the temperature dependence of hydrogen-bonded molecules. MRI uses the chemical shift of water found in tissue, and this technique is covered in Section 5.3. In high-resolution NMR spectroscopy the two classic systems are methanol, which can be used over an approximate temperature range 220–330 K, and ethylene glycol over the range 310–410 K. The chemical shift difference between the CH_3 and the OH protons in methanol, and the CH_2 and OH protons in glycol, is used to measure temperature (a small amount of concentrated HCl is usually added to both samples to collapse the multiplet structure). The original measurements were made at an operating frequency of 60 MHz,[13] with further refinements at this frequency by the same author,[14] subsequent confirmation at 60 MHz[15] and an extension to 220 MHz:[16] these measurements are summarized in Table 2. If deuterated, rather than protonated, methanol is used, then the equation of Van Geet can be applied simply by subtracting a constant equal to 1.7 K.[17] This correction occurs since the isotope effect of deuterium substitution affects the chemical shift of the residual CD_2H and OH proton differently.[18]

Table 2. Temperature calibrations for methanol and ethylene glycol

Ref.	Frequency	Methanol	Temperature range
Van Geet[14]	60 MHz	$T = 403.0 - 29.46 \mid \Delta\delta \mid - 23.83(\Delta\delta)^2$	175–313 K
Ammann[15]	60 MHz	$T = 409.0 - 36.54 \mid \Delta\delta \mid - 21.85(\Delta\delta)^2$	178–330 K
Raiford[16]	220 MHz	$T = 429.2 - 62.26 \mid \Delta\delta \mid - 13.85(\Delta\delta)^2$	239–309 K
		Ethylene glycol	
Van Geet[13]	60 MHz	$T = 466.0 - 101.64 \mid \Delta\delta \mid$	310–410 K
Ammann[15]	60 MHz	$T = 466.5 - 102.0 \mid \Delta\delta \mid$	273–416 K
Raiford[16]	220 MHz	$T = 466.5 - 101.42 \mid \Delta\delta \mid$	303–372 K

As mentioned in the Introduction, decoupling can give rise to sample heating that is not reflected by the VT reading. The first study of these effects used a sealed sample of ethylene glycol to measure heating of high ionic strength solutions in a 10 mm probe with wideband, alternating-phase, low-power technique for zero-residual-splitting (WALTZ)-16 decoupling at 400 MHz.[19] Temperature increases of 10.2 K for physiological saline, 6.9–9.2 K for red cell suspensions (76–25% hematocrit concentrations respectively), and 11.7 K for urine were recorded using decoupler fields of between 1700 and 1800 Hz. At high salt concentrations substantial thermal gradients were formed within the sample giving rise to broadened resonances. A plot of steady-state temperature increases vs. saline concentration is shown in Fig. 1. Other studies, particularly of proton-decoupled ^{13}C spectroscopy, are discussed in Section 3.2.1.

Variations on the proton chemical shift method have also been used for *in vivo* and biological applications. The temperature in cell culture perfusion systems[20] was measured using the water signal in the cell culture medium referenced with respect to the methyl resonance of pyruvate, acetate or lactate: in each molecule the methyl resonance was found to be insensitive to temperature and pH over a temperature range 304 to 323 K and pH range of 5.9 to 7.8. The proton chemical shift of H_2O decreased by 0.0107 ppm K^{-1}, in good agreement with the earlier results of Schneider and Hindman. In two other studies,[21,22] prompted by reports showing that cooling the brain during surgery has cryoprotective attributes, the linear difference in chemical shift

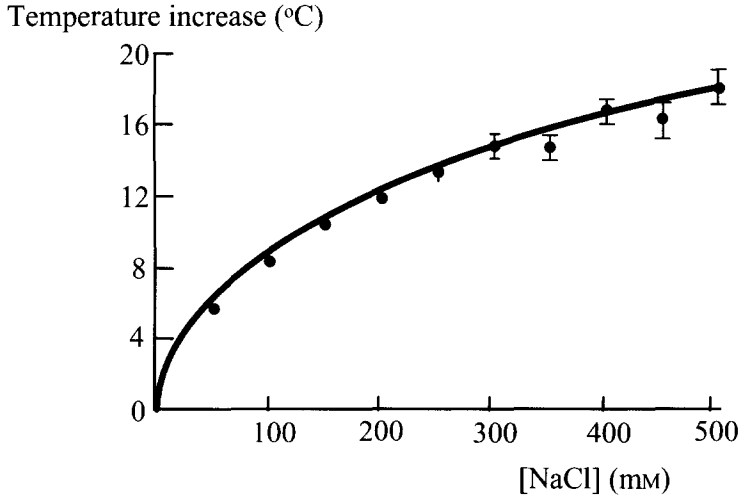

Fig. 1. Increases in steady-state temperature from WALTZ-16 decoupling of saline solutions containing 10% D_2O. (Figure from ref. 19, Copyright 1988 by Academic Press, reproduced by permission of the publisher.)

between the water and N-acetylaspartate (NAA) resonances with temperature was used to measure cooling in a pig brain animal model. Relative to NAA, the chemical shift of water had a sensitivity of -0.0104 ppm K^{-1}. Excellent agreement was found comparing NMR temperature measurements to those obtained using an optical-fibre probe. Human measurements[21] in normal infants gave results corresponding to a temperature in the thalamus of 311.2 ± 0.4 K, with the authors suggesting that the accuracy was adequate for studying pathologically and therapeutically induced temperature changes. Another method, also applicable to biological systems, was to use the difference in chemical shifts of the amide proton of NAA with respect to the N-CH_3 resonance of creatine at 3.022 ppm and the CH_3 resonance of NAA at 2.015 ppm.[23] The slope for *in vitro* rat brain cytosol and excised rat brain was found to be -0.00789 ppm K^{-1}.

One recent non-medical application used the water chemical shift to measure the rise in temperature associated with capillary electrophoresis (CE) microseparations,[24] a technique that can achieve extremely high separation efficiency[25,26] on very small amounts of material. Large voltages are applied across the capillary, and Joule heating generated as current passes through the resistive buffer can ultimately limit separation efficiency.[27,28] A model has been developed[29,30] which predicts substantial temperature increases within bands of lower conductivity relative to the surrounding buffer. In the first experimental verification of this model using NMR, Fig. 2 shows that the applied current and measured temperature tracked each other, except when a band of lower conductivity NaCl was introduced. This resulted in a local temperature more than 20 K higher than in the rest of the capillary, even though the current at any given time was constant throughout the length of the capillary.

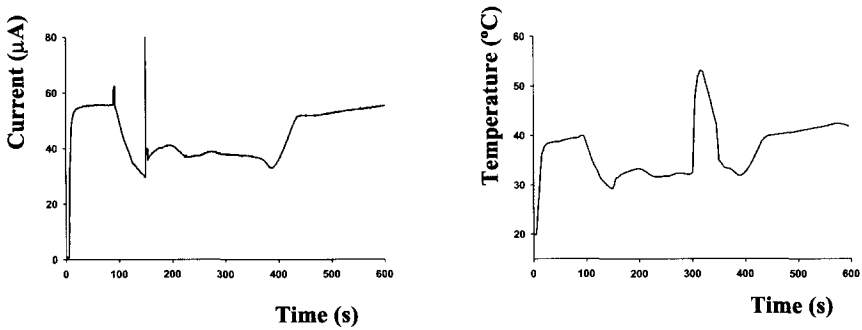

Fig. 2. (left) Graph of electrical current vs. time during a CE-NMR thermometry experiment. (right) Corresponding plot of intracapillary temperature vs. time. The peak in the temperature corresponds to the passage of the lower conductivity NaCl solution through the NMR coil. (Reprinted with permission from ref. 24, Copyright 2000 American Chemical Society.)

3.1.2. Proton chemical shifts in lanthanide complexes

An increase in the temperature dependence of proton chemical shifts is found for protons in a complex which chelates a lanthanide ion having one or more unpaired electrons. The chemical shift of the proton now becomes the sum of two terms. The diamagnetic term, δ_{dia}, is weakly temperature dependent, and represents the proton chemical shift if the lanthanide ion were absent. The second is a paramagnetic term, δ_{para}, which is highly temperature dependent, and in most transition metal complexes is the dominant component. The change in proton resonant frequency due to the paramagnetic term is referred to as the lanthanide induced shift (LIS). Within the complex, the closer the proton is to the lanthanide ion, the greater the LIS and the higher the temperature dependence of the proton chemical shift.

There are two mechanisms for the LIS. The first is the through-bond Fermi hyperfine contact shift (also referred to as the contact shift or scalar interaction) arising from a delocalization of the metal unpaired spin density onto the protons. The second term is a through-space pseudocontact (or dipolar) shift which arises from a dipolar interaction between the magnetic moment of the unpaired electrons on the metal and the protons. In general, Fermi contact interactions contribute paramagnetic shielding terms with a T^{-1} dependence and pseudocontact interactions involve terms in both T^{-1} and T^{-2} with the latter T^{-2} term usually dominant. The relative contributions from contact and pseudocontact terms depend upon the particular lanthanide ion: contact terms are generally small for ^{1}H but large for ^{13}C resonances in the ligand. The pseudocontact term is important for both ^{1}H and ^{13}C resonances, and the exact effect is dependent both upon the distance of the nucleus from, and its orientation with respect to, the paramagnetic centre. The net effect can actually lead to either shielding or deshielding of the nucleus. For example, in Eu^{3+} complexes a reduction in shielding is usual, whereas for Pr^{3+} there is generally an increase in shielding. Extensive studies and reviews on the contact and pseudocontact interactions have been published.[31-36]

A number of studies have exploited this large temperature dependence of proton chemical shifts in transition metal complexes. Two papers[37,38] have used thulium 1,4,7,10-tetra-azacyclododecane-1,4,7,10-tetrakis(methylene phosphonate) ($TmDOTP^{5-}$) for *in vitro* calibrations and *in vivo* experiments. The molecule, shown in Fig. 3, contains four magnetically equivalent phosphorus nuclei, and six magnetically non-equivalent groups of protons, with three shifted paramagnetically to low frequency and three to high frequency. Protons H_1 through H_4 are the ethylenic protons with H_1 and H_3 attached to one carbon and H_2 and H_4 to the other, and H_5 and H_6 are the methylene phosphonate protons. The temperature dependence at 298 K of the six protons, and the four magnetically equivalent phosphorus nuclei are shown in Table 3. The chemical shifts were found to be independent of concentration

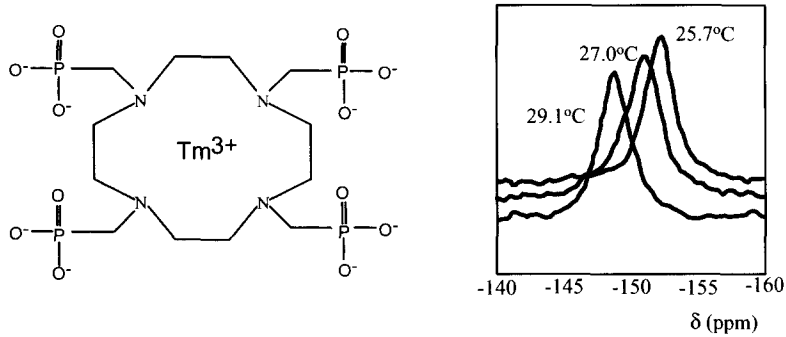

Fig. 3. (left) Molecular structure of $TmDOTP^{5-}$. (right) Section of the *in vivo* ^1H spectrum of $TmDOTP^{5-}$ at 25.7, 27.0 and 29.1 °C acquired using a surface coil placed over the abdomen of a rat. The chemical shift scale was established by assigning the water proton shift as 0 ppm. The spectra were acquired with 1024 averages using a *TR* of 30 ms and total acquisition time of 30 s. (Reprinted from ref. 37 by permission of John Wiley & Sons, Inc. Copyright ©1996 John Wiley.)

Table 3. Chemical shift temperature dependence and relaxation times in $TmDOTP^{5-}$ (adapted from refs 37 and 38)

Resonance	Chemical shift* (ppm)	Temperature dependence (ppm $°C^{-1}$)	T_1 (ms)	T_2 (ms)
H_1	−193.7	1.08 ± 0.09	0.53	0.56
H_2	+92.8	-0.54 ± 0.05		1.1
H_3	+72.7	-0.42 ± 0.04		1.2
H_4	+513.6	-2.88 ± 0.19		0.28
H_5	−398.8	2.19 ± 0.11		0.48
H_6	−155.7	0.87 ± 0.03	1.8	1.7
^{31}P	−350.7	2.18 ± 0.02	2.4	2.5

*The proton chemical shifts are measured with respect to TSP, the phosphorus with respect to 85% phosphoric acid at a pH of 7.6.

over the range 5–40 mM. *In vivo* experiments were also carried out at 200 MHz. The temperature dependence of the chemical shifts were found to be the same as for the *in vitro* calibrations. A warm or cold bag was placed close to the abdomen to change the temperature. Selective excitation pulses were necessary to suppress the large proton signal from water. NMR results shown in Fig. 3 agreed well with readings from a copper-constantan thermocouple placed beneath the muscle of the abdomen. In the second paper[38] the authors showed that in the temperature range 298 to 321 K the temperature sensitivity was not changed for pH changes between 6 and 8, and calcium concentrations up to 5.2 mM. The authors also showed that the thermal sensitivity, and also

robustness with respect to changes in B_0, could be increased by measuring the difference in chemical shifts of H_6 (shifted to low frequency) and H_3 (shifted to high frequency). This complex has also been used for the measurement of temperature gradients in high-resolution NMR, as described later in Section 3.1.4.

A second compound that has been used[39] is Ytterbium tetramethyl-1,4,7,10-tetraazacyclododecane-1,4,7,10-tetraacetic acid (DOTMA) with octa-coordinate bonding of the ligand to Yb via four nitrogen and four oxygen atoms. The twelve equivalent protons of the methyl groups have a resonance at -18 ppm relative to water, and show a temperature dependence of -0.04 ± 0.01 ppm K^{-1}. The chemical shift difference between the ac and axl proton resonances in the ligand was measured in human serum and found to be linear over a range of 308–318 K with a sensitivity of -0.41 ppm K^{-1}.

A series of papers have used a praesodymium complex, Pr-2-methoxyethyl-DO3A (Pr-MOE-DO3A),[40–45] shown in Fig. 4. The major contribution to the temperature dependence comes from the pseudocontact term, with a much smaller contribution from the contact term. The temperature dependence is, therefore, complex and non-linear over a large temperature range, but over a small range 303–323 K the dependence is highly linear. The temperature dependence of the chemical shift difference between the methoxy protons at -24 ppm and the water protons was measured in water, human plasma and tissue to be 0.12 ppm K^{-1}. There was some increase in linewidth with increasing pH, but no effect on the chemical shift. *In vivo* results in rats, shown in Fig. 4, have been acquired at 84 MHz with a surface coil placed on top of the liver. The authors suggested that a concentration of 1 mmol kg^{-1} might be needed for *in vivo* measurements, which is above typical concentrations for human contrast agents such as Gd-DTPA (0.1 mmol kg^{-1}), but well below the lethal dose (LD_{50}) of (Pr-MOE-DO3A) of 12.5 mmol kg^{-1}.

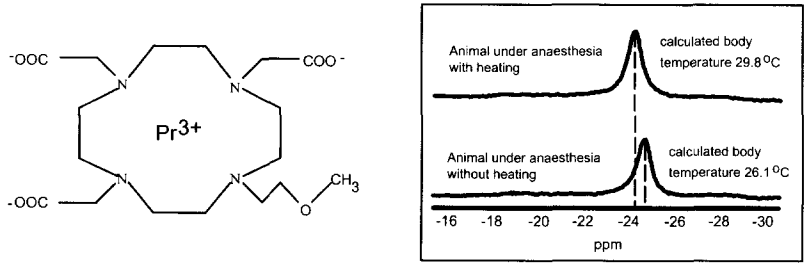

Fig. 4. (left) Chemical structure of Pr-MOE-DO3A. (right) *In vivo* spectra of Pr-MOE-DO3A recorded from the liver of a rat under different heating conditions. Only the region of the methoxy resonance is shown. The lower spectrum was acquired without heating the anaesthetized animal: the upper spectrum was acquired after the animal was warmed with a 44 °C water bed. (Reprinted from ref. 40 by permission of John Wiley & Sons, Inc. Copyright)

3.1.3. Phase-transition compounds and liquid crystals

Compounds undergoing solid–solid phase transitions have been used extensively for temperature calibrations in solid-state NMR, covered later in Section 4.1, but such compounds can also be used for calibrations in the liquid state. When solid, no resonances are observed, but sharp lines appear above the phase-transition temperature. Compounds that have been studied include[46] p-dichlorobenzene (326.4 K), cyclododecane (333.8 K), 2′-hydroxy-4′,5′-dimethylacetophenone (344.2 K), hexamethylcyclohexanetrione-1,3,5 (353.3 K), p-dibromobenzene (360.7 K), p-diacetylbenzene (386.0 K), p-diiodobenzene (402.6 K), 1,2,4,5-tetrachlorobenzene (413.1 K) and hexamethylbenzene (438.6 K).

Liquid crystals can also be used since the temperature-dependent residual static dipole–dipole coupling caused by the anisotropic orientational order produces, in turn, a temperature-dependent static splitting of the proton spectrum. The first study[47] used a 5% v/v solution of benzene in the room temperature mesophase ZLI-1132 liquid crystal in a 5 mm NMR tube. Over 60 lines were present in the spectrum (66 at 360 MHz and 64 at 600 MHz). The authors measured the frequency separation of the outermost lines as a function of temperature at 360 MHz, and fitted this to a third-order polynomial, giving:

$$\frac{\Delta\nu}{\mathrm{d}T} = -4080.13 + 27.353T - 0.04644T^2 \tag{5}$$

where $\Delta\nu$ is measured in Hz. This expression corresponds to a temperature sensitivity of 52.5 $\mathrm{Hz\,K^{-1}}$ at 296 K and 110 $\mathrm{Hz\,K^{-1}}$ at 330 K. If temperature gradients exist across the sample, then the lines will broaden, with the outer lines broadening more than the inner. Temperature gradients of up to 0.45 K were measured at a sample temperature of 325 K, although the exact spatial variation could not be estimated.

A simpler system has also been proposed,[48] namely CH_2Br_2 dissolved at 5% weight in N4 liquid crystal, which is nematic between 293 and 348 K. There are only two narrow lines in this spectrum, and at 305 K the temperature dependence of the splitting, was measured to be 40 $\mathrm{Hz\,K^{-1}}$ with a homogeneous linewidth of $\sim$1 Hz. This temperature probe was used to study temperature gradients in high-resolution NMR experiments, described in the next section.

3.1.4. Measurement of thermal gradients in high-resolution NMR

One of the most important applications of temperature measurement in high-resolution NMR spectroscopy is the estimation of temperature gradients, which normally form along the z-axis of the sample. If the temperature gradient is large enough, then convective flow can occur, in which the outer

layers of the liquid move upward and the inner ones downwards, both with laminar flow profiles. Convection occurs at temperature gradients given by:[48]

$$\frac{\mathrm{d}T}{\mathrm{d}z} > \frac{\kappa\nu}{g\alpha}\frac{RA}{r^4} \tag{6}$$

where α, ν and κ are the coefficients of thermal expansion, kinematic viscosity and thermal diffusivity of the fluid respectively, r is the radius of the NMR tube, g is acceleration due to gravity, and Ra is the theoretical Rayleigh number for the cylindrical geometry of the sample tube. The effects of convection are particularly deleterious in pulse sequences using pulsed magnetic field gradients. If it is assumed that the convection current has a constant laminar flow profile with velocity v, a spatially variant phase (ϕ) is introduced into the measured signal:

$$\phi = \exp\left[i\gamma v \int_0^t p(t')g(t')\mathrm{d}t'\right] \tag{7}$$

where $p(t')$ is the coherence order and $g(t')$ represents gradient pulses of strength g with duration t'. The spatially variant phase means that the magnetization is not completely refocused at the end of the sequence. In sequences using fixed strength gradients for coherence selection, the detected signal intensity is reduced. In sequences where measurements are made as a function of gradient strength, erroneous values for the desired parameter are obtained. For example, pulsed-field gradient diffusion measurements were found to give values of D which are too high,[49] and show a dependence of D on temperature well above the theoretical value. In this particular study, temperatures were measured using 10% $K_3Co(CN)_6$ in D_2O via the temperature sensitivity of the cobalt chemical shift, estimated to be 1.45 ppm K^{-1} (see Section 3.2.4). Assuming a linear temperature gradient, the authors used the linewidth of the cobalt resonance divided by the height of the coil to estimate the temperature gradient. They found that increased air flow and smaller diameter NMR tubes minimized the measured temperature gradient, as expected. Using a 2 mm o.d. sample tube and an air flow rate of 17 litres per minute, convection was reduced to a level such that the measured temperature dependence of D was very close to that predicted theoretically. In fact, even in the presence of convection, the value of D can be measured accurately using a gradient-compensated double-stimulated echo sequence.[50] The spatially variant phase, described in Eq. (7), was made independent of velocity by designing the gradient waveforms such that the first moment of the gradients (m_1) was zero:

$$m_1 = \int_0^t p(t')g(t')t'\,\mathrm{d}t' = 0 \tag{8}$$

The final sequence[50] also included an additional longitudinal eddy-current delay[51] and bipolar gradients to compensate for eddy-current effects.[52] Vastly improved results were achieved in terms of the absolute value of D measured and the temperature dependence of D, compared to the standard non-compensated sequence.

This principle of gradient compensation for convection can also be used in two-dimensional sequences using gradients for coherence selection. If a constant velocity distribution is considered over the range $-\upsilon_{max}$ to $+\upsilon_{max}$, then the signal intensity (S) is given by:[53]

$$S = \frac{1}{2\upsilon_{max}\int_{-\upsilon_{max}}^{\upsilon_{max}} \exp(-i\phi(\upsilon)\mathrm{d}\upsilon)} = \mathrm{sinc}(\upsilon_{max} m_1) \tag{9}$$

and the signal is expected to show a series of damped oscillations as the mixing time is increased as shown in Fig. 5. Compensated gradient waveforms[6] were derived for sequences such as gradient enhanced rotating frame Overhauser enhancement spectroscopy (GROESY)[54,55] and gradient enhanced nuclear Overhauser effect spectroscopy (GOESY),[56,57] waveforms which compensate

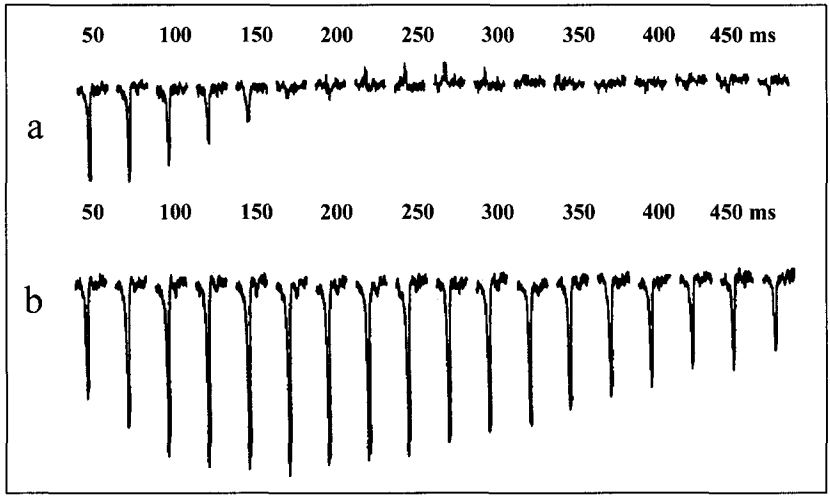

Fig. 5. Mixing time dependence of signal intensity from a GROESY experiment. The signal observed is the Leu NH signal at 8.26 ppm after selectively inverting the Orn CaH signal at 4.76 ppm. (a) Ordinary GROESY experiment. Convection currents in the sample lead to an oscillatory behaviour. (b) GROESY with the three gradient pulses weighted for each mixing time to achieve a zero first moment. (Fig. from ref. 53, Copyright 1998 by Academic Press, reproduced by permission of the publisher.)

by zeroing m_1 using principles derived from MRI.[58,59] Results from these compensation schemes are also shown in Fig. 5.

Since the compensation schemes outlined above rely on the presence of a well-conditioned velocity profile within the sample, it is important to be able to measure this profile directly. For this purpose, a sequence incorporating two mixing times was developed,[60] in which the value of the first mixing time was incremented and the second decremented by the same value of Δt_1. The velocity-dependent phase depends on the difference in the mixing times, whereas diffusion and relaxation effects depend upon the sum of the mixing times, which is constant. The authors also carried out temperature measurements using a 2-D chemical shift imaging (CSI) experiment with the thulium complex described in Section 3.1.2, using the separation between the proton peaks at −155 and +73 ppm. Representative results are shown in Fig. 6.

Finally, the thermal properties of a sample surrounded by air, as is normally the case, and surrounded by an oil (Krytox) have been investigated using the nematic crystal already described.[48] The onset of convection occurred at temperature gradients at about 0.2 K cm^{-1} for the tube immersed in Krytox, and an even smaller value of 0.03 K cm^{-1} for the stand-alone tube. Imaging experiments were carried out using a spin-echo sequence in the presence of a constant z-gradient (0.08 G cm^{-1}). For the stand-alone sample the temperature distribution was found to be highly non-linear with a much larger gradient at the bottom of the tube than at the top, as shown in Fig. 7. In the tube surrounded by Krytox, the gradient was approximately the same throughout the sample.

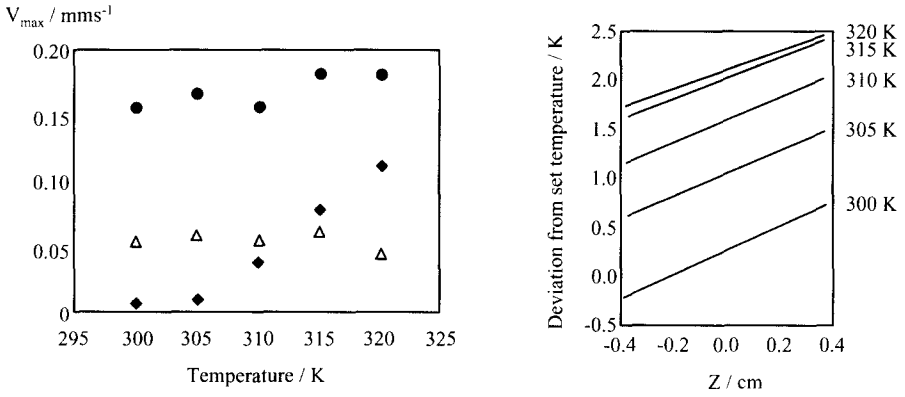

Fig. 6. (left) maximum measured convection velocities for H_2O (in D_2O) for a gas flow of 450 l hr^{-1}. The closed diamonds were measured in the absence of ^{13}C decoupling, the open triangles with a decoupler power of 1.5 W, and the closed circles with 6 W. (right) Temperature profiles measured using TmDOTP, flow rate 450 l hr^{-1} with ^{13}C decoupling at a power level of 1.5 W. (Fig. from ref. 60, Copyright 1999 by Academic Press, reproduced by permission of the publisher.)

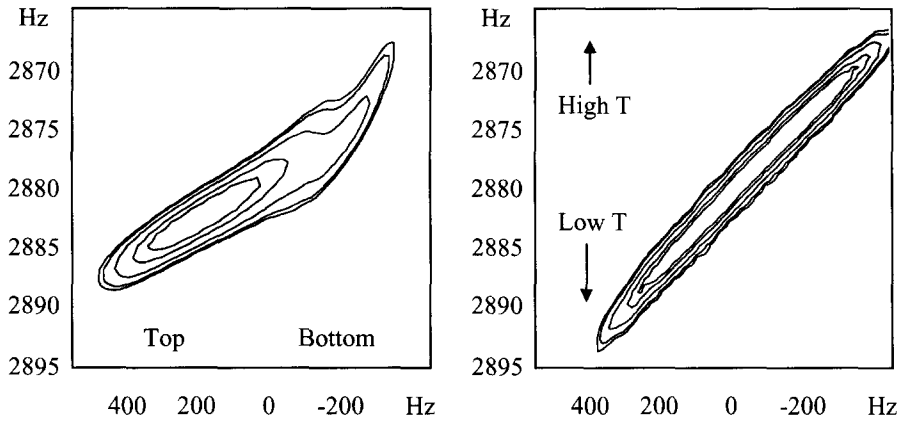

Fig. 7. Results from a study investigating the alteration on sample thermal properties induced by surrounding the sample with an oil bath. 2D contour plots without (left) and with (right) a Krytox oil bath. The horizontal axis corresponds to the position along the z-axis with a calibration of 200 $Hz\,cm^{-1}$ and the vertical axis calibration is 67 $Hz\,K^{-1}$. (Fig. from ref. 48, Copyright 1998 by Academic Press, reproduced by permission of the publisher.)

3.2. Heteronuclei

3.2.1. Carbon

After protons, ^{13}C is the most widely detected nucleus in NMR. Proton cross-polarization and decoupling are usually applied to increase the S/N, and these types of experiment can result in substantial sample heating. Many forms of ^{13}C-based NMR 'thermometers' have been proposed. The first such system[61] was based on the cis-trans conformational equilibrium of furfural, with the linewidths of carbon-3 and the aldehyde carbon being temperature-dependent. There are many disadvantages of linewidth-based measurements, and subsequent developments concentrated almost wholely on temperature-dependent ^{13}C chemical shifts. The first such system utilized a temperature-dependent lanthanide-induced pseudocontact shift in a complex of acetone-d_6 and ytterbium(III)I,1,1,2,2,3,3-heptafluoro-7,7-dimethyl-4,6-octadionate (Yb(fod)$_3$).[62] The δ_{CO} of the acetone-d_6, measured with respect to a CS_2 standard, was almost linearly dependent on $1/T$ with a small quadratic term over a range 200–315 K. If a small amount of protonated acetone was added, then the proton resonance, measured with respect to the protons of TMS, was also found to be temperature dependent:

$$\begin{aligned} ^{13}C:&\ T = (4505\Delta\delta^{-1} + 4640\Delta\delta^{-2} + 70.3) \pm 1.5 \\ ^{1}H:&\ T = (1264\Delta\delta^{-1} - 745\Delta\delta^{-2} + 88.6) \pm 1.5 \end{aligned} \tag{10}$$

A similar approach[63] used 4% v/v p-dioxane in a D_2O solution of ~0.04 M dysprosium nitrate in acetic acid/acetate buffer at pH 5.2. The dependence of the chemical shift separation between the p-dioxane and the acetate methyl resonances was measured to be 0.17 ppm K^{-1}.

The temperature dependence of a number of hydrocarbons has been tabulated,[64] all measurements being referenced to tetramethylsilane (TMS), which itself has a temperature coefficient of 0.012 ppm K^{-1} below 300 K. Most interestingly, the authors investigated the ^{13}C chemical shifts of compounds undergoing rapid chemical exchange. With conformationally inhomogeneous hydrocarbons, linear deshielding was observed with increasing temperature for all carbons not involved in rotational equilibria, but a marked and non-linear upfield shift for those carbon atoms which participate in gauche/trans conformational equilibria.[64]

The temperature dependence of the ^{13}C chemical shift of several haloalkanes showed that the thermal sensitivity was in the order I > Br > Cl,[65] paralleling the heavy atom effect. As a practical thermometer, iodomethane mixed with TMS (3 : 1 v/v) was deemed suitable for a temperature range 208 to 303 K, and di-iodomethane mixed with cyclooctane (5 : 1 v/v) for the range 293 to 448 K. The linear dependences were:

$$\frac{1}{T} = 0.0161 - 0.00057\Delta\delta_{TMS-CH_3I} \qquad \frac{1}{T} = 0.022 - 0.00022\Delta\delta_{cyclo-CH_2I_2} \quad (11)$$

The next development was a multinuclear system, which could potentially be used for measurements at low temperature using proton, fluorine and carbon.[66] The system consisted of 0.25 ml of perdeuterated toluene, 0.25 ml of C_6F_6 and 5.0 ml of $CHFCl_2$. However, for ^{13}C the chemical shift of the methyl carbon of the perdeuterated toluene showed only a weak temperature dependence of 0.004 ppm K^{-1}.

As mentioned previously, one of the major problems with high-powered proton decoupling is the temperature rise, and also temperature gradients, that can occur within the sample. The first ^{13}C-based investigation[67] of this phenomenon used a sealed tube thermometer consisting of a 1 : 1 v/v mixture of CCl_4 and $(CD_3)_2CO$, and measured the difference in chemical shift ($\Delta\delta$) between the carbonyl carbon and the carbon in CCl_4. A linear relationship was found at 67.89 MHz given by:

$$T = 5802.3 - 0.011\Delta\delta \quad (12)$$

When the ratio of the two components of the mixture was changed, then the graph of temperature against $\Delta\delta$ shifted downwards, but the slope remained the same. Results from the paper showed that large temperature rises were present using highly ionic solutions, but that only relatively small radial temperature

gradients were produced relative to the absolute temperature rise. The effects of thermal gradients were investigated further in two papers[68,69] in which the concept of 'ultrahigh'-resolution NMR was introduced. The authors determined that the practical limit to minimum attainable carbon linewidths was set by temperature gradients within the sample. Measurements of these gradients employed two resonances which had different chemical-shift temperature dependences, and these exhibit differential amounts of line-broadening caused by temperature gradients. A solution of acetone in 20% v/v cyclohexane-d_{12} was used, in which the ^{13}C chemical shifts of the carbonyl and methyl resonances at 50.3 MHz change by 0.0144 ppm K^{-1} and 0.006 ppm K^{-1} respectively, relative to the ^{2}H frequency of the lock. Representative results showed that at a decoupler power of 0.75 watts (W) and an air flow of 16 litres min^{-1} gave a temperature gradient of less than 0.01 K. Increasing the decoupler power to 4.4 W resulted in a gradient of 0.24 K. Increasing the air flow predictably reduced the temperature gradients for a given decoupler power.

The first system designed specifically for high temperatures, up to approximately 473 K, used the chemical shift difference between the carbonyl and α-carbons in a range of substituted acetic acids.[70] The temperature sensitivity arises primarily from the effects of intermolecular hydrogen bonding. The compounds studied included bromo-, chloro-, dichloro- and trichloro-acetic acid with temperature sensitivities of 0.0124, 0.0147, 0.019 and 0.021 ppm K^{-1}, respectively. The authors suggested dichloroacetic acid as being the preferred compound, due to its high thermal sensitivity and also the large temperature range (282–467 K) over which the compound is liquid. By using melting point standards the temperature dependence (converted to degrees Kelvin) was measured to be:

$$\Delta\delta = 111.95 - 0.01856T \tag{13}$$

The ability to measure low temperatures using ^{13}C is also important, and one very sensitive system was based on the temperature dependent ^{13}C chemical shifts for certain substituted semibullvalenes that exist as a pair of different valence tautomers.[71] Equilibration between tautomers occurs rapidly on the NMR timescale via non-degenerate Cope rearrangement, and this system is suitable for measurements from 100 to 300 K, using chlorodifluoromethane and perdeuterated dimethyl ether (3:1 or 4:1 v/v) as solvents. The two carbons 6 and 2, shown in Fig. 8, have very different chemical shifts, with the difference, in terms of an equilibrium constant K, given by:

$$\Delta\delta = \delta_6 - \delta_2 = \frac{K(\delta_{6b} - \delta_{2b}) + \delta_{6a} - \delta_{2a}}{1 + K} \tag{14}$$

The value of $\Delta\delta$ was measured over a temperature range 100–320 K and fitted to a fourth order polynomial shown in Fig. 8, with a sensitivity at 110 K

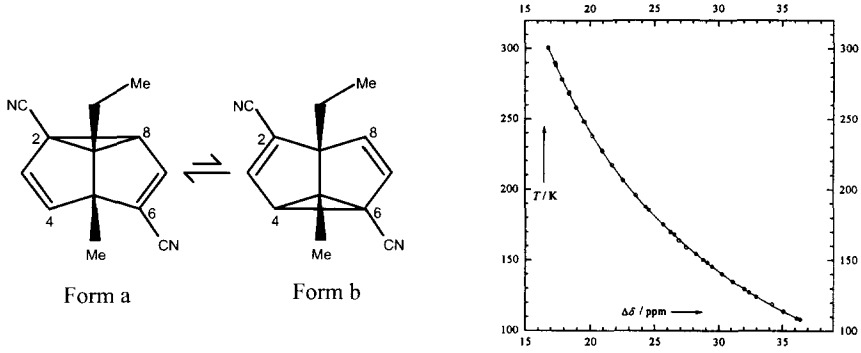

Fig. 8. (left) Schematic of the tautomerism of semibullvalenes and (right) the measured temperature dependence of the chemical shift difference between carbons 6 and 2. (Fig. from ref. 71, Copyright 1998 by Academic Press, reproduced by permission of the publisher.)

of 0.175 ppm K^{-1}. WALTZ-16 decoupling was shown to give minor temperature rises of 0.1–0.2 K between 200 and 300 K, with a rise of about 1 K being recorded close to 100 K. The only complication with this system is that the solvent dependence of the chemical shift difference is very large, and so each solution must be calibrated individually.

Most recently, a ^{13}C system was developed using tris(trimethylsilyl-methane),[72] which can be added to any solution. The compound is stable under basic, acidic, oxidizing and reducing conditions, and can be removed chromatographically. The temperature-dependent resonances move across the 2–5 ppm region of the ^{13}C spectrum which, for most samples, is free of resonances. Experiments carried out at 360 MHz showed a linear sensitivity of approximately 0.0028 ppm K^{-1} for the chemical shift difference between the methine and methyl carbons, over a range 133 to 333 K, for a number of solvents, with the methine signal showing the greater shift. For mixed solvents, linear extrapolation from the individual slopes gave errors of only a few per cent.

3.2.2. Fluorine

Fluorine has a high NMR sensitivity and, having similar chemical properties to protons, fluorine-substituted compounds are used widely in the pharmaceutical and medical industries. In addition to many studies carried out in the gas phase, the temperature dependence of the chemical shifts of liquid-state hexafluorobenzene, 1,4-ditrifluoromethylbenzene (DTFMB), 1,4-dibromo-tetrafluorobenzene (DBTFB) and $CFCl_3$ have been measured.[73,74] Plots of chemical shift vs. temperature were highly linear for hexafluorobenzene (0.0022 ppm K^{-1} from 280 to 340 K) and $CFCl_3$ (0.0048 ppm K^{-1} from 220 to

300 K), slightly non-linear for DTFMB, and highly non-linear for DBTFB. Other studies have characterized the temperature-dependent chemical shift difference between the fluorine resonances of $CF_2{=}CCl_2$ and $CFCl_3$,[75] the peak intensity ratio of the *cis*- and *trans*-isomers of perfluorodecalin,[76] and fluorine–proton and fluorine–fluorine scalar couplings. The latter studies were carried out using $CF_3CF_2CO_2H$ and $CF_3CF_2Cl_2$,[77] 2-fluorobenzotrifluorides,[78] perfluorotoluene,[79] 1,1,4,4-tetrafluoro-1,3-alkadienes[80] and many difluoroethylenes.[81] This work has been reviewed extensively.[82] In general, the temperature dependences were small, with a maximum value of roughly 2 Hz per 100 K.

Fluorine-based temperature measurements are also important for *in vivo* applications. A number of investigators have established that the T_1 value of fluorine nuclei in perfluorocarbons is inversely proportional to the partial pressure of oxygen.[83–86] This finding has formed the basis for a number of *in vivo* MRI studies where, for example, the oxygenation state of a tumour is investigated using an injected perfluorocarbon emulsion. However, the fluorine T_1 value is also temperature-dependent, since the dominant relaxation mechanism is dipole–dipole. Therefore, in such studies, changes in temperature should either be monitored by separate means, or ideally measured simultaneously using NMR. A temperature dependence of the pO_2 of approximately 3 mm $Hg\,K^{-1}$ has been measured[87] for the compound perfluorotripropylamine (FTPA). In perfluorotributylamine (FTBA), this value was estimated to be approximately 9 mm $Hg\,K^{-1}$.[88] In another study of an FTBA emulsion, a unique relationship was established for each resonance of the R_1 ($= 1/T_1$) relaxation rate with respect to the oxygen tension (P) and temperature (T' measured in °C):[89]

$$\begin{aligned}
&CF_3: && R_1 = 1.647 - 0.021T' + 0.027P - 2.08 \times 10^{-4}PT' \\
&\beta\text{-}CF_2: && R_1 = 3.363 - 0.043T' + 0.027P - 2.84 \times 10^{-4}PT' \\
&\gamma\text{-}CF_2: && R_1 = 2.967 - 0.038T' + 0.021P - 1.3 \times 10^{-4}PT' \\
&\alpha\text{-}CF_2: && R_1 = 2.432 - 0.030T' + 0.029P - 2.9 \times 10^{-4}PT'
\end{aligned} \tag{15}$$

If, therefore, either the temperature or oxygen tension is known *a priori*, then the R_1 need only be measured for one peak. If no prior information is available, then R_1 measurements of two peaks are needed. The authors made measurements *in vivo* in a murine tumour and Langendorff perfused rat heart. In further work,[90] three perfluorocarbons, perfluorooctylbromide (PFOB), FTPA, and FTBA, were characterized. The temperature dependence of the R_1 of the CF_3 resonances in each compound was studied. It was found that this dependence was much less than for the CF_2 groups over the temperature range 278 to 323 K. Results from FTBA from 240 to 343 K showed that R_1 was not linear with respect to temperature, with CSA being an important relaxation mechanism, especially for the CF_2 groups. Finally, other more limited *in vivo*

experiments have been performed using the temperature-dependent chemical shift difference between peaks in FTBA[91] and in PFOB.[92]

3.2.3. *Other non-metals: phosphorus, sodium, nitrogen and deuterium*

The temperature dependence of the chemical shift of a large number, nineteen in all, of trivalent phosphorus compounds was determined,[93] with results referenced to the temperature-independent[94] chemical shift of H_3PO_4. The largest values, 0.04–0.06 ppm K^{-1}, were found for ester and amide derivatives of phosphonous acids, but the effect was not strongly influenced by structural differences of groups attached to the trivalent phosphorus atom. Some tertiary phosphines showed a low frequency effect of between 0.01 and 0.025 ppm K^{-1} as temperature was decreased, and primary phosphines were the only compounds to exhibit a high frequency shift with lower temperature of 0.02–0.04 ppm K^{-1}. The authors also found that when the lone pair of electrons on phosphorus was used in bonding to a fourth atom, the temperature dependence was reduced markedly. The first ^{31}P thermometric system[95] used 0.1 M $(C_6H_5)_2P$ and 0.1 M $(C_6H_5)_3PO$ in toluene-d_8. The difference in chemical shifts ($\Delta\delta$) between the two ^{31}P resonances was linear between 183 and 343 K, with a sensitivity of 0.032 ppm K^{-1} at 40.5 MHz. When water was added to the mixture, the straight line plot of T vs. $\Delta\delta$ was shifted downwards, maintaining the same slope, since the chemical shift of $(C_6H_5)_3PO$ moved to high frequency due to the formation of hydrogen bonds.[96] The chemical shift difference between the α– and β–^{31}P resonances in neutral pH solutions of MgATP was shown to have a linear temperature dependence of 0.012 ppm K^{-1}.[97] Measurements were performed on a solution containing 10 mM ATP and 30 mM $MgCl_2$. The authors hypothesized that the temperature dependence reflects either a changing conformation, or the state of the metal ion chelation, of the polyphosphate chain. Refinements of this work were reported in a separate study.[98]

In $Na_4HTm[DOTP]$ a temperature-dependent ^{23}Na chemical shift of -0.51 ppm K^{-1} was reported[99] for a 40 mM solution in deionized water, and -0.48 ppm K^{-1} for a solution containing agarose, both over a temperature range of 297 to 319 K. Very short relaxation times were measured due to the strong quadrupolar relaxation of sodium, in addition to the influence of the unpaired electrons from thallium. A T_1 dependence of 0.1 ms K^{-1} was found, with T_1 increasing with temperature. Using this compound, the same group imaged the effects of RF heating from different configurations of surface coils using an agarose phantom.[100]

The deuterium nucleus, used normally for the lock channel, can be employed as an internal NMR thermometer.[101] Using two deuterated compounds, a power pseudo-FID can be constructed from either a conventional continuous wave (CW) deuterium sweep or a pulsed deuterium FID. The Fourier transform of this signal gives a Lorentzian line with double the natural

linewidth. By measuring the frequency difference between the resonances of the two compounds, and having calibrated this difference as a function of temperature, the sample temperature can be monitored continuously.

Finally, the temperature dependence of ^{15}N chemical shifts has been reported[102] for $^{15}NH_3$, $CH_3{}^{15}NH_2$, $(CH_3)_2{}^{15}NH$, $(CH_3)_3C^{15}N$ and $CH_3C^{15}N$: the coefficients were +0.043, +0.016, +0.005, +0.02 and −0.021 ppm K^{-1}, respectively. Over the temperature range 213 to 313 K there was almost no deviation from linearity. In primary and secondary amines in the liquid state, since the ^{15}N lone-pair of electrons are involved in any hydrogen bonding present, the ^{15}N resonance shifted to higher frequency with decreasing temperature, as seen for the first four compounds. The authors suggested that the ^{15}N resonance in the fifth compound $CH_3C^{15}N$ is dominated by the paramagnetic term, as opposed to the diamagnetic term for the other four compounds, and therefore the intermolecular interactions which displace electrons away from the ^{15}N nucleus lead to a decrease in the paramagnetic term and a low frequency shift of the ^{15}N resonance.

3.2.4. Transition metal complexes

The chemical shift of the metal ion in many transition metals complexes has a high thermal sensitivity. Early work explained this in terms of strong crystal field ligand theory. Using octahedral cobalt (III) complexes as examples, the residual paramagnetism of the ion can be interpreted in terms of the behaviour of the 3*d* electrons.[103–107] Since the interactions between these 3*d* electrons and the ligands are stronger than the interactions between the electrons themselves, the ground state of the cobaltic ion has $^1A_{1g}$ symmetry and a *d* electron configuration (t_{2g}).[6] The various excited states of the ion arise from configurations $(t_{2g})^{6-n}(e_g).^n$ Only one triply-degenerate excited state, the $^1T_{1g}$ state, actually contributes to the temperature-dependent paramagnetism by mixing with the ground state under the influence of a magnetic field. The value of this paramagnetism is inversely proportonal to the energy separation between the ground and excited $^1T_{1g}$ states. Therefore, the ground state of the complex consists of the electronic energy $E(A_{1g})$ plus the sequence of vibrational levels $(n_1+\frac{1}{2})h\omega_0$ where $n_1 = 0, 1, 2 \ldots$. The excited state then has the values $E(^1T_{1g})$ plus $(n_1^N + \frac{1}{2})h\omega_N$ where $n_1^N = 0, 1, 2 \ldots$. Temperature is important since the occupation of the ground vibrational states is described by a Boltzmann distribution, and the effective separation between the ground and excited states is therefore temperature dependent. Since the ligand field is never strong enough to force the ground state to be pure (t_{2g}),[6] there will be some interactions between the ground state and the $(t_{2g})^4(e_g)^2$ excited state,[105] but this effect is small. In addition, the t_{2g} and e_g orbitals are not pure atomic d orbitals due to mixing of the metal and ligand orbitals. Again, this effect is small. The resonance frequency for various cobaltic complexes[104] was found to increase by about 0.015% over the range

293–353 K. The temperature coefficient of $Co(CN)_6^{3-}$ was measured to be 1.38 ppm K^{-1} over a range 275–353 K, that of $Co(NO_2)_6^{3-}$ to be non-linear with a value of 2.85 ppm K^{-1} at 282 K and 3.04 ppm K^{-1} at 316 K, and that of $Co(NH_3)_6^{3+}$ also to be non-linear with a coefficient of 1.42 ppm K^{-1} at 283 K and 1.68 ppm K^{-1} at 348 K.[107] A value of 2.3 ppm K^{-1} was found for cobalt(III) trisacetylacetonate, $Co(acac)_3$, in toluene, 2.97 ppm K^{-1} for the same compound in chloroform, and 1.4 ppm K^{-1} for potassium hexacyanocobaltate (III) in aqueous solution.[106]

Although this theory predicts the temperature dependence of the metal chemical shifts, it also predicts, for example, that an isotope shift should be independent of the remoteness of substitution, since only the vibrational frequencies of the whole molecule are considered. In practice a large dependence of the isotope on the position of substitution is observed experimentally. A theory[108] which successfully explains both the intrinsic temperature dependence of the chemical shift and the observed isotope shifts is based on the expansion of the nuclear shielding as a function of powers of displacement coordinates. The intrinsic temperature-dependent nuclear shielding can be expressed as:

$$\sigma_0(T) - \sigma_0(300) \approx \left\{ \left(\frac{\partial \sigma}{\partial \Delta r} \right)_e + \frac{1}{3a} \left(\frac{\partial^2 \sigma}{\partial \Delta r^2} \right)_e \right\} \{ \langle \Delta r \rangle^T - \langle \Delta r \rangle^{300} \}_{\text{vib}} + \left(\frac{\partial \sigma}{\partial \Delta r} \right)_e \{ \langle \Delta r \rangle^T - \langle \Delta r \rangle^{300} \}_{\text{rot}} \quad (16)$$

where a is the Morse parameter, and the derivatives of the nuclear shielding ($d\sigma$) with respect to the displacement coordinates (Δr) are evaluated at the equilibrium bond length. Using values for isotope shifts, mean bond displacements and the mass dependence of bond length on ligand mass, the temperature sensitivity of the chemical shift can be calculated. Results have shown very good agreement with experiment. For vanadium chemical shifts in $V(CO)_6^-$ theoretical results gave −44.3 ppm over the range 190–340 K, compared to experimental values of −40 ppm. In these compounds the vibrational contribution to the shielding change was almost twenty times that of the rotational. For $Co(CO)_6^-$ a temperature change of −110 ppm over the range 280–360 K has been reported, and results from the model gave −100.5 ppm, with the vibrational contribution again the major factor. This theory can also predict the non-linear temperature dependence often found in molecules such as $Co(NH_3)_6^{3+}$, with linearity approached more closely at higher temperatures.

In addition to mechanistic studies, ^{59}Co is the transition metal that has found most widespread use in thermal measurements. Since it is a quadrupolar nucleus, a symmetric chemical environment around the central cobalt nucleus is necessary to observe narrow lineshapes for precise temperature measurements. ^{59}Co

detection was first suggested for measuring temperature and temperature gradients in high-resolution NMR.[109] The resonant frequency is very close to carbon, so standard probes can be used with little retuning. The compound $K_3Co(CN)_6$ was proposed for polar compounds, and $Co(acac)_3$ for organic solvents. The hexacyano compound had a linewidth of 2 Hz in D_2O with a sensitivity of 1.5 ppm K^{-1}, and $Co(acac)_3$ a linewidth of ~80 Hz in $CDCl_3$ and sensitivity of 3.15 ppm K^{-1}: concentrations of both compounds were 0.1 M. If the cobalt compound is placed inside the sample being studied, broadening of its lineshape is indicative of thermal gradients across the sample, as described in Section 3.1.4. For *in vivo* applications, the highly symmetric complex $[Co(H_2NCH_2CH_2NH_2)_3]Cl_3$ has been used.[110–113] This agent has a very short value of T_1 due to the coupling between the central cobalt ion and the nitrogen atoms in the ligand, which permits rapid data collection. The thermal sensitivy, both *in vivo* and *in vitro* was measured to be 1.4 ppm K^{-1}.[110,111] For *in vivo* animal experiments, the complex was encapsulated in liposomes before injection. Ultrasound heating of the liver[112] and microwave heating of tumours in rats[113]

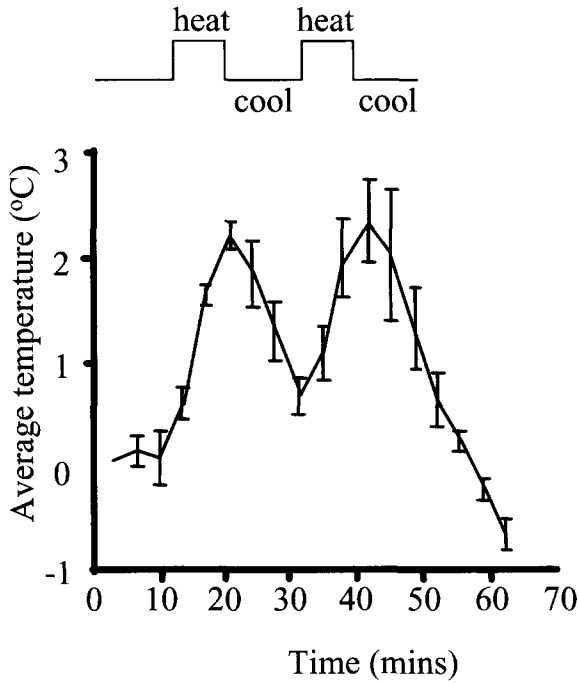

Fig. 9. Graph of temperature rise vs. time as a function of microwave heating (and subsequent cooling periods), in a tumour induced in a rat. The temperature was measured using a ^{59}Co chemical shift method. The error bars correspond to one standard deviation. (Fig. from ref. 113, Copyright 1996 by Academic Press, reproduced by permission of the publisher.)

have been carried out using this agent: results from the latter study are shown in Fig. 9.

For heavy metals, such as ^{195}Pt, the chemical shifts and the temperature dependence are largely determined by the paramagnetic term.[114–116] For example, in *trans*-$PtCl_2L_2$, where $L = (n\text{-}C_4H_9)_3P$, the dependence was -0.32 to -0.34 ppm K^{-1} over a temperature range of 250–345 K. *Cis*-$PtCl_2L''_2$, where L'' was $C_2H_5(C_6H_5)_2P$, had a larger coefficient of -0.54 ppm K^{-1}, and *cis*-$PtCl_4L'_2$, where L' was $(n\text{-}C_3H_7)_3P$, the largest value of -0.84 ppm K^{-1}. The Pt-hydrides studied had a much lower coefficient: for example, *trans*-$PtHClL'_2$ was measured to be only -0.15 ppm K^{-1}. The reduced paramagnetism observed in the halides was in agreement with the reduced sensitivity of the chemical shift to temperature. The Pt–P scalar coupling was also found to be temperature dependent[117] in *cis*- and *trans*-$[PtCl_2(PBu_3^n)_2]$, as shown in Fig. 10. The mechanism proposed by the authors involves the occupation of axial positions in the complex by solvent molecules. Competitive solvation,

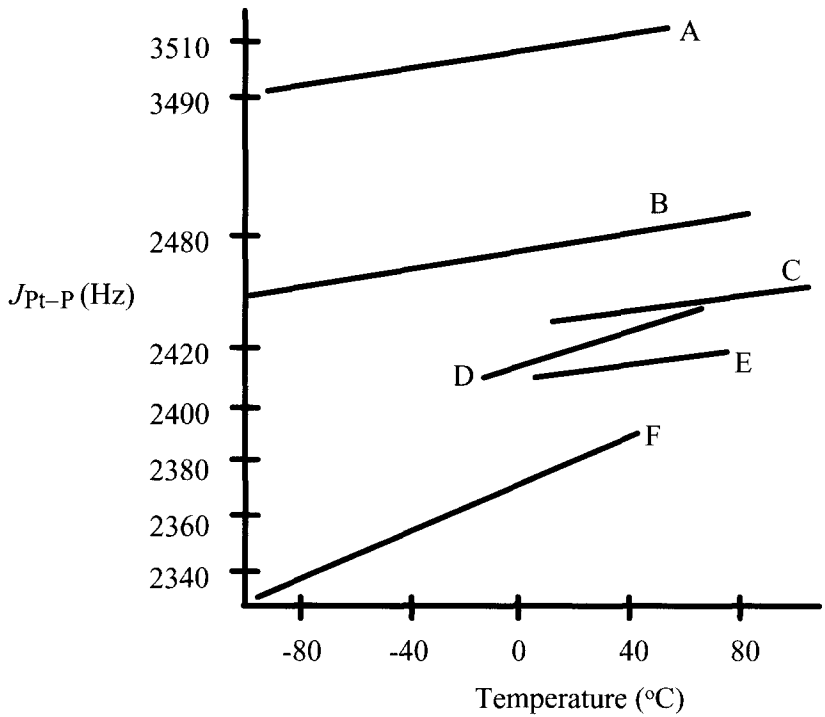

Fig. 10. Temperature dependence of $^1J_{Pt-P}$. (A) *cis*-$[PtCl_2(PBu^n_3)_2]$, 50 mg ml^{-1} in CH_2Cl_2; (B) *trans*-$[PtCl_2(PBu^n_3)_2]$, 50 mg ml^{-1} in n-hexane; (C) *trans*-$[PtCl_2(PBu^n_3)_2]$, neat; (D) *trans*-$[PtCl_2(PBu^n_3)_2]$, 50 mg ml^{-1} in CCl4; (E) *trans*-$[PtCl_2(PBu^n_3)_2]$, 50 mg ml^{-1} in butyric acid; (F) *trans*-$[PtCl_2(PBu^n_3)_2]$, 50 mg ml^{-1} in CH_2Cl_2. (Adapted with permission from ref. 117, Copyright 1976 NRC Research Press.)

occurring primarily in the plane including Cl–Pt–Cl, perpendicular to P–Pt–P, was postulated as possible. This would cause partial rehybridization of electron density at the Pt nucleus with a loss in s character of the Pt—Pt bonds, leading to a fall in the value of $^1J_{Pt-P}$. This effect would decrease with temperature, as increases in diffusion remove molecules from the solvation sphere, thus explaining the increase in $^1J_{Pt-P}$ with increasing temperature.

In ^{103}Rh-detected NMR the temperature dependence of the weighted mean ^{103}Rh chemical shift[118,119] of the *trans*-isomer of $[Rh(MeSCH_2CH_2SMe)_2Cl_2]^+Cl^-$ was found to be roughly -1.0 ppm K^{-1}. The ^{31}P and ^{103}Rh resonances in $Rh[(C_6H_5)_3P)_3Br$ had a dependence not greater than 0.02 ppm and -1 ppm K^{-1}, respectively, over the temperature range 235–280 K.[120]

Temperature-dependent ^{183}W chemical shifts have been characterized.[121,122] For three complexes, $W(\eta\text{-}C_6H_5)(CO)_2H\{P(OMe)_3\}$, $W(\eta\text{-}C_6H_5)(CO)_2H$ (PMe_2Ph), and $W(\eta\text{-}C_6H_5)(CO)_2H(PMePh_2)$, a chemical shift change of roughly 1.5 ppm K^{-1} occurred with increasing temperature.[121] A value of 0.16 ± 0.04 ppm K^{-1} in the range 274–332 K was found for Na_2WO_4 (2.31 molal aqueous solution) and 0.34 ± 0.16 ppm K^{-1} in the range 284–310 K for WCl_6 (0.88 molal in CS_2).[122]

In Cu(I), a d^{10} ion, complexes there are obviously no electronic transitions involving the ligand field splitting of partially filled *d* orbitals of the metal atom, transitions which would contribute to a paramagnetic term in the ^{63}Cu shielding. A typical measured temperature sensitivity of 0.055 ppm K^{-1} was an order of magnitude less than for other transition metals.[123]

For ^{55}Mn, a sensitivity of 0.016 ppm K^{-1} was measured for a $KMnO_4^-$ solution at a Larmor frequency of 19.087 MHz.[124] An extensive study of the temperature dependence of ^{55}Mn chemical shifts and linewidths contains data for more than 14 compounds.[125] Within the series of compounds $Mn(CNR)_6^{+,2+}$ the ^{55}Mn chemical shifts increased linearly with temperature over the range 238 to 318 K, with coefficients between roughly 0.4 and 0.7 ppm K^{-1}. The linewidths also decreased monotically with temperature for all *R* groups, except for methyl and ethyl, corresponding to a dominant quadrupolar relaxation mechanism, where the linewidth is inversely proportional to temperature. The increase in linewidth with temperature for these two smaller complexes was explained by assuming that spin-rotational relaxation was the dominant mechanism.

The temperature dependence of the ^{67}Zn chemical shift was measured between 253 and 343 K for 2 M $ZnCl_2$ (0.7 ppm K^{-1}), 4 M $ZnCl_2$ (0.48 ppm K^{-1}), 1.9 M $ZnBr_2$ (0.61 ppm K^{-1}), and 2.2 M $Zn(ClO_4)_2$ (no temperature dependence).[126] Zinc linewidths were also found to be highly temperature sensitive.

Measurements of ^{77}Se have been made using $Pd(Se_2CN\text{-}i\text{-}Bu_2)PPh_3Cl$, with the Se atom *trans* to the phosphine more temperature sensitive (0.32 ppm K^{-1}) than that *cis* to the phosphorus atom (0.13 ppm K^{-1}).[127] The authors proposed that this difference was caused by differential solvent–solute interactions since the Se atom in the *cis* position interacted little with the solvent due to steric

effects, and the chemical shift was also almost independent of solvent, unlike that for the Se atom in the *trans* position. The authors also reported the temperature sensitivity of the Se chemical shift in the compound $Zn(Se_2CNEt_2)_2$ with shifts of roughly 0.23 ppm K^{-1} in $CDCl_3$ and 0.16 ppm K^{-1} in CS_2. The T_1 increased with temperature for both compounds, and the authors concluded that, in the absence of dipole–dipole and scalar coupling, CSA must be the dominant relaxation mechanism.

Studies of ^{111}Cd[128] showed a shift of roughly 0.5 ppm K^{-1} in aqueous solutions of $CdCl_2$, $Cd(ClO_4)_2$, $CdSO_4$ and $Cd(NO_3)_2$. For ^{113}Cd a series of alkoxides showed a general reversible increase in Cd shielding of +0.10 ppm K^{-1} within the range 297–315 K.[129] For dimethylcadmium(I) the change was −0.17 ppm K^{-1}.

For ^{199}Hg, the chemical shifts of various cyclohexylmercuric systems were measured[130] at temperatures between 350 and 200 K. For many of the systems, there were two chemical shifts at lower temperatures, corresponding to the mercury atom being in the axial or equatorial position, and a single peak at higher temperatures. In general, the equatorial chemical shift was much more sensitive than the axial to temperature. For example, $C_6H_{11}HgOCOCH_3$ in CH_2Cl_2/pyridine had chemical shifts of −648(eq) and −556(ax) ppm (referenced to diphenylmercury in chloroform) at 245 K, and −633(eq) and −556(ax) at 215 K. Mercury resonances in 0.5 molal $Hg_2(NO_3)_2$ solution (−0.29 ppm K^{-1}) and 1 molal $Hg(NO_3)_2$ solution (−0.65 ppm K^{-1}) both in 1 molal HNO_3 were measured[131] in the temperature range 300–350 K.

Studies using ^{133}Cs[132, 133] showed an approximate −0.2 ppm K^{-1} shift for CsBr. The Cs chemical shift also changed with temperature for the complexation of cesium tetraphenylborate with 18-crown-6 in pyridine, due to the presence of four constituents in the equilibrium, and the temperature dependence of the equilibrium constants.[133]

The temperature dependent chemical shifts[134–138] of ^{51}V were comparable in magnitude to those for ^{59}Co and ^{195}Pt, with values of 1.17 ppm K^{-1} for $CpV(CO)_3py$, 1.2 ppm K^{-1} for $CpV(CO)_3THF$, 0.5 ppm K^{-1} for $V(CO)_3NO(PhP(CH_2CH_2PPh_2)_2)_2$ and 0.25 ppm K^{-1} for $[V(CO)_5CNCH_2CO_2Et]^-$.

Temperature sensitivities of between 0.14 and 0.22 ppm K^{-1} have been measured for ^{95}Mo resonances in [Mo(π-arene)$(CO)_3$] with higher shielding at lower temperature.[139]

The ^{93}Nb chemical shift in $(\eta_5\text{-}C_5H_5)Nb(CO)_4$ in tetrahydrofuran had a thermal sensitivity measured as 0.38 ppm K^{-1} from 210 to 340 K,[140] and the same compound in CH_2Cl_2 a value of 0.42 ppm K^{-1}. A linear decrease in shielding of the Nb nucleus, with increased temperature, of 0.25 ppm K^{-1} for $[CpNb(H)(CO)_3]^-$ and $[CpNb(D)(CO)_3]^-$ has been measured,[141] and also a non-linear decrease in linewidths with increased temperature for both of these compounds, indicative of increased molecular correlation times. $[Et_4N][Nb(CO)_6]$ in THF showed a linear temperature dependence with a sensitivity of 0.18 ppm K^{-1} over a range 203 to 323 K, and an increase in linewidth from 9.8 Hz (323 K) to 23 Hz (203 K).[142]

Finally, the T_1 and chemical shifts of ^{125}Te and ^{123}Te have been measured[143] as a function of temperature in $Te(CH_3)_2$. The linear dependence of the T_1 with temperature showed that spin-rotation was the dominant relaxation mechanism. An increase in temperature led to a low frequency shift of 0.128 ppm K^{-1} for $Te(CH_3)_2$ and 0.167 ppm K^{-1} for $TeCl_4$ in HCl.

3.2.5. Non-transition metals

Many studies have investigated the temperature dependence of the ^{205}Tl chemical shift and T_1 value. Tl is a good NMR probe for studies of the role of K^+ in biological systems since the ionic radii of the two nuclei are very close. The wide range of Tl chemical shifts can be interpreted in terms of a second-order paramagnetic contribution to the field at the Tl nucleus.[144] In both the crystalline and molten states, a linear paramagnetic shift with temperature has been observed. For TlCl, the temperature coefficient was approximately 1 ppm K^{-1}: more covalent thallium compounds showed a much reduced temperature dependence. In biological experiments, a Tl–valinomycin complex[145,146] showed a non-linear temperature increase of 10 ppm to higher frequency with an increase in temperature of 80 K. This shift to higher frequency also occurred in hexamethylphosphotriamide (34 ppm over 80 K), but to lower frequency in water (40 ppm over 80 K). The chemical shift vs. temperature for complexes of Tl with antibiotics nonactin, monactin and dinactin showed two distinct linear regions, one at high temperature with an incremental shift of 0.153 ppm K^{-1} and a low-temperature shift of 0.095 ppm K^{-1}, indicating two conformational species. The variation in Tl chemical shift with temperature has also been measured for a number of dimethylthallium(III) derivatives,[147,148] $Tl(CH_3)_2X$, all showing shifts to higher frequency with increasing temperature. In H_2O, $X = NO_3$ and $X = BF_4$ gave $d\delta/dT$ values of 0.44 and 0.46 ppm K^{-1} respectively with highly linear plots. In dimethylsulphoxide, $X = NO_3$ gave 0.25 ppm K^{-1} with slight curvature, and in CH_3OH, $X = O_2CCH_3$ and $X = BF_4$, 0.67 and 0.39 ppm K^{-1}, respectively, again with slight curvature. These results could be explained partially by the temperature dependence of ion formation in solution, where rapid exchange occurs, and the chemical shift of the Tl signal is an average of the weighted shifts of the two species. However, the authors concluded that the temperature dependence originates principally from vibrational effects within the $Tl(CH_3)_2^+$ cations and/or from vibrational effects involving the interaction of such species with coordinated solvent molecules.

Temperature-dependent chemical shifts of ^{119}Sn have been noted in Me_3SnCl/solvent complexes,[149] and via association in tin dialkoxides.[150] In n-butyltin trialkoxides the shifts were found to be highly non-linear with temperature, whereas for the t-butoxides $Me_2Sn(OBu^t)_2$ and $MeSn(OBu^t)_3$ linear increases in tin shielding with temperature were reported, corresponding to thermal sensitivities of 0.06 and 0.11 ppm K^{-1}, respectively.[151,152] The

dialkyltin dialkoxides $R^1{}_2Sn(OR^2)_2$ generally showed large non-linear decreases in shielding with temperature.

A few liquid state studies have been carried out using ^{207}Pb, but this nucleus has received most attention in magic angle spinning (MAS) studies, covered in Section 4.7. A temperature dependence of 1.88 ppm K^{-1} has been reported for aqueous solutions of lead nitrate.[153] A 0.5 ppm K^{-1} decrease in chemical shift with increasing temperature has also been measured for 2 M triisobutyllead acetate in acetic acid.[154] The T_1 of $Pb(ClO_4)_2$ at 10.4 MHz was found to increase with temperature from 243 to 308 K and then decreased above this temperature.[155] Of all the compounds studied, the temperature dependence of the ^{207}Pb chemical shift in liquid-crystalline phases of soaps has the highest value.[156] A series of even chain-length lead(II) carboxylates was investigated, with the highest dependence in the lamellar phase being 5.06 ppm K^{-1} for decanoate, and in the liquid phase 4.287 ppm K^{-1} for tetradecanoate. For all the chain-lengths studied, the dependence was 2.9 ppm K^{-1} or higher. The authors suggested that there are two mechanisms to explain the temperature dependence of the chemical shift. The first is the change in the mean excitation energy of the 6s6p electronic states of Pb(II) due to thermal motion of the ligands. The second involves the temperature dependence of the dissociation coefficient of lead(II) carboxylates, with the ^{207}Pb resonance being the average signal from different coordination species.

4. NMR TEMPERATURE MEASUREMENTS IN THE SOLID STATE

Variable temperature cross-polarization (CP) MAS spectroscopy is commonly used to study molecular structure, dynamics and reactivity in the solid state.[157–165] Accurate quantitative analysis requires knowledge of the exact sample temperature over a wide range of temperatures. There are several mechanisms by which the sample temperature is not reflected accurately by the temperatures recorded by the sensors, which are typically positioned at least a couple of centimetres from the sample itself, in the NMR probe. High radiofrequency power levels are used in CP and dipolar decoupling sequences, and any resultant sample heating is not detected by the sensors. This type of heating typically results in small radial thermal gradients within the sample. If the driving and bearing air temperatures are not very close in value, then significant longitudinal thermal gradients form, but even in the absence of this effect such gradients can be produced via heat losses at the ends of the sample. Frictional heating between the rotor and the bearing gas is also a major factor. A certain fraction of the kinetic energy of the spinning rotor is converted into an increase in the temperature of the bearing gas. This heats up the stator and the rotor and can again lead to temperature gradients within the sample. This effect is more pronounced at lower temperatures, since the heat capacities of the bearing gas and sample increase with

temperature. Joule-Thompson effects, which result from the expansion of the driving and bearing gases being forced through small holes, can result in either heating or cooling of the sample depending upon the temperature of the gases. Another mechanism of sample heating in conductive samples is the induction of eddy currents within the sample: this effect is characterized by a particularly large dependence of the sample temperature upon spinning rate. The effects of each of these mechanisms has been measured experimentally using the chemical compounds described in the following sections. Further details have been published elsewhere,[166] and a very useful and relevant review of solid-state probe design has been published recently.[167]

4.1. Phase transition calibration materials

Since neither the thermocouple nor VT air temperature readings are necessarily accurate measurements of the sample temperature, some method of calibration is required to determine the actual sample temperature under given conditions of sample spinning speed, air pressure and desired sample temperature(s). The most straightforward method is to use materials which show a significant spectral change associated with a phase transition at known temperature. Table 4 lists compounds which have been used for such calibrations. All the compounds listed undergo solid–solid phase transitions associated with changes in crystalline structure, with the exception of protonated and deuterated squaric acid (H_2SQ) which undergoes an antiferromagnetic–paraelectric phase transition. For example, in 1,4-diazabicyclo-[2,2,2]-octane (DABCO) the ^{13}C lineshape is dominated by dipolar coupling to ^{14}N below the transition temperature, and shows two broad unresolved lines. Above the phase-transition temperature of 351 K,

Table 4. Properties of phase-transition compounds used for NMR temperature calibrations in the solid state

Compound	Nucleus	Transition point (K)	Reference
P_4S_3	^{31}P	314	168
$RbNO_3$	^{87}Rb	437	169
$LiNaSO_4$	^{23}Na	791	169
hexamethylbenzene	^{13}C	115–120	170
NH_4NO_3	^{15}N	255,305,357,398,443	171
tetrakis(trimethylsilyl)silane	^{13}C	238–241	172,173
d-camphor	^{13}C	238	170
2,2-dimethylpropane-1,3-diol	^{13}C	315	172
CBr_4	^{13}C	320	169
1,4-diazabicyclo-[2,2,2]-octane	^{13}C	351	170
squaric acid	^{13}C	373	174
deuterated squaric acid	^{13}C	520	174

molecular reorientation averages the dipolar coupling to zero, and the ^{13}C resonance becomes a single line.

An NMR investigation of the phase transitions in ammonium nitrate[172] found that the 'apparent' sample temperature required to induce the IV to III phase transition depended upon the square of the spinning speed. The cause of this anomaly was the additional sample heating from frictional heating between the rotor and air bearing, which is related to the spinning speed. The exact effect of the spinning speed depended on factors such as the packing characteristics of the sample, the bearing-to-drive gas flow ratio, and the type of gas used.

Problems associated with using a solid–solid phase transition include the slow kinetics, requiring long times for thermal equilibration, and volume changes that can cause unstable spinning. A compound that can potentially overcome some of these limitations is squaric acid, which undergoes an antiferromagnetic–paraelectric phase transition at 373.2 K (or 520 K for the deuterated analogue). Below this temperature the H_2SQ crystal has a structure built up from pseudo-symmetric, hydrogen-bonded C_4O_4 units with four non-equivalent carbons. Above the phase-transition temperature the four carbons become equivalent. Initial ^{13}C CPMAS NMR temperature calibration experiments were run at 90 MHz with a small crystal to minimize temperature gradients.[174] The actual phase transition temperature was calculated by measuring the integrated area of the peaks corresponding to the high- and low-temperature phases, and calculating the temperature at which these were equal. This process is shown in Fig. 11. Temperature gradients were also measured using this compound. The authors varied the sample size and measured the corresponding temperature gradients across the sample. When

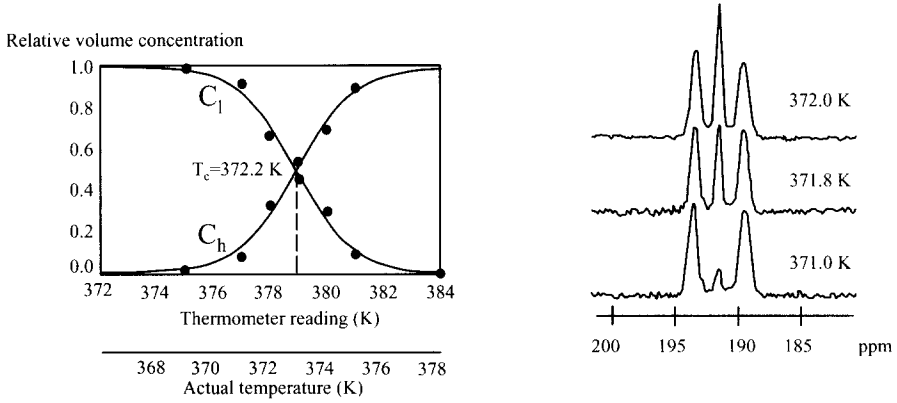

Fig. 11. (left) Relative volume concentration of the low- and high-temperature phases of squaric acid vs. temperature. (right) ^{13}C CPMAS spectra of squaric acid at temperatures close to the phase-transition point. (Adapted with permission from ref. 174, Copyright 1996 Elsevier.)

the rotor was filled to 25% capacity, there was a 0.4 K gradient across the sample. This increased to 2 K for a fully filled rotor.

4.2. Proton chemical shifts

The first temperature measurements in MAS were made[175] with a small 4 mm spherical sample of either ethylene glycol or methanol packed together with KBr into a rotor (the spinning sideband spectrum in the Br spectrum gives an accurate indication of spinning speed). The formula of Van Geet[13] was then used to calculate the temperature. A similar approach was to soak the solid of interest in methanol and measure the difference in chemical shift between the methyl and hydroxyl protons.[173] For calibration purposes the authors chose tetrakis(trimethylsilyl)silane (TTMSS) as the solid. An MAS probe, with double-bearing rotation mechanism, was used at 500 MHz with spin rates between 2 and 2.2 kHz. Sharp lines, around 20 Hz, were observed for the methyl and hydroxy protons. Adapting the Van Geet formula to 500 MHz gave results which corresponded within 3 K to measurements made using samarium acetate tetrahydrate (see Section 4.3) over a range 170–290 K. In order to double-check this calibration, the phase-transition temperatures of TTMSS and 2,2-dimethylpropane-1,3-diol (DMPD) were measured: values of 239 and 314 K respectively compared well to literature values of 238 and 315 K. Finally, the authors showed that the temperature measured by a thermocouple placed near the rotor was considerably lower than the actual sample temperature: this difference increased from 3 K at 330 K to 22 K at 185 K. Although this method has the advantage of being very simple, the solid must be chosen carefully so as not to interfere with the hydrogen bonding of the methanol in which it is soaked. In order to investigate further the relationship between spinning speed and sample temperature, another study[168] used a sample of crystalline KBr doped with ethylene glycol. They measured an exponential correlation between the sample temperature, T_{samp}, and spinning speed given by:

$$T_{samp} = T_{air} - 3.3 + 3.03\exp(0.31\nu_r) \tag{17}$$

where T_{air} was the ambient air inlet temperature, and the spinning speed, ν_r, was measured in kilohertz.

4.3. Carbon chemical shifts

The most commonly used compound for ^{13}C-based solid-state temperature measurements is samarium acetate tetrahydrate.[176] The Sm^{3+} is nine-coordinated by the oxygen atoms of three bidentate acetate ligands, two water molecules, and a bridging oxygen from an acetate ligand of an adjacent

molecule. The most useful signal was found to be the downfield carbonyl doublet, which consists of peaks in a 2 : 1 intensity ratio, corresponding to the two chelating-only and one chelating-and-bridging acetate groups, per unit cell, respectively. Least squares analysis of the data over the temperature range 77 K to 333 K gave the following equation:

$$\delta_{\text{ppm}} = -\frac{4867}{T} + 209 \tag{18}$$

Most lanthanides have a T^{-2} dependence for the dipolar shift, but Sm^{3+} is unique in that the T^{-1} term predominates. When the Sm^{3+} compound was blended with paradimethoxybenzene, an identical temperature sensitivity was obtained. The compound is most suited to low temperature studies, as low as 77 K, at which temperature the sensitivity is 0.82 ppm K^{-1}. Above room temperature (sensitivity 0.055 ppm K^{-1}), the change in δ as a function of T, relative to the NMR linewidth, became small and difficult to measure accurately. The upper limit was set by the compound undergoing a solid–solid phase transition at 343 K. It should be noted that the other two lines in the ^{13}C spectrum also showed a Curie law dependence on temperature.

4.4. Nitrogen chemical shifts

The first ^{15}N solid-state thermometer was based upon the tautomerism of 1,8-dihydro-5,7,12,14-tetramethyldibenzo(b,i)-1,4,8,11-tetraazacyclotetradeca-4,6,11,13-tetraene$^{15}N_4$(tetramethyldibenzotetraaza(14)annulene) (TTAA).[177,178] The tautomeric structures of TTAA are shown in Fig. 12. Four lines are observed from the four chemically inequivalent nitrogen atoms. The chemical shift differences between nitrogens a/b and c/d are given by:

$$\begin{aligned}
\frac{d\delta_{ab}}{dT} &= -3.72 \times 10^5 T^{-2} \left[\exp\left(-\frac{595}{T}\right) + 0.0771 \exp\left(-\frac{560}{T}\right) \right] \\
&\quad \times \left[1 + 2.18 \exp\left(-\frac{595}{T}\right) + 1.31 \exp\left(-\frac{560}{T}\right) \right]^{-2} \\
\frac{d\delta_{dc}}{dT} &= -3.645 \times 10^5 T^{-2} \left[\exp\left(-\frac{595}{T}\right) + 0.5656 \exp\left(-\frac{560}{T}\right) \right] \\
&\quad \times \left[1 + 2.18 \exp\left(-\frac{595}{T}\right) + 1.31 \exp\left(-\frac{560}{T}\right) \right]^{-2}
\end{aligned} \tag{19}$$

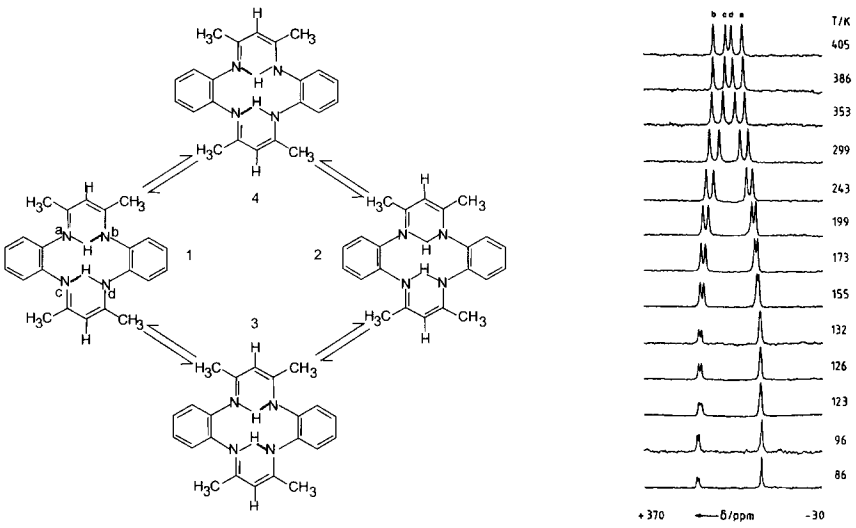

Fig. 12. (left) Four tautomeric forms of TTAA. (right) ^{15}N CPMAS NMR spectra of 95% ^{15}N-enriched TTAA at 9.12 MHz as a function of temperature. (Fig. from ref. 177, Copyright 1990 by Academic Press, reproduced by permission of the publisher.)

The maximum temperature sensitivity occurs at 200 K when $d\delta_{dc}/\delta_{dc}$ is 0.55 ppm K^{-1}. TTAA can potentially be used up to 502 K, which is its melting point, but the maximum temperature used in these studies was 405 K. It also is internally referenced and can be used for absolute temperature measurement. The authors used this compound to investigate the effects of sample spinning speed on both temperature gradients within, and the absolute temperature of, the sample. A commercial 5 mm high-speed CPMAS probe was used for the study. With 95% ^{15}N-enriched TTAA, there was a marked increase in the linewidth of the resonances, indicating a temperature gradient which was estimated to be 2 K, at sample temperatures between 130 and 300 K. Increasing the spinning rate from 2 to 13 kHz led to a sample temperature increase of 33 K. Plotting the measured temperature vs. the spinning rate (ν_r measured in Hz) gave quadratic relationships at two temperatures:

$$T = 0.21\nu_r^2 + 293 \text{ @ } T_{bi} \approx 294 \text{ K} \qquad T = 0.41\nu_r^2 + 167 \text{ @ } T_{bi} \approx 170 \text{ K} \quad (20)$$

where T_{bi} is the temperature of the bearing inlet air. The value of the coefficient of the quadratic term depends on the rotor material and the type of driving gas. As mentioned previously, the observation that ΔT decreases with increasing temperature can be explained by the increase of the heat capacities of the sample and the bearing gas.

4.5. Phosphorus chemical shifts

The ^{31}P nucleus has been used to monitor temperature in high-temperature CPMAS experiments using $(VO)_2P_2O_7$.[179] The compound is thermodynamically stable up to temperatures above 700 K, and has a Curie-law temperature dependence of the isotropic chemical shift at 121.5 MHz given by:

$$\delta = \frac{414.621}{T} + 1118.4 \tag{21}$$

where δ is referenced to ^{31}P in concentrated phosphoric acid. This gave a sensitivity of 0.0056 ppm K^{-1} at 273 K, and 0.00085 ppm K^{-1} at 700 K. The authors suggested that a double-tuned probe can be used with one channel tuned to ^{31}P and the second to the nucleus of interest. They also cautioned that, if hydrocarbons are used near 500 K, the agent catalyses the oxidation of C_4 hydrocarbons to maleic anhydride and so should be used in a sealed capillary.

4.6. Tin chemical shifts

The high thermal sensitivity exhibited by ^{119}Sn and ^{207}Pb (see next section) make these nuclei highly promising for accurate thermal measurements. The temperature dependence of ^{119}Sn chemical shifts in the liquid state has already been covered in Section 3.2.5. This temperature sensitivity can be amplified by incorporating lanthanides into the compounds used for solid-state studies. Three lanthanide stannates, $Nd_2Sn_2O_7$, $Sm_2Sn_2O_7$ and $Y_{1.8}Sm_{0.2}Sn_2O_7$ have been characterized[180] at a spinning speed of 4 kHz. One further lanthanide stannate, $Pr_2Sn_2O_2$, was proposed as a solid-state thermometer, and its high-temperature behaviour, together with that of the earlier compound $Sm_2Sn_2O_7$, investigated.[169] In all of these compounds the temperature dependence is dominated by the Fermi contact term, corresponding to the electron spin density of the unpaired *f* electron of the lanthanide being transferred to the *s* orbital on the tin atom.

The first compound studied, $Nd_2Sn_2O_7$, has a multiple line spectra, and so the isotropic resonance of each spinning-sideband manifold was determined by integration over the whole signal, and was assumed to be the peak for which the first moment vanishes. Over a temperature range of 236 K to 350 K a linear relationship was found between chemical shift and reciprocal temperature, with a sensitivity of 22 ppm K^{-1} at 236 K and 10 ppm K^{-1} at 350 K:

$$\delta = -\frac{1.23 \times 10^6}{T} - 89 \tag{22}$$

The second compound, $Sm_2Sn_2O_7$, was characterized over a temperature range of 190 to 349 K. This compound has the smallest anisotropy and narrowest linewidths of the paramagnetic lanthanide stannates studied. For all trivalent lanthanide ions except for Sm^{3+} and Eu^{3+} the first excited state is at a much higher energy than the ground state, and therefore only the lowest level is occupied at room temperature and below. In such a case the magnetic susceptibility is inversely proportional to temperature.[181] However, when there is a degenerate ground state and at least one degenerate excited state comparable to kT above the ground state, as with $Sm,^{3+}$ then both the first-order and second-order Zeeman perturbations have to be considered, and there is no simple dependence of the magnetic susceptibility on temperature. At temperatures below 600 K the isotropic resonance of $Sm_2Sn_2O_7$ exhibited a low frequency shift, and a high frequency shift above this temperature, as shown in Fig. 13. At the crossover point the first-order and second-order Zeeman perturbations cancelled out since they have opposite signs. By fitting the experimental data to equations derived previously,[182] the temperature dependence could be expressed as:

$$\delta = -105.1 - \frac{1}{6 + 8 \exp - \dfrac{1338}{T}} \times \left[\frac{6.0437 \times 10^5}{T} - 2168.6 + \left(\frac{10.243 \times 10^5}{T} + 2168.6 \right) \exp - \frac{1338}{T} \right] \quad (23)$$

This compound appeared very well suited to temperature measurements at very high temperatures, but obviously was not accurate close to the crossover temperature of 600 K. The sensitivity at 300 K was 1.1 ppm K^{-1}. At temperatures less than room temperature, the equation can be approximated by a straight line, Eq. (24), representing a sensitivity of 2.64 ppm K^{-1} at 190 K and 0.78 ppm K^{-1} at 349 K.

$$\delta = -\frac{9.53 \times 10^4}{T} + 223 \quad (24)$$

For the third compound, $Y_{1.8}Sm_{0.2}Sn_2O_7$ there are three ^{119}Sn resonances. One resonance, termed A, is temperature independent and represents the ^{119}Sn local environment $Sn(OY)_6$. Peaks B and C correspond to the local environments $Sn(OY)_5(OSm)$ and $Sn(OY)_4(OSm)_2$. The change in chemical shift between resonances A and B was found to be inversely proportional to temperature:

$$\delta_{AB} = -\frac{1.27 \times 10^4}{T} + 132 \quad (25)$$

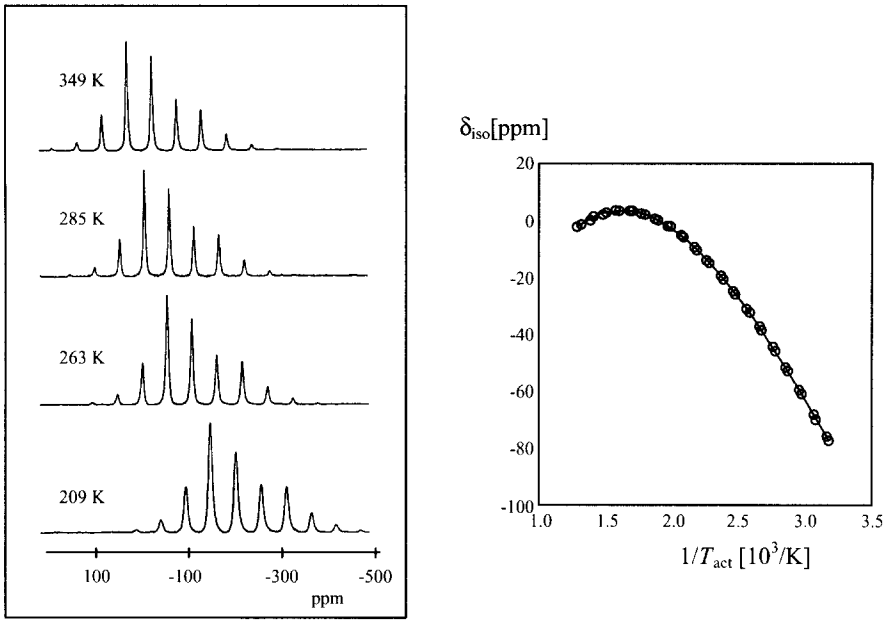

Fig. 13. (left) ^{119}Sn spectra of $Sm_2Sn_2O_7$ at four different temperatures. (right) Temperature dependence of the isotropic resonance. The estimated crossover temperature is 600 K. (Figures from refs. 169 and 180, Copyright 1995 by Academic Press, reproduced by permission of the publisher.)

The thermal sensitivity was 0.35 ppm K^{-1} at 190 K and 0.1 ppm K^{-1} at 349 K. Although this compound had a lower thermal sensitivity than the other two compounds, it is internally referenced and thus can be used for absolute temperature measurement. In a later publication[169] the properties of $Pr_2Sn_2O_2$ and $Sm_2Sn_2O_7$ were characterized using four phase-transition compounds, listed in Table 4, for temperature calibration, namely CBr_4, DABCO, $RbNO_3$ and $LiNaSO_4$. For the praesodymium, complex spectra were integrated to determine the isotropic resonance. Spectra were acquired over a temperature range of 310–790 K, and gave a temperature dependence of:

$$\delta = 119 - \frac{1.1312 \times 10^6}{T} \tag{26}$$

This resulted in a sensitivity of 14.1 ppm K^{-1} at room temperature, and a value of 2.7 ppm K^{-1} at the highest temperature studied, 790 K.

4.7. Lead chemical shifts

Lead has a relatively high sensitivity, with the ^{207}Pb isotope being 22.6% naturally abundant and having a gyromagnetic ratio approximately one-fifth that of protons. The development of a ^{207}Pb-based chemical shift thermometer has been carried out independently by two groups.[183,184] Both groups chose lead (II) nitrate, because the CSA of the static powder pattern can be removed at moderate spinning speeds giving relatively narrow lines, it can be used at high temperatures since it decomposes only above 700 K, and the compound is non-hygroscopic. A linear variation in the chemical shift from 210 to 330 K was measured,[183] with a slope of 0.70 ppm K^{-1}. The authors used this compound to investigate the thermal properties of different types of rotors. For example, Fig. 14 shows considerable differences between the properties of zirconia and silicon nitride.

The second research group[184] calibrated the lead chemical shift via the melting points of acetone, benzene and citric acid. In order to avoid broadening of the lead resonance due to temperature gradients, two thin disks

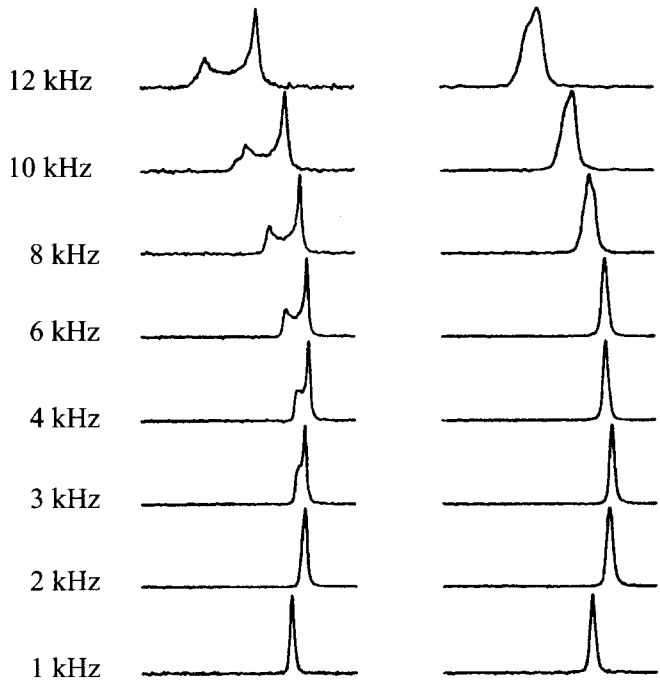

Fig. 14. ^{207}Pb solid-state NMR spectra of lead(II) nitrate at selected MAS speeds and ambient probe temperature in (left) a partially stabilized zirconia rotor and (right) a silicon nitride rotor. (Adapted with permission from ref. 183, Copyright ©1995 John Wiley & Sons Ltd.)

of lead nitrate were packed into the rotor, with the space between them filled with glass wool plugs. Thermal measurements were made between 143 and 423 K at a spinning speed of 2 kHz, and gave straight line dependence of chemical shift vs. temperature with a slope of 0.753 ppm K^{-1}. The authors suggested that the cause of this temperature-dependent chemical shift was thermal lattice expansion. They also showed that the sample temperature rose 3.8 K in increasing the spin rate from 2 to 5 kHz. The rate at which the temperature changed after a sudden change in the VT setting was investigated, as well as the nature of temperature gradients within the sample, as shown in Fig. 15.

Other investigators[185,186] have used lead nitrate for determining temperature in MAS probes, using a measured thermal sensitivity of 0.76 ppm K^{-1}. The temperature in the MAS chamber was found to be higher than that at the probe thermocouple, with the exact difference dependent upon the air temperature setting and the rotation frequency. Frictional heating was determined to be the dominant mechanism. Another group[187] used lead nitrate to compare two different methods of carrying out temperature jump MAS experiments, using laser and RF inductive heating respectively. In the first heating method 10.6 μm radiation from a CO_2 laser was focused onto the outside of a quartz MAS rotor. This technique can be used to obtain rapid and large temperature jumps, but as shown in Fig. 16 there was a large spatial dependence in temperature within the sample. In the second method, 130 kHz

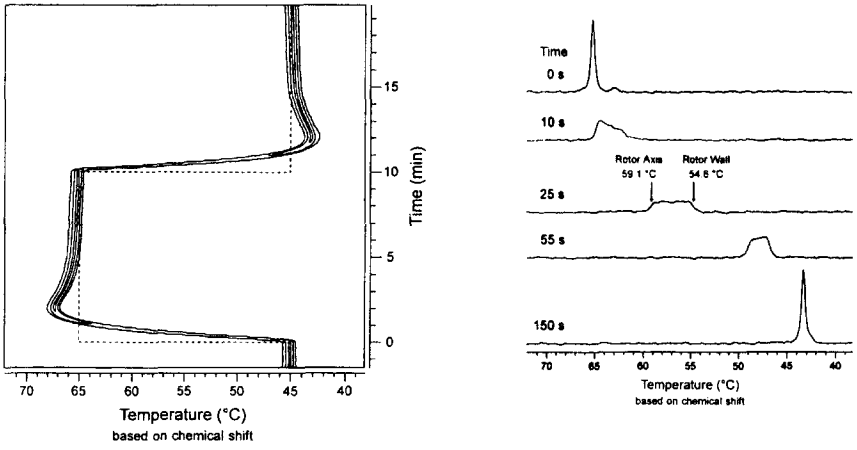

Fig. 15. (left) Contour plot of a series of 256 single scan spectra of lead nitrate, measured at 5 s intervals during a temperature pulse. The dashed line represents the setting of the temperature controller which was programmed to jump from 45 to 65 °C and then back to 45 °C ten minutes later. (right) Individual spectra from the series. The resonance broadens considerably as a result of temperature gradients associated with heat flow through the sample. (Fig. from ref. 184, Copyright 1995 by Academic Press, reproduced by permission of the publisher.)

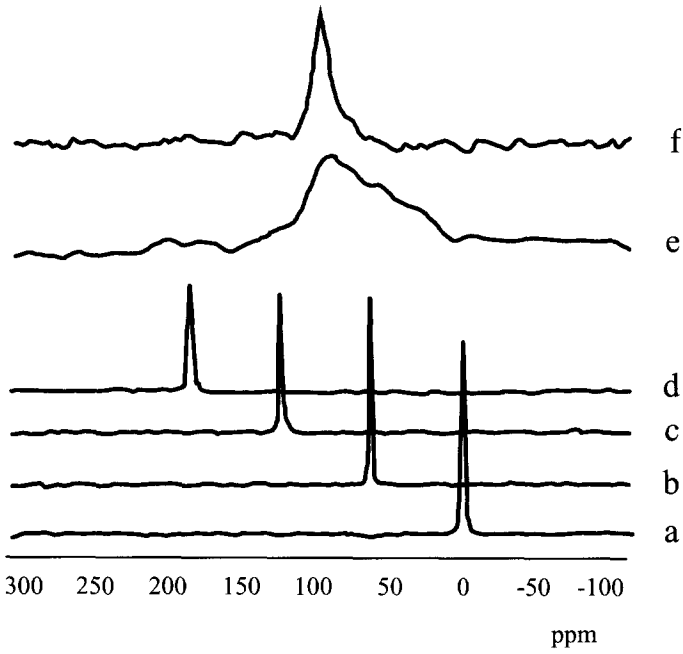

Fig. 16. ^{207}Pb MAS spectra indicating the temperature gradients using various heating methods. (a) 298 K; (b) hot gas heating at 373 K; (c) hot gas heating at 448 K; (d) hot gas heating at 523 K; (e) laser heating at 12 W; (f) inductive heating at 7.5 W. (Reprinted with permission from ref. 187, Copyright 1995 American Chemical Society.)

off-resonance RF was applied via the decoupler channel. As also shown in Fig. 16, this gave rise to a much smaller spatial temperature distribution within the sample.

Finally, a method has been suggested for non-spinning solid-state samples, where linewidths are intrinsically large.[188] This method was based on finding the chemical shift of the highest point of the spectrum, δ_{peak}, of a static lead nitrate sample. The sensitivity was measured to be 0.666 ppm K^{-1}.

5. *IN VIVO* TEMPERATURE MAPPING USING MAGNETIC RESONANCE IMAGING

There are a number of medical procedures which use heating or cooling to destroy pathological tissues such as cancer. These procedures include ablation, in which the tissue is heated rapidly to well above 343 K for short periods of time, hyperthermia, which heats tissue slowly to 315–318 K and maintains this temperature for extended periods, and cryotherapy, in which the tissue is

frozen. In each of these techniques, monitoring the temperature in both the tumour and the surrounding healthy tissue is of vital importance, since small temperature changes within the tumour have large effects on the efficacy of treatment, and increases in the temperature of healthy tissue have been shown to cause serious injury. Traditional invasive monitoring uses electrical or optical probes at only a very few pre-determined and fixed locations. These probes can also interfere with the geometry of the heating field. MRI offers the possibility of full three-dimensional, non-invasive thermal mapping by utilizing the temperature-dependent NMR parameters of tissue water. The following sections outline the major methods that have been developed, and their application *in vivo*. A phantom-based comparison of the thermal sensitivities of each of the proton-based methods (also included is the Pr-MOE-DO3A complex described in Section 3.1.2) has been published recently.[44] Also, the use of the various MRI-based methods for guidance of thermotherapy has been reviewed in a short paper.[189]

5.1. T_1-based techniques and applications

The T_1 of 'free' water is determined solely by intermolecular dipole–dipole interactions, and can be related to the temperature-dependent correlation time (τ_c):[190]

$$\frac{1}{T_1} = \frac{3\mu_0^2\hbar^2\gamma^4}{160\pi^2 r_{ij}^6}\left(\frac{\tau_c}{1+\omega_o^2\tau_c^2} + \frac{4\tau_c}{1+4\omega_o^2\tau_c^2}\right) \tag{27}$$

where r_{ij} is the distance between two spins. For small molecules, such as water, at the low frequencies used for MRI, $\omega_0\tau_c \ll 1$, and so T_1 is proportional to $(\tau_c)^{-1}$. The temperature dependence of τ_c can be expressed, to a first approximation, as:

$$\tau_c = \frac{4\eta a^3}{kT} \tag{28}$$

where a is the radius of the molecule treated as a sphere, and η is the viscosity. In this case T_1 becomes simply inversely proportional to T. A more accurate expression for τ_c is:

$$\tau_c = \tau_{c0}\exp\frac{E_{ia}}{kT} \tag{29}$$

where τ_{c0} is a constant, and E_{ia} is the activation energy for the ith mode of motion. This leads to an exponential expression for the temperature dependence of T_1:

$$T_1 \propto \exp\left(-\frac{E_a}{kT}\right) \tag{30}$$

where E_a is the activation energy for the T_1 process. Despite the apparent mathematical differences, the exponential function of Eq. (30) is highly linear over the temperature ranges used in the heating therapies already outlined. However, in tissue, water is present in both 'bound' (or 'associated') and free compartments, and additional relaxation mechanisms become important: for example, chemical exchange between free and associated water, and cross-relaxation between water and macromolecules via dipole–dipole interactions. This type of system can be described by the fast-exchange two-state (FETS) model.[191] If it is assumed that the system is in the fast chemical-exchange regime, then:

$$\frac{1}{T_1} = \frac{a}{T_{1a}} + \frac{1-a}{T_{1f} + \tau_a} \tag{31}$$

where T_{1a} is the T_1 of the associated water, a is the fraction of water that is associated, T_{1f} is the T_1 of the free water, and τ_a is the residence time of a proton in the restricted compartment. For tissues where the free state is the dominant factor in the relaxation process, Eq. (30) is still valid, but the proportionality constant and E_a are tissue dependent. Therefore, for *in vivo* applications, the temperature dependence of each type of sample needs to be calibrated carefully in order to make accurate temperature measurements, and tissue heterogeneity may lead to a multi-exponential dependence of T_1 upon temperature.

Linear relationships between T_1 and T^{-1} have been reported by a number of authors in frog muscle, mouse muscle and liver, and *ex vivo* samples of spleen, heart, lung, muscle and tumour tissues.[192–196] In this last study,[196] the authors in fact found three distinct temperature subranges. The first represented a reversible increase in T_1 with temperature, up to the maximum value of T_1 measured in the experiments. Above this temperature the T_1 decreased irreversibly until reaching a minimum value, after which it increased again. The dependence of tissue properties on temperature, as well as operating frequency, has been the subject of an extensive review article.[197] In a later publication the *in vitro* temperature dependence of T_1 in $CuSO_4$ solutions, oils, tissue-simulating solutions (bovine serum albumin, and a mixture of liposyn and ethanol), and egg white and yolk separations was investigated.[198] Over a small

temperature range a plot of T_1 vs. reciprocal temperature showed the expected linear relationship. For $CuSO_4$ solutions at 295 K the thermal sensitivity was 2.37% K^{-1} and for oil samples 3.59% K^{-1}. The value of E_a, given by the slope of T_1 vs. T^{-1} was different for each sample, reinforcing the need for calibration of each tissue type studied.

In order to make measurements relevant to medical therapy, the full spatial distribution of tissue heating must be known. This process involves using MRI techniques, with a pixel-by-pixel estimation within the images of the changes in the T_1 value. Since thermal changes during therapy may be rapid, fast imaging sequences, based on gradient echoes, are usually employed. For a simple gradient echo sequence, the image signal intensity (S) is given by:

$$S \propto M_0 \frac{\sin \alpha(1 - E_1)}{1 - \cos \alpha E_1} E_2^* \tag{32}$$

where $E_1 = \exp - (TR/T_1)$, $E_2^* = \exp - (TE/T_2^*)$, TR is the time between successive phase encoding steps, and TE the echo time. Changes in both M_0 and T_1 contribute to signal changes due to temperature (it is assumed that changes in T_2^* with temperature are very small). From Eq. (1) the value of M_0 is inversely proportional to temperature with a fractional change of approximately 0.32% K^{-1} at normal body temperature. In most studies, signal changes due to the temperature dependence of the T_1 value are the dominant factor, but the effect of M_0 must be included in all calculations.

The first temperature mapping experiments[199,200] measured a temperature sensitivity in blood of about 1.4% K^{-1}. A linear relationship[201] was found for agar gel, *in vitro* bovine muscle (283–333 K), *in vivo* rabbit thigh muscle (309–316 K) and calf muscle in human volunteers (300–312 K). The first imaging of laser–tissue interactions[202] in minced rabbit brain using a neodymium: yttrium–aluminium–garnet (Nd:YAG) laser at 1064 nm showed that temperatures below 318 K, corresponding to reversible tissue heating, gave reversible increases in T_1 and reversible decreases in M_0. As the temperature was increased to 318–333 K, corresponding to changes in cell metabolism and cellular water distribution, both reversible and irreversible increases in T_1 were found. Increasing the temperature further to above 333 K resulted in tissue coagulation and protein denaturation, which was reflected by an irreversible change in T_1, suggesting a fundamental limit to this measuring technique. Interstitial laser ablation was used,[203] as well as cryoablation, in both *ex vivo* and *in vivo* animal liver, with a spin-echo based rapid-acquisition-with-relaxation-enhancement (RARE) sequence. Over the range 283–323 K the mean intensity changed almost linearly with temperature by 1–2% K^{-1}, with a standard deviation of 5.4 K in the temperature. RF heating in volunteers[204] was also performed, with a reported 1.3% sensitivity in the change in T_1 value, and 2.4% K^{-1} in the diffusion coefficient (see Section 5.2).

The majority of studies have been in the area of focused ultrasound therapy. The first experiments[205,206] used a 2 second fast gradient echo sequence to investigate the effects of 4 seconds of continuous ultrasound irradiation. The MRI-derived temperature profiles agreed well with theoretical results using a Gaussian source thermal model. In a following study,[207] using an RF-spoiled gradient-recalled acquisition in the steady state (GRASS) sequence with images acquired every 1.35 seconds, the thermal sensitivity of the image signal intensity was estimated to be 1.5% K^{-1} in muscle. Representative images are shown in Fig. 17.

For very rapid imaging, a one-dimensional line-scanning technique[208] through the focal point of the ultrasound beam has been proposed. Fast mapping can also be achieved using an inversion-recovery fast low-angle shot (FLASH) sequence.[209] In a phantom and *ex vivo* study, a T_1-weighted fast spin-echo (FSE) sequence with a *TR* of 100 ms was shown to have a higher thermal sensitivity

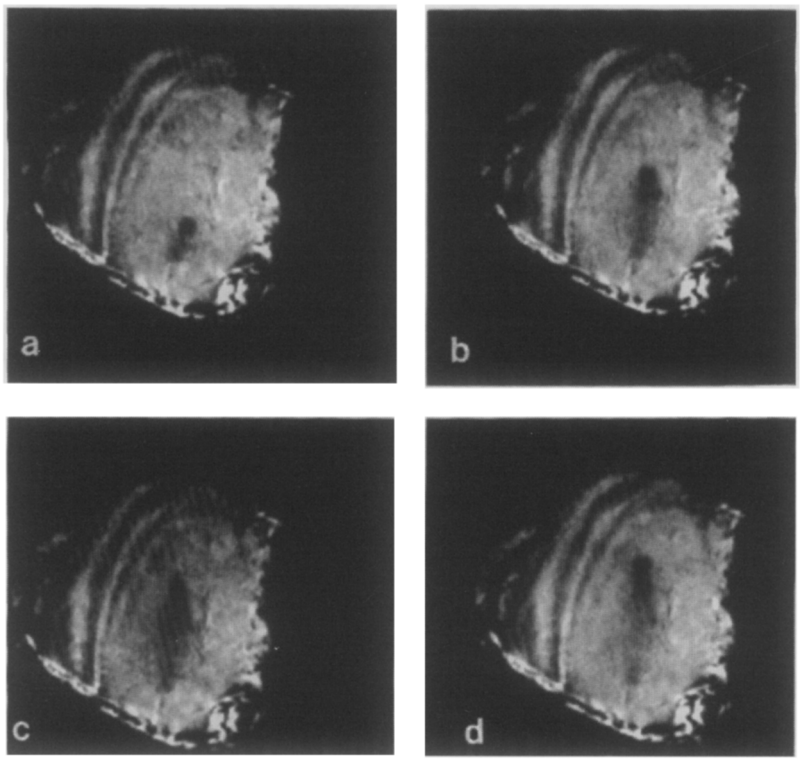

Fig. 17. A series of 2 s fast gradient refocused images (TR/TE/angle = 11/2.3/60) in the focal plane of a muscle specimen showing the displacement of a hot spot (dark area) by moving the focus of a 4 s ultrasound pulse, with a maximum acoustic intensity of 8100 $W cm^{-2}$, in a vertical direction (a–d). (Reprinted from ref. 207 by permission of John Wiley & Sons, Inc. Copyright ©1993 John Wiley.)

than either the spoiled or unspoiled GRASS sequences used previously.[210] An optimized spin-echo sequence (TR = 1200 ms, TE = 10 ms at 1.5 T) has also been used[211] to study cooling in human leg muscle. A T_1-weighted FSE sequence with an imaging time of 10 seconds was employed to monitor laser heating in the normal liver of anaesthetized rabbits.[212] No thermal quantitation was attempted, but the heating pattern could be followed by the decreased signal intensity on the images. A second laser study was performed on two patients with unresectable hepatocellular carcinomas.[213] After the light guide was placed with its tip in the centre of the tumour, continuous heating was used at a power of 5 W. T_1-weighted FLASH images were acquired every 30–40 seconds until the hypointense area reached the border of the predefined liver lesion. Patients with grade III/IV gliomas undergoing laser heating have also been studied. No quantitative thermal measurements were made, but monitoring was used to discontinue heating when the 'lesion size' matched the size of the tumour, or when the distance from the border to primary motor or language areas (determined using functional MRI) was less than 10 mm. Similar studies were performed by the same group on patients with high grade gliomas.[214] One of the first reports of MRI-monitored microwave-induced tissue heating[215] used a $\lambda/4$ monopole antenna, and irradiated *ex vivo* porcine myocardium with a power of 20 W for 10 minutes. Signal decreases, due to the elongation of the T_1 relaxation time, were recorded at 1.5 tesla using a T_1-weighted FLASH sequence. Again, no temperature quantitation was attempted.

The major problems associated with accurate temperature mapping using this approach are: (1) the tissue-specific nature of the thermal sensitivity of T_1 and the complex nature of relaxation in tissue, (2) the restriction to temperatures below 338 K, at which point protein denaturation occurs and changes in T_1 are related more to structural changes in the tissue than to the actual temperature, and (3) the fact that the T_1 is affected by changes in perfusion and regional blood volume, which are themselves altered by changes in temperature.[216] The extent and associated time lags of changes in perfusion are both a function of the nature of the heating. Muscle volume may also change. Altered rates of blood flow affect the measured T_1 since, if there is an inflow of blood which has a substantially longer T_1 than the tissue, the overall temperature sensitivity of the T_1 of the tissue will be less than if only the parenchyma were involved. These last factors are particularly relevant to slow heating, such as in hyperthermia, and have been investigated and modelled extensively.[217,218]

As a result of these problems, few *in vivo* studies now use the T_1 technique, although it is still widely used in non-medical applications where the complexities outlined above are not present. It is also the only technique which is currently capable of temperature monitoring in fat.[219,220] For example, a T_1-weighted saturation recovery TurboFLASH sequence with centric phase encoding order was used to study *ex vivo* muscle phantoms with varying degrees of fat content.[219] The signal change with temperature could be well-approximated by a linear relationship. A 10 K increase gave an 11% decrease

in signal intensity, with the change in M_0 contributing 3% and the change in T_1 8%. In the second paper,[220] using a T_1-weighted FSE sequence with an 8-echo train length (TE 17 ms), TR of 400 ms, and imaging time of 4 seconds, the authors reported a linear decrease in signal intensity of the fat with temperature with a slope of $0.97 \pm 0.02\%$ K^{-1}.

5.2. Molecular diffusion based techniques and applications

The basis for the temperature dependence of the water diffusion coefficient arises from the Stokes–Einstein equation, given previously as Eq. (3). This can also be expressed as:

$$D = D_{\text{inf}} \exp - \frac{E_a}{kT} \tag{33}$$

where D_{inf} is the diffusion coefficient at infinite temperature, and E_a is the activation energy for molecular diffusion, which corresponds to the breaking of two hydrogen bonds.[221] It is assumed that E_a is independent of temperature for the range relevant to medical applications. A typical value of E_a for biological systems is 0.2 eV at 293 K, corresponding to a high thermal sensitivity of more than 2% K^{-1} in the value of D. For temperature measurement, a series of diffusion-weighted images are acquired using an imaging version of the pulsed field gradient Stejskal–Tanner sequence.[222] The signal in a particular image voxel is given by:

$$S \propto \exp - \left[\gamma^2 G^2 \delta^2 D \left(\Delta - \frac{\delta}{3} \right) \right] \propto \exp(-bD) \tag{34}$$

where G is the strength of the diffusion encoding gradient, δ is the duration of the gradient, Δ is the time between the two gradient pulses, and b is the 'b factor' commonly used to characterize the diffusion weighting of a particular sequence. A series of images with different values of G are acquired and a pixel-by-pixel value of D calculated from Eq. (34). For rapid temperature estimation, often only two images are acquired at an initial temperature (T_i) and final temperature (T_f). The corresponding diffusion coefficients are calculated as D_i and D_f respectively. If T_i is known, then T_f can be estimated from:

$$T_f = \left(\frac{1}{T_i} - \frac{k}{E_a} \ln \frac{D_f}{D_i} \right)^{-1} \tag{35}$$

For $T_f - T_i \ll T_i$, this expression simplifies to:

$$T_f = T_i + \frac{kT_i^2}{E_a}\left(\frac{D_f - D_i}{D_f}\right) \tag{36}$$

The first thermal imaging study[223] measured temperatures in a polyacrylamide gel at 0.5 tesla. The values of D were measured as $(1.76 \pm 0.02) \times 10^{-3}$ mm^2 s^{-1} at 296.9 K and $(2.22 \pm 0.02) \times 10^{-3}$ mm^2 s^{-1} at 309.8 K. Phantom calibrations were also carried out using a 1.5 tesla whole body MRI system[224] and a 4.7 tesla animal scanner.[225] In a follow-up study at 1.5 tesla,[226] using a hexagonal phased array consisting of three pairs of flared dipole antennas operating at 130 MHz, results using the same saline-based acrylamide gel showed a single measurement accuracy of approximately 0.5 K within a voxel of less than one cubic centimetre: results are shown in Fig. 18. Diffusion measurements have also been used to measure temperature

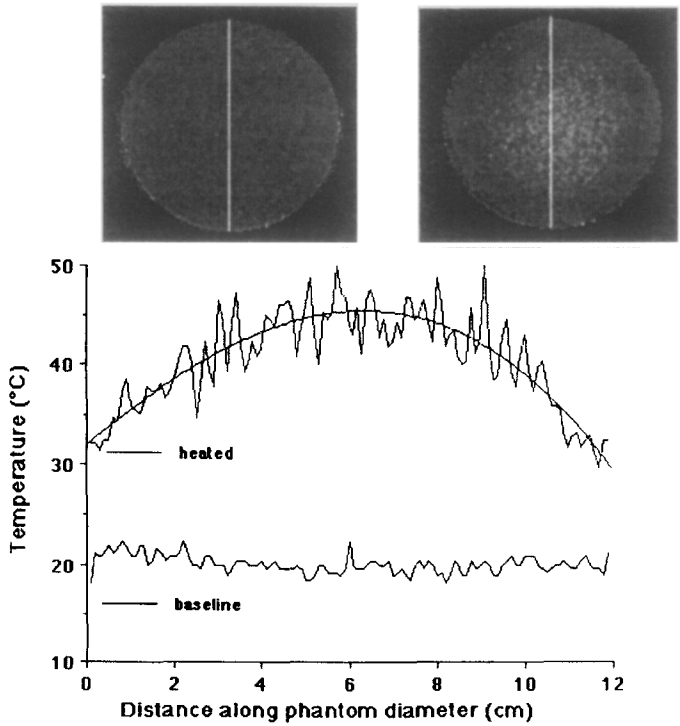

Fig. 18. MR diffusion images of a gel phantom before (left) and after (right) heating. The solid curve shown below the images is a polynomial fit to the data after heating. (Adapted with permission from ref. 226, Copyright 1992 Taylor & Francis.)

and regional blood volume simultaneously in muscle,[227] but with limited spatial resolution.

In vivo temperature sensitivities of the value of D were measured[228] to be 2% K^{-1} in brain tissue, 2.7% K^{-1} in muscle and 3% K^{-1} in water-based gels. MRI thermal maps have been compared[229] with numerical simulations based on a finite element based method that computes the electromagnetic induced power deposition, and then the temperature distribution. Two studies were performed on non-perfused homogeneous and heterogeneous phantom, and the MR and simulated distributions agreed for steady-state measurements. However, due to the long MR sampling time (approximately 4 minutes), poor agreement between the simulations and MR measurements was obtained for thermal transients.

The major problem with studies up to this point had been that conventional diffusion-weighted MRI is too motion sensitive for *in vivo* thermometry. Rapid diffusion-weighted echo-planar imaging (EPI) was evaluated in an attempt to reduce the sensitivity to motion.[230] Acrylamide gel was heated with a surface microwave applicator at 433 MHz, while *in vivo* heating of a dog was accomplished using an annular phased array at 130 MHz. The temperature sensitivity of D for the gel was measured to be $3.04 \pm 0.03\%$ K^{-1}. The *in vivo* temperature sensitivity of brain tissue was $1.9 \pm 0.1\%$ K^{-1}. Although EPI, in combination with cardiac gating, did reduce motion artefacts, standard errors for the *in vivo* temperature measurements were still much larger than for phantom experiments. Abdominal studies involving heating of the liver also require fast single-shot diffusion-weighted sequences to overcome motion artefacts, but the use of EPI is limited to the brain. One study evaluated an alternative fast imaging method, a diffusion-weighted single-shot RARE[231] sequence, with diffusion weighting from a stimulated-echo or spin-echo preparation sequence.[232] For human muscle studies the calf muscle was cooled with an ice bag, and a series of 15 images were acquired every three minutes. Temperature drops of up to 18 K were recorded, assuming a coefficient of 2.4% K^{-1}. Errors were estimated to be $\pm 2\%$, with a 2×2 mm^2 in-plane image resolution and a slice thickness of 8 mm. However, the authors noted that changes in blood flow and oxygen release from erythrocytes[233] will result in susceptibility changes that can also change the value of D.

The major disadvantage of using the value of D to measure temperature, apart from the motion susceptibility, is that several factors, other than temperature changes, can also cause changes in this value. For example, variable water content affects the value of D, and water content also changes as a result of heating. Tissue heterogeneity results in a spatial variation in the activation energy for molecular diffusion, giving different values of the thermal sensitivity within the tissue. Very careful characterization of a particular system is, therefore, necessary to be able to monitor temperature changes in biological systems.

5.3. Proton reference frequency methods

In Section 3.1.1, the dependence of the water chemical shift on temperature was described. The same dependence is found for water in tissue *in vivo*, and methods and applications based on the proton reference frequency (PRF) are involved in the vast majority of current *in vivo* temperature imaging studies.

5.3.1. Sample independence studies

The key to the acceptance of the PRF method is the tissue independence of the temperature coefficient.[234–236] The temperature dependence of the proton chemical shift was found to be essentially the same for 1% NaCl solution, 4% agar, boiled egg white and chicken muscle.[234] A similar study using freshly excised brain, muscle, liver and kidney tissues from rabbits and pigs measured the temperature coefficient for each of these, together with 2% agar gel, to be between -0.0097 and -0.0105 ppm K^{-1}.[235] Precooked samples, used to investigate the effects of heating history, gave very similar results. Another important factor is the 'reversibility' of the measurements. One study showed[236] that tissue could be cycled from 298 to 343 K and back again with the coefficient not changing with physiological changes associated with such a temperature cycle. A long-term reliability study[237] on agar phantoms found a highly reproducible calibration coefficient of 0.009 ± 0.001 ppm K^{-1} over a time period of six months.

5.3.2. Imaging methodologies

As outlined in Section 3.1.1., the mechanism which accounts for the temperature dependence of the proton chemical shift involves changes in both σ and χ_v. The local magnetic field at the nucleus (B_{nuc}) is given by:

$$B_{nuc}(T) = B_{mac}(1 - \sigma(T) - \tfrac{2}{3}\chi_v(T)) \tag{37}$$

where B_{mac} (often assumed to be equal to B_o) is the macroscopic magnetic field in the object. The quantity $\sigma(T)$ has been determined to be tissue independent, with a temperature dependence of roughly -0.01 ppm K^{-1}. Pure water is diamagnetic at room temperature with a χ_v of -9.03×10^{-6}, with this value increasing with temperature by 3×10^{-9} K^{-1}, largely due to the decrease in the density of water with increasing temperature.[238] The first imaging study used a three-dimensional chemical shift resolved sequence with two tubes of water at different temperatures.[239] Images corresponding to the different tubes were produced based on their different chemical shifts, but no thermal quantitation was attempted. The first quantitative study used a two-dimensional phase-encoded spectroscopic technique.[240] The same authors extended this approach to *in vivo* studies in the rat using spectral estimation techniques to calculate the

temperature in each voxel.[241] The major problems of these spectroscopic sequences for *in vivo* work are the long data acquisition times and poor spatial resolution.

The vast majority of experiments now measure the temperature-dependent phase changes in images obtained using gradient echo sequences. In such a sequence, with an echo time TE, and spatially dependent temperature change $\Delta T(x, y, z)$, the phase change ($\Delta\phi$) is given by:[242]

$$\Delta\phi(x, y, z) = -0.01\gamma TEB_0\Delta T(x, y, z) \tag{38}$$

Prior to initiation of the heating protocol, a number of baseline images are acquired at a stable and known temperature. A two-dimensional complex inverse Fourier transform is performed on the time-domain data to produce the required baseline phase images. During heating, images are acquired continuously, and maps of the temperature changes are obtained by subtraction of the baseline phase images from those produced during heating. Any time-dependent drifts in the main magnetic field can be corrected by placing phantoms external to the heated region, and interpolating the phase information from pixels corresponding to these phantoms to produce a two-dimensional correction map. The first studies carried out using this method were performed on phantoms[242] and *in vivo* leg muscle in volunteers[243] and showed that the PRF method has a much higher thermal sensitivity than diffusion-based methods. In the same year, a second study showed inductive heating of the cat brain using an asymmetric spin-echo sequence.[234]

Optimal data acquisition parameters[244] were derived by maximizing the S/N of the temperature-dependent phase difference images:

$$S/N_{\Delta\phi} = \frac{|\Delta\phi(\Delta T)|}{\sigma_{\Delta\phi}} \tag{39}$$

where $\Delta\phi(\Delta T)$ is the phase difference at the heated location and $\sigma_{\Delta\phi}$ is the standard deviation of the phase difference image where no heating occurs. When the S/N of the image is large, then the value of $\sigma_{\Delta\phi}$ can be expressed as:[245, 246]

$$\sigma_{\Delta\phi} \approx \frac{\sigma\sqrt{2}}{A} \tag{40}$$

where σ is the standard deviation of the Gaussian noise in the real and imaginary images, and A is the corresponding signal intensity. Substitution of Eq. (40) into Eq. (39), and subsequent differentiation with respect to TE, gives an optimal value of TE equal to T_2^*.

Alternative k-space data acquisition schemes using gradient echoes can also be used. One example is so-called 'spiral' imaging which can be used to increase the temperature sensitivity and decrease the total data acquisition time, since k-space is covered more efficiently.[247] However, the exact thermal sensitivity is a complicated expression which depends upon the spatial frequency content of the thermal changes. An alternative method of increasing imaging speed is to use a class of techniques called echo-shifted gradient echo imaging, in which the value of TE can actually be made larger than that of TR.[248–251] This is particularly important in low field studies[252] where the TE value must be very long, since the absolute change in phase per degree temperature change is smaller than at higher fields. It should also be noted that processing both magnitude and phase images[253] can be used to improve the temperature sensitivity. A complex difference image is produced which reflects both the increase in T_1, and also the temperature dependence of the image phase.

Although the temperature coefficient is tissue independent, the value of this constant does depend upon the geometry of the heating pattern, and its orientation with respect to B_o,[254–256] a fact that was not recognized in early studies and led to wide variations in the reported value of the temperature coefficient. This effect arises because the value of B_{mac} in Eq. (37) depends on the magnetic susceptibility distribution *throughout the entire object*. This distribution depends not only on the spatially variant temperature, $T(r)$, but also on the orientation of this temperature distribution with respect to B_o. Recognizing this, Eq. (37) becomes:

$$B_{nuc}(r, T(r)) = B_{mac}(r, T(r) - B_0(\sigma(T(r)) + \tfrac{2}{3}\chi_v(T(r))) \tag{41}$$

Experimental studies[255] used a cylindrically symmetric heating pattern within a spherical object to produce a radially symmetric temperature distribution. When the axis of the heating pattern was aligned parallel to B_o (z-axis) the corresponding heating maps were symmetric in the xy plane. The value of the temperature coefficient was calculated as $-0.0094\ \text{ppm}\,\text{K}^{-1}$, which is smaller than the value of $\sigma(T)$ for water. These results were confirmed by simulations using finite element models. However, when the heating axis was perpendicular to B_o eccentricity appeared in the phase maps. Along the z-axis, the temperature coefficient was measured to be $-0.0055\ \text{ppm}\,\text{K}^{-1}$, whereas the value was $-0.013\ \text{ppm}\,\text{K}^{-1}$ perpendicular to B_o. The same authors also investigated the effect of temperature-dependent changes in tissue electrical conductivity, which can cause the exact value of the temperature coefficient to depend upon the value of TE.[256] These changes in conductivity, in turn, cause changes in the phase retardation of the RF field from the NMR coil. The phase retardation depends on the values of the permittivity, permeability and electrical conductivity of the material being heated, and on the spatial distribution of the induced temperature changes. Since phase retardation also

depends upon distance, its effect will be depth dependent within the sample. In general, the authors concluded, this effect is only significant when large volumes are heated uniformly.

The major disadvantage of the PRF method is that it is unable to measure temperature accurately in tissues, such as breast, containing a significant lipid content. The value of σ was measured[257] to be almost independent of temperature for fat, and so temperatures cannot be measured in voxels containing both fat and water, since the relative proportions of fat and water in each voxel are not known. Lipid-suppression techniques can be used,[258] but the value of B_{mac} in Eq. (37) depends both on the spatial distribution of fat and tissue, and also on the spatial temperature distribution. In tissues, such as liver, with relatively small proportions of fat distributed homogeneously, lipid suppression can be incorporated successfully, but further work is needed on tissues such as the breast. The PRF and T_1 techniques have been compared for homogeneous and inhomogeneous muscle phantoms using localized laser heating and non-localized heating using circulating water.[259] In *ex vivo* muscle with no fat, the PRF method was more accurate and faster, but as outlined earlier, the presence of fat led to large errors in temperature measurement. The T_1 method also has problems in voxels containing water and fat, since relaxation is no longer monoexponential, but these can be overcome using lipid-suppression techniques.

A second problem is that, since phase difference images must be processed, the PRF method is susceptible to patient motion, particularly over the long acquisition times associated with hyperthermia treatment. A number of approaches have been developed recently to address this problem, although none has yet been implemented *in vivo*. The lipid resonance can potentially be used as an internal standard, and the acquisition of separate images from fat and water using frequency-selective excitation was shown to reduce the effects of motion-induced susceptibility changes in phantoms.[260] In a later paper, using *in vitro* liver samples, a fast echo-planar spectroscopic imaging sequence was also shown to reduce the detrimental effects of motion. An alternative method has been proposed,[261] in which multiple echoes rather than a single echo are acquired. Although the inherent temperature sensitivity is reduced, the sequence did improve temperature measurements in the presence of motion.

5.4. Applications of the proton reference frequency method

Most applications of the PRF method are to non-invasive monitoring of rapid tissue heating used to destroy a particular pathology. These methods not only measure temperature, but can also be used to calculate a derived parameter, the thermal dose, which is generally accepted as a good indication of full tissue coagulation and necrosis. The thermal dose depends on a cumulative

relationship between the temperature elevation and the duration of the exposure, and is calculated from:[262]

$$\text{Thermal dose} = \sum_{t=0}^{t_{\text{final}}} R^{(T_{\text{ref}} - T_{\Delta T})} \Delta t \tag{42}$$

where R is the isodose constant (0.5 for temperatures above 316 K and 0.25 for temperatures below 316 K), T_{ref} is the reference temperature (usually 316 K), $T_{\Delta t}$ is the average temperature during time interval Δt, and t_{final} is the sum of the heating and cooling times. Many of the studies described in the following sections have measured the spatial temperature distribution, calculated the thermal dose from these measurements, and finally, by comparing both temperature and thermal dose maps with post-mortem histology, attempted to define parameters which correspond to complete destruction of the heated tissue.

5.4.1. Laser tissue ablation

Laser-induced interstitial thermotherapy (LITT) destroys small, solid tumours by rapid heating from laser energy entering the target volume through interstitially placed optical fibres positioned through a needle.[263, 264] Laser light is absorbed by tissue close to the tip: heat then travels by conduction over a volume of several cubic millimetres and tumour necrosis results. Temperatures can reach up to 373 K, with typical increases of 30 to 40 K above initial conditions. MRI monitoring can be used to monitor the location and spatial extent of the heated region. The first LITT study[265] with the PRF used an echo-shifted TurboFLASH sequence in gel phantoms and post-mortem porcine brain, with images acquired every 1.3 seconds. A Nd : YAG laser was used at a wavelength of 1064 nm and a power of 3.8 W. The authors obtained accurate temperature measurements, compared to thermocouple readings, using MRI with a maximum deviation of only 1.8 K. In a second animal study,[266] temperature maps were correlated with tissue damage using cadaver pig brains using a FLASH sequence, with 1 minute temporal resolution. The authors found that the histologically determined size of the lesion was well represented by the MRI contours corresponding to a temperature of 333–338 K. The first human study[267] used LITT in a patient with an astrocytoma. A 7-Fr Teflon sheath was inserted into the brain with the tip placed roughly 8 mm from the margin of the tumor. A light guide was introduced and connected to a standard Nb : YAG laser with a power of 4 W. FLASH images were acquired every 20 seconds, and irradiation was stopped when the 333–338 K isotherm reached the margin of the tumour, ten minutes after treatment was started. The maximum temperature, recorded close to the tip of the light guide, was more than 353 K. A contrast-enhanced MRI study immediately after therapy again

showed that size of the necrotic area corresponded well with the 333–338 K isotherm. Very little sign of coagulation-induced tissue phase changes was noted.

Potential problems associated with temperature mapping during LITT application have also been investigated.[254,268,269] An extensive analysis of errors caused by macroscopic changes in the global χ_v of tissue was presented.[254] These effects could cause errors up to 4 K near the laser applicator for the particular set-up used in the study. By estimating the geometry of the heat source with respect to the main magnetic field, a simple first-order correction reduced the absolute error to ± 1 K. The effects of simulated respiration on the accuracy of temperature measurements has been investigated using phantoms and *ex vivo* porcine liver.[268] The authors concluded that motion introduced relatively small errors in the temperature maps. Finally, it was shown that, even though the temperature during laser heating is changing continuously during data acquisition, the resulting image point spread function is not noticeably degraded.[269]

The most recent study used interstitial laser coagulation in an *in vivo* canine prostate model.[270] Histological damage to the prostate was correlated to two thermal models: one was predictive using a threshold temperature of 324 ± 2 K, and the other using a thermal dose of approximately 200 minutes at 316 K. Representative thermal images are shown in Fig. 19.

5.4.2. Ultrasound-mediated hyperthermia and tissue ablation

Focused ultrasound produces well-defined, tight heating patterns either from a single transducer, or from a phased array of transducers. PRF calibrations using focused ultrasound were shown to give a value of the temperature coefficient in agreement with other heating methods.[271] The effects of focused ultrasound on brain tissue have been investigated[272] using a rabbit model, with a piece of the skull removed to allow sonication. Using low electrical power (3.5 W), a temperature rise of 8 K was produced with no evidence of lesion production using follow-up MR contrast-enhanced imaging, or conventional

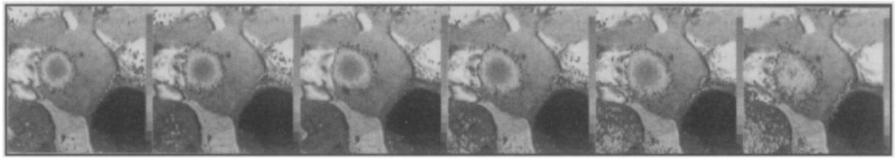

Fig. 19. MR-derived thermal maps during interstitial laser coagulation studies in an *in vivo* canine prostate gland. The thermal maps are overlaid on a magnitude (localizer) image. The heated areas can be seen as the light coloured annulus growing in size with time (left–right). (Reprinted from ref. 270 by permission of John Wiley & Sons, Inc. Copyright ©2000 John Wiley.)

histology. Increasing the power to 7 W and above did produce lesions and larger temperature increases. These results are important because they suggest that low power ultrasound can be used to localize the heating pattern, before high power is used to destroy the tumour. The same group[273] used a series of sonications with a focused transducer to induce necrosis within an implanted tumor. There was a linear relationship between the acoustic power and maximum temperature rise in 10 second insonations. The usual small heating zone could be increased in size, for application to larger tumours, by placing a plastic lens in front of the transducer as shown in Fig. 20. This increased the size of the lesions produced from 3.7 to 5 mm.

The boundary of an isothermal dose value of 240 min at the reference temperature of 316 K is a common choice to predict the size of the necrosed tissue in muscle. However, animal studies using the PRF[274] found that this choice might actually underestimate the actual lesion size *in vivo*, since it defines only the coagulation necrosis which occurs immediately after sonication, whereas more tissue damage may in fact be produced by different mechanisms post-sonication. The authors also found a large variation in the lesion diameter (0 to 6.9 mm with mean value 4 mm) induced *in vivo* in different locations and different animals under identical sonication parameters. The authors postulated that these variations arise from differences in the intervening tissues (attenuation and diffraction) and target tissue inhomogeneities (absorption and perfusion rate). The mean experimental lesion diameter was significantly less than the simulated value of 5.6 mm, probably due to tissue scattering of the ultrasound beam. In a separate study on lesion induction[275] a threshold temperature of 327 K held for 10 seconds gave very similar accuracies, in terms of lesion volume, to the value of the thermal dose. Further studies[276] on the prediction of a threshold for tissue damage used acoustic power, maximum temperature and thermal dose as measures. Using a phased-array sector-vortex

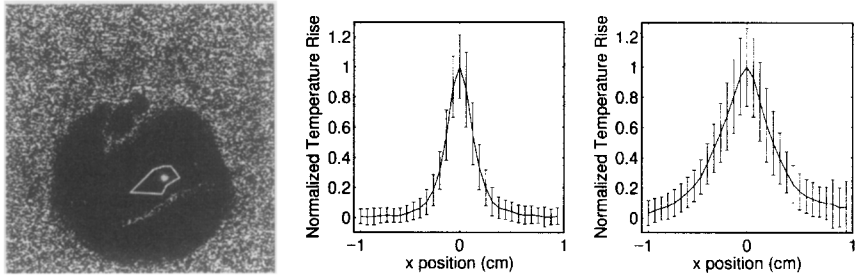

Fig. 20. Average spatial temperature profiles produced by ultrasound sonications given in tumours implanted in the skeletal muscle of rabbits. (left) Phase difference image showing a localized area of heating, (middle) corresponding temperature profile across the focus; (right) profile across the focus with a plastic lens placed in front of the transducer. (Reprinted from ref. 273 by permission of Wiley-Liss, Inc., a subsidiary of John Wiley & Sons, Inc., Copyright ©1998 John Wiley.)

ultrasound transducer to produce a relatively large, uniform heating pattern, the authors determined that acoustic power was not a good measure of tissue damage, but obtained good correlations with areas that received thermal doses of above 31.2 equivalent minutes at 316 K and areas in which the temperature rose above 323.5 K.

Differential temperature increases have been measured[277] as a function of intersonication time for multiple localized sonications, used to treat a large area. A delay of 50–60 seconds was found to be optimal for uniform geometries of the destroyed tissue. With shorter delays, larger areas of tissue than were desired were destroyed. The heating properties of an MRI-compatible phased array ultrasound applicator, designed for heating of the prostate, have also been investigated[278] using both *in vitro* and *in vivo* samples.

One exciting, recent development is the demonstration of real-time closed-loop feedback control of focused ultrasound heating using the PRF method.[279] In the first implementation, a target temperature rise of 30 K was chosen for *in vivo* experiments in rats. Power to the ultrasound transducer was switched on and off depending upon the temperature measured at the target location. *Ex vivo* experiments compared two different control strategies: the first which used the difference between the desired and actual temperature and set the generator amplitude accordingly, and the second which measured the slope of the last three temperature data points to modify the generator amplitude. A smoother curve was obtained with the second method. The first method is more prone to overshoot when the temperature rises rapidly, whereas the second is more sensitive to noise and has a lower time resolution. In a second paper, the authors incorporated information about the temperature gradients, and also a realistic physical model of local energy deposition and heat conduction.[280] Temperature 'rise-times' of less than 1 minute were shown to be possible, as illustrated in Fig. 21. Finally, the PRF method has been used for real-time correction of complex ultrasound heating patterns.[281] As an alternative to

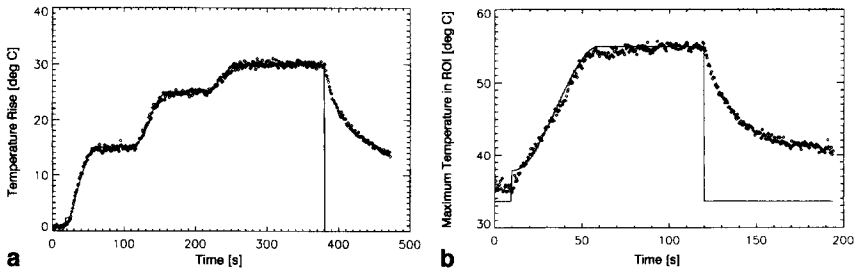

Fig. 21. Temperature evolution of the focal point in closed-loop FUS heating experiment; (left) fresh meat sample and (right) *in vivo* rat thigh muscle. The solid line represents the desired temperature profile and the individual points correspond to the experimental data. (Reprinted from ref. 280 by permission of John Wiley & Sons, Inc. Copyright ©1998 John Wiley.)

using phased array transducers to heat large tissue volumes, double spiral trajectories of the ultrasound focal point of a single transducer, produced by mechanical movement of the transducer, can be used. After the first spiral, the spatial-thermal information was processed in real time to correct the trajectory of the second spiral.

5.4.3. Microwave and RF tissue heating

Microwave and RF heating can be used for the non-invasive destruction of tumours, either by ablation at high temperatures or hyperthermia at lower temperatures. Both techniques have the advantage that, unlike ultrasound, they can be used to heat through bone and air, but they typically produce much more diffuse heating patterns than ultrasound. The first study using the PRF technique measured brain temperature in canines which were undergoing whole body hyperthermia.[282] The particular heating geometry used resulted in the authors reporting very low values of the temperature coefficient. Heating in phantom and *ex vivo* bovine liver samples at very low field (0.2 tesla) was reported[283] using a reduced encoding technique to increase imaging speed. Data acquisition times as low as 13 seconds in the phantoms gave reasonable results. Experimental and theoretical results were compared for interstitial microwave heating at 915 MHz in polyacrylamide gels, designed to mimic the conductive and dielectric properties of muscle[284] with the results in good agreement. *In vivo* rabbit brain studies have been performed using an interstitial microwave antenna at 915 MHz, with variable power settings of 30 to 100 W.[285] Three holes were drilled through the skull. The antenna, a 1×12 mm helical emitting element, was placed in one of these holes, a fibreoptic probe was placed in the second, and a second temperature probe in the third. A fast spoiled gradient echo sequence was used to image every 20 seconds. After the heating protocol had finished T_1-weighted, T_2-weighted and gadolinium-enhanced images were acquired to determine the extent of the lesions, and for subsequent non-quantitative comparisons with histology. Reasonable correlations were found between the degree of damage and the temperature phase maps.

The first human work involved monitoring hyperthermia in humans with sarcomas in the distal lower extremity.[286] Good agreement was found between the MRI temperatures and those measured simultaneously with invasive fibreoptic probes. The most recent study concerned percutaneous interstitial microwave thermoablation in five patients with prostate cancer.[287] Temperatures in the prostate were monitored both by MRI and by invasive thermocouples. Real-time processing gave thermal MRI maps of the heated region every 13 seconds. The aim was to attain a sustained temperature of 323 K for 20 minutes in the prostate gland while not exceeding 353 K at any point. The authors reported excellent correlation between thermally devitalized regions and those that showed substantial heating on the MRI phase images.

5.4.4. *Other* in vivo *applications*

The PRF method has been used[288,289] to measure the ultrasound absorption coefficient of tissue, the value of which is difficult to obtain using invasive temperature measurements. The tissue sample was placed in a block of agarose gel and heated by ultrasound. The energy absorbed by the tissue diffuses slowly into the surrounding gel. Knowing the thermal capacity of the gel, and the temperature distribution measured by MRI, an estimate of the total absorbed energy can be made. The ultrasound pressure absorption coefficient (α) can be calculated as:

$$\alpha = \frac{\rho C \int \Delta T(V) \mathrm{d}V}{2 \int I_0(s) \mathrm{d}s \Delta x \Delta t} \tag{43}$$

where $\Delta T(V)$ is the temperature elevation distribution in the calorimeter apparatus, ρC is the thermal capacity of gel and tissue over volume V, Δt is the duration of insonation, Δx is the thickness of the tissue in the direction of ultrasonic propagation, and $I_0(s)$ is the ultrasound intensity distribution incident on the tissue sample (measured separately). Using a 1 MHz transducer, a sample of freshly excised bovine liver gave an absorption coefficient of 0.058 cm^{-1}, which is well within the range of values measured using other techniques.

MRI monitoring of ultrasonic heating has also been used to investigate the feasibility of thermally induced gene expression.[290] The concept is to use a heat-inducible promoter to regulate expression based on a well-targeted heat distribution. The authors used focused ultrasound at 1.47 MHz to determine whether they could alter the regulation of heat shock protein (hsp70) in the leg muscle of a rat. Using an RF spoiled gradient echo sequence, they first turned on the ultrasound at low energy to ensure that heating was occurring at the correct location, and then heated the region for 45 minutes to between 315 and 318 K (at the periphery and centre of the region respectively). A further 45 minutes was allowed for gene expression before the rat was euthanized. The induction of expression of hsp70 was analysed with Northern blotting techniques, and showed a differential expression of between 3 and 67 compared to control animals.

The PRF method can also been used[291] to study temperature changes from percutaneous hot saline injection therapy (PSIT), a new technique aimed at treating hepatic tumours.[292] Until this study was performed, temperature distributions within the tumour had not been measured. *Ex vivo* pig livers were used initially with saline, heated to 373 K, fed through a 21 gauge Teflon catheter. *In vivo* experiments used rabbits, with the liver pulled out of the abdomen. A close correspondence was found between the macroscopic lesion size, determined histologically, and the area of tissue on the images which was heated to 328 K.

Temperature monitoring of proton-decoupled ^{13}C-detected spectroscopy experiments in monkey brain showed that a WALTZ-4 decoupling scheme with

a power of 2.7 W resulted in an increase in temperature after 4 minutes of 2 K.[293] These results show that caution is necessary for future human experiments. The United States Food and Drug Administration (FDA) guidelines for humans recommend that temperature increases should be less than 1 K for the whole body, and that local heating should not result in temperatures greater than 311 K in the head, 312 K in the body, and 313 K in the extremities.

Finally, the PRF method was used to measure temperature distributions in phantoms mimicking the effect of counter-current flow in large blood vessels.[294] This effect can produce heterogeneous temperature distributions *in vivo*, even from spatially homogeneous heating sources. Experimental results agreed well with numerical simulations.

6. NON-MEDICAL APPLICATIONS OF TEMPERATURE MAPPING

Emerging areas in which non-invasive temperature measurement is important include the study of heat transfer and mass transport in porous media (geological and chemical engineering applications) and agricultural processing. In the first area, the temperature and velocity of interstitial flows has been measured through model capillaries and glass bead packed beds.[295] Temperature measurements were made using the T_1 method with a fast imaging sequence, and subsequently velocity images were produced using a bipolar gradient imaging sequence. In a second paper,[296] the authors introduced a new method, in which the usual inversion pulse used for T_1 mapping is replaced by a series of tagging pulses, for simultaneous measurements of both temperature and flow.

Many important technical problems in food processing could be addressed with a technique to measure temperatures non-invasively inside solid foods during heat-sterilization. Detailed knowledge of the heat transfer coefficient is required to ensure that all parts of the product achieve the required temperature exposure to guarantee a microbiologically safe product. MRI is a promising technique for direct measurement of heat transfer, as opposed to having to use conservative model-based estimations which result in higher than necessary temperatures being used. MRI heating studies have been published using diffusion, T_1 and the PRF methods,[297-302] and a recent review has been published.[303] Recent results from microwave heating and subsequent cooling of food phantoms[304] showed reasonable agreement between the MRI-derived temperature maps and those measured using infra-red techniques.

ACKNOWLEDGEMENTS

This review was written while on sabbatical leave at the Physics Institute at the University of Würzburg, Am Hubland, Germany. The author would like to

thank Professor Axel Haase and all members of the EP-V research group for help in many aspects of the preparation of this manuscript. Many useful suggestions and corrections were also provided by Dr. Nadine Smith at Penn State University.

REFERENCES

1. C. J. Jameson and H. J. Osten, *Annu. Rep. NMR Spectrosc.*, 1986, **17**, 1.
2. M. E. Packard and J. T. Arnold, *Phys. Rev.*, 1951, **83**, 210.
3. J. T. Arnold and M. E. Packard, *Phys. Rev.*, 1951, **19**, 1608.
4. W. G. Schneider, H. J. Bernstein and J. A. Pople, *J. Chem. Phys.*, 1958, **28**, 601.
5. L. W. Reeves, *Trans. Faraday Soc.*, 1959, **55**, 1684.
6. J. C. Davis Jr. and K. S. Pitzer, *J. Phys. Chem.*, 1960, **64**, 886.
7. J. C. Davis Jr., K. S. Pitzer and C. N. R. Rao, *J. Phys. Chem.*, 1960, **64**, 1744.
8. N. Muller and R. C. Reiter, *J. Chem. Phys.*, 1965, **42**, 3265.
9. T. W. Marshall and J. A. Pople, *Mol. Phys.*, 1958, **1**, 199.
10. A. D. Buckingham, *Can. J. Chem.*, 1960, **38**, 300.
11. J. I. Musher, *J. Chem. Phys.*, 1962, **37**, 34.
12. J. C. Hindman, *J. Chem. Phys.*, 1966, **44**, 4582.
13. A. L. Van Geet, *Anal. Chem.*, 1968, **40**, 2227.
14. A. L. Van Geet, *Anal. Chem.*, 1970, **42**, 679.
15. C. Ammann, P. Meier and A. E. Merbach, *J. Magn. Reson.*, 1982, **46**, 319.
16. D. S. Raiford, C. L. Fisk and E. D. Becker, *Anal. Chem.*, 1979, **51**, 2050.
17. E. W. Hansen, *Anal. Chem.*, 1985, **57**, 2993.
18. H. Batiz-Hernandez and R. A. Bernheim, *Prog. Nuc. Magn. Reson. Spectrosc.*, 1967, **3**, 67.
19. W. A. Bubb, K. Kirk and P. W. Kuchel, *J. Magn. Reson.*, 1988, **77**, 363.
20. N. W. Lutz, A. C. Kuesel and W. E. Hull, *Magn. Reson. Med.*, 1993, **29**, 113.
21. E. B. Cady, P. C. D'Souza, J. Penrice and A. Lorek, *Magn. Reson. Med.*, 1995, **33**, 862.
22. R. J. T. Corbett, A. R. Laptook, G. Tollefsbol and B. Kim, *J. Neurochem.*, 1995, **64**, 1224.
23. C. Arus, Y.-C. Chang and M. Barany, *J. Magn. Reson.*, 1985, **63**, 376.
24. M. E. Lacey, A. G. Webb and J. V. Sweedler, *Anal. Chem.*, 2000, **72**, 4991.
25. W. A. Gobie and C. F. Ivory, *J. Chromatogr.*, 1990, **516**, 191.
26. K. L. Davis, K.-L. Liu, M. Lanan and M. D. Morris, *Anal. Chem.*, 1993, **65**, 293.
27. J. H. Knox and K. A. McCormack, *Chromatographia*, 1994, **38**, 207.
28. J. R. Veraart, C. Gooijer and H. Lingeman, *Chromatographia*, 1997, **44**, 129.
29. A. Vinther and J. Soeberg, *J. Chromatogr.*, 1991, **559**, 3.
30. A. Vinther and J. Soeberg, *J. Chromatogr.*, 1991, **559**, 27.
31. B. Bleaney, *J. Magn. Reson.*, 1972, **8**, 91.
32. B. R. McGarvey, *J. Magn. Reson.*, 1979, **33**, 445.
33. E. W. Stout and H. S. Gutowsky, *J. Magn. Reson.*, 1976, **24**, 389.
34. R. J. Kurland and B. R. McGarvey, *J. Magn. Reson.*, 1970, **2**, 286.
35. R. S. Drago, J. I. Zink, R. M. Richman and W. D. Perry, *J. Chem. Educ.*, 1974, **51**, 371.
36. R. S. Drago, J. I. Zink, R. M. Richman and W. D. Perry, *J. Chem. Educ.*, 1974, **51**, 464.
37. C. S. Zuo, J. L. Bowers, K. R. Metz, T. Nosaka, A. D. Sherry and M. E. Clouse, *Magn. Reson. Med.*, 1996, **36**, 955.
38. C. S. Zuo, K. R. Metz, Y. Sun and A. D. Sherry, *J. Magn Reson.*, 1998, **133**, 53.
39. S. Aime, M. Botta, M. Fasano, E. Terreno, P. Kinchesh, L. Calabi and L. Paleari, *Magn. Reson. Med.*, 1996, **35**, 648.

40. T. Frenzel, K. Roth, S. Kossler, B. Raduchel, H. Bauer, J. Platzek and H. H. Weinmann, *Magn. Reson. Med.*, 1996, **35**, 364.
41. P. Konstanczak, P. Wust, B. Sander, S. Schrunderm, T. Frenzel, W. Wlodarczyk, T. Vogl, G. Muller and R. Felix, *Strahl. Onkol.*, 1997, **173**, 106.
42. M. Hentschel, P. Wust, W. Wlodarczyk, T. Frenzel, B. Sander, N. Hosten and R. Felix, *Int. J. Hyperthermia*, 1998, **14**, 479.
43. M. Hentschel, W. Dreher, P. Wust, S. Roll, D. Leibfritz and R. Felix, *Phys. Med. Biol.*, 1999, **44**, 2397.
44. W. Wlodarczyk, M. Hentschel, P. Wust, R. Noeske, N. Hosten, H. Rinneberg and R. Felix, *Phys. Med. Biol.*, 1999, **44**, 607.
45. M. Hentschel, M. Findeisen, W. Schmidt, T. Frenzel, W. Wlodarczyk, P. Wust and R. Felix, *MAGMA*, 2000, **10**, 52.
46. M. L. Kaplan, F. A. Bovey and H. N. Cheng, *Anal. Chem.*, 1975, **47**, 1703.
47. R. D. Farrant and J. C. Lindon, *Magn. Reson. Chem.*, 1994, **32**, 231.
48. N. Hedin and I. Furo, *J. Magn. Reson.*, 1998, **131**, 126.
49. W. J. Goux, L. A. Verkruyse and S. J. Salter, *J. Magn. Reson.*, 1990, **88**, 609.
50. A. Jerschow and N. Muller, *J. Magn. Reson.*, 1997, **125**, 372.
51. D. P. Hinton and C. S. Johnson, Jr., *J. Phys. Chem.*, 1993, **97**, 9064.
52. D. Wu, A. Chen and C. S. Johnson, Jr., *J. Magn. Reson. A*, 1995, **115**, 260.
53. A. Jerschow and N. Muller, *J. Magn. Reson.*, 1998, **132**, 13.
54. P. Adell, T. Parella, F. Sanchez-Ferrando and A. Virgili, *J. Magn. Reson. B*, 1995, **108**, 77.
55. C. Dalvit and G. Bovermann, *Magn. Reson. Chem.*, 1995, **33**, 156.
56. J. Stonehouse, P. Adell, J. Keeler and A. J. Shaka, *J. Am. Chem. Soc.*, 1994, **116**, 6037.
57. K. Stott, J. Keeler, Q. N. Van and A. J. Shaka, *J. Magn. Reson.*, 1997, **125**, 302.
58. J. M. Pope and S. Yao, *Conc. Magn. Reson.*, 1993, **5**, 281.
59. J. L. Duerk and O. P. Simonetti, *Conc. Magn. Reson.*, 1993, **5**, 105.
60. N. M. Loening and J. Keeler, *J. Magn. Reson.*, 1999, **139**, 334.
61. S. Combrisson and T. Prange, *J. Magn. Reson.*, 1975, **19**, 108.
62. H-J. Schneider, W. Freitag and M. Schommer, *J. Magn. Reson.*, 1975, **18**, 393.
63. P. J. Smolenaeres, M. T. Kelso and J. K. Beattie, *J. Magn. Reson.*, 1983, **52**, 118.
64. H-J. Schneider and W. Freitag, *J. Am. Chem. Soc.*, 1976, **98**, 478.
65. D. W. Vidrine and P. E. Peterson, *Anal. Chem.*, 1976, **48**, 1301.
66. J. Bornais and S. Brownstein, *J. Magn. Reson.*, 1978, **29**, 207.
67. J. J. Led and S. B. Petersen, *J. Magn. Reson.*, 1978, **32**, 1.
68. A. Allerhand, R. E. Addleman and D. Osman, *J. Am. Chem. Soc.*, 1985, **107**, 5809.
69. S. R. Maple and A. Allerhand, *J. Magn. Reson.*, 1986, **66**, 168.
70. L. D. Field, S. Sternhall and W. Veigel, *Org. Magn. Reson.*, 1984, **22**, 221.
71. H. Quast, M. Huebes, A. Dunger and H.-H. Limbach, *J. Magn. Reson.*, 1998, **134**, 236.
72. W. H. Sikorski, A. W. Sanders and H. J. Reich, *Magn. Reson. Chem.*, 1998, **36**, S118.
73. A. K. Jameson and C. J. Jameson, *J. Am. Chem. Soc.*, 1973, **95**, 8559.
74. C. J. Jameson, A. K. Jameson and S. M. Cohen, *J. Magn. Reson.*, 1975, **19**, 385.
75. R. A. Newmark and R. E. Graves, *J. Phys. Chem.*, 1968, **72**, 4299.
76. S. R. Thomas, *SPIE Medicine XIVV/PACS IV*, 1986, **626**, 7.
77. W. S. Brey Jr. and K. C. Ramey, *J. Chem. Phys.*, 1963, **39**, 844.
78. J. Jonas and H. S. Gutowsky, *J. Chem. Phys.*, 1965, **42**, 140.
79. H. S. Gutowsky, J. Jonas, F-M. Chen and R. Meinzer, *J. Chem. Phys.*, 1965, **42**, 2625.
80. K. L. Servis and J. D. Roberts, *J. Am. Chem. Soc.*, 1965, **87**, 1339.
81. A. M. Ihrig and S. L. Smith, *J. Am. Chem. Soc.*, 1972, **94**, 34.
82. J. W. Emsley, L. Phillips and V. Wray, *Prog. NMR Spectrosc.*, 1977, **10**, 85.
83. P. Parhami and B. M. Fung, *J. Phys. Chem.*, 1983, **87**, 1928.
84. C. F. Kong, G. M. Holloway, P. Parhami and B. M. Fung, *J. Phys. Chem.*, 1984, **88**, 6308.

85. L. C. Clark Jr, J. L. Ackerman and S. R. Thomas, 1985, in *Advances in Experimental Medicine and Biology, Vol. 180: Oxygen Transport to Tissue IV*, (eds D. Bruley and D. Reneau) Plenum Publishing, New York, pp. 835–845.
86. R. P. Mason and P. P. Antich, *Artif. Cells Blood Substit. Immobil. Biotechnol.*, 1994, **22**, 1361.
87. J. E. Fishman, P. M. Joseph, M. J. Carvlin, M. Saadi-Elmandjra, B. Mukherji and H. S. Sloviter, *Invest. Radiol.*, 1989, **24**, 65.
88. B. A. Berkowitz, C. A. Wilson, D. L. Hatchell and R. E. London, *Magn. Reson. Med.*, 1991, **21**, 233.
89. R. P. Mason, H. Shukla and P. P. Antich, *Magn. Reson. Med.*, 1993, **29**, 296.
90. H. P. Shukla, R. P. Mason, D. E. Woessner and P. P. Antich, *J. Magn. Reson. B*, 1995, **106**, 131.
91. B. A. Berkowitz, J. T. Handa and C. A. Wilson, *NMR Biomed.*, 1992, **5**, 65.
92. A. G. Webb, *Bull. Magn. Reson.*, 1995, **17**, 214.
93. M. D. Gordon and L. D. Quin, *J. Magn. Reson.*, 1976, **22**, 149.
94. J. R. Van Wazer, C. H. Dungan and M. M. Crutchfield, *Topics Phosphorus Chem.*, 1967, **5**, 46.
95. F. L. Dickert and S. W. Hellmann, *Anal. Chem.*, 1980, **52**, 996.
96. G. E. Maciel and R. V. James, *Inorg. Chem.*, 1964, **3**, 1650.
97. R. K. Gupta and P. Guppta, *J. Magn. Reson.*, 1980, **40**, 587.
98. S. Widmaier, T. Heoss, J. Breuer, W-I. Jung, G. J. Dietze and O. Lutz, *J. Magn. Reson. B*, 1996, **113**, 16.
99. E. M. Shapiro, A. Borthakur, N. Bansal, J. S. Leigh and R. Reddy, *J. Magn. Reson.*, 2000, **143**, 213.
100. E. M. Shapiro, A. Borthakur and R. Reddy, *MAGMA*, 2000, **10**, 114.
101. K. Roth, *Magn. Reson. Chem.*, 1987, **25**, 429.
102. M. Alei Jr., A. E. Florin, W. M. Litchman and J. F. O'Brien, *J. Phys. Chem.*, 1971, **75**, 932.
103. N. F. Ramsey, *Phys. Rev.*, 1950, **78**, 699.
104. W. G. Proctor and F. C. Yu, *Phys. Rev.*, 1951, **81**, 20.
105. J. S. Griffith and L. E. Orgel, *Trans. Faraday Soc.*, 1957, **53**, 601.
106. R. Freeman, G. R. Murray and R. E. Richards, *Proc. Roy. Soc. A.*, 1957, **242**, 455.
107. G. R. Benedeck and R. Englman, *J. Chem. Phys.*, 1963, **39**, 3349.
108. C. J. Jameson, D. Rehder and M. Hoch, *J. Am. Chem. Soc.*, 1987, **109**, 2589.
109. G. C. Levy, J. T. Bailey and D. A. Wright, *J. Magn. Reson.*, 1980, **37**, 353.
110. M. R. Niesman, B. Khoobehi, R. L. Magin and A. G. Webb, *J. Liposome Res.*, 1994, **4**, 741.
111. A. G. Webb, M. Wong, L. J. Wilmes, M. Niesman, K. S. Kolbeck, R. L. Magin and K. S. Suslick, *Int. J. Hyperthermia*, 1995, **11**, 821.
112. N. B. Smith, A. G. Webb, D. S. Ellis, L. J. Wilmes and W. D. O'Brien, *IEEE Trans. Ultrason. Ferroelectr. Freq. Control*, 1995, **42**, 489.
113. A. G. Webb and E. C. Wiener, *J. Magn. Reson. B.*, 1996, **111**, 90.
114. T. H. Brown and S. M. Cohen, *J. Chem. Phys.*, 1973, **58**, 395.
115. S. M. Cohen and T. H. Brown, *J. Chem. Phys.*, 1974, **61**, 2985.
116. W. McFarlane, *J. C. S. Dalton*, 1974, 324.
117. K. R. Dixon, M. Fakley and A. Pidcock, *Can. J. Chem.*, 1976, **54**, 2733.
118. W. McFarlane, *Chem. Commun.*, 1969, 700.
119. H. C. E. McFarlane, W. McFarlane and R. J. Wood, *Bull. Soc. Chim. Belges*, 1976, **85**, 864.
120. T. H. Brown and P. J. Green, *J. Am. Chem. Soc.*, 1970, **92**, 2359.
121. H. C. E. McFarlane, W. McFarlane and D. S. Rycroft, *J. C. S. Dalton*, 1976, 1616.
122. J. Banck and A. Schwenk, *Z. Physik B*, 1975, **20**, 75.
123. W. McFarlane and D. S. Rycroft, *J. Magn. Reson.*, 1976, **24**, 95.
124. O. Lutz and W. Steinkilberg, *Z. Naturforsh.*, 1974, **A29**, 1467.
125. R. M. Nielson and S. Wherland, *Inorg. Chem.*, 1985, **24**, 3458.
126. B. W. Epperlein, H. Kruger, O. Lutz and A. Schwenk, *Z. Naturforsh.*, 1974, **A29**, 1553.

127. W. H. Pan and J. P. Fackler, *J. Am. Chem. Soc.*, 1978, **100**, 5783.
128. H. Krueger, O. Lutz, A. Schwenk and C. Stricker, *Z. Physik A*, 1974, **266**, 233.
129. J. D. Kennedy and W. McFarlane, *J. C. S. Perkin II*, 1977, 1187.
130. P. F. Barron, D. Doddrell and W. Kitchung, *J. Organomet. Chem.*, 1977, **139**, 361.
131. H. Kruger, O. Lutz, A. Nolle and A. Schwenk, *Z. Physik A*, 1975, **273**, 325.
132. J. D. Halliday, R. E. Richards and R. R. Sharp, *Proc. Roy. Soc. A*, 1969, **313**, 45.
133. E. Mei, J. L. Dye and A. I. Popov, *J. Amer. Chem. Soc.*, 1977, **99**, 5308.
134. C. Deverall, K. Schaumburg and H. J. Bernstein, *J. Chem. Phys.*, 1968, **49**, 1276.
135. D. Rehder, *Bull. Magn. Reson.*, 1982, **4**, 33.
136. F. Naumann and D. Rehder, *Inorg. Chem. Acta*, 1984, **84**, 117.
137. K. Ihmels and D. Rehder, *Organometallics*, 1985, **4**, 1340.
138. M. Hoch and D. Rehder, *J. Organomet. Chem.*, 1985, **288**, C25.
139. A. F. Masters, R. T. C. Brownlee, M. J. O'Connor and A. G. Wedd, *Inorg. Chem.*, 1981, **20**, 4183.
140. W. A. Herrmann, H. Biersack, M. L. Ziegler, K. Weidenhammer, R. Siegel and D. Rehder, *J. Am. Chem. Soc.*, 1981, **103**, 1692.
141. F. Naumann, D. Rehder and V. Pank, *J. Organomet. Chem.*, 1982, **240**, 363.
142. H-C. Bechthold and D. Rehder, *J. Organomet. Chem.*, 1982, **233**, 215.
143. P. Granger and S. Chapelle, *J. Magn. Reson.*, 1980, **39**, 329.
144. S. Hafner and N. H. Nachtrieb, *J. Chem. Phys.*, 1964, **40**, 2891.
145. R. W. Briggs and J. F. Hinton, *J. Magn. Reson.*, 1978, **32**, 155.
146. R. W. Briggs and J. F. Hinton, *J. Magn. Reson.*, 1979, **33**, 363.
147. P. J. Burke, R. W. Mathews, I. D. Cresshull and D. G. Gillies, *J. C. S. Dalton*, 1981, 132.
148. M. J. Forster, D. G. Gillies and R. W. Mathews, *J. Magn. Reson.*, 1985, **65**, 497.
149. V. N. Torocheshnikov, A. P. Tupciauskas, N. M. Sergeyev and Y. A. Ustynyuk, *J. Organomet. Chem.*, 1972, **35**, C25.
150. P. J. Smith, R. F. M. White and L. Smith, *J. Organomet. Chem.*, 1972, **40**, 341.
151. J. D. Kennedy, W. McFarlane, P. J. Smith, R. F. M. White and L. Smith, *J. C. S. Perkin II*, 1973, 1785.
152. J. D. Kennedy, *J. C. S. Perkin II*, 1977, 242.
153. O. Lutz and G. Stricker, *Phys. Lett. A*, 1971, **35**, 397.
154. G. E. Maciel and J. L. Dallas, *J. Am. Chem. Soc.*, 1973, **95**, 3039.
155. R. M. Hawk and R. R. Sharp, *J. Magn. Reson.*, 1973, **10**, 385.
156. H. D. Burrows, C. F. G. C. Geraldes, T. J. T. Pinheiro, R. K. Harris and A. Sebald, *Liq. Cryst.*, 1988, **3**, 853.
157. J. R. Lyerla, C. S. Yannoni and C. A. Fyfe, *Acc. Chem. Res.*, 1982, **15**, 208.
158. J. F. Haw, *Anal. Chem.*, 1988, **60**, 559A.
159. O. Knop, R. E. Wasylishen, M. A. White, T. S. Cameron and M. J. van Oort, *Can. J. Chem.*, 1990, **68**, 412.
160. Q. Xu, T. Eguchi and H. Nakayama, *Bull. Chem. Soc. Jpn.*, 1992, **65**, 2264.
161. F. G. Riddell, P. G. Bruce, P. Lightfoot and M. Rogerson, *J. C. S. Chem. Commun.*, 1994, **209**.
162. S. J. Hayes and C. M. Dobson, *J. Am. Chem. Soc.*, 1991, **113**, 463.
163. D. C. Apperly, N. A. Davies, R. K. Harris, S. Eller, P. Schwarz and R. D. Fischer, *J. C. S. Chem. Commun.*, 1992, **740**.
164. A. B. Aliev, K. D. M. Harris and D. C. Apperly, *J. Chem. Soc. Chem. Commun.*, 1993, 251.
165. C. Dybowski and S. Bai, *Anal. Chem.*, 2000, **72**, 1R.
166. J. F. Haw, G. C. Campbell and R. C. Crosby, *Anal. Chem.*, 1986, **58**, 3172.
167. F. D. Doty, Solid state probe design, in *Encyclopedia of Nuclear Magnetic Resonance*, (ed. D. M. Grant and R. K. Harris) John Wiley and Sons, New York. Vol. 7, pp. 4475, 1996.
168. T. Bjorholm and H. J. Jakobsen, *J. Magn. Reson.*, 1989, **84**, 204.
169. G-J. M. P. van Moorsel, E. R. H. van Eck and C. P. Grey, *J. Magn. Reson. A*, 1995, **113**, 159.

170. J. F. Haw, R. A. Crook and R. C. Crosby, *J. Magn. Reson.*, 1986, **66**, 551.
171. K. L. Anderson-Altmann and D. M. Grant, *J. Phys. Chem.*, 1993, **97**, 11096.
172. A. E. Aliev, K. D. M. Harris and D. C. Apperley, *J. C. S. Chem. Commun.*, 1993, **251**.
173. A. E. Aliev and K. D. M. Harris, *Magn. Reson. Chem.*, 1994, **32**, 366.
174. A. N. Klymachov and N. S. Dalal, *Solid State Nucl. Magn. Reson.*, 1996, **7**, 127.
175. A. D. English, *J. Magn. Reson.*, 1984, **57**, 491.
176. G. C. Campbell, R. C. Crosby and J. F. Haw, *J. Magn. Reson.*, 1986, **69**, 191.
177. B. Wehrle, F. Aguilar-Parilla and H-H. Limbach, *J. Magn. Reson.*, 1990, **87**, 584.
178. F. Aguilar-Parilla, B. Wehrle, H. Braunling and H. H. Limbach, *J. Magn. Reson.*, 1990, **87**, 592.
179. H. Pan and B. C. Gerstein, *J. Magn. Reson.*, 1991, **92**, 618.
180. C. P. Grey, A. K. Cheetham and C. M. Dobson, *J. Magn. Reson. A*, 1993, **101**, 299.
181. J. H. van Vleck, 1931, *The Theory of Electric and Magnetic Susceptibilities*, Oxford University Press, Oxford.
182. E. D. Jones, *Phys. Rev.*, 1969, **180**, 455.
183. L. C. M. van Gorkom, J. M. Hook, M. B. Logan, J. V. Hanna and R. E. Wasylishen, *Magn. Reson. Chem.*, 1995, **33**, 791.
184. A. Bielecki and D. P. Burun, *J. Magn. Reson. A*, 1995, **116**, 215.
185. G. Neue, C. Dybowski, M. L. Smith, M. A. Hepp and D. L. Perry, *Solid State Nucl. Magn. Reson.*, 1996, **6**, 241.
186. G. Neue and C. Dybowski, *Solid State Nucl. Magn. Reson.*, 1997, **7**, 333.
187. D. B. Ferguson and J. F. Haw, *Anal. Chem.*, 1995, **67**, 3342.
188. P. A. Beckmann and C. Dybowski, *J. Magn. Reson.*, 2000, **146**, 379.
189. B. Quesson, J. A. de Zwart and C. T. W. Moonen, *J. Magn. Reson., Imag.*, 2000, **12**, 525.
190. N. Bloembergen, E. M. Purcell and R. V. Pound, *Phys. Rev.*, 1948, **73**, 679.
191. J. R. Zimmerman and W. E. Brittin, *J. Phys. Chem.*, 1957, **61**, 1328.
192. E. D. Finch and L. D. Homer, *Biophys. J.*, 1974, **14**, 907.
193. B. M. Fung, *Biophys. J.*, 1977, **18**, 235.
194. B. M. Fung and T. McGaughy, *Biochim. Biophys. Acta*, 1974, **343**, 663.
195. B. M. Fung, D. L. Durham and D. A. Wassil, *Biochim. Biophys. Acta*, 1975, **399**, 191.
196. C. J. Lewa and Z. Majewska, *Bull. Cancer (Paris)*, 1980, **67**, 525.
197. P. A. Bottomley, T. H. Forster and R. E. Argersinger, *Med. Phys.*, 1984, **11**, 425.
198. T. R. Nelson and S. M. Tung, *Magn. Reson. Imag.*, 1987, **5**, 189.
199. D. L. Parker, V. Smith, P. Sheldon, L. E. Crooks and L. Fussel, *Med. Phys.*, 1983, **10**, 321.
200. D. L. Parker, *IEEE Trans. Biomed. Eng.*, 1984, **31**, 161.
201. R. J. Dickinson, A. S. Hall, A. J. Hind and I. R. Young, *J. Comput. Assist. Tomogr.*, 1986, **10**, 468.
202. F. A. Jolesz, A. R. Bleier, P. Jakab, P. W. Ruenzel, K. Huttl and G. J. Jako, *Radiology*, 1988, **168**, 249.
203. R. Matsumoto, K. Oshio and F. A. Jolesz, *J. Magn. Reson. Imag.*, 1992, **2**, 555.
204. A. S. Hall, M. V. Prior, J. W. Hand, I. R. Young and R. J. Dickinson, *J. Comput. Assist. Tomogr.*, 1990, **14**, 430.
205. K. Hynynen, A. Darkazanli, C. A. Damianou, E. Unger and J. F. Schenck, *Eur. Urol.*, 1993, **23**, 12.
206. H. E. Cline, J. F. Schenk, R. D. Watkins, K. Hynynen and F. A. Jolesz, *Magn. Reson. Med.*, 1993, **30**, 98.
207. H. E. Cline, K. Hynynen, C. J. Hardy, R. D. Watkins, J. F. Schenk and F. A. Jolesz, *Magn. Reson. Med.*, 1994, **31**, 628.
208. C. J. Hardy, H. E. Cline and R. D. Watkins, *J. Comput. Assist. Tomogr.*, 1994, **18**, 476.
209. C. Schwarzbauer, J. Zange, H. Adolf, R. Deichmann, U. Noth and A. Haase, *J. Magn. Reson. B*, 1995, **106**, 178.

210. R. Matsumoto, R. V. Mulkern, S. G. Hushek and F. A. Jolesz, *J. Magn. Reson., Imag.*, 1994, **4**, 65.
211. E. Mietzsch, M. Koch, M. Schaldach, J. Werner, B. Bellenberg and K. U. Wentz, *Med. Biol. Eng. Comput.*, 1998, **36**, 673.
212. P. R. Morrison, F. A. Jolesz, D. Charous, R. V. Mulkern, S. G. Hushek, R. Margolis and M. P. Fried, *J. Magn. Reson. Imag.*, 1998, **8**, 57.
213. C. Bremer, T. Allkemper, J. Menzel, U. Sulkowski, E. Rummeny and P. Reimer, *J. Magn. Reson. Imag.*, 1998, **8**, 235.
214. P. Reimer, C. Bremer, C. Horch, C. Morgenroth, T. Allkemper and G. Schuierer, *J. Magn. Reson. Imag.*, 1998, **8**, 240.
215. H. J. Schwarzmaier and T. Kahn, *Magn. Reson. Med.*, 1995, **33**, 729.
216. J. F. Toussaint, K. K. Kwong, F. M'Kparu, R. M. Weiskoff, P. J. Laraia and H. L. Kantor, *Magn. Reson. Med.*, 1996, **35**, 62.
217. I. R. Young, J. W. Hand, A. Oatridge and M. V. Prior, *Magn. Reson. Med.*, 1994, **32**, 358.
218. I. R. Young, J. W. Hand, A. Oatridge, M. V. Prior and G. R. Forse, *Magn. Reson. Med.*, 1994, **31**, 342.
219. C. Bohris, W. G. Schreiber, J. Jenne, I. Simiantonakis, R. Rastert, J-J. Zabel, P. Huber, R. Bader and G. Brix, *Magn. Reson. Imag.*, 1999, **17**, 603.
220. K. Hynynen, N. McDannold, R. V. Mulkern and F. A. Jolesz, *Magn. Reson. Med.*, 2000, **43**, 901.
221. D. C. Chang, H. E. Rorschach, B. L. Nichols and C. F. Hazlewood, *Ann. NY. Acad. Sci.*, 1973, **204**, 434.
222. E. O. Stejskal and J. E. Tanner, *J. Chem. Phys.*, 1965, **42**, 288.
223. D. Lebihan, J. Delannoy and R. L. Levin, *Radiology*, 1989, **171**, 853.
224. J. Delannoy, C-N. Chen, R. Turner, R. L. Levin and D. Le Bihan, *Magn. Reson. Med.*, 1991, **19**, 333.
225. Y. Zhang, T. V. Samulski, W. T. Joines, J. Mattiello, R. L. Levin and D. Lebihan, *Int. J. Hyperthermia*, 1992, **8**, 263.
226. T. V. Samulski, J. Macfall, Y. Zhang, W. Grant and C. Charles, *Int. J. Hyperthermia*, 1992, **8**, 819.
227. D. Morvan, A. L.-Willig, A. Malgouyres, C. A. Counod, P. Jehenson and A. Syrota, *Magn. Reson. Med.*, 1993, **29**, 371.
228. T. V. Samulski, S. T. Clegg, S. Das, J. MacFall and D. M. Prescott, *Int. J. Hyperthermia*, 1994, **10**, 389.
229. S. T. Clegg, S. K. Das, Y. Zhang, J. Macfall, E. Fullar and T. V. Samulski, *Int. J. Hyperthermia*, 1995, **11**, 409.
230. J. Macfall, D. M. Prescott, E. Fuller and T. V. Samulski, *Int. J. Hyperthermia*, 1995, **11**, 73.
231. J. Hennig, A. Nauerth and H. Friedburg, *Magn. Reson. Med.*, 1992, **27**, 142.
232. K. A. Il'yasov and J. Hennig, *J. Magn. Reson. Imag.*, 1998, **8**, 1296.
233. T. E. Conturo, R. C. McKinsry, E. Akbudak and B. H. Robinson, *Magn. Reson. Med.*, 1996, **35**, 399.
234. Y. Ishihara, A. Calderon, H. Watanabe, K. Okamoto, Y. Suzuki, K. Kuroda and Y. Suzuki, *Magn. Reson. Med.*, 1995, **34**, 814.
235. R. D. Peters, R. S. Hinks and R. M. Henkelman, *Magn. Reson. Med.*, 1998, **40**, 454.
236. S. J. Graham, M. J. Bronskill and R. M. Henkelman, *Magn Reson Med.*, 1998, **39**, 198.
237. T. Wu, K. R. Kendall, J. P. Felmlee, B. D. Lewis and R. L. Ehman, *Med. Phys.*, 2000, **27**, 221.
238. J. S. Philo and W. M. Fairbank, *J. Chem. Phys.*, 1980, **72**, 4429.
239. L. D. Hall and S. L. Talagala, *J. Magn. Reson.*, 1985, **65**, 501.
240. K. Kuroda, K. Abe, S. Tsutsumi, Y. Ishihara, Y. Suzuki and K. Satoh, *Biomed. Therm.*, 1993, **13**, 43.
241. K. Kuroda, Y. Suzuki, Y. Ishihara, K. Okamoto and Y. Suzuki, *Magn. Reson. Med.*, 1996, **35**, 20.

242. J. De Poorter, C. De Wagter, Y. De Deene, C. Thomsen, F. Stahlberg and E. Achten, *J. Magn. Reson. B*, 1994, **103**, 234.
243. J. De Poorter, C. De Wagter, Y. De Deene, C. Thomsen, F. Stahlberg and E. Achten, *Magn. Reson. Med.*, 1995, **33**, 74.
244. A. H. Chung, K. Hynynen, V. Colucci, K. Oshio, H. E. Cline and F. A. Jolesz, *Magn. Reson. Med.*, 1996, **36**, 745.
245. N. J. Pelc, M. A. Bernstein, A. Shimakawa and G. H. Glover, *J. Magn. Reson. Imag.*, 1991, **1**, 405.
246. H. Gubdjartsson and S. Patz, *Magn. Reson. Med.*, 1995, **34**, 910.
247. R. J. Stafford, J. D. Hazle and G. H. Glover, *Magn. Reson. Med.*, 2000, **43**, 909.
248. J. A. de Zwart, P. van Gelderen, D. J. Kelly and C. T. W. Moonen, *J. Magn. Reson. B*, 1996, **112**, 86.
249. C. T. W. Moonen, G. Liu, P. van Gelderen and G. Sobering, *Magn. Reson. Med.*, 1992, **26**, 184.
250. G. Liu, G. Sobering, A. W. Olson, P. van Gelderen and C. T. W. Moonen, *Magn. Reson. Med.*, 1993, **30**, 68.
251. G. Liu, G. Sobering, J. Duyn and C. T. Moonen, *Med. Phys.*, 1997, **24**, 269.
252. Y. C. Chung, J. L. Duerk, A. Shankaranarayanan, M. Hampke, E. M. Merkle and J. S. Lewin, *J. Magn. Reson. Imag.*, 1999, **9**, 138.
253. H. E. Cline, K. Hynyen, E. Schneider, C. J. Hardy, S. E. Maier, R. D. Watkins and F. A. Jolesz, *Magn. Reson. Med.*, 1996, **35**, 309.
254. R. Stollberger, P. W. Ascher, D. Huber, W. Renhart, J. Radner and F. Ebner, *J. Magn. Reson. Imag.*, 1998, **8**, 188.
255. R. D. Peters, R. S. Hinks and R. M. Henkelman, *Magn. Reson. Med.*, 1999, **41**, 909.
256. R. D. Peters and R. M. Henkelman, *Magn. Reson. Med.*, 2000, **43**, 62.
257. J. De Poorter, *Magn. Reson. Med.*, 1995, **34**, 359.
258. J. A. de Zwart, F. C. Vimeux, C. Delalande, P. Canioni and C. T. W. Moonen, *Magn. Reson. Med.*, **42**, 1999, 53.
259. F. Bertsch, J. Mattner, M. K. Stehling, U. Muller-Lisse, M. Peller, R. Loeffler, J. Weber, K. Messmer, W. Wilmann, R. Issels and M. Reiser, *Magn. Reson. Imag.*, 1998, **16**, 393.
260. K. Kuroda, K. Oshio, A. H. Chung, K. Hynynen and F. Jolesz, *Magn. Reson. Med.*, 1997, **38**, 845.
261. R. V. Mulkern, L. P. Panych, N. J. McDannold, F. A. Jolesz and K. Hynynen, *J. Magn. Reson. Imag.*, 1998, **8**, 493.
262. S. A. Sapareto and W. C. Dewey, *Int. J. Radiat. Oncol. Biol. Phys.*, 1984, **10**, 787.
263. K. Matthewson, P. Coleridge-Smith, J. P. O'Sullivan, T. C. Northfield and S. G. Brown, *Gastroenterology*, 1987, **93**, 550.
264. A. H. Dachman, J. A. McGehee, T. E. Beam, J. A. Burriss and D. A. Powell, *Radiology*, 1990, **176**, 129.
265. T. Harth, T. Hahn, M. Rassek, B. Schwabe, H. J. Schwarzmaier, J. S. Lewin and U. Modder, *Magn. Reson. Med.*, 1997, **38**, 238.
266. C. P. Schulze, T. Kahn, T. Harth, J-J Schwarzmaier and R. Schober, *J. Magn. Reson. Imag.*, 1998, **8**, 115.
267. T. Kahn, T. Harth, J. G. W. Kiwit, J-J Schwarzmaier, C. Wald and U. Kodder, *J. Magn. Reson. Imag.*, 1998, **8**, 160.
268. J. Heisterkamp, N. A. A. Matheijssen, R. v. Hillegersberg, J. J. van Vaals, J. S. Lameris, J. Stoker and J. N. M. Ijzermans, *Magn. Reson. Med.*, 1999, **41**, 919.
269. L. P. Panych, M. I. Hrovat, A. R. Bleier and F. A. Jolesz, *J. Magn. Reson. Imag.*, 1992, **2**, 69.
270. R. D. Peters, E. Chan, J. Trachtenberg, S. Jothy, L. Kapusta, W. Kucharczyk and R. M. Henkelman, *Magn. Reson. Med.*, 2000, **44**, 873.
271. K. Kuroda, A. H. Chung, K. Hynynen and F. A. Jolesz, *J. Magn. Reson. Imag.*, 1998, **8**, 175.
272. K. Hynynen, N. I. Vykhodtseva, A. H. Chung, V. Sorrentino, V. Colucci and F. A. Jolesz, *Radiology*, 1997, **204**, 247.

273. N. McDannold, K. Hynynen, D. Wolf, G. Wolf and F. Jolesz, *J. Magn. Reson., Imag.*, 1998, **8**, 91.
274. A. H. Chung, F. A. Jolesz and K. H. Hynynen, *Med Phys.*, 1999, **26**, 2017.
275. S. J. Graham, L. Chen, M. Leitch, R. D. Peters, M. J. Bronskill, F. S. Foster, R. M. Henkelman and D. B. Plewes, *Magn. Reson. Med.*, 1999, **41**, 321.
276. N. L. McDannold, R. L. King, F. A. Jolesz and K. H. Hynynen, *Radiology*, 2000, **216**, 517.
277. N. J. McDannold, F. A. Jolesz and K. H. Hynynen, *Radiology*, 1999, **211**, 419.
278. N. B. Smith, M. T. Buchanan and K. Hynynen, *Int. J. Radiat. Oncol. Biol. Phys.*, 1999, **43**, 217.
279. F. C. Vimeux, J. A. de Zwaart, J. Paulussiere, R. Fawaz, C. Delalande, P. Canioni, N. Grenier and C. T. W. Moonen, *Invest. Radiol.*, 1999, **34**, 190.
280. R. Salomir, F. C. Vimeux, J. A. de Zwart, N. Grenier and C. T. W. Moonen, *Magn. Reson. Med.*, 2000, **43**, 342.
281. R. Salomir, J. Palussiere, F. C. Vimeux, J. A. de Zwart, B. Quesson, M. Gauchet, P. Lelong, J. Pergrale, N. Grenier and C. T. W. Moonen, *J. Magn. Reson. Imag.*, 2000, **12**, 571.
282. J. R. MacFall, D. M. Prescott, H. C. Charles and T. V. Samulski, *Med. Phys.*, 1996, **23**, 1775.
283. S. Sinha, T. Oshiro, U. Sinha and R. Lufkin, *J. Magn. Reson. Imag.*, 1997, **7**, 918.
284. I. A. Vitkin, J. A. Moriarty, R. D. Peters, M. C. Kolios, A. S. Gladman, J. C. Chen, R. S. Hinks, J. W. Hunt, B. C. Wilson, A. C. Easty, M. J. Bronskill, W. Kucharczyk, M. D. Sherar and R. M. Henkelman, *Med. Phys.*, 1997, **24**, 269.
285. J. A. Moriarty, J. C. Chen, C. M. Purcell, L. C. Ang, R. S. Hinks, R. D. Peters, R. M. Henkelman, D. B. Plewes, M. J. Bronskill and W. Kucharczyk, *J. Magn. Reson. Imag.*, 1998, **8**, 128.
286. D. L. Carter, J. R. MacFall, S. T. Clegg, X. Wan, D. M. Prescott, H. C. Charles and T. V. Samulski, *Int. J. Radiat. Oncol. Biol. Phys.*, 1998, **40**, 815.
287. J. C. Chen, J. A. Moriarty, J. A. Derbyshire, R. D. Peters, J. Trachtenberg, S. D. Bell, J. Doyle, R. Arrelano, G. A. Wright, R. M. Henkelman, R. S. Hinks, S-Y. Lok, A. Toi and W. Kucharczyk, *Radiology*, 2000, **214**, 290.
288. Y. Wang and D. B. Plewes, *Magn. Reson. Med.*, 1999, **42**, 158.
289. Y. Wang, J. W. Hunt, F. S. Foster and D. B. Plewes, *IEEE Trans. Ultrason. Ferroelectr. Freq. Control*, 1999, **46**, 1192.
290. D. P. Madio, P. van Gelderen, D. DesPres, A. Olson, J. A. de Zwart, T. W. Fawcett, N. J. Holbrook, M. Mandel and C. T. W. Moonen, *J. Magn. Reson. Imag.*, 1998, **8**, 101.
291. S. Okuda, K. Kuroda, K. Oshio, R. V. Mulkern, V. Colucci, P. R. Morrison, O. Kainuma and F. A. Jolesz, *J. Magn. Reson. Imag.*, 2000, **12**, 330.
292. N. Honda, Q. Guo, H. Uchida, H. Ohishi and Y. Hiasa, *Radiology*, 1994, **190**, 53.
293. Y. Ishihara, H. Watanabe, K. Okamoto, T. Kanamatsu and Y. Tsukada, *Magn. Reson. Med.*, 2000, **43**, 796.
294. O. I. Craciunescu, T. V. Samulsi, J. R. MacFall and S. T. Clegg, *IEEE Trans. Biomed. Eng.*, 2000, **47**, 435.
295. K. Ogawa, S. Hirai, I. Okamoto and K. Okazaki, *Thermal Sci. Eng.*, 1999, **7**, 1.
296. K. Ogawa, M. Tobo, N. Iriguchi, S. Hirai and K. Okazaki, *Magn. Reson. Imag.*, 2000, **18**, 209.
297. X. Z. Sun, J. B. Litchfield and S. J. Schmidt, *J. Food Sci.*, 1993, **68**, 168.
298. G. Hulbert, J. B. Litchfield and S. J. Schmidt, *J. Food Sci.*, 1995, **70**, 780.
299. J. B. Litchfield, *J. Magn. Reson. Anal.*, 1996, **2**, 172.
300. C. A. Kantt, A. G. Webb and J. B. Litchfield, *J. Food Sci.*, 1997, **62**, 1.
301. G. J. Hulbert, J. B. Litchfield and S. J. Schmidt, *J. Food. Eng.*, 1997, **34**, 193.
302. C. A. Kantt, S. J. Schmidt, C. E. Sizer, S. Palaniappan and J. B. Litchfield, *J. Food. Sci.*, 1998, **63**, 305.
303. A. G. Webb and J. B. Litchfield, Magnetic resonance temperature mapping, in *Advances in Magnetic Resonance in Food Science*, (eds. P. S. Belton, B. P. Hills and G. A. Webb) Royal Society of Chemistry, Cambridge, 1999, pp. 245.
304. K. P. Nott, L. D. Hall, J. R. Bows, M. Hale and M. L. Patrick, *Magn. Reson. Imag.*, 2000, **18**, 69.

Structural Studies of Amino Acids, Polypeptides and Proteins in the Solid State by ^{1}H CRAMPS NMR

AKIRA SHOJI,[1] HIDEAKI KIMURA,[1] and HISASHI SUGISAWA[2]

[1]*Department of Biological Sciences, Gunma University, Tenjin-cho, Kiryu-shi, Gunma 376–8515, Japan*

[2]*NMR Applications Laboratory, Application and Research Center, Analytical Instruments Division, JEOL Ltd., 3-1-2, Musashino, Akishima-shi, Tokyo 196-0021, Japan*

1. Introduction 69
2. Theoretical background 70
   2.1. History of high-resolution solid-state ^{1}H NMR 70
   2.2. Features of ^{1}H CRAMPS NMR 75
   2.3. Adjustment for ^{1}H CRAMPS measurements 78
   2.4. Experimental determination of scaling factor of BR-24 80
   2.5. Measurement conditions of ^{1}H CRAMPS NMR 83
   2.6. Confirmation of modulation 83
3. Experimental evidence 84
   3.1. Structural studies of α-amino acid crystals by ^{1}H CRAMPS NMR 84
   3.2. Conformational study of synthetic polypeptides by ^{1}H CRAMPS NMR 97
   3.3. Conformational study of natural fibrous proteins and their model polypeptides by ^{1}H CRAMPS NMR 113
   3.4. Determination of amide proton chemical shift 128
   3.5. Determination of N—H bond lengths from the dipolar spinning sideband pattern of amide ^{1}H signals 141
   Acknowledgements 147
   References 147

1. INTRODUCTION

Times are currently very exciting in the field of NMR research. From initial research into the proton nucleus of solutions, the science has developed over the past 50 years to the stage where the space structure of proteins is now being analysed.

ANNUAL REPORTS ON NMR SPECTROSCOPY
VOLUME 45 ISBN 0-12-505445-9

In the field of organic chemistry, high-resolution solid-state NMR research has been applied to the study of spin $\frac{1}{2}$ nuclei which contain very small amounts of carbon and nitrogen. The cross-polarization magic angle spinning (CP-MAS) method is commonly used in the high-resolution solid-state studies of organic compounds using ^{13}C and ^{15}N NMR measurements.

Research into high-resolution solid-state NMR studies of proton nuclei containing relatively high isotopic abundance has tended to lag behind the other research, even though the quality and quantity of information that may be gained from such techniques using the hydrogen nucleus is potentially very great.

Why has solid-state high-resolution NMR of the proton nucleus been retarded?
How can this research be made more accessible?
What kind of knowledge does this research offer?

It is hoped that this chapter will answer some of these questions.

A study example concerning the solid structure of α-amino acid, polypeptide and a protein is given to introduce the basis of the chemical shift of proton NMR precisely, and studies to do this have only recently been undertaken. Some interesting work has been done, including the discrimination of amino acid crystal polymorphism, conformational analysis of polypeptides and fibrous proteins, and the determination of the N—H bond length in polypeptides.

We introduce research results from recent proton Combined Rotation and Multiple Pulse Spectroscopy (CRAMPS) NMR of α-amino acids, polypeptides and proteins. Proton CRAMPS NMR research has only just begun and has the possibility of wide-ranging future development.

2. THEORETICAL BACKGROUND

2.1. History of high-resolution solid-state ^1H NMR

The first successful nuclear magnetic resonance (NMR) measurements were made by E. M. Purcell *et al.*[1] at Harvard, and F. Bloch *et al.*[2] at Stanford, independently in 1946. They observed the proton (^1H) signal of the hydrogen nucleus of samples of paraffin wax (solid) and water (liquid), respectively. Their success in observing the proton signal was based on using samples in which the relaxation time was short.

In 1951, J. T. Arnold *et al.*[3] measured the ^1H NMR spectra of first acetic acid, then ethanol. They discovered the concept of 'chemical shift' and the relative 'intensities' of signals corresponding to the number of protons, as shown in Fig. 1. This fact enabled the ^1H NMR method (that is to say, high-resolution NMR) to be applied to research in chemistry. Shortly after this, the main thrust of NMR research changed to the study of structures using solution ^1H NMR.

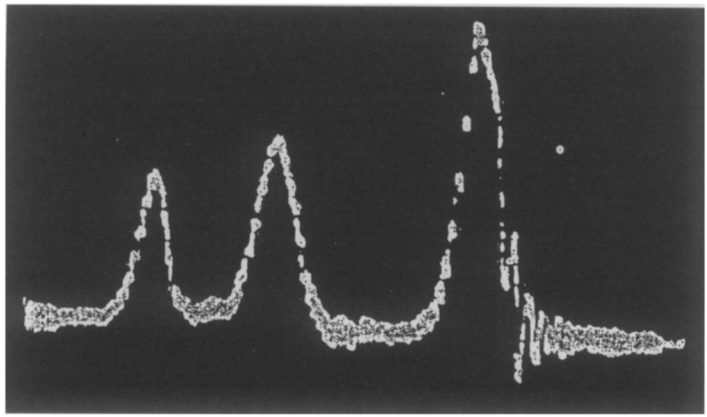

Fig. 1. Oscillograph trace of the nuclear induction signal from ethyl alcohol. The peaks from left to right represent OH, CH_2, and CH_3 (from ref. 3). Reproduced with permission from the American Institute of Physics.

High-resolution solid-state ^{1}H NMR spectroscopy has been remarkably late in developing, because it gave only very broad line spectra (half-widths of several tens of kilohertz) without structure, and therefore, information such as chemical shifts and scalar spin–spin couplings was lost completely. The cause of the broad linewidths in solid-state ^{1}H NMR spectra originates mainly from chemical shift anisotropy, heteronuclear dipolar coupling, and homonuclear dipolar coupling (see ref. 4. concerning the historical perspectives of NMR).

The frequency observed in NMR spectroscopy corresponds to the energy change ($\Delta E = h\Delta\nu$). The energies and eigenvalues of the Hamilton operator are defined by the following expressions in the rotating frame:

$$H = H_Z + H_S + H_\sigma + H_{CSA} + H_{DD(homo)} + H_{DD(hetero)} + H_Q$$

where H_Z is the Zeeman interaction, H_S is the scalar spin–spin interaction, H_σ is the isotropic chemical shift interaction, H_{CSA} is the anisotropic chemical shift interaction, $H_{DD(homo)}$ is the homonuclear dipole–dipole interaction, $H_{DD(hetero)}$ is the heteronuclear dipole–dipole interaction, and H_Q is the quadrupolar interaction.

In this respect, the NMR active nuclei behave differently and they can be divided into four groups as follows.

Group 1: spin 1/2 and high natural abundance (^{1}H, ^{19}F, etc.)
Group 2: spin 1/2 and low natural abundance (^{13}C, ^{15}N, ^{29}Si, etc.)
Group 3: integer spin (^{2}H, ^{14}N, etc.)
Group 4: half-integer spin (^{11}B, ^{17}O, ^{23}Na, ^{27}A, etc.)

In the nuclei belonging to Groups 1 and 2 (spin 1/2), H_Q is zero. Thus, NMR experiments with nuclei of Group 2 have pioneered in the development of

high-resolution solid-state NMR, with applications in chemistry, because it is not too difficult to average to zero the anisotropic chemical shift interaction and the heteronuclear dipole–dipole interaction. For this group, the CP-MAS method is most commonly used.[5] By contrast, measurements with nuclei from Group 1 are very difficult, because their high natural abundance leads to strong homogeneous homonuclear dipole–dipole interactions. Homonuclear dipolar decoupling is relatively difficult in this system. In the case of high-resolution solid-state ^{1}H NMR, we have to make homonuclear and heteronuclear dipolar interactions and the anisotropic chemical shift equal to zero to observe the isotropic chemical shift interaction.

The discovery of MAS by E. R. Andrew *et al.*[6] in 1959 was a happy piece of news for scientists who were eagerly looking forward to measuring high-resolution solid-state NMR spectra. It was found that the origin of dipolar broadening and chemical shift anisotropy in NMR spectra was removed by specimen rotation at 54.74° which is the zero point of the angular factor $(3\cos^2\theta - 1)/2$ in the second Legendre polynomial. Terms H_{CSA}, $H_{DD(homo)}$, and $H_{DD(hetero)}$ contain this angular factor. MAS can effectively remove the broadening due to H_{CSA}, $H_{DD(homo)}$ and $H_{DD(hetero)}$. This certainly sounds fine in theory, but it is not so easy in practice. Although elimination of anisotropic interactions in spin 1/2 nuclei by MAS has found widespread application, removal of the homonuclear dipolar interaction in rigid solids proved to be much more difficult. A. Samoson *et al.*[7] reported at EENC 2000 and ENC 2000 that they successfully rotated their sample at 45–50 kHz. This is not enough for the decoupling of homonuclear dipolar interactions between protons, even using the best modern technique. The approach to high-resolution ^{1}H NMR in solids using MAS alone has made recent significant developments, however, resolution of the spectra still leaves a lot to be desired. The ^{1}H–^{1}H homonuclear dipolar interaction is the greatest hold-up to high-resolution ^{1}H NMR in solids, although MAS very effectively decouples the chemical shift anisotropy and heteronuclear dipolar interaction.

In 1968, J. S. Waugh *et al.*[8] reported a new method for removal of the homonuclear dipolar interaction using multiple pulses (WAHUHA-4; Waugh, Huber and Haeberlen; 4 pulses/cycle), which is shown in Fig. 2. Homonuclear dipolar decoupling by multiple-pulse irradiation is termed 'MAS in spin space'.[9] In general, we consider that the magnetization of the z direction is

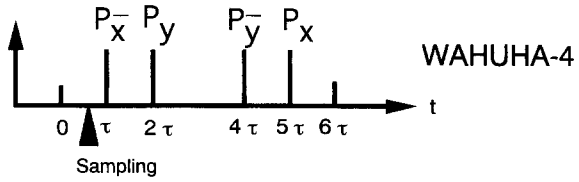

Fig. 2. Pulse sequence of WAHUHA-4 (see ref. 8).

rotated to the y direction by a 90° pulse in the x direction in the rotating frame. This process can be reworded as 'the rotating frame is pushed down in the opposite direction of the fallen direction of the magnetization by the 90° pulse'. This system is called a 'toggling frame'. In the toggling frame, the magnetization does not move, but the direction of the Hamiltonians changes. Therefore, the homonuclear dipolar Hamiltonian, but not the magnetization, is rotated by WAHUHA-4 around the $(\pm 1, \pm 1, \pm 1)$ axis, which gives the magic angle of 54.74° on the z axis. This motion in spin space allows the homonuclear dipolar Hamiltonian to average out to zero under sufficiently short pulse spacing. Stroboscopic data sampling synchronized with the cycle time of WAHUHA-4 is carried out. Other Hamiltonians such as the chemical shift and heteronuclear dipolar Hamiltonians are also affected by the multiple pulse. For example, each of the three chemical shift Hamiltonians, I_z, I_y and I_x remain for 2τ during the multiple pulse. In the case of short cycle time, these three chemical shift Hamiltonians are averaged. Therefore, the direction of the average Hamiltonian of the chemical shift is the magic angle 54.74° on the z axis whose direction is $(1, 1, 1)$. This means that the chemical shift is scaled down by $1/\sqrt{1+1+1}$ under WAHUHA-4.

On the basis of WAHUHA-4, multiple-pulse sequences have been developed in order to reduce the higher-order terms of the dipolar Hamiltonian in the Magnus expansion and the effects of pulse imperfections. Small error terms in the multiple pulse cycle lead to large problems. Among the various multiple-pulse sequences, MREV-8[10] (Mansfield, Rhim, Elleman and Vaughan; 8 pulses/cycle) and BR-24[11] (Burum and Rhim; 24 pulses/cycle) are the most sophisticated (Fig. 3). The BR-24, in particular, averages out the homonuclear dipolar interaction up to the third order in the Magnas expansion: the MREV-8 averages out the H_{DD} up to first order. As with WAHUHA-4, chemical shifts are scaled by MREV-8 and BR-24. The theoretical scaling factors, which are the scaled chemical shifts, are as follows: WAHUHA-4, $1/\sqrt{3} = 0.571$; MREV-8,

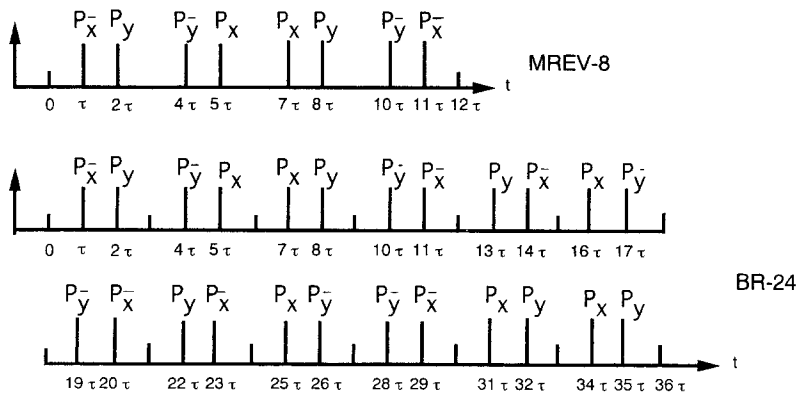

Fig. 3. Pulse sequences of MREV-8 and BR-24 (see refs 10 and 11).

$\sqrt{2}/3 = 0.47$; BR-24, $2/(3\sqrt{3}) = 0.385$. Although there is a problem in that chemical shift is scaled down, we nevertheless do have a method for $^1H-^1H$ homonuclear decoupling at present.

In 1977, B. C. Gerstein *et al.*[12–15] combined MAS and a multiple-pulse sequence into CRAMPS (Combined Rotation And Multiple Pulse Spectroscopy), which is a high-resolution solid-state NMR method for spin 1/2 and high natural abundance such as ^1H and ^{19}F. First, they successfully obtained the high-resolution solid-state ^{19}F NMR of KEL-F using 2.5 kHz MAS and MREV-8, as shown in Fig. 4. This study showed the potential for high-resolution ^1H NMR in solids. Several months later they successfully measured the first high-resolution solid-state ^1H NMR of 4,4′-dimethylbenzophenone[14] using 2.0 kHz MAS and MREV-8 in spite of the indistinct chemical shift axis (Fig. 5). The $^1H-^1H$ homonuclear dipolar interaction and ^1H chemical shift anisotropy were made to disappear by use of multiple pulses and MAS, respectively, and only the ^1H isotropic chemical shift and the scalar spin–spin interaction appear in a CRAMPS spectrum. Therefore, a high-resolution solid-state ^1H NMR spectrum can be obtained by the CRAMPS method of ^1H. ^1H CRAMPS has not yet been used as a general tool for structural analysis, but we predict that it will be popular in the future, because problems such as unreliable chemical shifts, linewidth broadening, and the difficulty of adjustment have been improved by the development of more sophisticated and reliable hardware.

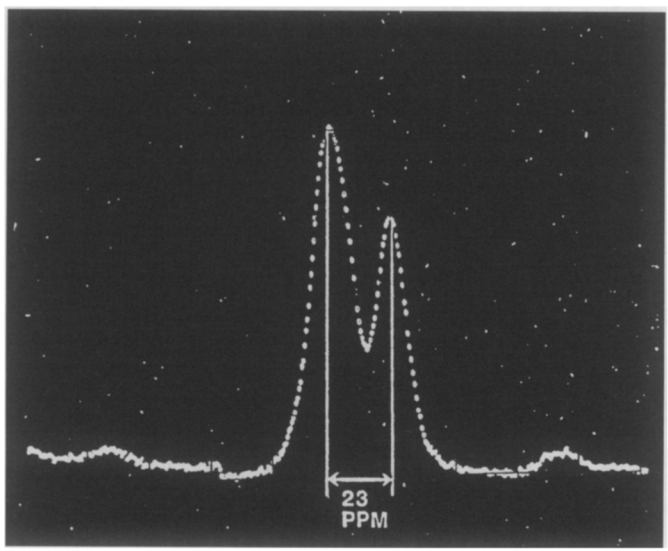

Fig. 4. ^{19}F CRAMPS spectra of KEL-F. (2.5 kHz MAS and MREV-8) (from ref 4). Reproduced with permission from John Wiley & Sons Limited.

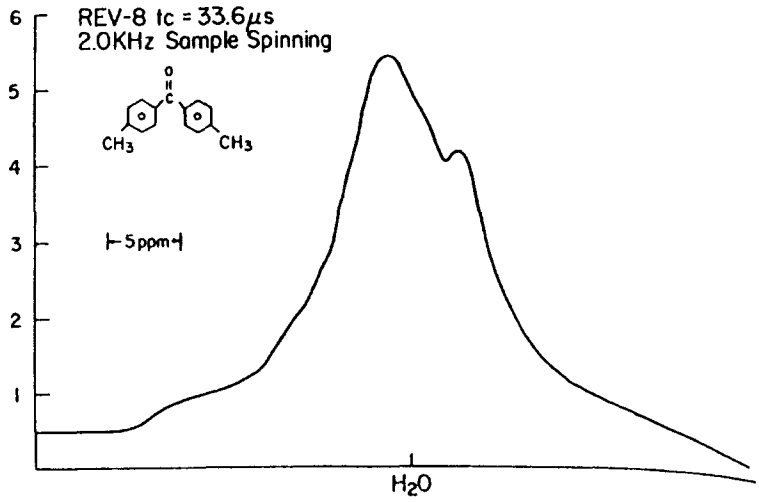

Fig. 5. ^{1}H CRAMPS spectra of 4,4′-dimethylbenzophenone (2.0 kHz MAS and MREV-8) (from ref. 14). Reproduced with permission from the American Institute of Physics.

2.2. Features of ^{1}H CRAMPS NMR

As described above, the combination of MAS with multiple-pulse excitation is called 'CRAMPS'. CRAMPS is an excellent way to achieve a high-resolution solid-state ^{1}H or ^{19}F NMR spectrum. ^{1}H CRAMPS possesses many advantages compared with CP-MAS NMR: (1) it requires only small amounts of sample (10–15 mg or 1/10th that of ^{13}C NMR measurements); (2) measurement time can be about 1/50th (<5 min) of that of ^{13}C NMR; (3) quantitative analysis is possible; and (4) essential information on the ^{1}H nucleus can be obtained directly. However, the ^{1}H CRAMPS method has some disadvantages such as problems of linewidth broadening and an unreliable chemical shift scale. The problem of the unreliable chemical shift scale has been resolved by experimental determination of the scaling factor and correction of drift using an internal standard,[16] as shown in Fig. 6. The ^{1}H chemical shift can be determined within the error limit of ±0.1 ppm in the important region (0–15 ppm) for organic compounds. The residual broadening has been resolved by solid-state 2D HETCOR (HETero-nuclear CORrelation) spectra.[17,18] The 2D HETCOR technique allows the resolution of ^{1}H CRAMPS to be tied to the higher resolution associated with ^{13}C chemical shifts.

Figure 7 shows some examples of spectra to enable discussion of the features of ^{1}H CRAMPS:[19] (a) malonic acid, (b) adipic acid, (c) durene, (d) benzoic acid, (e) polystyrene, and (f) poly(butanediol terephthalate). Aliphatic compounds such as malonic acid and adipic acid give very highly resolved spectra, whereas the resolution of aromatic compounds such as durene and benzoic acid are worse

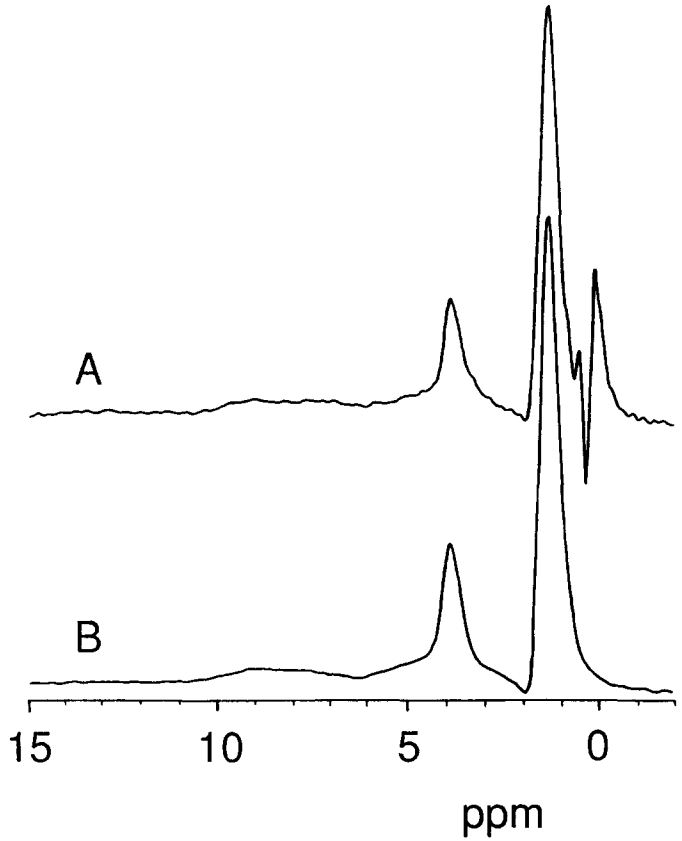

Fig. 6. ^{1}H CRAMPS spectra of poly(L-alanine) (A) with silicon-rubber as an internal standard and (B) without an internal standard. The ^{1}H CRAMPS spectra were recorded first without internal standard and calibrated afterwards with internal silicon-rubber, in order to estimate exact ^{1}H chemical shifts within an error limit of ± 0.1 ppm (from ref. 16). Reproduced with permission from the American Chemical Society.

due to the large anisotropy in the molecular susceptibility. Furthermore, amorphous samples such as polystyrene and poly(butanediol terephthalate) lead to lower resolution because of conformational dispersion. For these systems, it is supposed that the $^{1}H-^{1}H$ homonuclear dipolar interaction is sufficiently decoupled in all the CRAMPS spectra shown because of the observed differences in linewidth. Therefore, the measured spectrum may be approaching the limit to the theoretical resolution of CRAMPS.

The direction of the average Hamiltonian of the chemical shift tilts from the z-axis because a multiple pulse is used in the measurement of CRAMPS. As a result, the CRAMPS spectrum is different from the conventional solid-state high-resolution NMR spectrum as explained below.

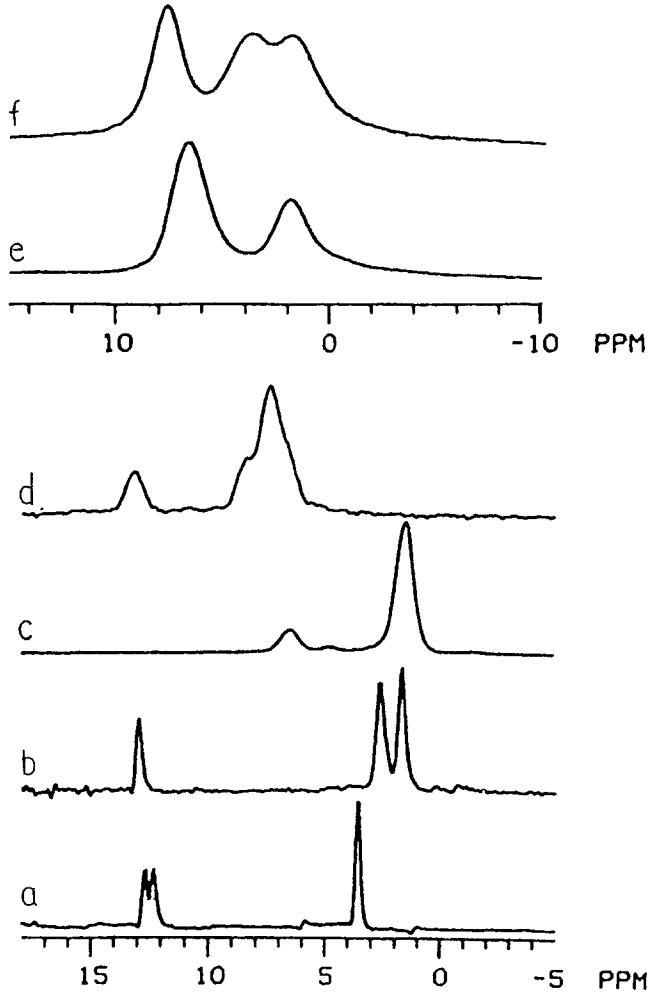

Fig. 7. Some ^{1}H CRAMPS spectra (from ref. 19): (a) malonic acid, (b) adipic acid, (c) durene, (d) benzoic acid, (e) polystyrene, and (f) poly(butanediol terephthalate). Reproduced with permission from the American Chemical Society.

1. *Chemical shift scaling*

The frequency axis is scaled because of the tilted chemical shift Hamiltonian.

2. *Interference of multiple pulse with MAS*

The theory of the multiple pulse assumes that the magnetization returns to the initial state after application of the pulse. But the direction of the internuclear vectors relative to the static field is changed by the MAS spinning rotor. In the case that the multiple pulse cycle time is close to the MAS rotation

period, the resolution of CRAMPS becomes poor due to interference. Bronnimann *et al.*[19,20] found that the resolution begins to deteriorate if the ratio of spin period to BR-24 cycle time is less than about 5. Therefore, a MAS speed of 1.5–2.0 kHz is generally used with BR-24 because the BR-24 cycle time is about 100 μs in general. It is possible, on the other hand, to increase the MAS speed with MREV-8, which has a cycle time of about 30 μs. Molecular motion also possibly interferes with the resolution of CRAMPS.

3. *Image signal*

A very large image signal appears in CRAMPS spectra because the x-component of the magnetization is different from the y-component. Therefore, half of the spectral region is abandoned. However, some quadrature-phase detection CRAMPS (QD-CRAMPS) methods which cancel the image signal have been reported.[21]

4. *Carrier signal*

The carrier signal also appears in CRAMPS spectra. We have to set the carrier signal not to overlap the meaningful sample signals.

Recently, some new high-resolution solid-state ^{1}H NMR methods have been developed besides CRAMPS. First, high magnetic field ^{1}H spectroscopy at high MAS spinning speed averages both the anisotropy of the chemical shift and the homonuclear dipolar interaction to be zero.[7,22] This has the advantages that this method gives non-scaled chemical shifts and signal narrowing of the ^{1}H with directly attached quadrupolar nuclei. However, the problem of bad resolution remains. Second, MAS ^{1}H spectroscopy at high spinning speed using phase modulated Lee-Goldburg (PMLG) decoupling uses the same approach as CRAMPS, but the ^{1}H–^{1}H homonuclear dipolar interaction is made to disappear by PMLG decoupling.[23] The PMLG decoupling method can be used with high-speed MAS, however, high-speed MAS of around 15 kHz is possible, even with CRAMPS measurement at WAHUHA-4.

2.3. Adjustment for ^{1}H CRAMPS measurements

Proton CRAMPS demands a highly efficient spectrometer to avoid measurement difficulties. The main demands on the machine are as follows.

1. Probe:
   - uniform RF field (<5%);
   - the Q value is not so high (30–80).
2. Power amplifier:
   - high generating power (≥500 watts);
   - low noise.
3. Synthesizer:
   - sharp beginning and end of pulses (<50 ns);
   - precise setting of pulse of phases (≤0.2°);
   - rapid switching of phases (<300 ns).
4. Receiver:
   - short dead time (<1 μs).

At present, NMR spectrometers such as the Chemagnetics CMX and Bruker DSX are sufficient for CRAMPS, because the adjustment procedure for CRAMPS experiments has been simplified. Even a standard CP-MAS probe is sometimes used for CRAMPS measurements on the Bruker machines.

The most important process for CRAMPS measurement is to generate nearly ideal rectangular pulses and to cancel out pulse imperfections. The probe adjustments of magic angle and the shim are matters of common knowledge. Plaster of Paris ($CaSO_4 \cdot H_2O$) which is easily obtained, provides a good sample for magic angle adjustments of the ^{1}H CRAMPS probe. 'Silicone rubber (Si-rubber)' should be used as the standard sample for shim adjustment because it gives a single and sharp ^{1}H signal less than 10 Hz wide at 300 MHz, and at 0.12 ppm from TMS (Tetramethyl silane). The centre of the rotor should be loaded with only a small amount of sample in order to decrease the inhomogeneity of the radiofrequency (RF) field.

The power amplifier and probe should be tuned to generate a near-ideal rectangular pulse at the maximum power. However, it is impossible to obtain a perfect rectangular pulse; accordingly, the length and phase of pulses should be carefully adjusted. This pulse adjustment procedure is called 'pulse tuning cycle'. For the pulse tuning cycle, silicon rubber may be used as the standard sample (MAS 1.2–1.5 kHz). The pulse tuning cycle should be carried out while observing the FID of the standard sample. First, we have to set the irradiation frequency on the centre peak to remove the offset effect. We can see the mono exponential decay, and we should change the receiver phase to maximize the in-phase signal. Next, in order to set the precise 90°_x pulse length, a $(90^\circ_x - \tau -)_n$ pulse sequence is used (the filter should be fully opened). This pulse sequence has constant phase, pulse length and window. Signal detection is carried out for every four-pulse window. In the case of a precise 90°_x pulse length, the signal intensity repeats as 1, 0, −1, 0. Therefore, the FID has three parallel lines as shown in Fig. 8A. The same adjustment of the 90° pulse length applies to 90°_{-x}, 90°_y, and 90°_{-y}, with $(90^\circ_x - \tau -)_n$, $(90^\circ_y - \tau -)_n$, and $(90^\circ_{-y} - \tau -)_n$ sequences, respectively. Next, in order to correct the phase difference between x and $-x$, the $(90^\circ_x - \tau - 90^\circ_{-x} - \tau -)_n$ pulse sequence is used (filter wide open). In the case of precise phase differences of 180°, the data intensity repeats as 1, −1, 1, −1, therefore, the FID has two parallel lines, as shown in Fig. 8B. Finally, in order to correct the phase difference between x and y, the pulse sequence $(90^\circ_x - \tau - 90^\circ_y - \tau - 90^\circ_x - \tau - 90^\circ_y - \tau -)_n$ is used. In the case of ideal modulation, the FID appears as shown in Fig. 8C. The phase difference between x and $-y$ should also be modulated by $(90^\circ_x - \tau - 90^\circ_{-y} - \tau - 90^\circ_{-y} - \tau - 90^\circ_x - \tau -)_n$ sequence. This adjustment of pulse length and phase necessarily meets it and should be repeated.[24]

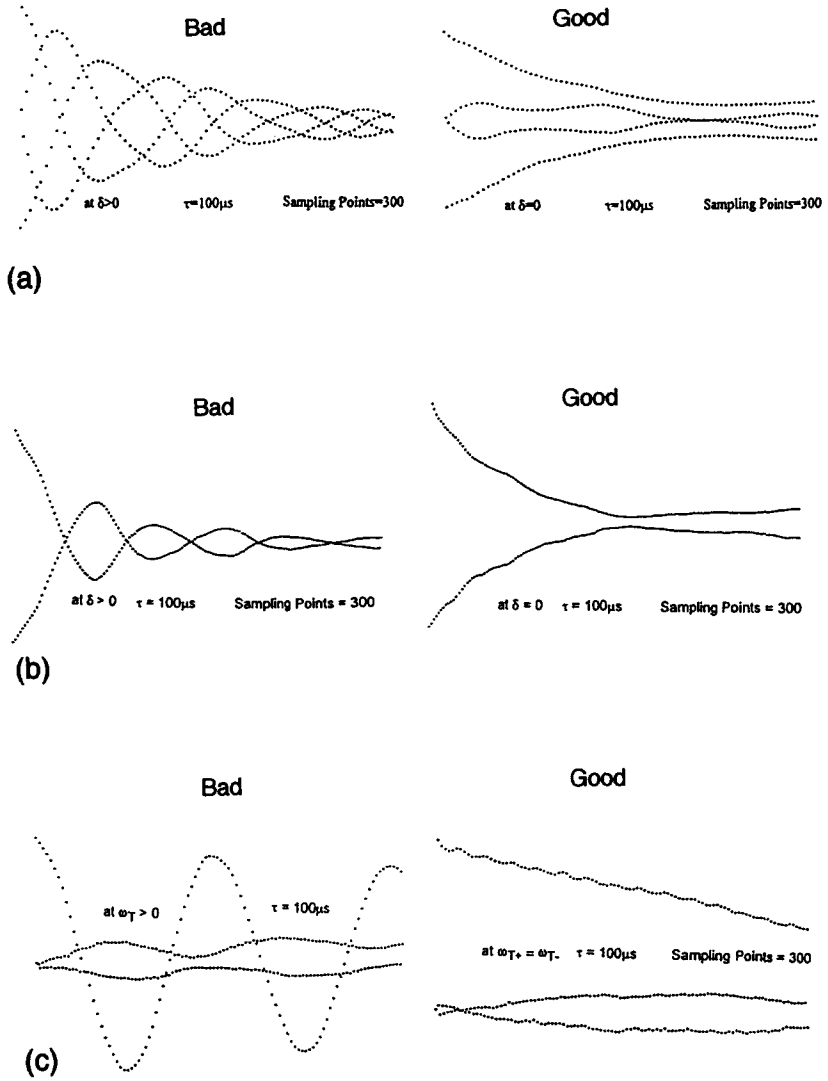

Fig. 8. FID response of protons obtained with (A) the $(90^\circ{}_x - \tau -)_n$ pulse, (B) the $(90^\circ{}_x - \tau - 90^\circ{}_{-x} - \tau -)_n$ pulse, and (C) $(90^\circ{}_x - \tau - 90^\circ{}_{-y} - \tau - 90^\circ{}_x - \tau - 90^\circ{}_x - \tau -)_n$ pulse sequences before (left) and after (right) adjustment.

2.4. Experimental determination of scaling factor of BR-24

The scaling factor of the BR-24 or MREV-8 sequences is a little smaller than the theoretical value (MREV-8: 0.471; BR-24: 0.385) for ideal square pulses. The scaling factor depends on the pulse length, the cycle time, the pulse sequence, and properties of the machine. However, it is impossible to make a

perfect rectangular pulse. In such a case, we have to determine the scaling factor experimentally, in order to discuss the ^{1}H chemical shifts of ^{1}H CRAMPS spectra in detail. We now show how to calculate the scaling factor of the BR-24 experiment.

The CRAMPS measurement of Si-rubber is repeated under the same conditions, but the centre of the observed frequency is changed in increments of 500 Hz (Fig. 9). The ratio between the peak shift of Si-rubber and differences in the observation frequency (500 Hz) is the scaling factor.

Fig. 10 shows plots of the peak shifts of silicon rubber vs. the offset frequency. From the gradient of this graph, the scaling factor of the BR-24 is shown to be 0.40. The experimental value is relatively close to the theoretical value (0.385), but it is clear from Fig. 10 that the chemical shift has a systematic error if the chemical shift is calculated from the slope alone, because the straight line does not pass through the origin. Therefore, we have to estimate first the error limit of the ^{1}H chemical shifts, calculated using the defined scaling factor (0.40) in order to discuss the ^{1}H chemical shift in detail.

Figure 11 shows plots of the ^{1}H chemical shift error (δ_{error}) against the measured value ($\delta_{measure}$) of the peak shift of silicon rubber, where $\delta_{measure}$ is determined from the offset frequency dependency of the peak shift. δ_{error} is the difference between the calculated chemical shift value (δ_{calcd}) using 0.40 and the

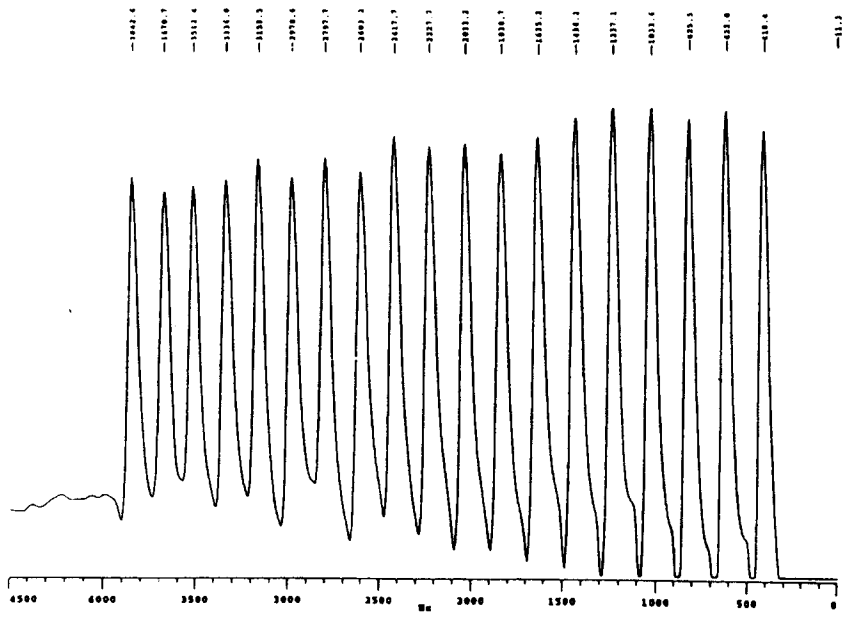

Fig. 9. ^{1}H CRAMPS spectra of Si-rubber measured under the same conditions, with the centre of the observed frequency changed in increments of 500 Hz.

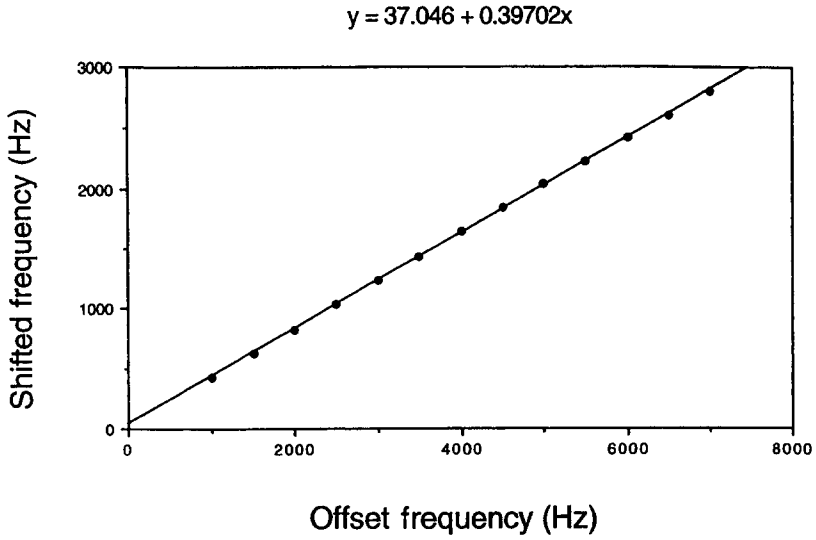

Fig. 10. Plots of the peak shifts of silicon-rubber vs. the offset frequency. The ratio between the peak shift of Si-rubber and differences in the observation frequency (500 Hz) is the scaling factor, which can be determined as 0.40.

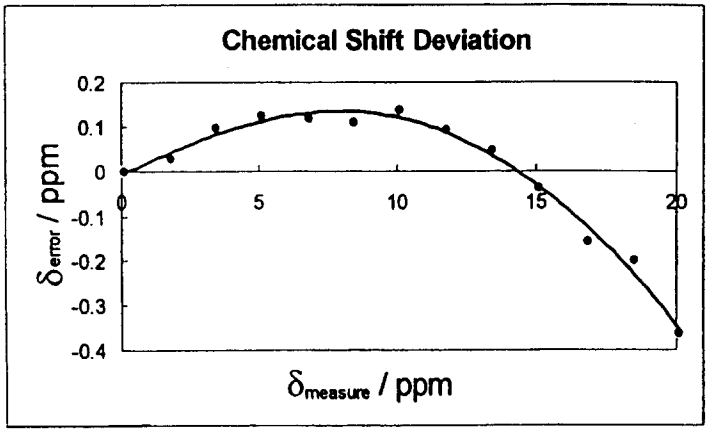

Fig. 11. Plots of the ^{1}H chemical shift error (δ_{error}) against the actual observed value ($\delta_{measure}$) of the peak shift of silicon-rubber. The deviation of the scaling factor can be determined within the order of 0.1 ppm over the range 0 to 15 ppm (see ref. 16). Reproduced with permission from the American Chemical Society.

measured value ($\delta_{error} = \delta_{calcd} - \delta_{measure}$). Thus, it has been confirmed that the deviation of the scaling factor is of the order of 0.1 ppm in the important region (0–15 ppm) for organic compounds in ^{1}H NMR measurement. This is acceptable for solid NMR spectra.

2.5. Measurement conditions of ^{1}H CRAMPS NMR

The pulse length must be as short as possible. We have set the power to provide a $\pi/2$ pulse of about 1.3 μs on the 5 mm Chemagnetics CRAMPS probe, and 1.8 μs on the 4 mm Bruker CP-MAS probe.

The value of τ (which is the total time of the pulse and the window after a single pulse) should be set as short as possible in order to increase the resolution. The pulse length, the dead time of the receiver, and the sampling time should be included in 2τ. In our work, we set the τ value to about 3 μs for the BR-24. For the MREV-8, on the other hand, we set τ to be less than 2.5 μs.

An MAS frequency of 1.5–2.0 kHz is generally used with the BR-24 to prevent interference between the MAS and the multiple-pulse sequence. MAS frequency of 5–6 kHz is possible with MREV-8.

The BR-24 cycle time is about 100 μs as usual. Then, sampling of the signal each cycle gives an effective accessible spectral width of around 40 ppm, taking into account the BR-24 scaling factor and the image signal. The spectral width of around 40 ppm is sufficient for protons, given the generally small shift range and shielding anisotropy. On the other hand, the cycle time of MREV-8 is generally as short as 30 μs. The effective accessible spectral width is around 200 ppm using quadrature-phase sampling, taking into account the MREV-8 scaling factor.

2.6. Confirmation of modulation

Adipic acid ($HOOC(CH_2)_4COOH$) is a good test sample for measurement of ^{1}H CRAMPS performance (Fig. 12).[24] The α and β methylene groups (α and β with respect to the carboxyl position) are distinguished from each other in the

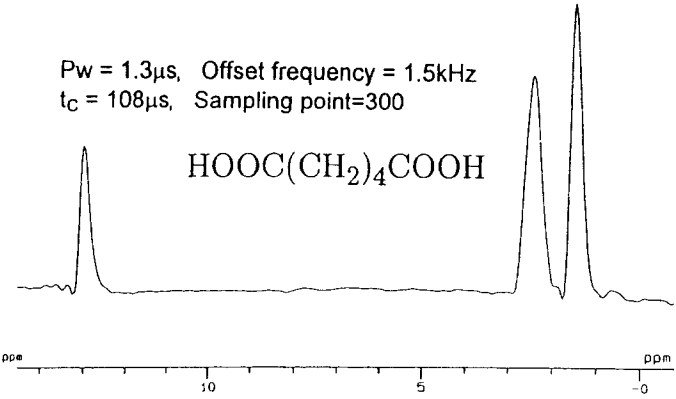

Fig. 12. 300 MHz ^{1}H CRAMPS spectra of adipic acid (1.5 kHz MAS; BR-24; $\tau = 3$ μs; repetition time = 30 s; accumulation = 2 times).

spectrum of adipic acid. It is important to check the resolution of the spectrum, the scaling factor (when the β methylene peak is 1.5 ppm, the carboxyl peak should be 13.0 ± 0.2 ppm), and the MAS speed and magic angle, before starting measurements.

3. EXPERIMENTAL EVIDENCE

3.1. Structural studies of α-amino acid crystals by ^{1}H CRAMPS NMR[25]

The recently developed high-resolution solid-state NMR technique proton CRAMPS NMR has become a very useful research tool, corresponding to X-ray crystallography, and enabling the study of crystal structure polymorphs of amino acids. In this chapter, we first discuss a recent research example application to crystal structure analysis of polymorphic forms of some typical α-amino acids in order to test the power of ^{1}H CRAMPS NMR, compared with ^{13}C and ^{15}N NMR methods.

It is well known that α-amino acids have polymorphic forms,[26,27] and the most basic factor which determines the crystal structure of α-amino acids is a hydrogen-bonding network between the cationic amino group (NH_3^+) and anionic carboxyl group (COO^-). The crystal structures of most α-amino acids have been analyzed by the X-ray diffraction method.[26–33] ^{1}H CRAMPS NMR studies of the structure of polymorphic forms of α-amino acid crystals are few in number,[34,35] although there have been many reports on the relationship between the ^{1}H, ^{13}C, and ^{15}N chemical shifts and hydrogen-bond lengths of other organic compounds (including oligopeptides and polypeptides) in the solid state.[36–40]

For this, we describe two different stages of crystals such as glycine polymorphs [α-form (α-glycine)[28,29] and γ-form (γ-glycine)[30]] and L-histidine polymorphs [A-form (A-histidine)[31] and B-form (B-histidine)[32]].

3.1.1. ^{13}C CP-MAS, ^{15}N CP-MAS and ^{1}H CRAMPS NMR measurements

The ^{13}C CP-MAS and ^{15}N CP-MAS NMR measurements were performed on a JEOL EX-270W spectrometer operating at 67.80 MHz (for ^{13}C) and 27.25 MHz (for ^{15}N), equipped with a CP-MAS accessory. The contact time was 5 ms. The $\pi/2$ pulse width was typically 4.4 μs for both ^{13}C and ^{1}H under CP conditions and 6.9 μs for both ^{15}N and ^{1}H. The spectral width was 27 kHz (^{13}C) and 20 kHz (^{15}N), and the number of data points was 8 K. Spectra were usually accumulated from about 300 measurements (for ^{13}C CP-MAS) and 500–1500 measurements (for ^{15}N CP-MAS) to achieve a reasonable signal-to-noise ratio for the samples. The ^{13}C chemical shifts were calibrated indirectly by external adamantane (δ 29.5 ppm relative to tetramethylsilane (TMS; $(CH_3)_4Si$)). The ^{15}N chemical shifts were calibrated indirectly by external

$^{15}NH_4Cl$ (δ = 18.0) relative to a saturated $^{15}NH_4NO_3$ (δ = 0 ppm) solution in H_2O. The experimental errors of the ^{13}C and ^{15}N chemical shift values are estimated to be less than $\pm$0.2 and $\pm$0.3 ppm, respectively.

The ^{13}C CP-MAS NMR measurement was partly performed on a Chemagnetics CMX 300 spectrometer operating at 75.49 MHz. In this case, the contact time was 1.5 ms and the repetition time was 5 s. The $\pi/2$ pulse width, spectral width, and number of data points were 2.5 μs, 30 kHz, and 4 k points, respectively.

The ^{1}H CRAMPS NMR measurement was performed on a Chemagnetics CMX 300 spectrometer operating at 300.16 MHz, equipped with a 5 mm CRAMPS probe. The BR-24 pulse sequence[41] was used, and $\pi/2$ pulse width was 1.3 μs. The rotational frequency was exactly controlled in the range 1.5 to 2.0 kHz, and the cycle time of BR-24 was 108 μs. The recycle delay was 10 s and spectra were usually accumulated 32 times to achieve a reasonable signal-to-noise ratio for the samples. The ^{1}H chemical shift was calculated with a scaling factor of 0.40 for all samples, which was determined experimentally. The ^{1}H CRAMPS spectra were recorded first without internal standard, and calibrated afterwards with internal Si-rubber (δ = 0.12) relative to TMS (δ = 0). The typical half-width was 30 Hz, and the total measurement time for one sample was usually 5 min.

3.1.2. ^{1}H CRAMPS NMR study of glycine crystals

Glycine occurs in many natural proteins and it is a main component in silk fibroins and collagen fibrils. The three polymorphs of glycine crystals are commonly known as α-, β-, and γ-glycine. Glycine molecules are linked through N—H $\cdots$ O=C hydrogen bonds. These three glycine polymorphs have nearly the same conformation but different hydrogen bond networks. The crystal structure of α-glycine (monoclinic; $P2_1/n$ space group and four molecules per cell) was first determined by Albrecht and Corey[28] and then refined by Marsh.[29] The crystal structures of both β-glycine (monoclinic; $P2_1$ space group and two molecules per cell) and γ-glycine (hexagonal; $P3_1$ space group with three molecules per cell) were determined by Iitaka.[30,33] The γ-glycine is most stable at room temperature and converts to α-glycine on heating to 165 °C. In contrast, β-glycine is very unstable, and therefore NMR data have been reported only for α-glycine and γ-glycine.

Crystals of α-glycine and γ-glycine were grown from a saturated aqueous solution by slow evaporation of the solvent, and from an aqueous solution containing acetic acid by slow cooling, respectively. The structure of both glycine crystals was confirmed by their characteristic bands in the IR spectra[42] (NH_3^+ rocking vibration: α-form, 1135 and 1115 cm^{-1}, γ-form, 1152 and 1126 cm^{-1}; CH_2 rocking vibration: α-form, 914 and 896 cm^{-1}, γ-form: 929 and 888 cm^{-1}; COO- wagging vibration: α-form, 699 cm^{-1}, γ-form: 683 cm^{-1}).

Schematic representations of the structures of α-glycine and γ-glycine are shown in Fig. 13.

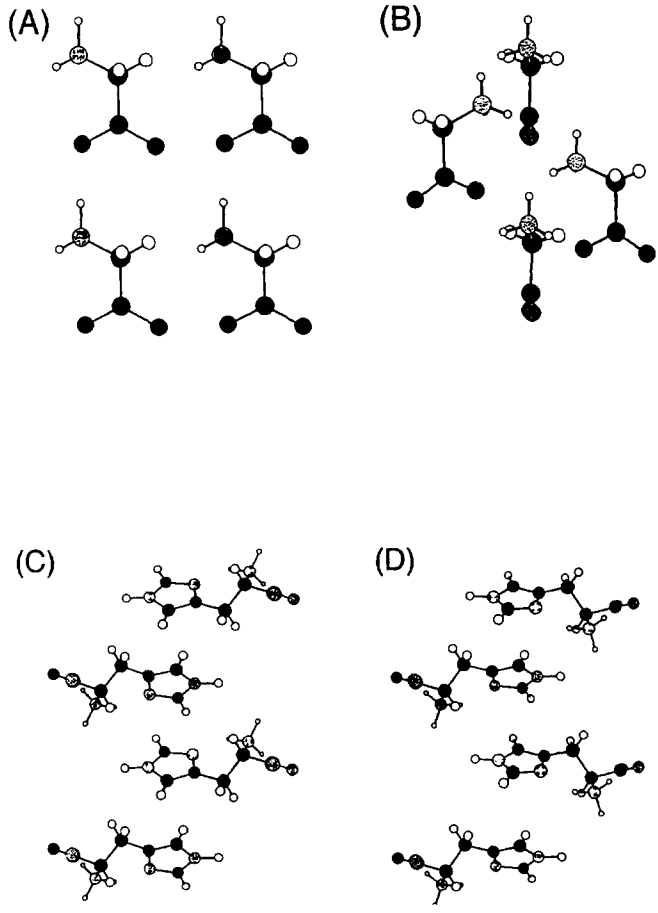

Fig. 13. Schematic structures of two polymorphs of the glycine and L-histidine molecules: (A) α-glycine; (B) γ-glycine; (C) A-histidine; and (D) B-histidine structures (from ref. 25). Reproduced with permission from Elsevier Science.

^{13}C and ^{15}N CP-MAS NMR spectra of α-glycine and γ-glycine. Figure 14 shows the 75.49 MHz ^{13}C CP-MAS NMR spectra and the peak assignment of (A) α-glycine and (B) γ-glycine, and the ^{13}C and ^{15}N chemical shifts of glycine polymorphs are summarized in Table 1. The C=O (carboxyl: singlet) and C^{α} (α-methylene: doublet) signals appear at 176.4, and 44.0 and 43.6 ppm (major) respectively for α-glycine, and they appear at 174.6, and 42.9 and 42.5 ppm (major) respectively for γ-glycine. The peaks at around 280 and 70 ppm are due to spinning sidebands of the carboxyl carbon. It is noteworthy that the two

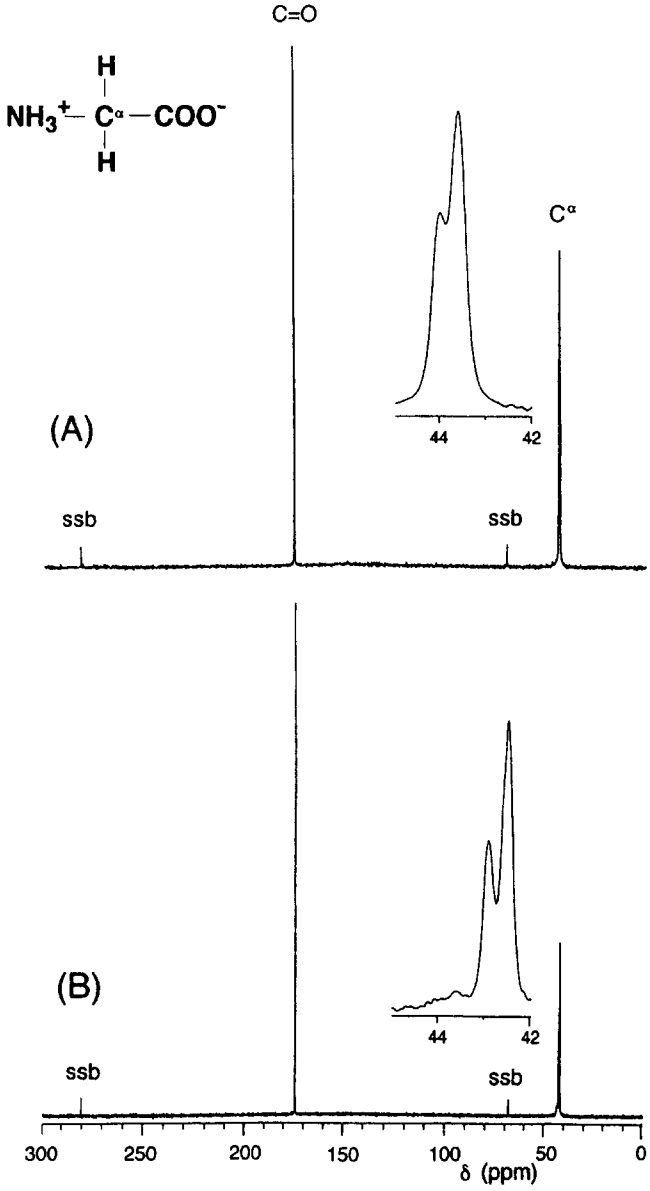

Fig. 14. 75.5 MHz ^{13}C CP-MAS NMR spectra of glycine crystals: (A) α-glycine and (B) γ-glycine. The peaks at around 280 and 70 ppm are due to spinning sidebands (ssb) of the carboxyl carbon (from ref. 25). Reproduced with permission from Elsevier Science.

Table 1. ^{1}H, ^{13}C, and ^{15}N chemical shift values of α-glycine and γ-glycine (from ref. 25)

	^{1}H chemical shift, δ (ppm)			^{13}C chemical shift, δ (ppm)			^{15}N chemical shift, δ (ppm)
	NH_3^+	H^α		C=O	C^α		NH_3^+
α-glycine	8.5	4.4	3.4	176.4	44.0	43.6	11.6
γ-glycine	8.9	3.3		174.6	42.9	42.5	12.3

polymorphs of glycine are distinguishable by the ^{13}C CP-MAS NMR spectra. The ^{13}C chemical shifts of the C=O and C^α signals in α-glycine are 1.8 and 1.1 ppm to high frequency respectively from those in γ-glycine, which are significantly larger than the ^{13}C chemical shift error limit ($\pm$0.2 ppm). Judging from the ^{13}C chemical shift data, the structure of commercial glycine crystals (Ajinimoto Co.) (C=O: 176.5 ppm; C^α: 44.0 and 43.5 ppm) and those reported elsewhere (C=O: 176.46 ppm; C^α: 43.67 ppm)[43] are assumed to be typical α-glycine. Peak splitting of the C^α signal is due to dipolar coupling between C^α and quadrupolar ^{14}N nuclei,[44,45] as shown in Fig. 14. This was confirmed by the evidence that the C^α signal of ^{15}N isotope-labelled glycine (99 atom%: MSD Isotopes) gave a sharp singlet peak (δ = 43.9), the intensity of which is equal to that of the C=O signal (δ = 176.6), as shown in Fig. 15. This was confirmed also by the fact that the ^{13}C CP-MAS NMR spectra (JEOL EX-400 W; 100.40 MHz for ^{13}C) gave a singlet C^α peak (δ = 43.9) (figure not

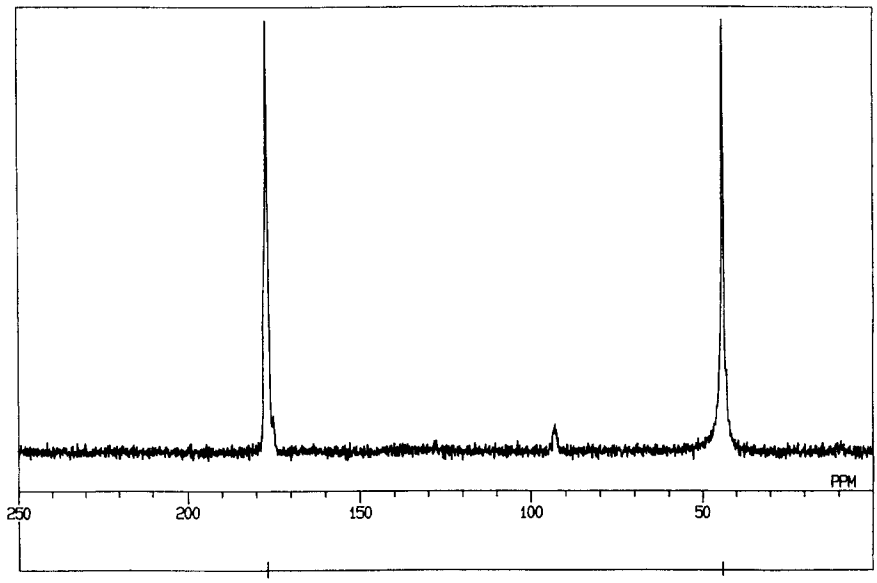

Fig. 15. 67.8 MHz ^{13}C CP-MAS NMR spectra of fully ^{15}N-labelled α-glycine crystal.

shown). Thus, it is important to utilize a high-field NMR machine (more than 400 MHz for ^{1}H), in order to determine these exact ^{13}C chemical shift values for structural analysis of naturally abundant amino acids.

Figure 16 shows the 27.25 MHz ^{15}N CP-MAS NMR spectra of α-glycine and γ-glycine. The amino ^{15}N signal of α-glycine appears 0.7 ppm to low frequency compared with that of γ-glycine. Since the ^{15}N chemical shift error is less than ± 0.3 ppm, it may be somewhat difficult to distinguish clearly between these two forms from ^{15}N chemical shifts in this case.

Glycine has often been used as a standard reference for ^{13}C and ^{15}N CP-MAS NMR measurements.[43,46] In such cases, one must pay careful attention

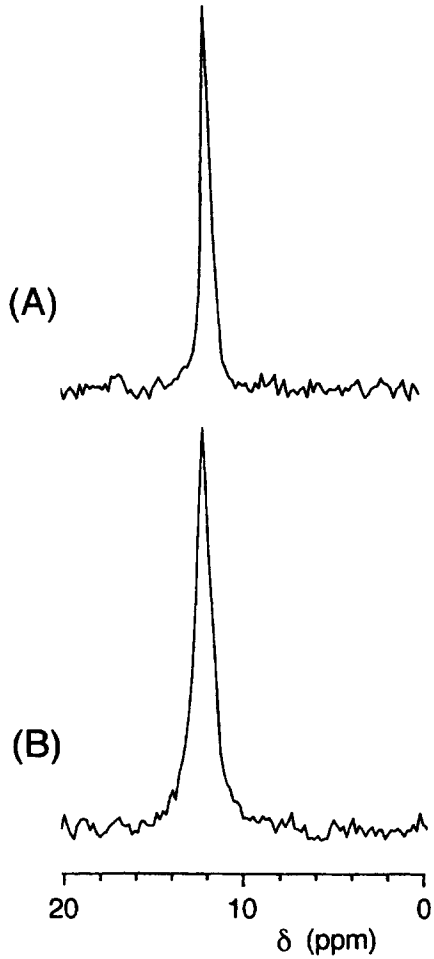

Fig. 16. 27.3 MHz ^{15}N CP-MAS NMR spectra of glycine polymorphs: (A) α-glycine and (B) γ-glycine crystals (from ref. 25). Reproduced with permission from Elsevier Science.

to the use of glycine as a chemical shift standard, because (especially) the ^{13}C chemical shift depends on polymorphic forms of glycine (see Figs 14 and 16, and Table 1). Fortunately, however, glycine can be used as a standard reference material as before, because the magic angle, resolution, and CP condition can be adjusted irrespective of chemical shift values and because the polymorphic form of almost all commercial glycine is the α-form only. Thus, the ^{13}C and ^{15}N chemical shifts are useful for the structural analysis of glycine polymorphs, although the chemical shift differences are not large.

^1H CRAMPS NMR spectra of α-glycine and γ-glycine. Figure 17 shows the ^1H CRAMPS NMR spectra of (A) α-glycine and (B) γ-glycine crystals, together with each peak assignment. It is noteworthy that the H^α signal of α-glycine splits into two peaks (4.4 and 3.4 ppm) of equal height but that of γ-glycine gives a sharp singlet peak (3.3 ppm). The reason for this peak splitting may be attributable to a difference in the magnetic surroundings of two nonequivalent H^α protons in α-glycine, whereas they are equivalent and give a single peak in γ-glycine. The ^1H CRAMPS NMR spectra of glycine reported previously[44,47] gave two equal H^α signals only. Therefore, the polymorphs of the glycine crystals mentioned above were assumed to be α-glycine crystal. In contrast, this ^1H CRAMPS NMR spectrum of γ-glycine crystal was the first measurement.[25]

The amino ^1H chemical shift of α-glycine (8.5 ppm) was 0.4 ppm to low frequency compared with that of γ-glycine (8.9 ppm), as shown in Fig. 17. The amino ^1H chemical shift is affected by homonuclear dipolar interaction between the amino ^1H and the quadrupolar ^{14}N nuclei. It is generally accepted that the strength of intermolecular hydrogen bonds in α-glycine crystals (N—H···O: 2.850, 2.949, and 3.074 Å) is weaker than those of γ-glycine (N—H···O: 2.801, 2.817, and 2.970 Å), according to evidence obtained from X-ray diffraction analysis[26,28–30] and IR spectroscopy.[42] Thus, the amino proton chemical shift difference between α-glycine and γ-glycine can be explained by intermolecular hydrogen bond lengths, and therefore the ^1H CRAMPS NMR is very useful for the structural analysis of glycine crystals.

3.1.3. ^1H electrostatic potential (ESP) charge calculation of glycine

In order to explain why the H^α signal of α-glycine was separated into two equal peaks (doublet) and that of γ-glycine was a singlet, the ^1H electrostatic potential (ESP) charges of α-glycine and γ-glycine crystals have been calculated by the MNDO method. The cluster model building of glycine crystals and the ESP charge calculation for them were performed with the Cerius2 program, which is a software package developed by Molecular Simulation Inc. The cluster model for the α-glycine is composed of 16 glycine molecules in four unit cells (2*a, 1*b, 2*c). The cluster model for the γ-glycine is composed of 16 glycine molecules which are left in the core after removing the surrounding 24

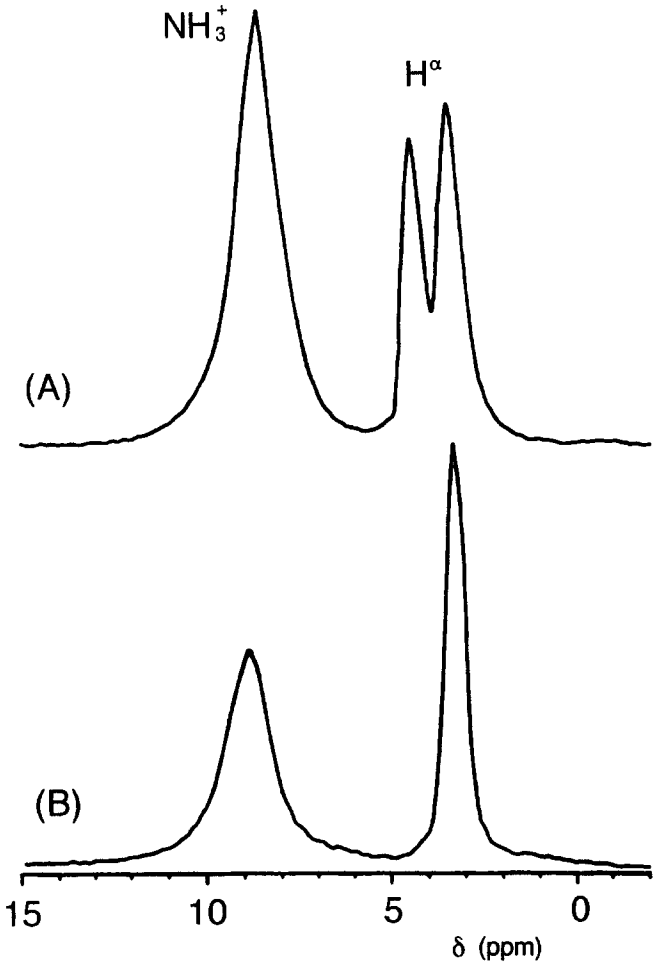

Fig. 17. 300.2 MHz ^{1}H CRAMPS NMR spectra of glycine polymorphs: (A) α-glycine and (B) γ-glycine crystals (from ref. 25). Reproduced with permission from Elsevier Science.

molecules from 40 molecules in eight unit cells (2*a, 2*b, 2*c). The ESP charges were calculated by the MNDO method with MOPAC 6.01 for such a cluster model (one calculation unit) without prior structural optimization. Since a periodic boundary condition cannot be used, the ESP charges for the results were selected from the glycine molecule located as near to the centre as possible in the cluster: two molecules for the α-glycine and one molecule for the γ-glycine.

As a result, the ESP charges on α-methylene protons of α-glycine were a set of (0.130, 0.336) and (0.101, 0.320), and those of γ-glycine were a set of (0.056, 0.192). The averaged values of α-glycine were a set of (0.121, 0.328). The

separation of the two methylene protons in α-glycine (0.207) is about 50% more than in γ-glycine (0.136), and the mean value in γ-glycine (0.124) is very close to the smaller value in α-glycine (0.121). This result agrees with the ^1H chemical shift results of polymorphs of glycine crystals.

3.1.4. ^1H CRAMPS NMR study of L-histidine crystals

The polymorphic forms of L-histidine are known as A-histidine and B-histidine. The crystal structures of both A-histidine (orthorhombic; $P2_12_12_1$ space group and four molecules per cell) and B-histidine (monoclinic; $P2_1$ space group and

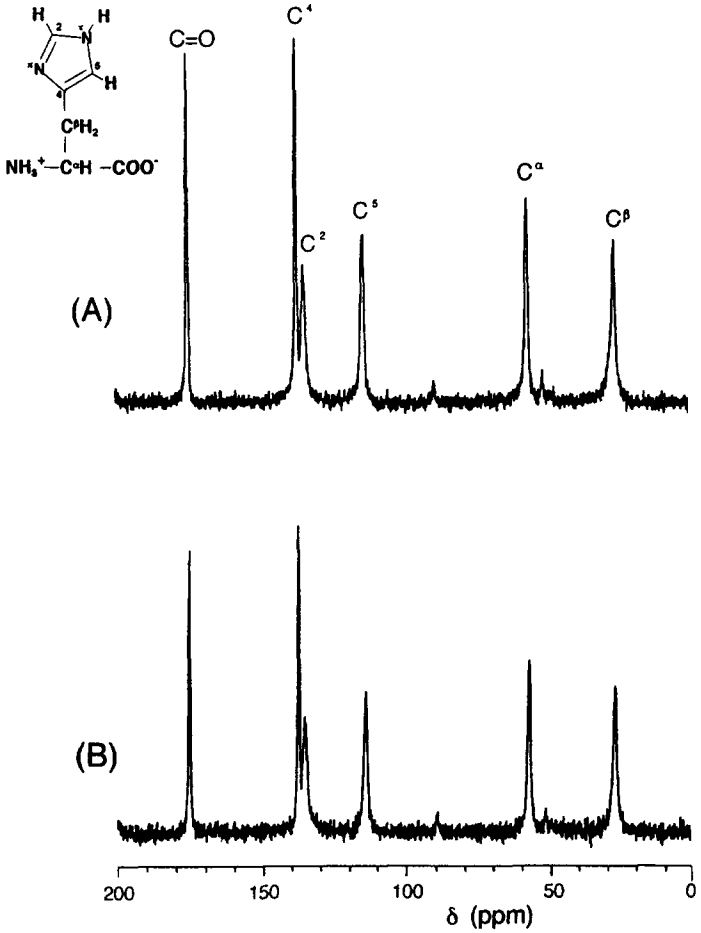

Fig. 18. 67.80 MHz ^{13}C CP-MAS NMR spectra of L-histidine polymorphs: (A) A-histidine and (B) B-histidine. Numbering of side-chain structure is done by the systematic IUPAC nomenclature (see ref. 25). Reproduced with permission from Elsevier Science.

two molecules per cell) forms were determined by Madden.[31,32] The molecular conformations of these two forms are similar and stabilized by weak intramolecular hydrogen bonding (N—H $\cdots$ N$^{\pi}$) between the amino ^{1}H and N$^{\pi}$ of the imidazole ring. These molecular chains are linked to each other by intermolecular hydrogen bonds (N$^{\pi}$—H $\cdots$ O) between N$^{\pi}$H of the imidazole ring and carboxyl oxygen of neighbouring chains (head-to-tail). These chains line up alternately in opposite directions and neighbouring molecular layers are linked to each other by an intermolecular hydrogen bond (N—H $\cdots$ O) between the amino group and carboxyl oxygen, as shown in Fig. 13. The L-histidine polymorphs have nearly the same conformation but different hydrogen-bond networks, and the A-histidine form is more stable than B-histidine at room temperature. The face and back of the A-histidine molecules alternately change by a two-fold screw, but the two sides of B-histidine do not change. Schematic representations of the structures of A-histidine and B-histidine are shown in Fig. 13.

The crystal mixture of A-histidine (needle-like crystals) and B-histidine (plate-like crystals) were grown from an aqueous solution by slow evaporation of the solvent, and then only needle-like crystals were collected.[27,48] The crystals of B-histidine were obtained from an aqueous ethanol solution.[27,48] There was some clear differences in the IR spectra of A-histidine and B-histidine, although the overall spectra are very similar: A-histidine; 939 (very

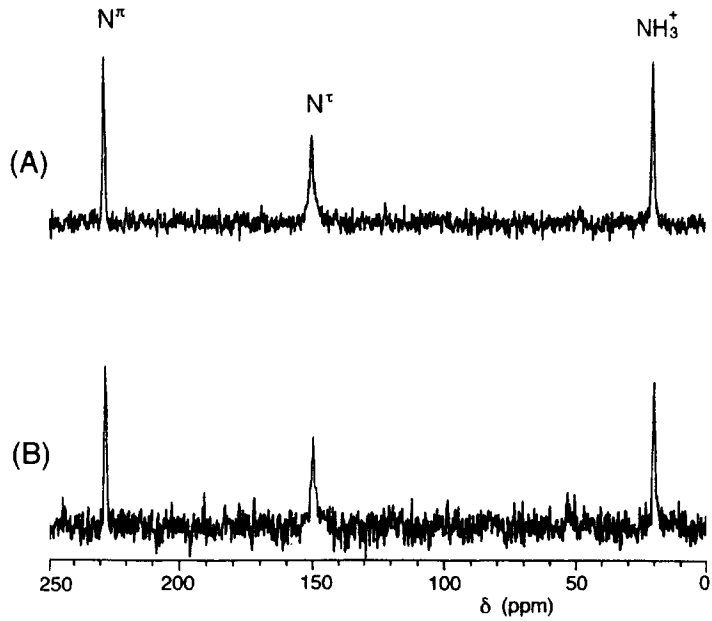

Fig. 19. 27.3 MHz ^{15}N CP-MAS NMR spectra of L-histidine polymorphs: (A) A-histidine and (B) B-histidine (from ref. 25). Reproduced with permission from Elsevier Science.

weak), 831 (strong), 796 (strong), and 783 cm^{-1} (weak), and B-histidine; 1175 (weak), 839 (weak) and 831 (medium), 797 (medium) and 777 cm^{-1} (medium) (fig. not shown). Thus, it is easy to distinguish these two polymorphs of L-histidine from IR spectra.

^{13}C and ^{15}N CP-MAS NMR spectra of A-histidine and B-histidine Figures 18 and 19 show the 67.80 MHz ^{13}C CP-MAS and 27.25 MHz ^{15}N CP-MAS NMR spectra respectively of L-histidine polymorphic crystals, A-histidine and B-histidine. The ^{13}C CP-MAS NMR spectra show solid high-resolution signals separated into six regions. Their assignment and chemical shifts are shown in Table 2. It can be easily admitted that the polymorphic forms of L-histidine can not be distinguished from ^{13}C CP-MAS NMR spectra, because the ^{13}C chemical shifts are nearly the same in these crystals.

Next, ^{15}N CP-MAS NMR spectra shows high-resolution ^{15}N signals separated into three regions for the L-histidine polymorphs. It is impossible to distinguish between A-histidine and B-histidine from ^{15}N CP-MAS NMR at the present stage, because the three ^{15}N chemical shifts are the same, as shown in Table 2.

^{1}H CRAMPS NMR spectra of A-histidine and B-histidine. Figure 20 shows the ^{1}H CRAMPS NMR spectra of A-histidine and B-histidine. The ^{1}H CRAMPS NMR spectra of these polymorphs show high-resolution proton signals and they are assigned as shown in Table 2. The peak at around 6.5 ppm arises from an artefact, which is shown as an asterisk in Fig. 20. It is particularly remarkable that the NH_3^+ and H^2 signals of A-histidine moves upfield by 0.2–0.3 ppm compared with the corresponding ^{1}H signals of B-histidine, whereas only the H^5 signal of A-histidine moves downfield by 0.2 ppm. As a result, we can easily distinguish the polymorphic forms of L-histidine based on the ^{1}H chemical shift differences between the H^2 and H^5 signals (A-histidine: 0.4 ppm; B-histidine: 0.9 ppm), which are obviously meaningful. These chemical shift displacements may be attributed to a difference in magnetic surroundings of the NH_3^+ proton, indicating that the two polymorphs of L-histidine have a similar hydrogen-bond network.

From these results, it was concluded that the polymorphic forms of L-histidine can be readily distinguished by ^{1}H CRAMPS NMR spectra, even when it is quite difficult to distinguish using the ^{13}C and ^{15}N CP-MAS NMR spectra. From the ^{1}H CRAMPS NMR measurement, it is concluded that the ^{1}H chemical shifts of α-amino acid crystals are very sensitive to a small difference in the magnetic surroundings of protons as well as that in the hydrogen-bond network. Accordingly, the solid ^{1}H CRAMPS NMR is a very useful means for structural analysis of L-histidine crystals.

In conclusion, the polymorphic forms of some α-amino acid crystals such as a glycine and L-histidine have been successfully studied by ^{1}H CRAMPS NMR spectra. For glycine crystals, the H^{α} signals of α-glycine splits into two peaks

Table 2. ^{1}H, ^{13}C, and ^{15}N chemical shift values of A-histidine and B-histidine (from ref. 25)

	^{1}H chemical shift, δ (ppm)						^{13}C chemical shift, δ (ppm)						^{15}N chemical shift, δ (ppm)		
	H^{τ}	NH_3^+	H^2	H^5	H^{α}	H^{β}	C=O	C^4	C^2	C^5	C^{α}	C^{β}	N^{π}	N^{τ}	NH_3^+
A-histidine	13.9	8.9	5.5	5.1	3.9	2.7	175.3	137.6	135.2	114.0	57.5	27.2	228.3	150.0	20.3
B-histidine	14.0	9.1	5.8	4.9	4.0	2.7	175.5	137.7	135.5	114.1	57.6	27.5	228.1	149.8	20.0

Note: The hydrogen, carbon, and nitrogen atoms of L-histidine were numbered by the systematic IUPAC nomenclature.
Correction: We have corrected the assignment of C^2 and C^4 signals, which was confirmed by 2D ^{1}H–^{13}C HETCOR NMR spectra (data not shown).

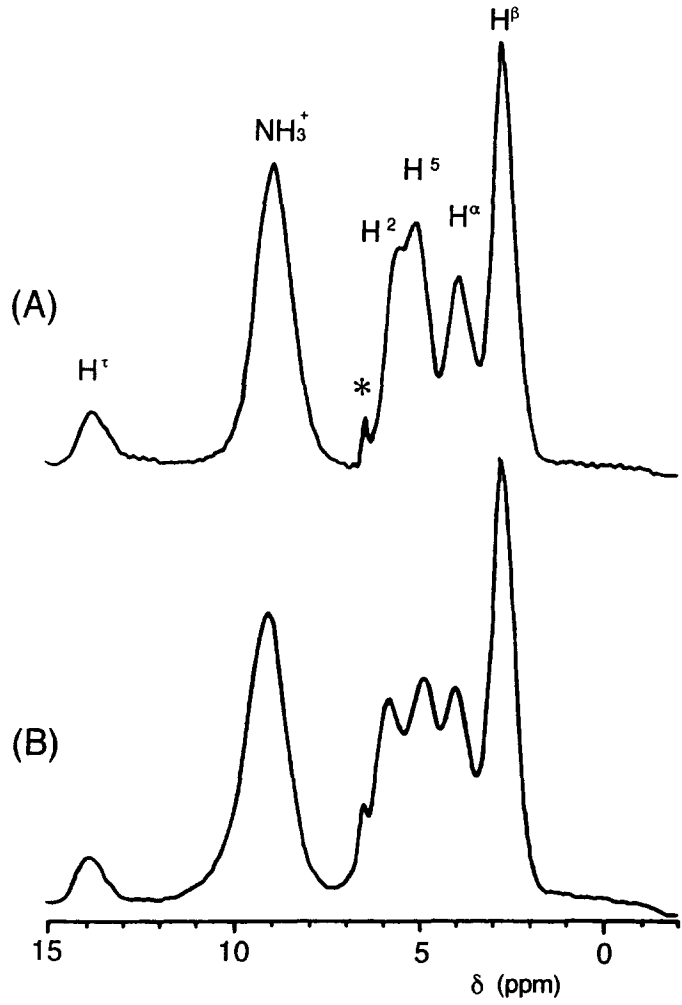

Fig. 20. 300.2 MHz ^{1}H CRAMPS NMR spectra of L-histidine polymorphs: (A) A-histidine and (B) B-histidine. The peak at around 6.5 ppm, shown with an asterisk (*), is due to an artefact (from ref. 25). Reproduced with permission from Elsevier Science.

but that of γ-glycine gives a single peak, which were confirmed qualitatively by the ^{1}H ESP charge calculation of α-glycine and γ-glycine. In contrast, the ^{1}H chemical shift difference between the H^2 and H^5 signals of L-histidine crystals becomes a key point in distinguishing between the crystal forms A-histidine and B-histidine. We must admit that the ^{1}H chemical shift is very sensitive to the magnetic surroundings of these crystal structures. It is useful and effective to measure the ^{1}H chemical shifts of α-amino acid crystals by ^{1}H CRAMPS NMR, if we wish to know how to distinguish their polymorphs, even if neither

the ^{13}C nor ^{15}N CP-MAS NMR methods are successful. It is hoped to accumulate more ^{1}H chemical shift data for other α-amino acid, oligopeptide, and polypeptide crystals in the future.

3.2. Conformational study of synthetic polypeptides by ^{1}H CRAMPS NMR[16,45]

'Can ^{1}H CRAMPS NMR become an effective means for conformational analysis of polypeptides and proteins in the solid state?' In order to answer this question, in this section, we focus on and discuss a study on correlation between the ^{1}H chemical shifts and the main-chain conformation (secondary structure) of synthetic polypeptides.[16,45] Homopolypeptides and copolypeptides are useful as models for structural analysis of natural proteins. Homopolypeptide is the simplest and the most basic model polypeptide for NMR studies of proteins.

The right-handed α-helix (α-helix), antiparallel β-sheet (β-sheet) and parallel β-sheet (β_P-sheet) forms are the most well-known conformations in proteins. Otherwise the left-handed α-helix (α_L-helix), polyglycine I (PGI) and II (PGII), polyproline I (PPI) and II (PPII), and left-handed ω-helix (ω_L-helix) are known conformations in model polypeptides. If we are successful in determining the solid conformation of synthetic polypeptides based on high-resolution solid-state NMR, we would obtain a very powerful means of conformational analysis of proteins. Recently, a number of papers have reported the study of correlation between the conformations mentioned above and the ^{13}C, ^{15}N and ^{1}H chemical shifts.[49–66] In such studies, it is clear that the ^{13}C chemical shifts of the α-carbon (C^{α}) and β-carbon (C^{β}), as well as the ^{15}N chemical shifts of the amide nitrogen, depend on their main-chain conformations. In such a situation, it may be expected that the ^{1}H chemical shifts of the α-proton (H^{α} combined with C^{α}), β-proton (H^{β} combined with C^{β}), and amide proton (H^{N}; combined with amide nitrogen) play an important role in conformational determination of polypeptides and proteins in the solid state. Shoji and coworkers have studied these features in various kinds of homopolypeptides:[16,45] poly(L-alanines) (PLA), poly(L-leucines) (PLL), poly(γ-benzyl-L-glutamates) (PBLG), poly(L-valines) (PLV),[67] polyglycines (PG), poly(L-prolines) (PP),[67] and cyclic dipeptides[16] such as cyclic(L-alanyl-L-alanyl) (LL) and cyclic(L-alanyl-D-alanyl) (LD). Using these samples having characteristic differences in conformation, they systematically tested the power of ^{1}H CRAMPS NMR to carry out structural analysis in the solid state. Furthermore, it seems valuable to test also the advantages of specific deuterium labelling of polypeptides in the solid state. We will therefore discuss the ^{1}H CRAMPS NMR results of selectively deuterium (2D)-labelled poly(γ-benzyl-L-glutamates) (PBLG-d).[67–69]

For these homopolypeptides, the following three problems need to be solved: (1) Is it feasible to assign the ^{1}H signals and to clarify the relation between

Table 3. Synthetic condition, characteristics, and ^{1}H and ^{13}C chemical shifts of homopolypeptides (from refs 16, 64 and 67)

Sample[a]	DP_n[b]	Synthetic method	Conformation[e]	H^{α}	H^{β}	C=O	C^{α}	C^{β}
H-[Ala]$_8$-NHBu	—	activated ester	β-sheet	5.1	1.2	171.8	48.2	19.9
[Ala]$_n$−1	16	NCA	α-helix[f]	5.0, 3.9	1.3			
[Ala]$_n$−5	65	NCA	α-helix	3.9	1.4	176.4	52.4	14.9
[Leu]$_n$−1	$A/I^c = 5$	NCA	β-sheet[g]	5.5	1.5	170.5	50.5	43.3
[Leu]$_n$−2	$A/I^c = 100$	NCA	α-helix	4.0	1.6	175.7	55.7	39.5
H-[Glu(OBzl)]$_6$-OBzl	—	activated ester	β-sheet	5.2	2.4	171.0	51.2	29.0
[Glu(OBzl)]$_n$	h.m.w[d]	NCA	α-helix	4.0	2.2	175.6	56.4	25.6
[Glu-(OBzl)]$_n$-d_2	h.m.w[d]	NCA	α-helix	4.0	2.2			
[Glu-(OBzl)]$_n$-d_7	h.m.w[d]	NCA	α-helix	—	—			
[Val]$_n$−1	5	NCA	β-sheet	5.0	1.8	171.8	58.4	32.4
[Val]$_n$−5	100	NCA	β-sheet	5.0	1.9			
PG I	h.m.w[d]	NCA	Polyglycine I (β-sheet)	4.3	—	169.2	44.3	—
PG II	h.m.w[d]	NCA	Polyglycine II (3_1-helix)	3.7	—	172.7	42.5	—
cyclo[L-Ala-L-Ala]		activated ester	boat	4.3	1.4	172.1	49.5	15.6, 18.0
cyclo[L-Ala-D-Ala]		activated ester	planar	4.7	1.5	167.9	49.7	21.0
				H^{α}	H^{δ}	C=O	C^{α}	C^{δ}
PP I	h.m.w[d]	NCA	Polyproline I	4.2	3.6	171.7	59.3	48.4
PP II	h.m.w[d]	NCA	Polyproline II	4.0	3.0	170.6	58.5	47.3

[a] Abbreviations: Ala, L-alanine; Leu, L-leucine; Glu(OBzl), γ-benzyl L-glutamate; NHBu, *n*-butyl amide; OBzl, benzyl ester; PG, polyglycine; NCA, *N*-carboxy-α-amino acid anhydride; α-helix, right-handed α-helix; β-sheet, anti-parallel β-sheet.
[b] The number-averaged degree of polymerization.
[c] The molar ratio of the monomer (A) to the initiator (I), which corresponds to the theoretical number-averaged degree of polymerization.
[d] High molecular-weight (fibrous) sample.
[e] Conformations of the samples were determined from ^{13}C and/or ^{15}N CP-MAS NMR, IR and far-IR spectroscopic methods.
[f] Containing small amounts of β-sheet.
[g] Containing only a small amount of α-helix.

the ^{1}H chemical shifts and the main-chain conformation in the solid state? (2) Is it useful to apply a selective deuterium labelling technique to separate a specific ^{1}H signal? (3) Is it possible to improve the poor resolution of ^{1}H CRAMPS using two-dimensional (2D) ^{1}H–^{13}C HETCOR (HETeronuclear-CORrelation)?[64, 70–74]

For the cyclic dipeptides, furthermore, the authors discuss the possibility of applying ^{1}H CRAMPS NMR to study ring conformation, such as boat, chair and planar forms.

3.2.1. Conformational analysis of polypeptides based on α-proton chemical shifts

A variety of homopolypeptides were synthesized by the N-carboxy α-amino acid anhydride (NCA), activated ester, or azide methods[65, 66, 75–77] except for deuterium labelled samples[68–69] and polyglycines.[64] The physical state of these samples is in general a semicrystalline state. Poly(glycine) (MW = 5200) was purchased from Sigma Chemical Company.

Conformational characterization of these samples was made on the basis of conformation-dependent ^{13}C chemical shifts determined from CP-MAS NMR, the characteristic bands in IR and far-IR spectra[78, 79] and X-ray diffraction data.[80, 81] Synthetic conditions and characteristics of these samples are summarized in Table 3.

Poly(L-alanine) (PLA), poly(L-leucine) (PLL), and poly(γ-benzyl L-glutamate) (PBLG): α-helix and β-sheet forms. Figure 21 shows the ^{1}H CRAMPS NMR spectra of poly(L-alanines): (A) H-[Ala]$_8$-NHBu (monodispersed octapeptide, β-sheet form), (B) [Ala]$_n$-1 (averaged degree of polymerization (DP_n) is about 16, mixture of α-helix and β-sheet forms), and (C) [Ala]$_n$-5 ($DP_n \approx 65$, α-helix) in the solid state. The ^{1}H CRAMPS NMR spectra of PLA show three regions in the proton signals. Each proton signal can be easily assigned to H^N, H^α and H^β from high frequency, although the resolution is not always good compared with the ^{1}H NMR spectra in solution. From these spectra, it is clear that (1) ^{1}H chemical shift of the H^α signal is conformation-dependent [α-helix (3.9 ppm) and β-sheet (5.1 ppm)]; (2) ^{1}H chemical shift of the H^β signals is almost conformation-independent [1.2–1.4 ppm] at the present resolution; and (3) H^N signal is broad due to residual dipolar coupling between amide ^{1}H and quadrupolar ^{14}N nuclei.[44] Thus, the chemical shift of the H^α signal in the α-helix is shielded by 1.2 ppm compared with that in the β-sheet, indicating that the H^α signal is a useful fingerprint for conformational analysis of PLA in the solid state.

Figure 22 shows the ^{1}H CRAMPS NMR spectra of poly(L-leucines): (A) [Leu]$_n$-1 (mostly β-sheet and a few α-helix form) and (B) [Leu]$_n$-2 (α-helix) in the solid state. These ^{1}H spectra are solid high-resolution signals separated into three regions (NH, H^α, and side-chain protons), which is a similar result to that of PLA. From these spectra, it is clear that (1) the chemical shift of the H^α

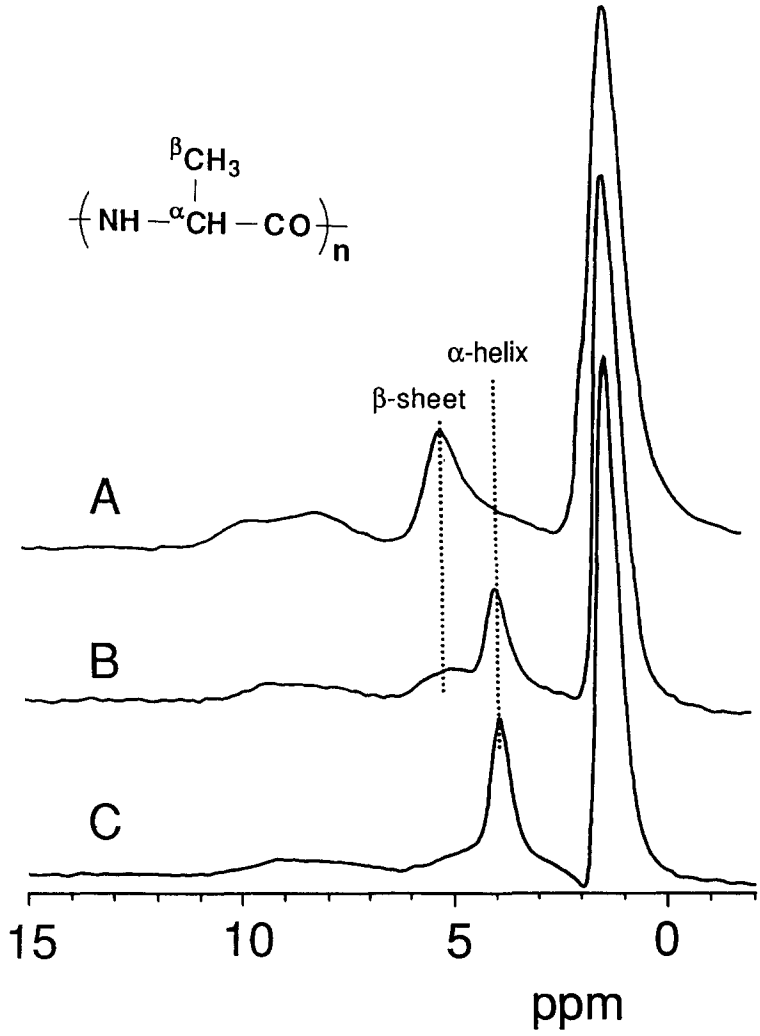

Fig. 21. 300 MHz ^{1}H CRAMPS NMR spectra of poly(L-alanines); (A) H-[Ala]$_8$-NHBu (β-sheet form), (B) [Ala]$_n$-1 (averaged degree of polymerization $DP_n \approx 16$, α-helix + β-sheet forms), and (C) [Ala]$_n$-5 ($DP_n \approx 65$, α-helix) (from ref. 16). Reproduced with permission from the American Chemical Society.

signal is conformation-dependent [α-helix: 4.0 ppm, β-sheet: 5.5 ppm]; (2) the chemical shifts of the H^{β}, H^{γ}, (1.5–1.6 ppm, overlapping) and H^{δ} signals (0.8–0.9 ppm) are almost conformation-independent; and (3) the H^N signal is so broad as to be almost nondetectable. It is especially noteworthy that the ^{1}H chemical shift region of the H^{α} signal is fully separated from that of the side-chain signals, in spite of the fact that the L-leucine residue has a bulky side

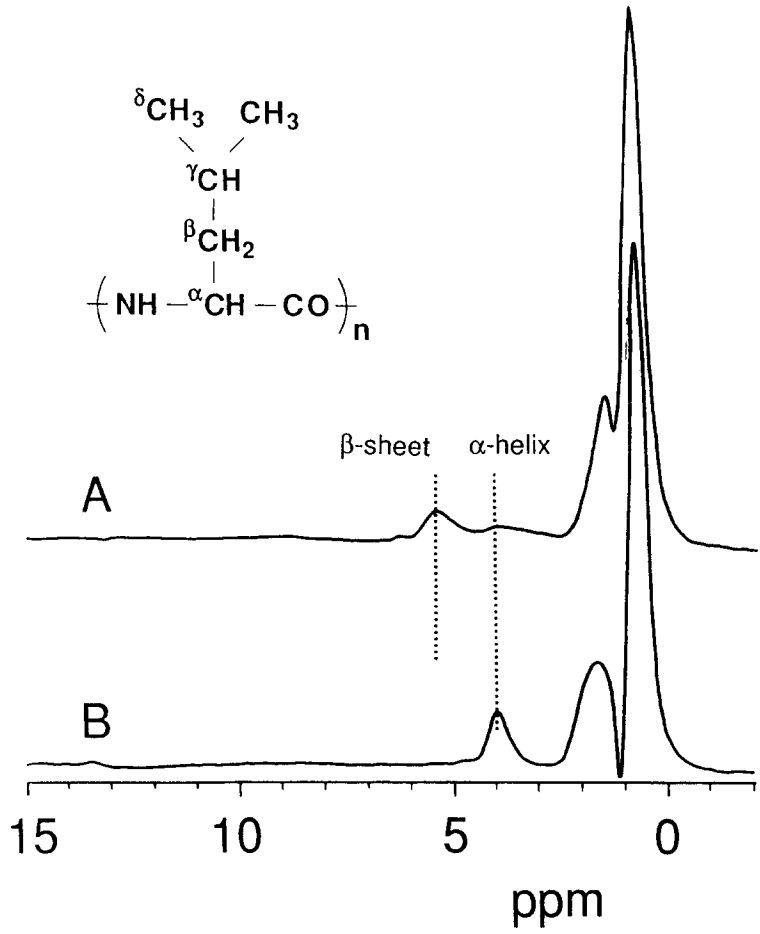

Fig. 22. 300 MHz ^{1}H CRAMPS NMR spectra of poly(L-leucines); (A) $[Leu]_n$-1 (β-sheet), and (B) $[Leu]_n$-2 (α-helix). Reproduced with permission from the American Chemical Society.

group. Thus, we can distinguish the conformation of PLLs from the conformation-dependent ^{1}H chemical shift of the H^α signal, indicating that this strategy is very useful for conformational analysis of polypeptides in the solid state.

Figure 23 shows the ^{1}H CRAMPS NMR spectra of poly(γ-benzyl L-glutamate); (A) H-$[Glu(OBzl)]_6$-OBzl (β-sheet) and (B) $[Glu(OBzl)]_n$ (α-helix) in the solid state. Interestingly, the ^{1}H signals separated into three regions (H^N, overlapping with phenyl and benzyl protons; H^α; and H^β plus H^γ signals) for PBLG, which is similar to the case of PLA and PLL. Since the γ-benzyl L-glutamate residue has a side-chain benzyl ester, it affects peak broadening, and thus the ^{1}H NMR signals become broad over the wide range of chemical shifts.

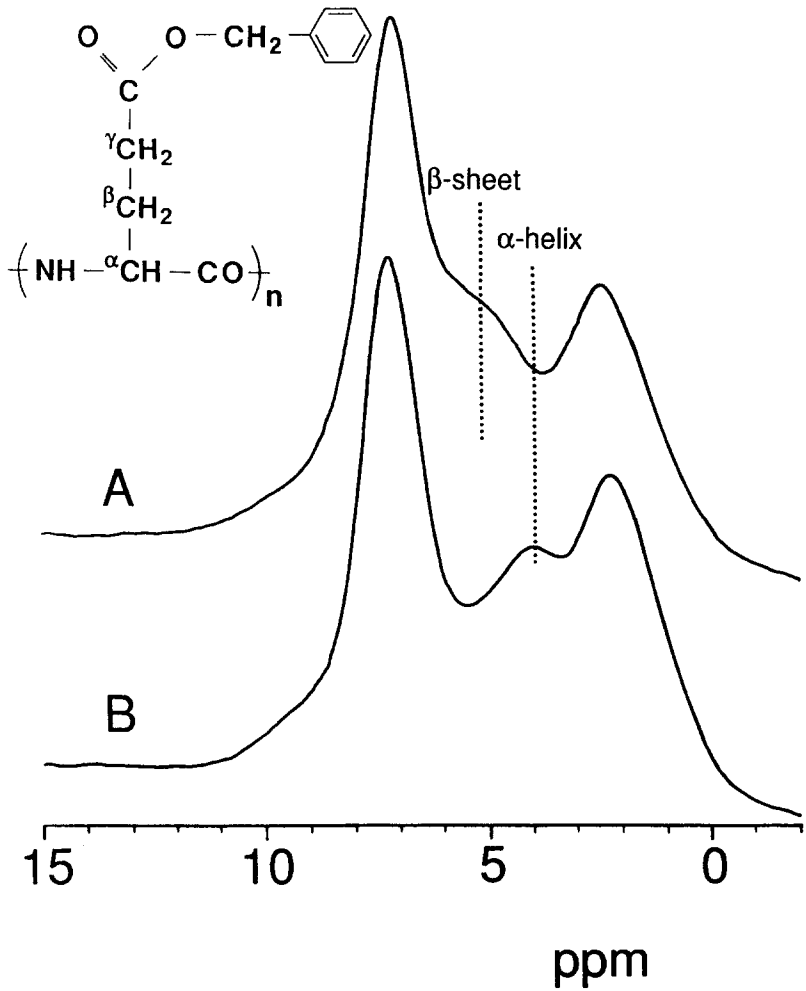

Fig. 23. 300 MHz ^{1}H CRAMPS NMR spectra of poly(γ-benzyl L-glutamates); (A) H-[Glu(OBzl)]$_6$-OBzl (β-sheet), and (B) [Glu(OBzl)]$_n$ (α-helix) (from ref. 16). Reproduced with permission from the American Chemical Society.

However, it is possible to recognize that (1) the chemical shift of the H^α signal is conformation-dependent [α-helix (4.0 ppm) and β-sheet (nearly 5.2 ppm)]; (2) the chemical shifts of the H^β and H^γ signals seem almost conformation-independent (2.2–2.4 ppm, overlapping); and (3) the NH signal overlaps the phenyl and benzyl protons (7.1–7.2 ppm), which are almost nondetectable. The chemical shift of the H^α signal in the α-helix is to low frequency by 1.2 ppm compared with that in the β-sheet form, which is quite reasonable. Thus, the chemical shift of the H^α signal of PBLG is also useful for conformational analysis in the solid state.

From the above results, it is concluded that the ^{1}H chemical shift of the H^{α} signal is important and useful for conformational analysis of these homopolypeptides in the solid state: α-helix (3.9–4.0 ppm) and β-sheet (5.1–5.5 ppm).

Poly(L-valine) (PLV)[67]*: chain-length dependence of ^{1}H chemical shifts.* Figure 24 shows the ^{1}H CRAMPS NMR spectra of poly(L-valines); (A) $[Val]_n$-1 (DP_n is about 5, β-sheet form) and (B) $[Val]_n$-5 (DP_n = 100, β-sheet) in the solid state. The shoulder peak around 1.2–1.5 ppm in spectrum A is assigned to the —N—CH_2— peak of the *n*-butylamide (—NHBu) group. It is well known that PLV is easily stabilized in β-sheet form whereas it is very difficult to take an

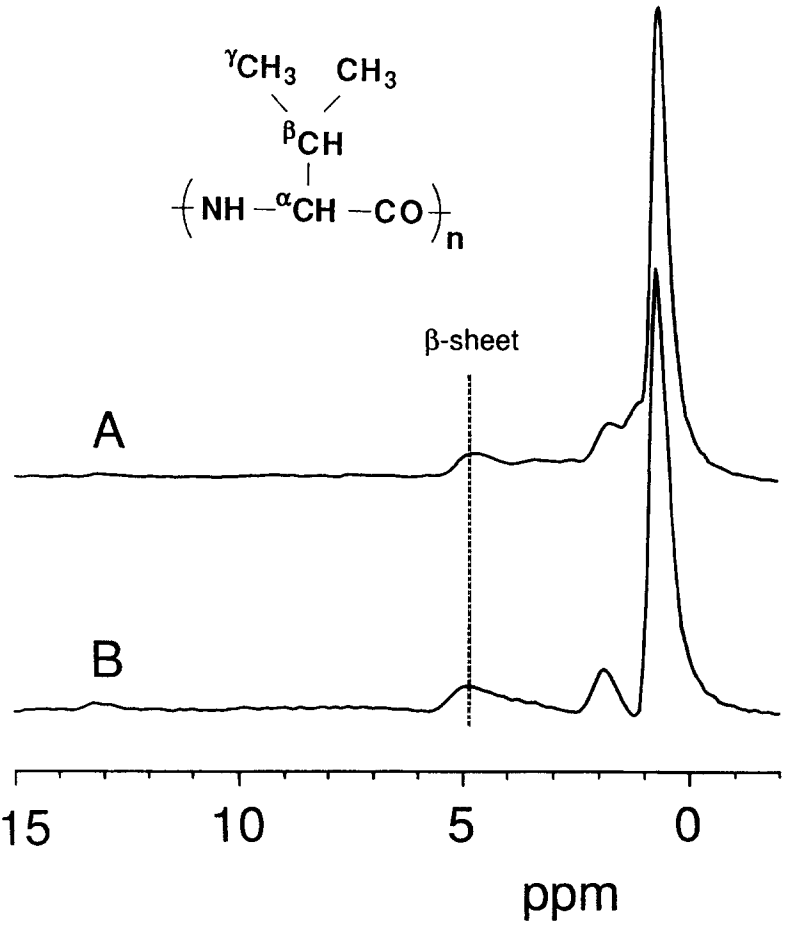

Fig. 24. 300 MHz ^{1}H CRAMPS NMR spectra of poly(L-valines): (A) $[Val]_n$-1 ($DP_n \approx 5$, β-sheet form) and (B) $[Val]_n$-5 ($DP_n \approx 100$, β-sheet).

α-helix due to the steric hindrance of the side-chain. For this series, ^1H CRAMPS NMR spectra show the separated three peak regions. They are assigned to H^N, H^α, and $H^\beta + H^\gamma$ signals from the high frequency side. From Fig. 24, it is confirmed that (1) the end chemical shift of the H^α signal does not depend on the degree of polymerization, because the stable conformation of PLVs used here is the β-sheet (5.0 ppm) form alone and it does not change with increasing molecular weight; (2) the chemical shifts of the H^β and H^γ peaks are

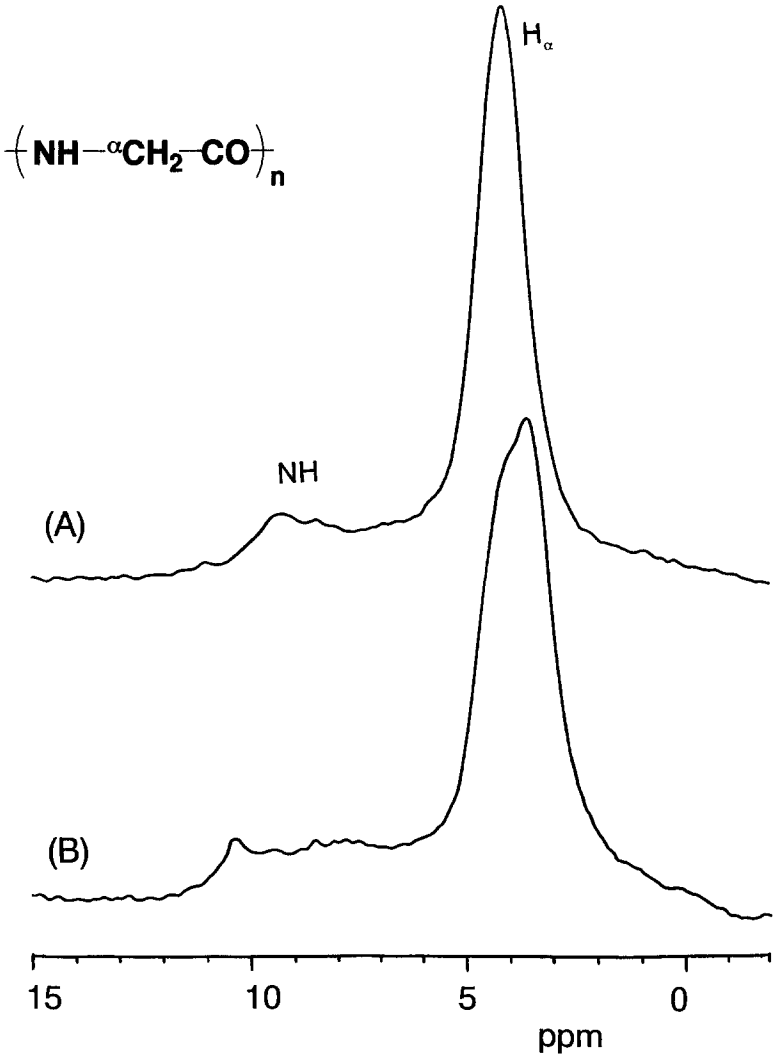

Fig. 25. 300 MHz ^1H CRAMPS NMR spectra of polyglycines: (A) PGI (polyglycine I) and (B) PGII (polyglycine II) forms (from ref. 64). Reproduced with permission from the American Chemical Society.

also independent of the degree of polymerization [H^{β}: 1.8–1.9 ppm; H^{γ}: 0.7–0.8 ppm]; and (3) amide ^{1}H signal is broad due to residual dipolar coupling. Thus, the chemical shifts of the H^{α}, H^{β}, and H^{γ} signals are independent of the degree of polymerization for PLV (β-sheet form). This fact confirms the view that the main cause of the ^{1}H chemical shift displacement is not the degree of polymerization but the conformation of the polypeptides.

Polyglycine (PG) and poly(L-proline) (PP): PGI and PGII, and PPI and PPII forms. Figure 25 shows the ^{1}H CRAMPS NMR spectra of polyglycines: (A) PGI (polyglycine I) and (B) PGII (polyglycine II) forms. In polyglycines, it is admitted that PGI (antiparallel β-sheet) and PGII (intermolecular hydrogen-bonded 3_1-helix) forms are stable in the solid state.[81] The ^{1}H CRAMPS NMR spectra of PG shows high-resolution proton signals separated into two regions (H^N and H^{α}). In this series, it has been found that (1) the ^{1}H chemical shifts of the H^{α} signals are conformation-dependent ($\delta = 4.3$, PGI; $\delta = 3.7$, PGII); and (2) the amide ^{1}H signal is, however, relatively broad due to residual dipolar coupling. As a result, the ^{1}H chemical shift of the H^{α} signal of PGI is to high frequency by 0.7 ppm from that of the PGII. This indicates that the ^{1}H chemical shift of the H^{α} signal is useful for conformational analysis of solid PG, whereas the chemical shift difference of the H^{α} signal is relatively small between PGI and PGII forms.

In addition, it has been found that the ^{1}H chemical shift of the H^{α} signal of PGI (β-sheet) is to low frequency by 0.6–1.2 ppm from those of other β-sheet polypeptides such as PLA, PLL, PBLG, and PLV. From the standpoint of the ^{1}H chemical shifts, glycine residue is a special α-amino acid compared with other common α-amino acids and it contains no asymmetric carbon atom, which is very convenient for the conformational analysis of polypeptides and proteins. However, one should carefully pay attention to the H^{α} chemical shifts of glycine residue, because the H^{α} chemical shifts of both PGI and PGII are near to that of the α-helix (3.9–4.0 ppm). Accordingly, it is noteworthy that the ^{1}H chemical shift of PG is very useful in assigning the H^{α} signal from other common amino acid residues and in analysing the main-chain conformation of silk fibroins and collagen fibrils, which will be discussed later.

Figures 26 and 27 show the ^{1}H CRAMPS and ^{13}C CP-MAS NMR spectra of poly(L-prolines), respectively: (A) PPI and (B) PPII forms in the solid state. Because the proline residue does not have amide proton, it cannot form N—H···O=C hydrogen bonding. For this reason, however, the proline residue fits in a unique structure. The main-chain conformation of PPII is a left-handed 3_1-helix,[82] which is similar to that of the left-handed PGII, although it is quite different in terms of hydrogen bonding. PPII is also an important basic structure found in collagen as well. The ^{1}H CRAMPS NMR spectra of PP shows high-resolution signals separated into three regions (H^{α}; H^{δ}; $H^{\beta} + H^{\gamma}$). On the other hand, it is known that PPI takes a right-handed 10_3 helix.[82]

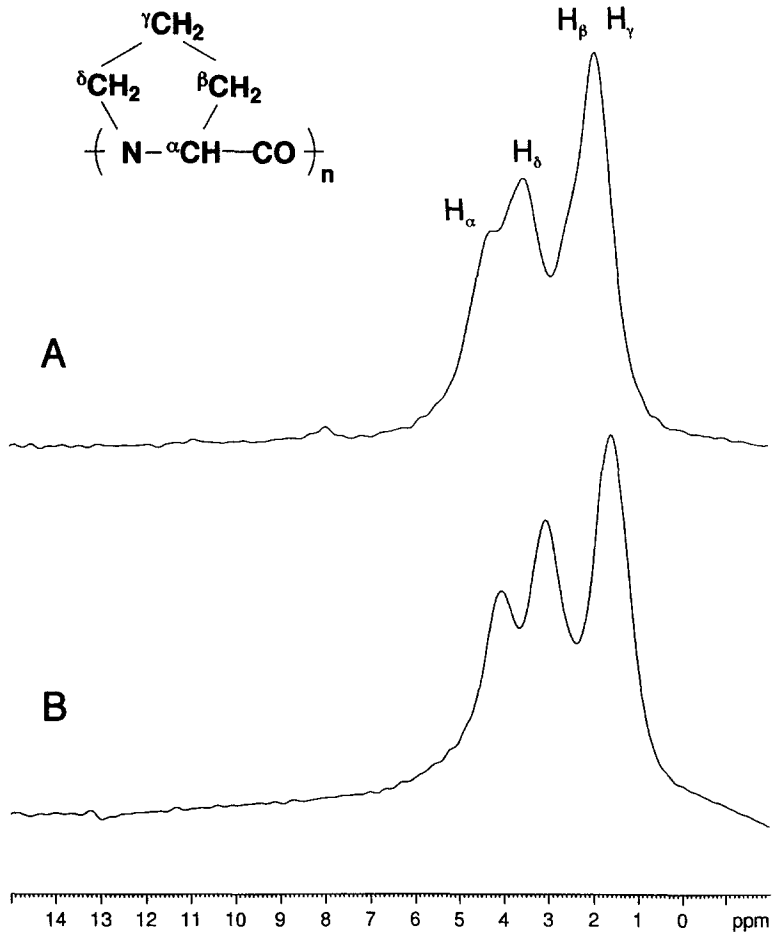

Fig. 26. 300 MHz ^{1}H CRAMPS NMR spectra of poly(L-prolines): (A) PPI (polyproline I) and (B) PPII (polyproline II) forms.

From Fig. 26, it is deduced that (1) the chemical shift of the H^{δ} signal is conformation-dependent (δ = 3.6, PPI; δ = 3.0, PPII); (2) the chemical shift of the H^{α} signal is almost conformation-independent (δ = 4.2, PPI; δ = 4.0, PPII); and (3) the chemical shifts of the H^{β} and H^{γ} peaks are slightly conformation-dependent (δ = 1.9, PPI; δ = 1.6, PPII). The chemical shift of the H^{δ} signal of the PPI is 0.6 ppm to high frequency from that of the PPII, suggesting that this peak is a useful fingerprint for conformational analysis of PP in the solid state. It is the first case in which the ^{1}H chemical shifts of the side-chains depend significantly on the main chain conformation of the PP, but the main-chain H^{α} does not depend on the conformation. Therefore, first of all, it is most important to confirm the assignment of individual ^{1}H signals in

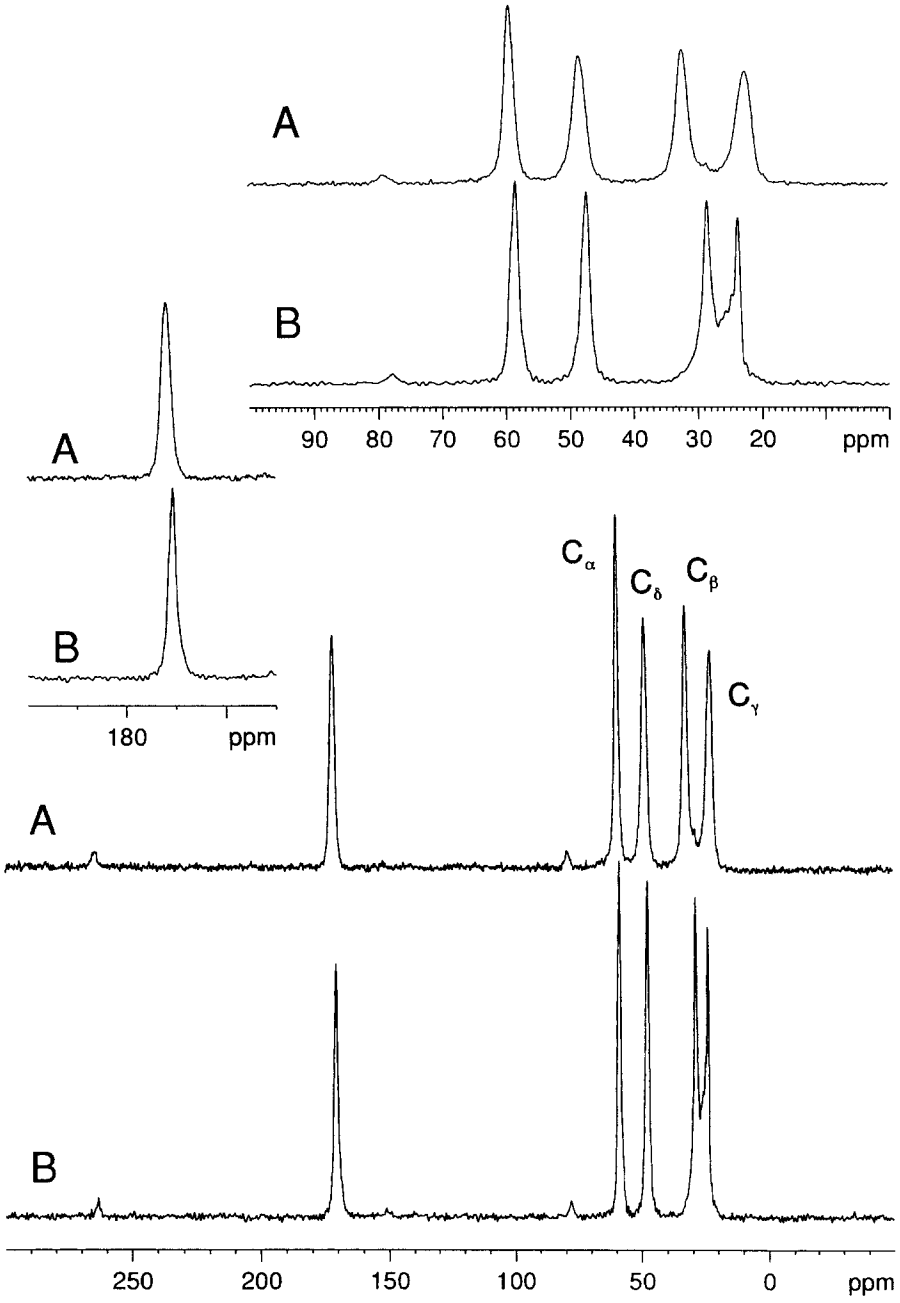

Fig. 27. 75.5 MHz ^{13}C CP-MAS NMR spectra of poly(L-prolines): (A) PPI and (B) PPII forms.

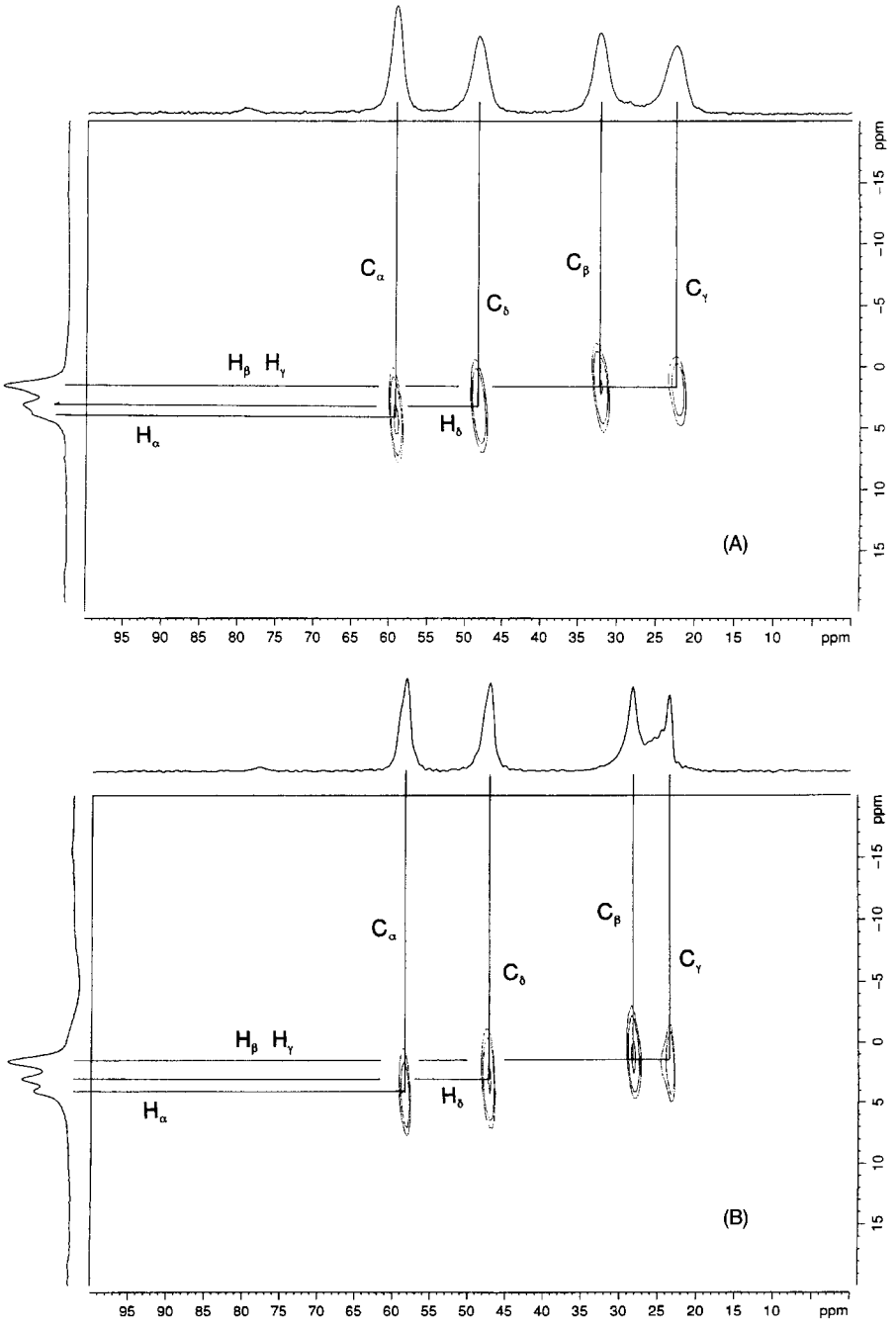

Fig. 28. 2 D $^{1}H-^{13}C$ HETCOR NMR spectra of poly(L-prolines): (A) PPI and (B) PPII forms.

conformational analysis. For this purpose, it looks promising to apply the two-dimensional (2D) ^{1}H–^{13}C heteronuclear correlation (HETCOR) NMR measurement.[64,70–74] In the case of PP, it is easy to separate the individual ^{1}H peaks of PPs on the basis of the well-resolved ^{13}C signals (Fig. 27), because the ^{1}H–^{13}C correlations are clear in the 2D spectra for ^{1}H–^{13}C pairs, as shown in Fig. 28. This fact will be discussed later.

3.2.2. *Comparison of the ^{1}H chemical shift data of amino acid residues in the solid-state and in solution*

It is very interesting to compare the ^{1}H chemical shift data in the solid state with those in solution, especially for the H^α chemical shift.[83–85] According to the solution ^{1}H NMR data summarized in the references, it is possible to estimate the chemical shift value of the H^α signal in the α-helix and β-sheet forms. That is, they can be concretely determined by the addition of -0.38 ppm (α-helix) and 0.38 ppm (β-sheet) to the H^α value in the random coil state, which has been determined in solution measurements.[83] It is necessary to level the standard of both ^{1}H chemical shifts, when comparing solid state and solution values. The difference between the chemical shift of both standard materials can fortunately be disregarded, because TMS and DSS are used as the standard in the solid state and in the solution, respectively. The differences of the ^{1}H chemical shifts between in the solid state and in solution are as follows: (1) for the α-helical polypeptides mentioned above, the H^α chemical shifts in the solid state (3.9–4.0 ppm from TMS) are identical with those in the solution data (3.94–3.95 ppm from DSS); (2) in the β-sheet polypeptides, in contrast, the H^α chemical shifts measured in the solid state (4.9–5.5 ppm from TMS) are 0.2–0.8 ppm to high frequency from those estimated in the solution data (4.70–4.71 ppm from DSS).[83] This comparison shows a very interesting and important finding. It is not a reason to estimate H^α chemical shifts of β-sheet polypeptides in solution according to the method described above. However, it does highlight that more careful attention must be given to determining the ^{1}H chemical shifts of β-sheet polypeptides using the solution data proposed by Wishart *et al.*[83–85]

3.2.3. *Conformational study of cyclic dipeptides by ^{1}H CRAMPS NMR: cyclo(L-alanyl-L-alanyl) and cyclo(L-alanyl-D-alanyl)*

Figure 29 shows the ^{1}H CRAMPS NMR spectra of cyclic dipeptides, cyclo[L-Ala-L-Ala](LL) and cyclo[L-Ala-D-Ala](LD) in the solid state. The ^{1}H CRAMPS NMR spectra show a simple solid high-resolution proton signal pattern separated into three regions (H^N, H^α and H^β) for LL and LD. It is known that the ring conformation of LL is a boat form (C^β: equatorial) and that of LD is a planar form in the solid state (by X-ray crystal diffraction analysis). From Fig. 29, it can be seen that (1) the chemical shift of the H^α signal is different

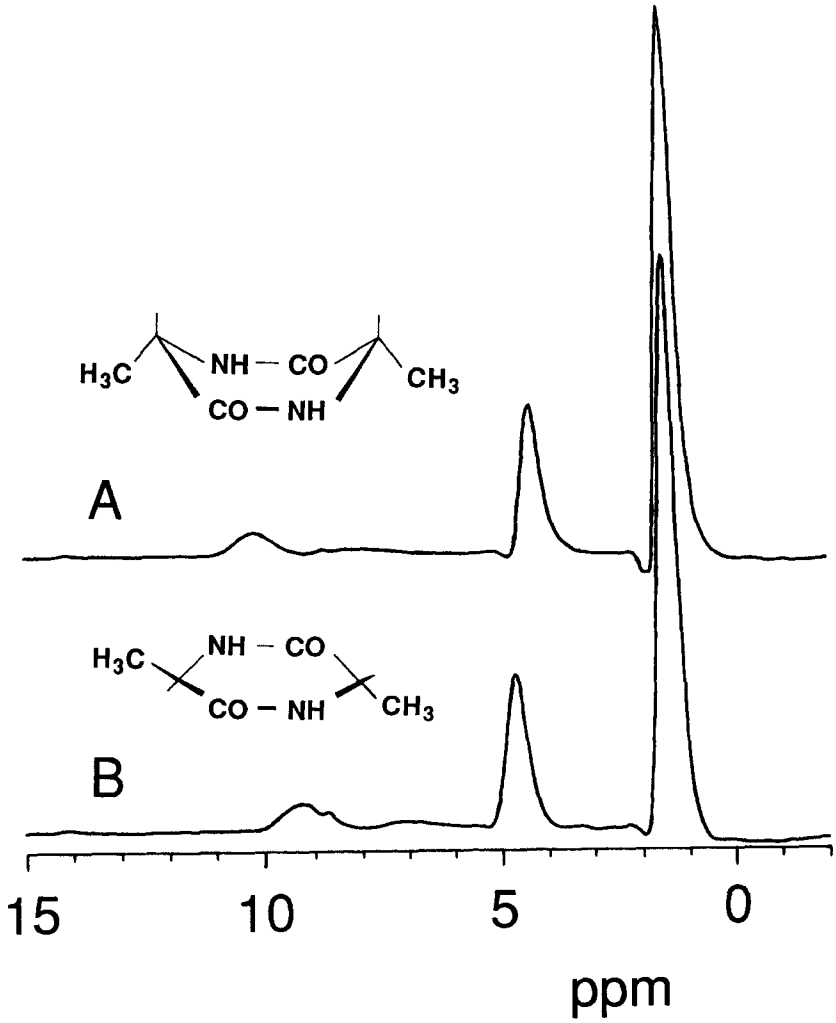

Fig. 29. 300 MHz ^{1}H CRAMPS NMR spectra of cyclic dipeptides: (A) cyclo[L-Ala-L-Ala] (LL) and (B) cyclo[L-Ala-D-Ala](LD) (from ref. 16). Reproduced with permission from the American Chemical Society.

between LL (4.3 ppm) and LD (4.7 ppm); (2) the chemical shifts of the H^{β} signals are almost identical for LL and LD (1.4–1.5 ppm); and (3) the chemical shift of the amide ^{1}H signal is quite different between LL (10.3 ppm) and LD (9.3 ppm), although the amide ^{1}H signal shows an asymmetric doublet pattern which may be caused mainly by the quadrupolar effect of ^{14}N. The chemical shift difference of the H^{α} signals can be attributed mainly to the differences in ring conformation in the solid state.

According to the X-ray crystal diffraction analysis by E. Sletten *et al.*,[80] the intermolecular hydrogen bond lengths (—O···H—) are 1.89 Å and 1.91 Å for LL and 1.94 Å (equivalent) for LD, respectively. The chemical shift difference of the amide ^{1}H signal between LL and LD may be explained by considering an intermolecular hydrogen-bonding effect as well as its ring conformation. However, we can not determine the true amide ^{1}H chemical shift and therefore hydrogen bond lengths because of the quadrupolar coupling of ^{14}N. The ^{1}H signal line shape bonded directly to ^{14}N of LL and LD exhibits a symmetric singlet pattern in spite of the heteronuclear dipolar interaction between quadrupolar ^{14}N nuclei and amide protons. However, the amide ^{1}H chemical shifts are not true because of the heteronuclear dipolar interactions between quadrupolar ^{14}N and amide ^{1}H.[16] It is of value to measure the true amide ^{1}H chemical shift in this series, and the ^{15}N-labelled LL and LD are needed for future work. Later, we will discuss how to obtain true NH chemical shifts for PLA and PLL (Section 3–4).

3.2.4. *Conformational study of specific deuterium-labelled polypeptides by ^{1}H CRAMPS NMR*

Specific deuterium-labelled samples of poly(γ-benzyl L-glutamates) were synthesized by Hiraoki *et al.*[68,69] In general, specific isotope labelling is a very powerful tool to aid assigning complicated signals. The NMR method utilizes isotopic labelling to advantage. Proton signals often overlap each other on ^{1}H CRAMPS NMR spectra because the resolution is not good. In such cases, a specific deuterium labelling technique sometimes enables one to observe separately a specific proton only and to eliminate all other unnecessary ^{1}H peaks.

Figure 30 shows the ^{1}H CRAMPS NMR spectra of PBLG: (A) $[Glu(OBzl)]_n$ (natural abundance), (B) $[Glu(OBzl)]_n$-d_2 (γ-protons deuterated, film), and (C) $[Glu(OBzl)]_n$-d_7 (benzyl protons deuterated, film). All these samples have an α-helix conformation, and their signals have been assigned. It is evident that the signal intensity at 2.3 ppm of $[Glu(OBzl)]_n$-d_2 (B) is lower than that of $[Glu(OBzl)]_n$ (A), indicating that the H_γ signal of $[Glu(OBzl)]_n$-d_2 has fully disappeared, as shown in Fig. 30 (A) and (B). This shows that specific deuterium labelling is useful for removing a specific proton signal from the overlapping signals of polypeptides in ^{1}H CRAMPS spectra.

It is recognized that the signal of all benzyl protons is clearly removed in deutrated samples of the benzyl group $[Glu(OBzl)]_n$-d_7, but the signal-to-noise (S/N) ratio and the resolution are not sufficient, as shown in Fig. 30(C). In spite of adopting a very long recycle delay time of 200 s in NMR measurements (the routine recycle delay is 10 s), measurement of the appropriate spectrum of a $[Glu(OBzl)]_n$-d_7 sample is not successful. The most likely reason for this may be a heteronuclear dipolar–dipolar interaction between proton and deuterium. For instance, if it is assumed that the distance between a proton and deuterium in

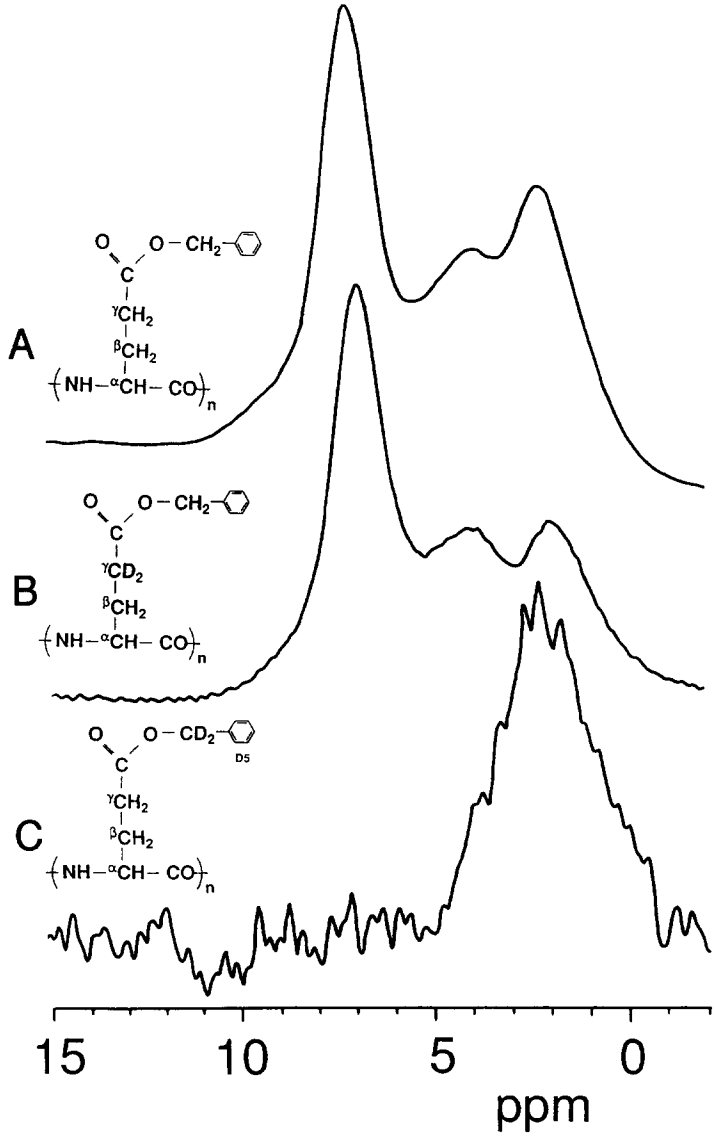

Fig. 30. 300 MHz ^{1}H CRAMPS NMR spectra of poly(γ-benzyl L-glutamates): (A) $[Glu(OBzl)]_n$ (natural abundance, powder), (B) $[Glu(OBzl)]_n$-d_2 (γ-protons deuterated, film prepared from the chloroform solution), and (C) $[Glu(OBzl)]_n$-d_7 (benzyl protons deuterated, film prepared from the chloroform solution).

PBLG is 2.0 Å, the magnitude of the dipolar interaction is estimated at 2.3 kHz.[15] Although the MAS speed has been selected at 2.0 kHz for the BR-24 pulse sequence to give the best spectral resolution for homonuclear decoupling of ^{1}H, this MAS speed is not sufficient to eliminate the ^{1}H–^{2}H dipolar interaction. Thus, deuterium labelling is useful for exact assignment and to remove the specific signals in ^{1}H CRAMPS spectra, if the amount of deuterium substitution is not great and if the resolution is sufficient to get a good spectrum.

3.2.5. Two-dimensional ^{1}H–^{13}C HETCOR NMR measurement[67]

Figure 28 shows the two-dimensional ^{1}H–^{13}C HETCOR NMR spectra of poly(L-prolines): (A) PPI and (B) PPII. The solid-state ^{1}H–^{13}C HETCOR NMR measurements were performed on a Bruker DSX 300 spectrometer operating at 300 MHz, equipped with a 4 mm CP-MAS probe.[64,74] The pulse sequence proposed by Burum *et al.*[70] was utilized for HETCOR, and the BLEW-24 pulse sequence was used for homonuclear decoupling of ^{1}H. The $\pi/2$ pulse width was 2.8 μs for both ^{13}C and ^{1}H under CP conditions. The spinning speed was set to 5.0 kHz. The ^{1}H chemical shift using BLEW-24 was calculated with a scaling factor 0.29 for all samples, which is a reasonable value.

It is possible to separate and assign the ^{1}H signals of the PPs using 2D HETCOR spectra, because the correlations are clearly resolved in the two-dimensional spectra for proton–carbon pairs. The 2D HETCOR technique allows resolution of ^{1}H CRAMPS to be tied to the higher resolution associated with ^{13}C chemical shifts.[64,70–74]

The ^{1}H chemical shift of the H^α proton signal is important and useful for conformational analysis of polyglycine (δ = 4.3, PGI; δ = 3.7, PGII) in the solid state. On the other hand, the H^δ chemical shift is useful for conformational analysis of poly(L-prolines) (δ = 3.6, PPI; δ = 3.0, PPII). Special attention should be given to the fact that the H^α chemical shifts of glycine and L-proline residues are near to the value of the α-helix form (3.9–4.0 ppm). In such a case, the 2D ^{1}H–^{13}C HETCOR technique is helpful in separating the ^{1}H signals. It is appropriate that the glycine and L-proline residues are given special treatment because the glycine residue does not have an asymmetric carbon atom and because the L-proline residue does not have an amide proton.

Next, we describe the application to the structural analysis of natural fibrous proteins in the solid state based on ^{1}H chemical shifts, mainly of the H^α signal of the model polypeptides.

3.3. Conformational study of natural fibrous proteins and their model polypeptides by ^{1}H CRAMPS NMR[64,74]

In the previous section, it was shown that the conformation of solid polypeptides can be determined based on the ^{1}H chemical shift. This implies

that the conformation of natural proteins may be inferred from ^{1}H chemical shifts as well as ^{13}C and ^{15}N chemical shifts in the solid state. Therefore, we describe, in this section, studies of some natural fibrous proteins such as silk fibroins and collagen fibrils as an application of the utility of ^{1}H CRAMPS NMR to the structural analysis of proteins in the solid state. It usually happens that some ^{1}H signals overlap each other in silk fibroins and collagen fibrils due to the resolution limit of ^{1}H CRAMPS. This may be solved partly by improvement of the resolution limit in ^{1}H CRAMPS using two-dimensional $^{1}H-^{13}C$ HETCOR (HETeronuclear-CORrelation), which is useful for improving the practical value of CRAMPS for the conformational analysis of proteins.

Three silk fibroin samples with known amino-acid sequences and conformations have been investigated: (1) *Tussah Antheraea pernyi* (α-helix form), (2) *Bombyx mori*-I (silk I form), (3) *Bombyx mori*-II (silk II form).[82,86–88] It is known that, generally, *Antheraea pernyi* consists mainly of 51% L-alanine, 24% glycine, and 11% L-serine residues, the secondary structure of which is an α-helix. By contrast, *Bombyx mori* contains approximately 43% glycine, 32% L-alanine, and 15% L-serine residues,[82,89] the secondary structure of which is known to be silk I and silk II forms. It is confirmed that the silk II form agrees with the same conformation as a β-sheet form. However, the structure of the silk I form has not yet been determined, although various models have been proposed.[61,63,82,89] The *Bombyx mori* silk fibroin contains mainly a repeating amino-acid sequence unit of [Ala-Gly-Ala-Gly-Ser-Gly].[82,90] Thus, it is anticipated that the ^{1}H chemical shifts of a more simplified model polypeptide such as $[Ala\text{-}Gly]_{12}$ will be a good guide to the model for the assignment of the NMR spectra of these silk fibroins in the solid state. The ^{1}H chemical shifts of $[Ala\text{-}Gly]_{12}$ will be clarified in comparison with their conformations. Very recently, it was found by Kishi *et al.*[74] that a series of the model polypeptides $[Ala\text{-}Gly]_n$ ($n = 6-12$) take a stable silk I form following treatment with an aqueous LiBr solution (9M).

Next, we discuss the collagen, which takes the triple helix structure.[82,90] The amino acid sequence of collagen fibril consists of the repeating amino-acid sequence unit $[Gly\text{-}Xaa\text{-}Yaa]_n$, where Xaa and Yaa are frequently occupied by prolyl (Pro) and 4-hydroxyprolyl (Hyp) residues, respectively. It is well known that the sequential model polypeptides such as $[Pro\text{-}Ala\text{-}Gly]_n$ or $[Pro\text{-}Pro\text{-}Gly]_n$ take the triple-helix conformation similar to that of collagen, as studied by X-ray diffraction[82,90] and ^{13}C, ^{15}N CP-MAS NMR.[62,82] This section focuses on the structure of $[Pro\text{-}Ala\text{-}Gly]_n$, and the collagen structure as described by ^{1}H CRAMPS NMR.

Some natural fibrous proteins and sequential model polypeptides have been used as follows: (1) *Tussah Antheraea perni* silk fibroin [α-helix form], (2) *Bombyx mori* silk fibroin [silk I and II forms], (3) poly(L-alanyL-glycine) $[Ala\text{-}Gly]_{12}$ [silk I and II], (4) collagen fibril [triple-strand helix], and (5) poly(L-prolyl-L-alanyL-glycine) $[Pro\text{-}Ala\text{-}Gly]_n$ [triple-strand helix].

Silk fibroins adopting different kinds of conformations were prepared as follows.[60,91] α-Helical *Tussah Antheraea perni* (α-helix form) was prepared by air-drying from the posterior division of the silk gland at 20 °C. *Bombyx mori*-I (silk I form) was prepared by air-drying from the silk gland for 1 day at 20 °C. *Bombyx mori*-II (silk II form) was prepared by immersion in methanol.

Collagen fibrils of Wister rat tail tendon (9 weeks, female) was used.[60]

Mono-dispersed sequential polypeptides $[Ala\text{-}Gly]_{12}$ and $[Pro\text{-}Ala\text{-}Gly]_n$ were used as the models of *Bombyx mori* silk fibroin and collagen fibrils, respectively. The well-defined sequential polypeptide $[Ala\text{-}Gly]_{12}$ was synthesized by a solid-phase peptide synthetic method,[64,74] which was performed on a PerSeptive Biosystems 9050 Plus PepSynthesizer. The procedure for synthesizing $[Pro\text{-}Ala\text{-}Gly]_n$ was reported in a previous paper.[62]

Conformational characterization of these samples was made on the basis of conformation-dependent ^{13}C and ^{15}N chemical shifts determined from CP-MAS NMR and also from the characteristic bands in the IR spectra. Synthetic conditions and characteristics of these samples are summarized in Table 4.

^{1}H CRAMPS NMR measurements of the silk fibroins and the model polypeptide, $[Ala\text{-}Gly]_{12}$, were performed on a Chemagnetics CMX 300 spectrometer operating at 300 MHz, equipped with a 5 mm CRAMPS probe. The $\pi/2$ pulse width was 1.3 μs. ^{1}H CRAMPS NMR measurements of collagen fibril and the model polypeptide, $[Pro\text{-}Gly\text{-}Ala]_n$, were performed on Bruker Avance DSX-300 spectrometer operating at 300 MHz equipped with a 4 mm CP-MAS probe. The $\pi/2$ pulse width was 1.8 μs. The BR-24 pulse sequence was used for homonuclear decoupling of ^{1}H. The rotational frequency was controlled at 2.0 kHz. The cycle time was 108 μs, corresponding to a t of 3 μs. Rotational frequency was controlled at 1.9 kHz. The recycle delay was 10 s and spectra were usually accumulated 64 times. Si-rubber ($\delta = 0.12$) relative to TMS ($\delta = 0$) was used as an internal standard. The ^{1}H chemical shift was calculated with a scaling factor 0.40 for all samples.

The solid-state ^{1}H–^{13}C HETCOR NMR measurements were performed on a Bruker DSX 300 spectrometer operating at 300 MHz, equipped with a 4 mm CP-MAS probe. The measurement conditions were as mentioned above.

3.3.1. Conformational study of silk fibroins by ^{1}H CRAMPS NMR

Figure 31 shows the 300 MHz ^{1}H CRAMPS NMR spectra of three silk fibroins: (A) *Tussah Antheraea pernyi* (α-helix), (B) *Bombyx mori*-I (silk I form), and (C) *Bombyx mori*-II (silk II form) fibroins. They give highly resolved ^{1}H CRAMPS NMR spectra in the solid state, which are the first high-resolution solid-state ^{1}H CRAMPS NMR spectra of such natural proteins, as far as we know. The ^{1}H signals of these fibroins are separated basically into four regions (H^N, side-chain phenyl, H^α, and side-chain protons).

The ^{1}H NMR spectrum of *Tussah Antheraea pernyi* fibroin is roughly similar to that of α-helical PLA except for the side-chain phenyl proton signals, as

Table 4. Synthetic conditions, conformational characteristics, and ^{1}H and ^{13}C chemical shifts of natural fibrous proteins and their model polypeptide samples (from refs 64 and 67)

Sample[a]	Synthetic method[b] or origin; treatment	Conformation[c]	H^{α}	H^{β}	C=O	C^{α} [d]	C^{β} [e]
Tussah Antheraea pernyi	silk gland; air-drying at 20 °C	α-helix	4.0	1.5	176.9, 173.5	53.2, 43.4	16.8
Bombyx mori-I	silk gland; air-drying at 20 °C	Silk I	3.9	1.6	177.2, 171.2	51.7, 44.1	17.3
Bombyx mori-II	silk gland; immersion in methanol	Silk II	5.0, 3.9	1.2	172.6, 170.2	49.2, 42.9	20.2
$[Ala\text{-}Gly]_{12}$-I	Fmoc; dialysis from LiBr solution	Silk I	3.6	1.5	177.4, 170.6	51.3, 43.9	17.2
$[Ala\text{-}Gly]_{12}$-II	Fmoc; as synthesized	Silk II	5.0, 3.6	1.2	173.2, 169.8	49.6, 43.5	21.5
Collagen Fibril	Wister rat tail tendon (9 weeks, female)	triple helix	3.8	1.4	174.1, (170)[f]	49.6, 43.0	17.2
$[Pro\text{-}Ala\text{-}Gly]_n$	Activated ester	triple helix	4.2	1.5	174.1, 169.8	48.2, 42.3	17.6

[a] Abbreviations: $[Ala\text{-}Gly]_{12}$, well-defined poly(L-alanyl-glycine) (24mer); $[Pro\text{-}Ala\text{-}Gly]_n$, poly(L-prolyl-L-alanyl-glycine); *Tussah Antheraea pernyi* (silk fibroin); *Bombyx mori* (silk fibroin).

[b] Fmoc, 9-Fluorenylmethoxy carbonyl (method).

[c] Conformations of these samples were determined by ^{13}C and/or ^{15}N CP-MAS NMR, and IR spectroscopic methods.

[d] ^{13}C chemical shifts of α-carbons of alanine and glycine residues.

[e] ^{13}C chemical shift of β-methyl carbon of alanine residue.

[f] Shoulder peak.

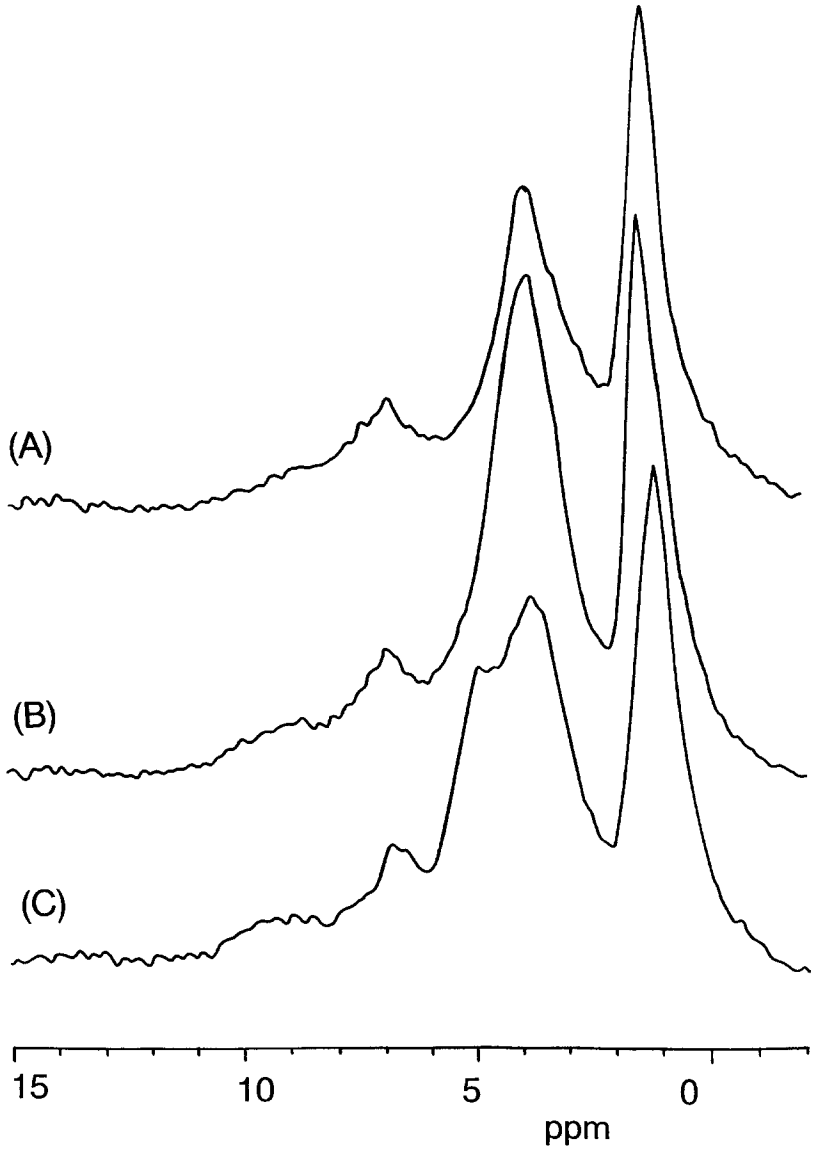

Fig. 31. 300 MHz ^{1}H CRAMPS NMR spectra of silk fibroins (64 scans): (A) *Tussah Antheraea pernyi* fibroin (α-helix), (B) *Bombyx mori*-I (silk I form), and (C) *Bombyx mori*-II (silk II form). Peak assignment: H^N, 10–8 ppm; side-chain phenyl, 6.9 ppm; H^α, 3.9–5.0 ppm; side-chain, 1.6–1.2 ppm (from ref. 64). Reproduced with permission from the American Chemical Society.

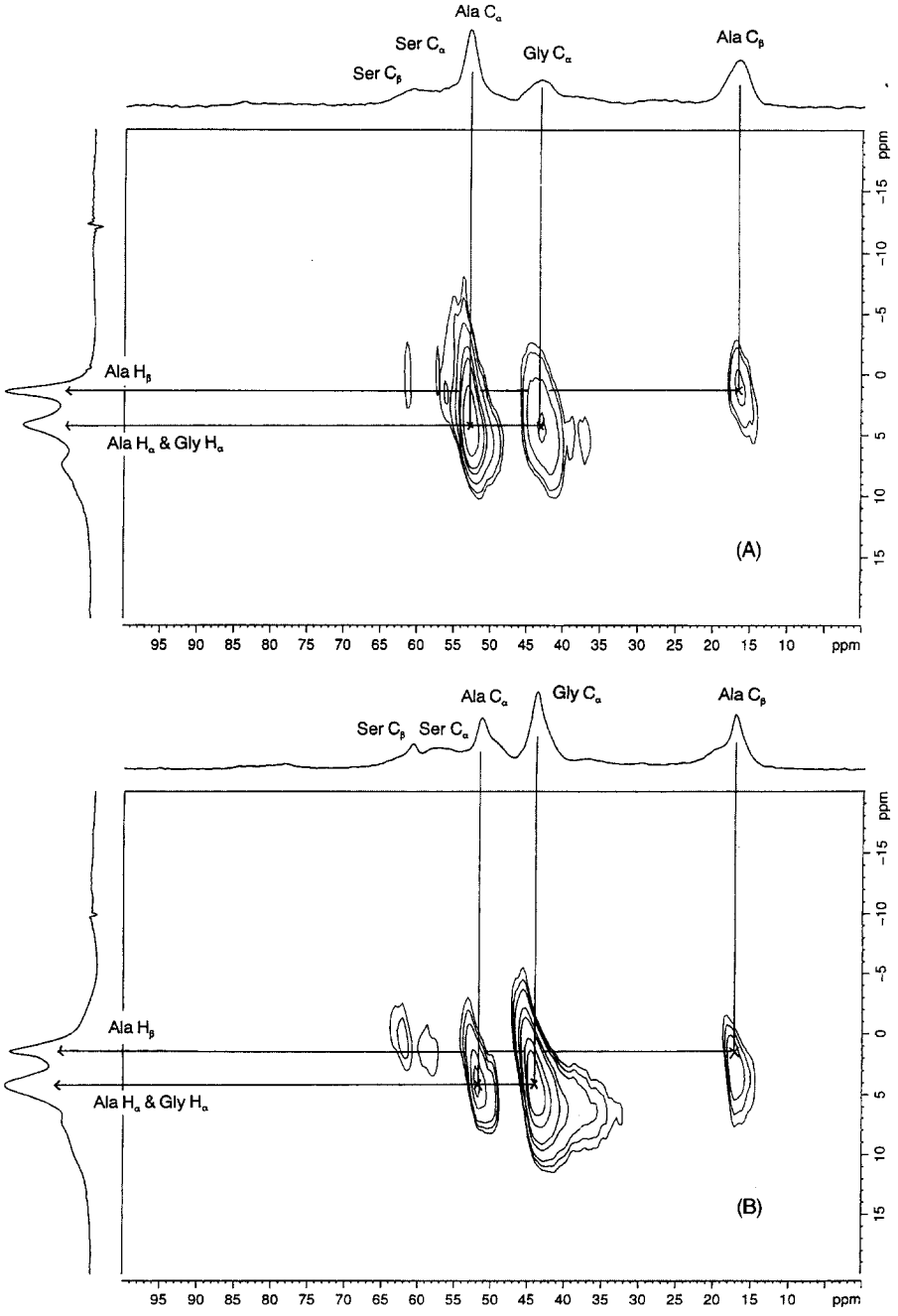

Fig. 31. (*continued*).

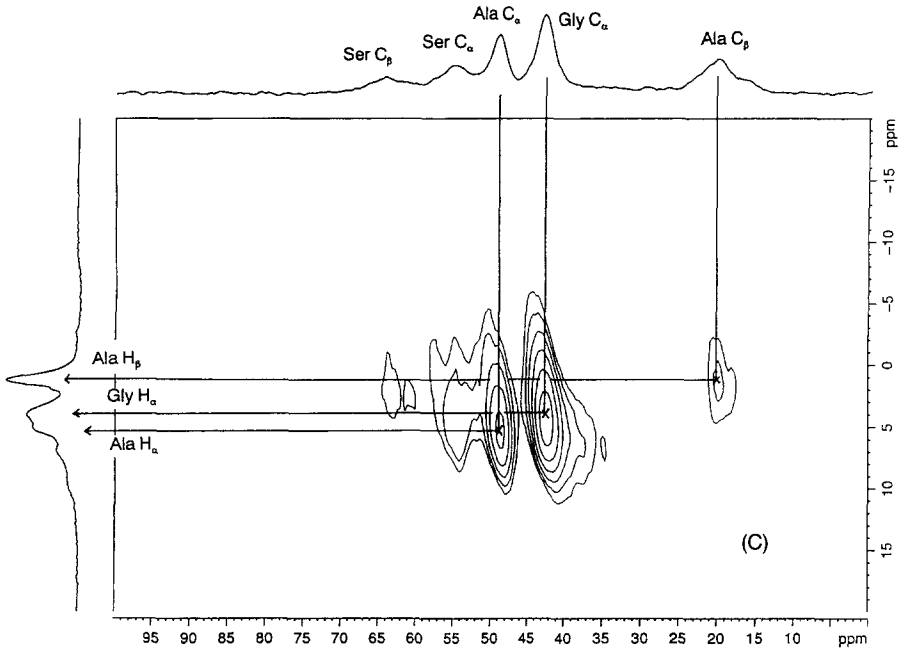

Fig. 32. 2D ^{1}H–^{13}C HETCOR NMR spectra of silk fibroins: (A) *Tussah Antheraea pernyi* fibroin (α-helix), (B) *Bombyx mori*-I (silk I), and (C) *Bombyx mori*-II (silk II) (from ref. 64). Reproduced with permission from the American Chemical Society.

shown in Fig. 31. This is deduced from the fact that the *Tussah Antheraea pernyi* contains approximately 51% L-alanine residues and takes an α-helix form. The H^α chemical shift of α-helical *Tussah Antheraea pernyi* fibroin (4.0 ppm) agrees very closely with that of α-helical PLA (3.9 ppm).[16] Moreover, the H^β proton chemical shifts of L-alanine residues in the *Tussah Antheraea pernyi* fibroin (δ = 1.5) agree with that of α-helical PLA (δ = 1.4). These results indicate that the conformational aspects of *Tussah Antheraea pernyi* fibroin may be inferred on the basis of the conformation-dependent ^{1}H chemical shifts of the model polypeptides (PLA). Thus, ^{1}H CRAMPS NMR can be diagnostic for the conformational analysis of silk fibroins in the solid state.

Next, we describe the ^{1}H NMR spectra of the two forms of *Bombyx mori* fibroins, silk I and silk II (β-sheet) forms, as shown in Fig. 31 (B) and (C). It should be noted that the amino-acid sequence (primary structure) of these two samples is completely identical, but their main-chain conformations are different. As expected, these two conformations are quite different to each other in terms of ^{1}H CRAMPS NMR spectra. The H^α signals of *Bombyx mori*-I (silk-I) and *Bombyx mori*-II (silk-II) showed a singlet (δ = 3.9) and doublet (δ = 5.0 and 3.9), respectively. In addition, the chemical shift of the H^β protons

(mainly from L-alanine residues) of *Bombyx mori*-I (δ = 1.6) is different from that of *Bombyx mori*-II (δ = 1.2). It is clear in this case that the chemical shifts of side-chain protons depend on the conformation, i.e. silk I and silk II. This is a very important result because it is confirmed that the ^{1}H chemical shifts of the side-chains in polypeptides are principally conformation-dependent, although the H^β chemical shift of α-helix polypeptides is near to that of β-sheet polypeptides. Thus, the chemical shifts of the H^α and side-chain H^β signals are useful for conformational analysis of *Bombyx mori* silk fibroins in the solid state. It is also noteworthy that the chemical shift difference between the H^α and H^β protons may be regarded as significant between *Tussah Antheraea pernyi* (α-helix) (4.0–1.5 = 2.5 ppm) and *Bombyx mori*-I (3.9–1.6 = 2.3 ppm). Although the ^{1}H chemical shift differences between these two protons are relatively small, the ^{15}N chemical shift differences are clearly distinguished (Ala: α-helix, δ = 97.7; silk I, δ = 102.0, Ser: α-helix, δ = 97.7; silk I, δ = 95.4, Gly: α-helix, δ = 84.7; silk I, δ = 86.9).[59] The peak intensity of the side-chain protons of *Tussah Antheraea pernyi* fibroin is higher than that of *Bombyx mori*, which can be explained in terms of the difference in L-alanine content between them. Thus, it is considered that the side-chain proton signals of the silk fibroins are associated mainly with the H^β methyl protons of the L-alanine residues. Accordingly, we can easily distinguish between *Tussah Antheraea pernyi* (α-helix) and *Bombyx mori*-I fibroins from the peak intensity ratio of H^β against H^α in the ^{1}H CRAMPS NMR spectra.

Thus, ^{1}H CRAMPS NMR is a useful tool for conformational analysis of silk fibroins in the solid state, although an unsolved problem still remains: Why does the shape of the H^α signals of *Bombyx mori* change with conformation? In order to answer this question, 2D ^{1}H–^{13}C HETCOR NMR measurements seem valid. This technique is helpful in providing well-resolved proton chemical shift information for silk fibroins, where it is impossible to resolve the proton resonance with ^{1}H CRAMPS alone.

3.3.2. Two-dimensional ^{1}H–^{13}C HETCOR NMR study of silk fibroins

Figure 32 shows the 2D ^{1}H–^{13}C HETCOR NMR spectra of silk fibroins: (A) *Tussah Antheraea pernyi* (α-helix), (B) *Bombyx mori*-I (silk I), and (C) *Bombyx mori*-II (silk II) silk fibroin in the solid state. Individual ^{1}H signals can be easily assigned on the basis of the corresponding ^{13}C signals,[60] because the ^{1}H–^{13}C cross-peaks are clearly resolved in the 2D spectra for proton–carbon pairs. From Fig. 32, it is clear that: (1) the H^α chemical shift (mainly of the L-alanine residue) is the same as that of the glycine residue in *Tussah Antheraea pernyi* and *Bombyx mori*-I; (2) in contrast, the H^α chemical shift (of the L-alanine residue) is downfield (1.1 ppm) from that of the glycine residue in *Bombyx mori*-II; and (3) the H^α and H^β peaks of L-serine residue appear at around 1.5–2.5 ppm in 2D spectra, although the L-serine content is very low compared with the L-alanine or glycine content in *Bombyx mori* fibroin. Consequently, it

can be admitted that the H^{α} signals of the glycine and L-alanine residues overlap in *Tussah Antheraea pernyi* and *Bombyx mori*-I, but that the H^{α} signal of the glycine residue is distinguished from that of the L-alanine residue in *Bombyx mori*-II.

Thus, the 2D HETCOR technique allows the resolution of ^{1}H CRAMPS to be tied to the higher resolution associated with ^{13}C chemical shifts. However,

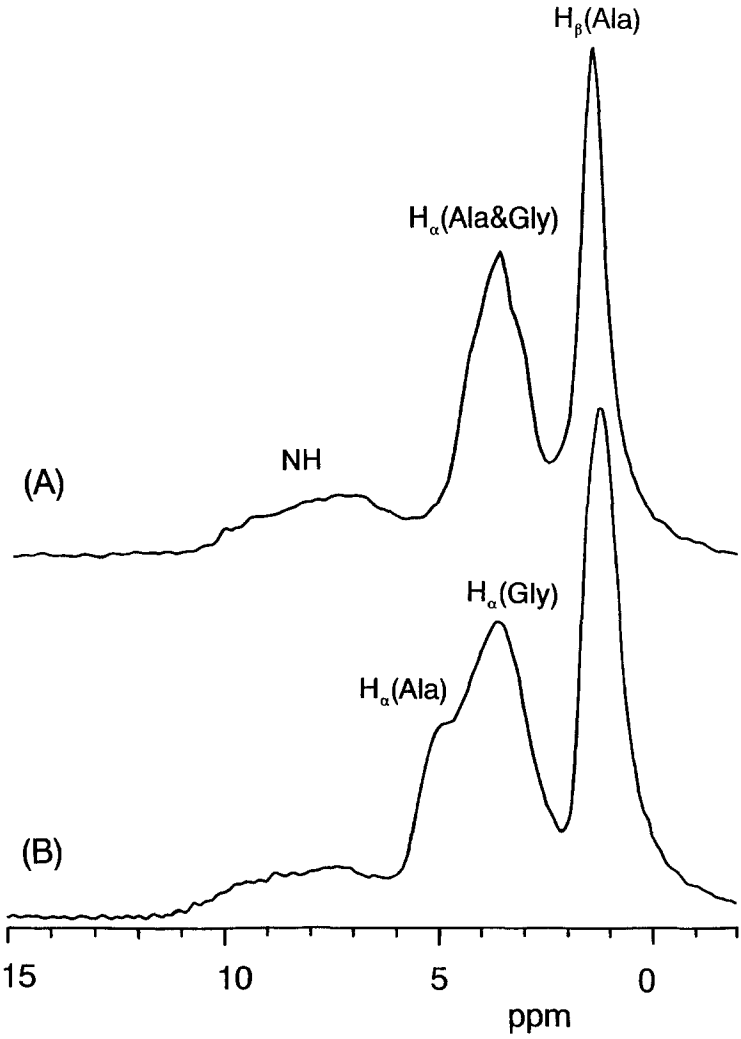

Fig. 33. 300 MHz ^{1}H CRAMPS NMR spectra of well-defined poly(L-alanyl-glycines): (A) $[Ala\text{-}Gly]_{12}$-I (silk I) and (B) $[Ala\text{-}Gly]_{12}$-II (silk II). Peak assignment: H^N, 10–8 ppm; H^{α}, 5.0–3.6 ppm; H^{β}, 1.2–1.5 ppm (from ref. 64). Reproduced with permission from the American Chemical Society.

2D HETCOR NMR has the disadvantage of having a small scaling factor, which leads to a larger error in ^1H chemical shifts. Accordingly, it is necessary to confirm the observation mentioned above with a well-defined simple model polypeptide of *Bombyx mori*, $[Ala\text{-}Gly]_{12}$, which is described in the following subsection.

3.3.3. ^1H CRAMPS NMR study of a silk fibroin model polypeptide

Figure 33 shows the ^1H CRAMPS NMR spectra of monodisperse poly(L-alanyl-glycines), (A) $[Ala\text{-}Gly]_{12}$-I (silk I)[74] and (B) $[Ala\text{-}Gly]_{12}$-II (silk II), in the solid state. Poly(L-alanyl-glycines) can be used as a model polypeptide of *Bombyx mori* silk fibroin, because it consists of an alternating sequence of L-alanine and glycine residues, and because the X-ray diffraction pattern of *Bombyx mori*[82,90] is similar to that of $[Ala\text{-}Gly]_{12}$.[81,89] As shown in Fig. 33, the ^1H CRAMPS NMR spectra of $[Ala\text{-}Gly]_{12}$ shows highly resolved signals separated into three regions (H^N, H^α and H^β), it was deduced from the spectra that: (1) the H^α signals of L-alanine and glycine residues overlapped ($\delta = 3.6$) and gave a singlet peak in $[Ala\text{-}Gly]_{12}$-I, whereas those of $[Ala\text{-}Gly]_{12}$-II separated into two peaks ($\delta = 5.0, 3.6$); (2) the H^β chemical shift of L-alanine residue in the silk I form ($\delta = 1.5$) appears to high frequency compared with that in the silk II form ($\delta = 1.2$); and (3) the NH signal is relatively broad. As expected, the ^1H CRAMPS spectra of $[Ala\text{-}Gly]_{12}$-I and $[Ala\text{-}Gly]_{12}$-II are quite similar to that of *Bombyx mori*-I and *Bombyx mori*-II, respectively.

Figure 34 shows the 2D ^1H–^{13}C HETCOR NMR spectra of (A) $[Ala\text{-}Gly]_{12}$-I (silk I form) and (B) $[Ala\text{-}Gly]_{12}$-II (silk II form) in the solid state. Figure 34 shows that: (1) the H^α chemical shift of the L-alanine residue in $[Ala\text{-}Gly]_{12}$-I is almost the same as that of the glycine residue (overlapping); (2) the H^α chemical shift of the L-alanine residue in $[Ala\text{-}Gly]_{12}$-II, in contrast, is to high frequency from that of the glycine residue, and they are separated (doublet). These results indicate that the H^α chemical shift of L-alanine residue is almost the same as that of glycine residue in the silk I form for $[Ala\text{-}Gly]_{12}$-I and *Bombyx mori*-I. This tendency agrees well with the result obtained from 2D HETCOR spectra of *Bombyx mori*-I and $[Ala\text{-}Gly]_{12}$-I.

From 2D HETCOR measurements, it is easily deduced that the H^α chemical shifts of both the L-alanine and glycine residues in $[Ala\text{-}Gly]_{12}$-I are close to those in *Bombyx mori*-I. Furthermore, the H^α chemical shifts of the glycine residue in $[Ala\text{-}Gly]_{12}$-I and *Bombyx mori*-I are also close to those of PG II ($\delta = 3.7$). On the other hand, the H^β chemical shift of the L-alanine residue in $[Ala\text{-}Gly]_{12}$-I ($\delta = 1.5$) agrees with the side-chain ^1H chemical shift of *Bombyx mori*-I ($\delta = 1.6$). Thus, all signals of the ^1H CRAMPS spectra of *Bombyx mori*-I can be assigned [$\delta = 10$–8, H^N; $\delta = 6.9$, phenyl protons mainly of L-tyrosine residue; $\delta = 3.9$, H^α (mainly of Ala and Gly residues); $\delta = 1.6$, side-chains (mainly H^β of Ala residue)].

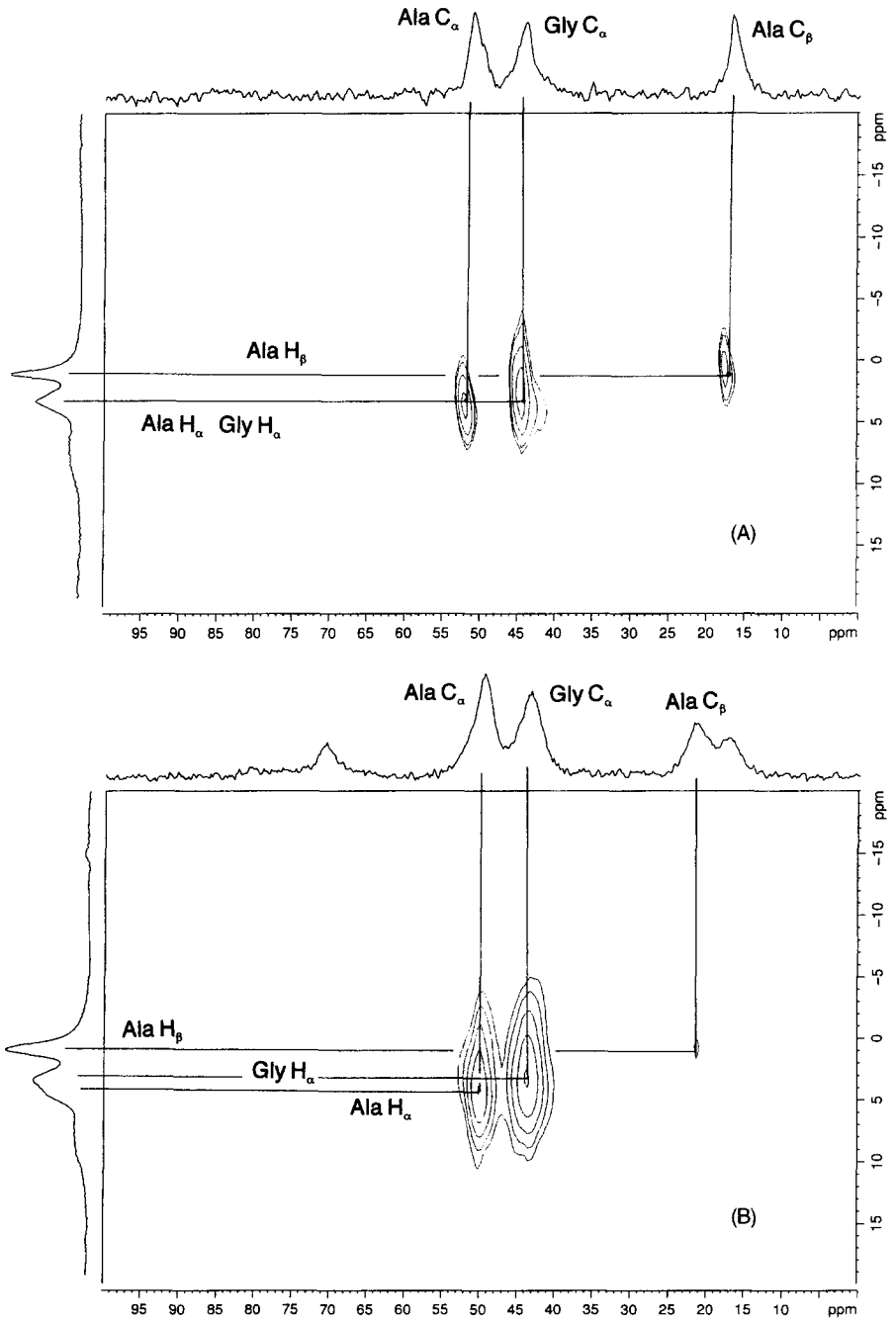

Figure 34. 2D ^{1}H–^{13}C HETCOR spectra of $[Ala\text{-}Gly]_{12}$: (A) $[Ala\text{-}Gly]_{12}$-I (silk I) and (B) $[Ala\text{-}Gly]_{12}$-II (silk II).

By contrast, the H^{α} chemical shifts of [Ala-Gly]$_{12}$-II (δ = 5.0 and 3.6) are close to those of *Bombyx mori*-II (δ = 5.0 and 3.9). The H^{α} chemical shift values of [Ala-Gly]$_{12}$-II agree with those of PLA (δ = 5.1) (Fig. 21) and PGI (δ = 4.3) (Fig. 25) adopting the β-sheet form, respectively. The most interesting result is that the H^{α} chemical shift of the glycine residue does not change between silk I and silk II forms (in both *Bombyx mori* and [Ala-Gly]$_{12}$), whereas that of the L-alanine residue shows apparent conformation dependency. Thus, the ^1H chemical shifts of the Ala and Gly residues may offer key information to clarify the silk I structure. On the other hand, the H^{β} chemical shift of [Ala-Gly]$_{12}$-II (δ = 1.2) agrees completely with that of PLA adopting a β-sheet form. These results show that the ^1H chemical shifts of the well-defined model polypeptides are useful for the structural analysis of silk fibroins in the solid state. Peak assignment of the ^1H NMR spectrum of *Bombyx mori*-II was made as follows: δ = 10–8, H^N; δ = 6.9, phenyl protons mainly of L-tyrosine residues; δ = 5.0, H^{α} of all amino acid residues (mainly of Ala residue) except for glycine; δ = 3.9, H^{α} of Gly residue; δ = 1.2, side-chains (mainly H^{β} of Ala).

Now it is clear that the ^1H chemical shift reflects the conformation of model polypeptide [Ala-Gly]$_{12}$ and natural silk fibroins such as *Tussah Antheraea pernyi* and *Bombyx mori* silk fibroins. It is confirmed that the well-defined [Ala-Gly]$_{12}$ is a suitable model for the structural study of natural silk fibroins (silk I and silk II forms) using high-resolution solid-state NMR. As a result, the ^1H peak assignment of the silk fibroins on the basis of the conformation-dependent ^1H chemical shifts of model polypeptides can be determined utilizing ^1H CRAMPS NMR and ^1H–^{13}C 2D HETCOR NMR, as described in this section. The chemical shift results of model polypeptides [Ala-Gly]$_{12}$ synthesized by Shoji *et al.* play an important role in determining new structures for silk I and silk II forms, as very recently proposed by Lazo and Downing.[88]

3.3.4. Two-dimensional ^1H–^{13}C HETCOR NMR study of collagen fibrils and model polypeptides[67]

Figure 35 shows the ^1H CRAMPS NMR spectra of (A) poly(L-prolyl-L-alanyl-glycine) [Pro-Ala-Gly]$_n$ (triple helix) and (B) collagen fibril (triple helix) in the solid state. Highly resolved ^1H NMR spectra of collagen fibril and its model polypeptide have been obtained. The spectra are separated into three regions (H^N + side-chain phenyl; H^{δ} of Pro and Hyp residues + H^{γ} of Hyp residue + H^{α}; and other side-chain protons) in collagen fibril and [Pro-Ala-Gly]$_n$. The spectral features of the ^1H NMR of collagen fibril are similar to but a little different from those of [Pro-Ala-Gly]$_n$. Since both samples have a triple-helix conformation as established by X-ray diffraction and ^{13}C CP-MAS NMR analysis (Fig. 36), the difference between the two may be ascribed mainly to the ^1H signals of the Hyp residue of collagen fibril. In such a situation, we have to confirm the assignment of proton peaks for collagen fibril and [Pro-Ala-Gly]$_n$

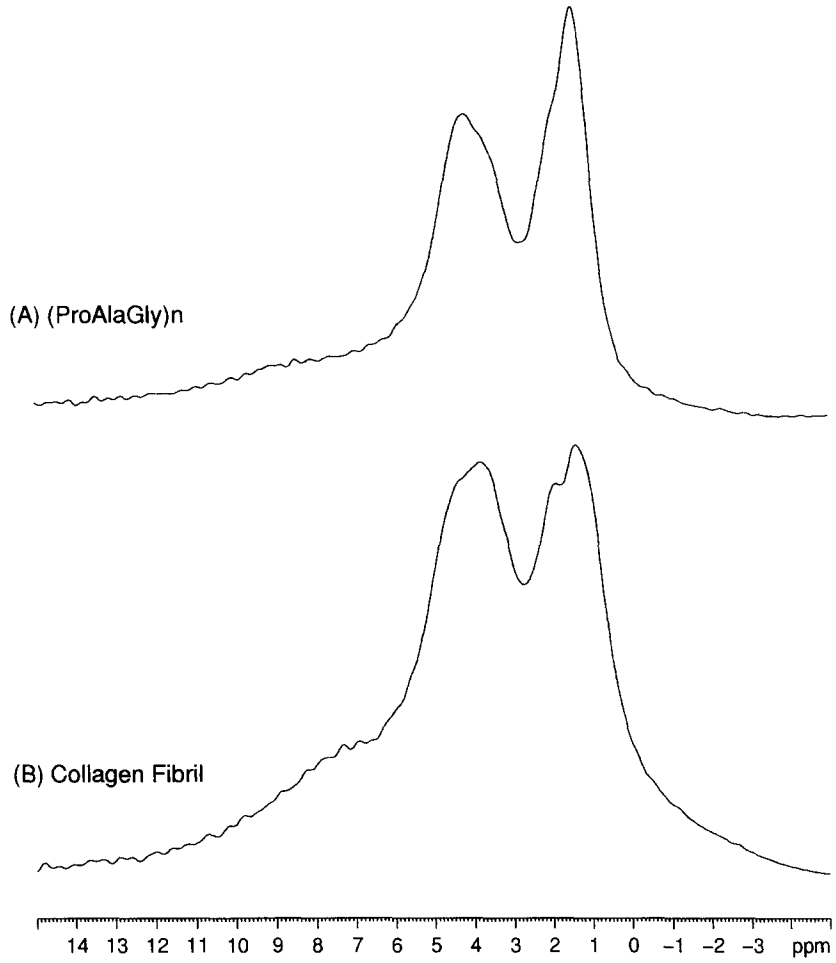

Fig. 35. 300 MHz ^{1}H CRAMPS NMR spectra of (A) $[Pro\text{-}Ala\text{-}Gly]_n$ (triple-stranded helix), and (B) collagen fibril (triple-stranded helix). Peak assignment: H^N, 10–8 ppm; side-chain phenyl, 8–7 ppm; H^{δ} of L-proline residue and H^{α}, 4.3–3.8; other side-chain protons, 1.6–1.9 ppm.

in order to analyse the structure in more detail. This requires the 2D $^{1}H-^{13}C$ HETCOR NMR measurement of collagen fibril and $[Pro\text{-}Ala\text{-}Gly]_n$.

Figure 37 shows the 2D $^{1}H-^{13}C$ HETCOR NMR spectra of (A) $[Pro\text{-}Ala\text{-}Gly]_n$ collagen fibril and (B) $[Pro\text{-}Ala\text{-}Gly]_n$ in the solid state. The ^{1}H signals of collagen fibril and $[Pro\text{-}Ala\text{-}Gly]_n$ were assigned reasonably on the basis of the ^{13}C signal assignments. From Fig. 37, it is found that: (1) the H^{β}, H^{γ} and H^{δ} chemical shifts of the Pro residue in $[Pro\text{-}Ala\text{-}Gly]_n$ are similar to those in the collagen fibril; (2) the H^{α} chemical shift of the Gly residue in $[Pro\text{-}Ala\text{-}Gly]_n$ is, on the other hand, to high frequency of that in the collagen fibril, whereas the

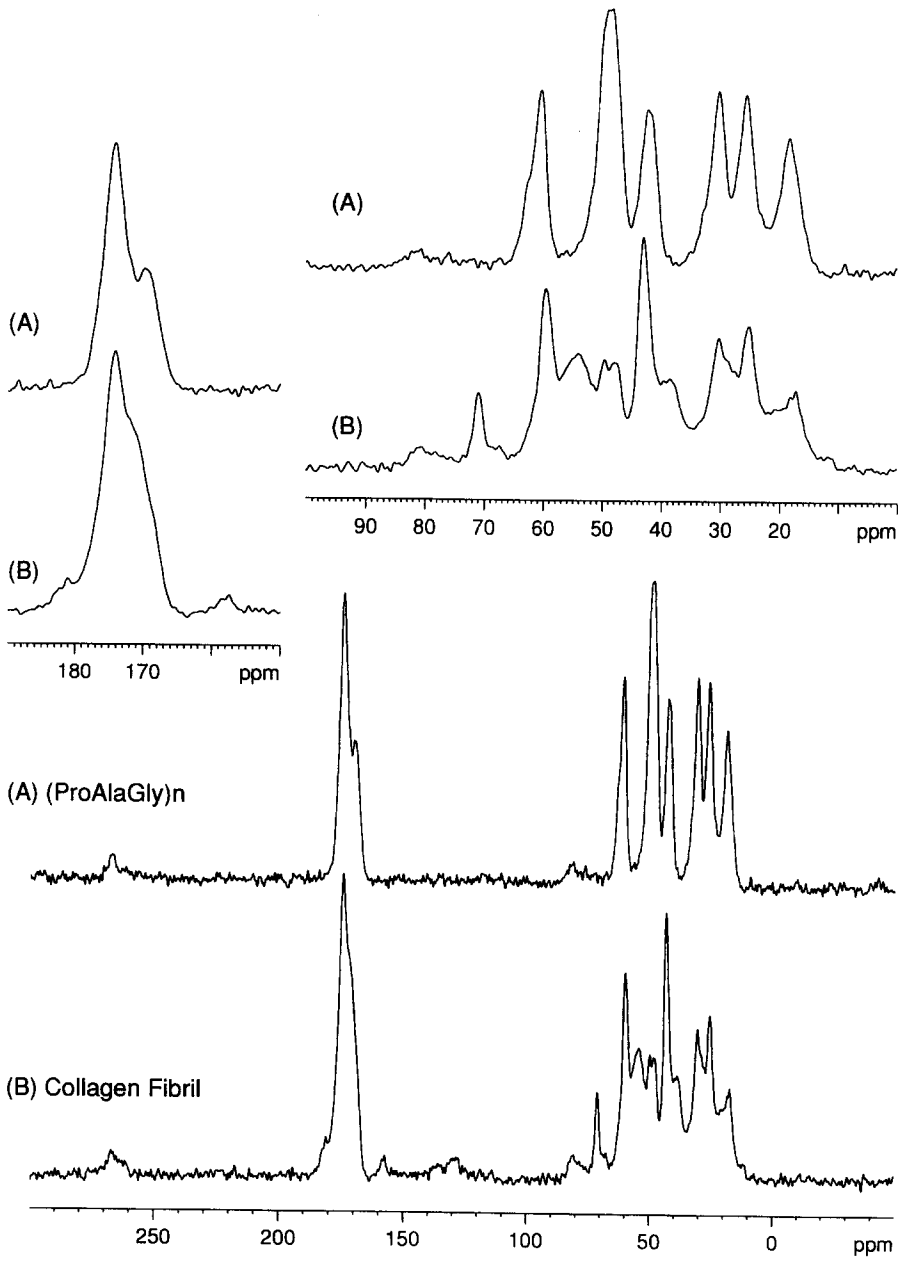

Fig. 36. 75.5 MHz ^{13}C CP-MAS NMR spectra of (A) $[Pro\text{-}Ala\text{-}Gly]_n$ (triple-stranded helix), and (B) collagen fibril (triple-stranded helix). Peak assignment: ($[Pro\text{-}Ala\text{-}Gly]_n$, C=O: 174.1 (Pro and Ala); 169.8 (Gly) ppm, C^{α}: 60.3 (Pro); 48.2 (Ala); 42.3 (Gly) ppm, C^{β}: 18.4 (Ala) ppm, and collagen fibril: C=O: 174.1 (Pro and Ala); ca.170 (Gly; shoulder) ppm, C^{α}: 59.6 (Pro); 49.6 (Ala); 43.0 (Gly) ppm, C^{β}: 17.3 (Ala) ppm.

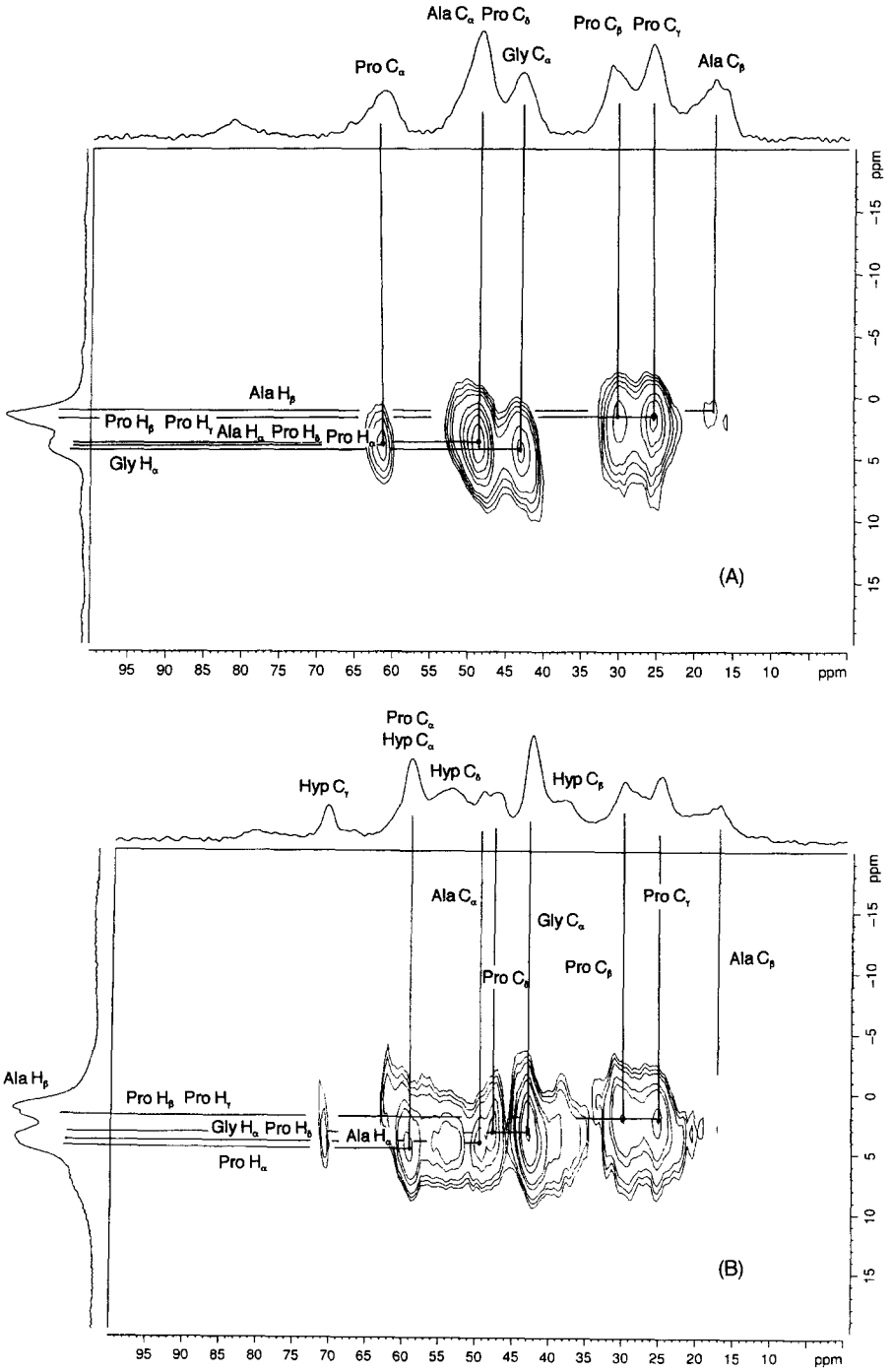

Fig. 37. 2D ^{1}H–^{13}C HETCOR spectra of (A) [Pro-Ala-Gly]$_n$, and (B) collagen fibril.

H^{α} chemical shifts of the Ala and Pro residues in $[Pro\text{-}Ala\text{-}Gly]_n$ are to low frequency from those in the collagen fibril; and (3) the H^{α}, H^{β}, H^{γ}, and H^{δ} signals of the Hyp residue in the collagen fibril can be seen as significant.

The H^{β} chemical shift of L-alanine residue in collagen fibril has not been decided exactly because the $^1H-^{13}C$ cross-peak has not been observed clearly, as shown in Fig. 37(B). This is probably because the L-alanine content is low in collagen fibril compared to that in $[Pro\text{-}Ala\text{-}Gly]_n$. This was supported by the signal intensity of the ^1H signals around 1.4 ppm, which indicates the L-alanine content. On the other hand, one of the main reasons for the differences of the signal pattern around 3.8–4.2 ppm may be ascribed to the difference in Ala and Hyp contents. It is evident that the H^{α} chemical shifts of the Gly, Ala, and Pro residues in $[Pro\text{-}Ala\text{-}Gly]_n$ are somewhat different from those in the collagen fibril. The C^{α} chemical shifts of these residues in $[Pro\text{-}Ala\text{-}Gly]_n$ (Pro; 59.6 ppm, Ala; 49.6, Gly; 43.0 ppm) are also different from those of the collagen fibril (Pro; 60.3, Ala; 48.2, Gly; 42.3 ppm), although the carbonyl carbon chemical shift is almost identical ($\delta = 174.1$). This is undeniable evidence that $[Pro\text{-}Ala\text{-}Gly]_n$ is a good structural model for the collagen fibril. In conclusion, ^1H CRAMPS NMR is a useful tool for the structural analysis of natural proteins in the solid state. Furthermore, it is noteworthy that the information from ^1H CRAMPS is considerably augmented by the use of $^1H-^{13}C$ HETCOR NMR.

3.4. Determination of amide proton chemical shift[45]

In the previous section, we showed that the chemical shifts of the H^{α} signal, which were successfully determined by ^1H CRAMPS, are very useful for the structural analysis of α-amino acids, polypeptides and natural proteins in the solid state. The fact that the main-chain conformation (secondary structure) of solid polypeptides can be determined by the ^1H chemical shift is an important discovery. Recently the problem of a very broad amide proton (H^N) signal (which contains essential information about hydrogen bonding) was resolved and the true H^N chemical shift was determined.[45] It is known that H^N signal broadening is caused by the residual dipolar couplings between the quadrupolar ^{14}N nuclei and the amide protons. The $^1H-^{14}N$ dipolar coupling causes an asymmetric doublet pattern which disturbs the determination of the true H^N chemical shift in the ^1H NMR spectra.[44,45] Such a dipolar broadening has never been observed in solution NMR because the dipolar coupling is averaged out by the rapid molecular motion.

In this section, therefore, we describe two approaches used to get a sharp and normal H^N signal. The first method uses some fully ^{15}N-labeled (99 atom%) polypeptides such as poly(L-alanine-^{15}N) ($[Ala^*]_n$) and poly(L-leucine-^{15}N) ($[Leu^*]_n$), to eliminate the effects of the quadrupolar ^{14}N nuclei. The second method compares the ^1H CRAMPS NMR spectra measured at two distinct

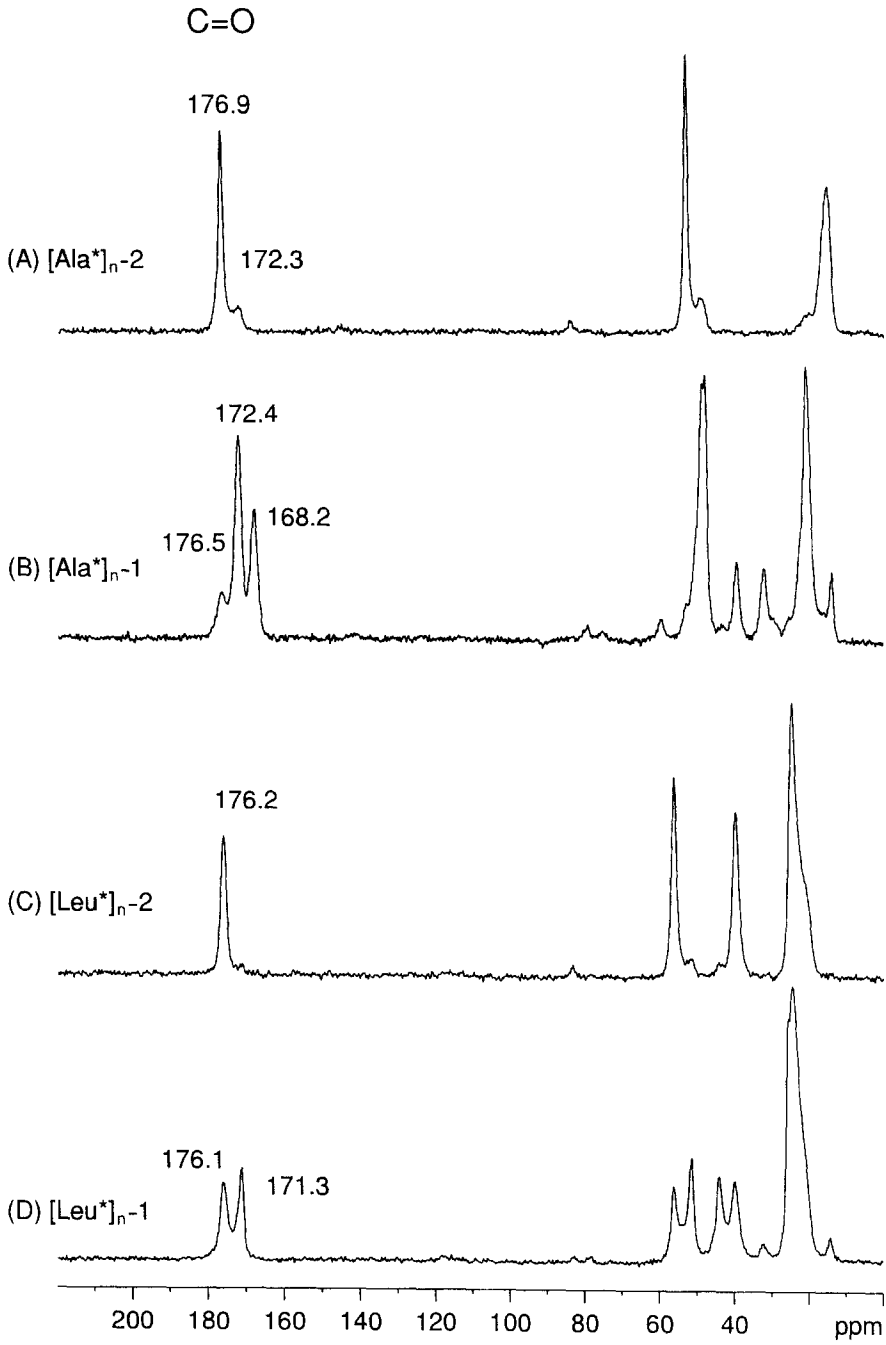

Fig. 38. 75.5 MHz ^{13}C CP-MAS NMR spectra of fully ^{15}N-labelled poly(L-alanines) and poly(L-leucines): (A) fully ^{15}N-labelled $[Ala^*]_n$-2 (molar ratio of the monomer to initiator (A/I) = 100; 99 at.% purity of ^{15}N, α-helix); (B) fully ^{15}N-labelled $[Ala^*]_n$-1 (A/I = 4; 99 at.% purity of ^{15}N; β-sheet); (C) fully ^{15}N-labelled $[Leu^*]_n$-2 (A/I = 100; 99 at.% purity of ^{15}N; α-helix); (D) fully ^{15}N-labelled $[Leu^*]_n$-1 (A/I = 5; 99 at.% purity of ^{15}N; β-sheet + α-helix).

spinning speeds (2.0 kHz [standard speed] and 3.5 kHz [faster speed]), to reduce the magnitude of the dipolar broadening between the ^{15}N nuclei and the amide protons. By applying these techniques, the exact amide proton chemical shifts of solid polypeptides adopting the α-helix and β-sheet forms for $[Ala^*]_n$ $[Leu^*]_n$ and have been successfully determined. In this section, we report on these conformation-dependent H^N chemical shifts and discuss the correlation between the H^N chemical shift and the conformation (including hydrogen bonds) of the polypeptides in the solid state.

A well-defined monodisperse penta(L-alanine)-*n*-butylamide H-$[Ala]_5$-NHBu was synthesized by an activated ester method[74] and other natural abundant polypeptides, $[Ala]_n$-5, $[Leu]_n$-1 and $[Leu]_n$-2, were synthesized by the N-carboxy α-amino-acid anhydride (NCA) method.[45] Fully ^{15}N-labelled homopolypeptides, $[Ala^*]_n$ (99 at.% of ^{15}N purity; MASSTRACE, Inc.) and $[Leu^*]_n$ (99 at.% of ^{15}N purity; MASSTRACE, Inc.), which show characteristic differences in conformation such as the α-helix and β-sheet forms, were prepared by the heterogeneous polymerization of the corresponding NCAs in acetonitrile with *n*-butylamine as an initiator. Conformational characterization of these samples was made on the basis of the conformation-dependent ^{13}C and ^{15}N chemical shifts determined from the CP-MAS NMR method and from the characteristic bands in the IR and far-IR spectra. Figs. 38 and 39 show the 75.5 MHz ^{13}C and 30.4 MHz ^{15}N CP-MAS NMR spectra respectively of these fully ^{15}N-labelled (99 at.% purity of ^{15}N) homopolypeptides adopting the α-helical and β-sheet forms: (A) $[Ala^*]_n$-2 (α-helix), (B) $[Ala^*]_n$-1 (β-sheet), (C) $[Leu^*]_n$-2 (α-helix), (D) $[Leu^*]_n$-1 (β-sheet) in the solid state. Synthetic conditions and conformational characteristics of these samples are summarized in Table 5, together with the ^1H chemical shift data.

Solid-state ^1H CRAMPS NMR spectra were measured with a Chemagnetics CMX 300 spectrometer operating at 300 MHz. The internal standard was Si-rubber ($\delta = 0.12$) relative to $(CH_3)_4Si$ ($\delta = 0$). BR-24 and MREV-8 pulse sequences were applied. The radio frequency (RF) powers and duration windows (τ) of these pulse sequences were adjusted so as to obtain the best resolution for adipic acid.

BR-24 pulse sequence[41] A 90° pulse width of 1.3 μs is used for the BR-24 pulse sequence. The cycle time of the BR-24 is 108 μs, corresponding to a τ of 3 μs. The MAS rotational frequency is controlled at 2.0 kHz. The ^1H chemical shift has been calculated with a scaling factor of 0.40 for all samples, which was determined experimentally.

MREV-8 pulse sequence[92] The 90° pulse width is 1.1 μs for the MREV-8. The cycle time of the MREV-8 is 28.8 μs, corresponding to a τ of 2.4 μs, and the rotational frequency is 3.5 kHz. The ^1H chemical shift is calculated with a scaling factor of 0.53 for all samples, which was determined experimentally. The carrier frequency must be selected carefully to avoid the carrier noise

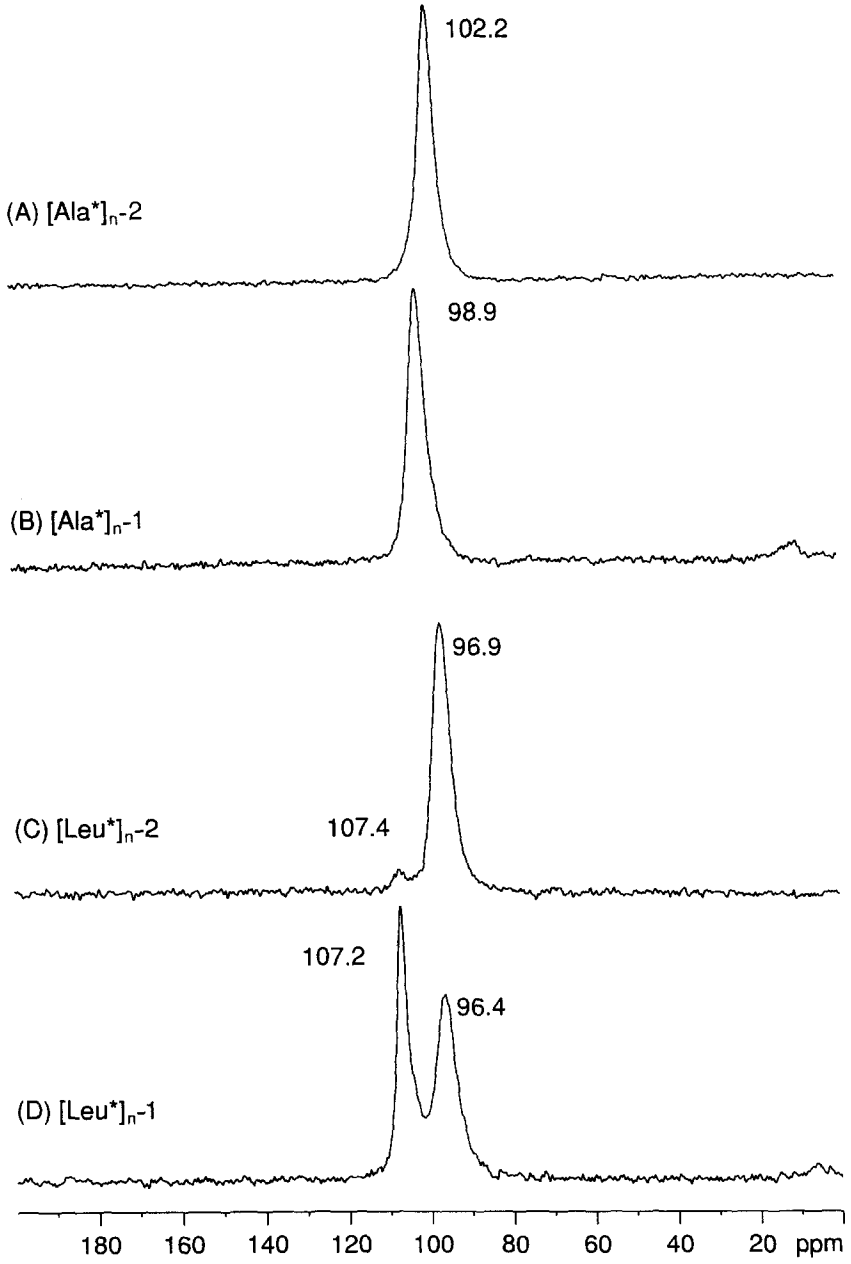

Fig. 39. 30.4 MHz ^{15}N CP-MAS NMR spectra of fully ^{15}N-labelled poly(L-alanines) and poly(L-leucines): (A) fully ^{15}N-labelled [Ala*]$_n$-2 (α-helix); (B) fully ^{15}N-labelled [Ala*]$_n$-1 (β-sheet); (C) fully ^{15}N-labelled [Leu*]$_n$-2 (α-helix); (D) fully ^{15}N-labelled [Leu*]$_n$-1 (β-sheet + α-helix).

Table 5. Synthetic conditions, conformational characteristics, and ^1H chemical shifts of homopolypeptides (from refs 16 and 45)

Sample[a]	A/I[b]	Conformation[c]	^1H chemical shift δ (ppm) $H^{\beta e}(+H^{\gamma e})$	$H^{\delta e}$	H^{α}	H^{Nf}
H-[Ala]$_5$-NHBu	—	β-sheet	1.2		5.0	8.4
[Ala]$_n$-5	65	α-helix	1.4		3.9	8.2
[Ala*]$_n$-1	4	β-sheet	1.2		5.2	8.6
[Ala*]$_n$-2	100	α-helix	1.4		4.0	8.0
[Leu]$_n$-1	5	β-sheet[d]	0.9	1.5	5.5	—
[Leu]$_n$-2	100	α-helix	0.8	1.7	4.0	8.2
[Leu*]$_n$-1	5	β-sheet (+α-helix)	0.9	1.6	5.4 (4.0)	9.1 (8.2)
[Leu*]$_n$-2	100	α-helix	0.8	1.6	4.0	8.1

[a] Abbreviations: Ala, L-alanine; Ala*, fully ^{15}N-labelled L-alanine; Leu, L-leucine; Leu*, fully ^{15}N-labelled L-leucine; NHBu, *n*-butyl amide; α-helix, right-handed α-helix; β-sheet, anti-parallel β-sheet.
[b] The molar ratio of the monomer (A) to the initiator (I), which corresponds to the theoretical number-averaged degree of polymerization.
[c] Conformations of these samples were determined by ^{13}C and ^{15}N CP-MAS NMR, IR and far-IR spectroscopic methods.
[d] Containing a small amount of α-helix.
[e] Side-chain protons (H^{β}, H^{γ}, and H^{δ}).
[f] Amide proton measured using the MREV-8 pulse sequence at 3.5 kHz MAS speed.

overlapping the peaks of the samples. Under these conditions, the resolution of adipic acid was maintained at the 3.5 kHz of the rotational frequency.

3.4.1. Observation of the amide ^1H signal of ^{15}N-labelled poly(L-alanines)

Figure 40 shows the ^1H CRAMPS NMR spectra of (A) [Ala]$_n$-5 (natural abundance of ^{15}N, α-helix form), (B) [Ala*]$_n$-2 (99 at.% purity of ^{15}N, α-helix), (C) H-[Ala]$_5$-NHBu (natural abundance of ^{15}N, β-sheet), and (D) [Ala*]$_n$-1 (99 at.% purity of ^{15}N, mainly β-sheet form containing a small amount of α-helix) in the solid state, using the BR-24 pulse sequence at 2.0 kHz MAS speed. The ^1H CRAMPS NMR spectra gave high-resolution proton signals in the three regions (NH, H^{α} and H^{β}) for poly(L-alanines). The conformational characterization of [Ala]$_n$-5, [Ala*]$_n$-2, H-[Ala]$_5$-NHBu and [Ala*]$_n$-1 has been confirmed by the H^{α} chemical shifts (α-helix: 3.9 ppm, β-sheet: 5.1 ppm), which are in good agreement with the results obtained from ^{13}C and ^{15}N CP-MAS NMR (Figs. 38 and 39), IR and far-IR spectra. Additional peaks around 3.2–3.5 ppm in spectra C and D, and small peaks at 5.7 ppm in spectra A and D are assignable to the proton peak of —N—CH_2— (*n*-butylamide group) and an artefact, respectively.

It is noteworthy that the line shape of the ^{15}NH proton signal of [Ala*]$_n$-2 (α-helix) and [Ala*]$_n$-1 (β-sheet), in which the quadrupolar effect is absent,

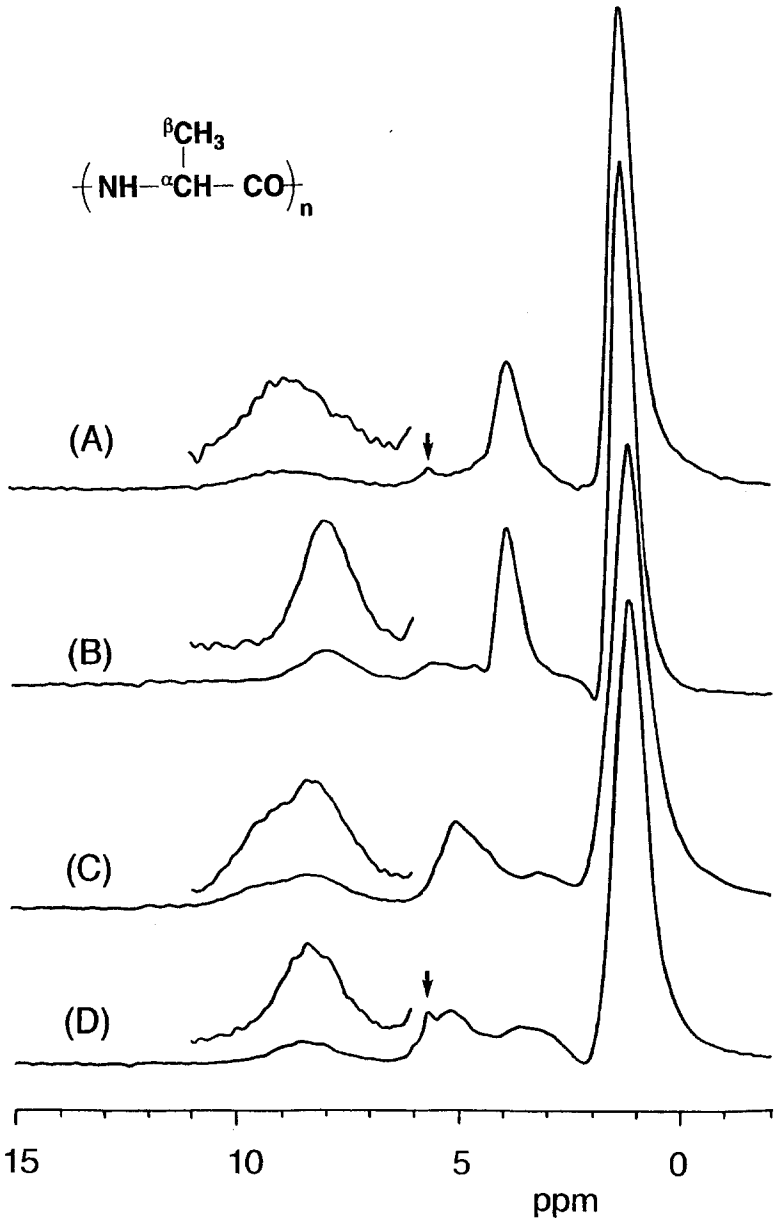

Fig. 40. 300 MHz ^{1}H CRAMPS NMR spectra of α-helical and β-sheet poly(L-alanines) using the BR-24 pulse sequence at 2.0 kHz MAS speed: (A) $[Ala]_n$-5 (DP_n = 65; α-helix); (B) $[Ala^*]_n$-2 (^{15}N, α-helix); (C) H-$[Ala]_5$-NHBu (β-sheet); (D) $[Ala^*]_n$-1 (^{15}N; β-sheet). Peak assignment: H^N, 8.0–8.9 ppm; H^α, 3.9–5.2 ppm, H^β, 1.2–1.4 ppm. Note: —N—CH_2— peak (3.2–3.5 ppm) of *n*-butylamide group, and artefact (↓ sign) (5.7 ppm) (from ref. 45). Reproduced with permission from the American Chemical Society.

exhibits a normal symmetric singlet pattern. In contrast, the line shape of the ^{14}NH proton signal of $[Ala]_n$-5 and H-$[Ala]_5$-NHBu exhibits a different kind of asymmetric doublet pattern, this being attributable to the quadrupolar effect. The ^{15}NH proton signal of the ^{15}N-labelled poly(L-alanine) ($[Ala^*]_n$-2, α-helix) is obviously sharp compared to the ^{14}NH proton signal of naturally abundant $[Ala]_n$-5. The half-width of the signal of $[Ala^*]_n$-2 (1.3 ppm) is smaller than that of the ^{14}NH proton signal of the natural abundant sample $[Ala]_n$-5 (2.3 ppm), as shown in Fig 40(A) and (B). Thus, it is apparent that the quadrupolar ^{14}N nuclei is responsible for the signal broadening, and that the asymmetric line shape of the ^{14}NH proton peak, aside from the ^{15}NH proton signal, is still broad relative to the H^{α} and H^{β} signals. The ^{1}H CRAMPS NMR spectra of α-helical ^{15}N-labelled poly(L-alanine), enabled the true ^{15}NH proton chemical shift ($\delta = 8.0$) to be determined, whereas the ^{14}NH proton chemical shift of $[Ala]_n$-5 could not be determined because of quadrupolar splitting. Thus, determination of the true ^{15}NH proton chemical shift of α-helical poly(L-alanine) can be achieved by substituting the quadrupolar ^{14}N with ^{15}N nuclei.

Next, we describe the use of the poly(L-alanine) adopting the β-sheet form to determine the NH proton chemical shift characteristic to β-sheet conformation and to check the effect of conformation on NH proton signal broadening and line shape. As shown in Fig. 40(C) and (D), the half-width of the NH proton signals of H-$[Ala]_5$-NHBu and $[Ala^*]_n$-1 was 2.4 and 1.5 ppm, respectively, which are similar to those of α-helical poly(L-alanines). The ^{14}NH line shape of H-$[Ala]_5$-NHBu exhibits a typical asymmetric doublet pattern, but which is quite different from that of the α-helical poly(L-alanine). The true ^{15}NH proton chemical shift could not be determined from the normal singlet pattern of $[Ala^*]_n$-1 because of the low S/N ratio.

Thus, it is concluded that (1) the quadrupolar ^{14}N nuclei are responsible for NH signal broadening and the asymmetric line shape; (2) the asymmetric line shape is different for α-helix and β-sheet conformations; and (3) the true ^{15}NH proton chemical shift of α-helical $[Ala^*]_n$-2 can be determined (8.0 ppm) but that of $[Ala^*]_n$-1 (β-sheet) is difficult to determine because of the low S/N ratio using BR-24 pulse sequences at 2.0 kHz MAS speed.

3.4.2. Observation of the amide ^{1}H signal of ^{15}N-labelled poly(L-leucines)

Figure 41 shows the ^{1}H CRAMPS NMR spectra of α-helical and β-sheet poly(L-leucines) using the BR-24 pulse sequence at 2.0 kHz MAS speed: (A) $[Leu]_n$-2 (natural abundance, α-helix), (B) $[Leu^*]_n$-2 (99 at.%^{15}N, α-helix), (C) $[Leu]_n$-1 (natural abundance, β-sheet) and (D) $[Leu^*]_n$-1 (99 at.%^{15}N, β-sheet) in the solid state. The ^{1}H NMR spectra show high-resolution signals (H^N, H^{α} and side-chain protons) of poly(L-leucines). The conformations of $[Leu]_n$-2 and $[Leu^*]_n$-2, and $[Leu]_n$-1 and $[Leu^*]_n$-1 are confirmed independently by the H^{α} chemical shift (α-helix; 4.0 ppm, β-sheet; 5.5 ppm). The peak around 4.0 ppm in Fig. 41(C) and (D) indicates that the samples take the α-helix component,

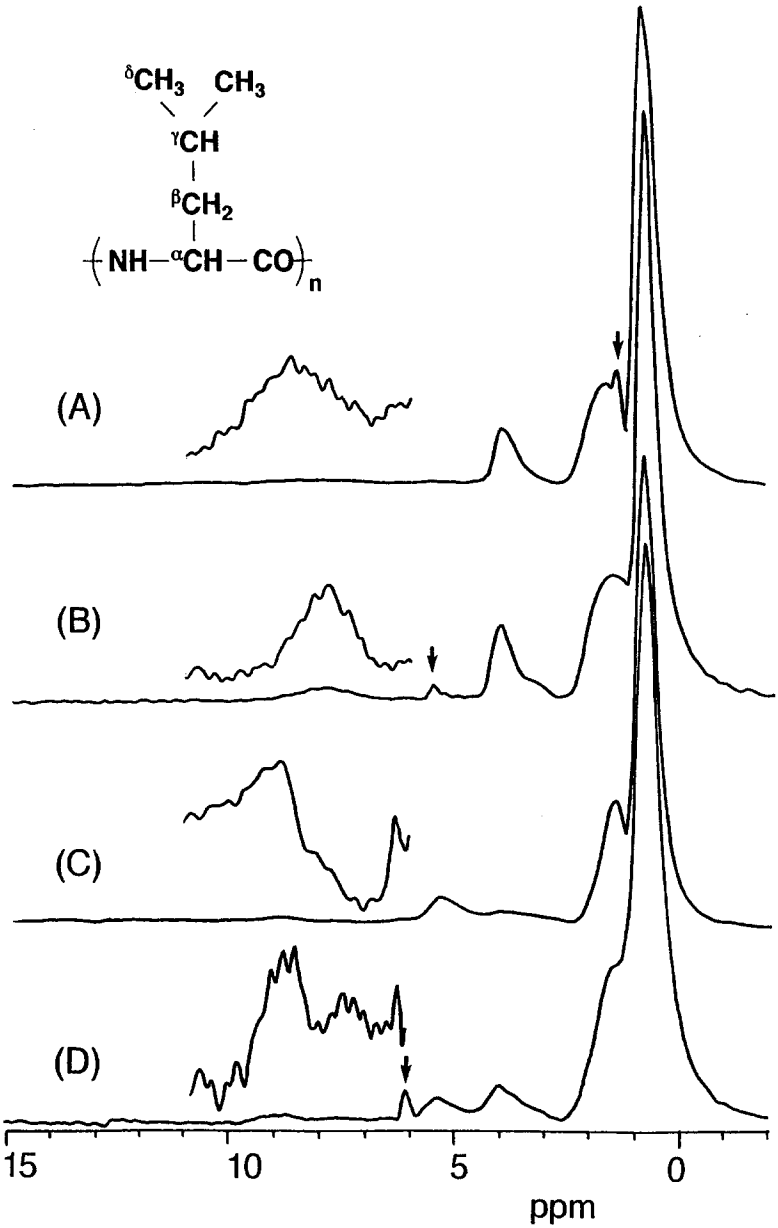

Fig. 41. 300 MHz ^{1}H CRAMPS NMR spectra of α-helical and β-sheet poly(L-leucines) using the BR-24 pulse sequence at 2.0 kHz MAS speed: (A) $[Leu]_n$-2 (α-helix); (B) $[Leu^*]_n$-2 (^{15}N, α-helix); (C) $[Leu]_n$-1 (β-sheet); (D) $[Leu^*]_n$-1 (^{15}N, β-sheet + α-helix). Peak assignment: H^N, 8.2–9.1 ppm; H^α, 4.0–5.5 ppm, H^β and H^γ, 1.5–1.7 ppm, H^δ, 0.8–0.9 ppm. Note: artefacts (↓) (which appeared at 1.3 ppm in (A), at 5.6 ppm in (B), and at 6.1 ppm in (D)) (from ref. 45). Reproduced with permission from the American Chemical Society.

which was confirmed by the IR and ^{13}C CP/MAS measurements. Also, the small peak around 1.3 ppm in (A), 5.6 ppm in (B), and 6.1 ppm in (D) is an artefact.

The ^{15}NH proton signal of $[Leu^*]_n$-2 (B), in which the quadrupolar effect is absent, became somewhat sharper compared to the ^{14}NH proton signal of the natural abundant $[Leu]_n$-2 (A). The half-widths of the NH signal of $[Leu]_n$-2 and $[Leu^*]_n$-2 are 1.8 and 1.3 ppm, respectively, which are nearly the same as those of poly(L-alanines). However, the relative intensity of the ^{15}NH proton signal of $[Leu^*]_n$-2 is much lower than that of $[Ala^*]_n$-2, which may be related to the ratio of the number of amide protons to the side-chain protons. The line shape of the ^{15}NH proton signal of $[Leu^*]_n$-2 exhibits an isotropic singlet pattern, whereas that of the ^{14}NH signal of $[Leu]_n$-2 is very broad and undetermined (maybe an asymmetric doublet), as shown in Fig. 41(A). Accordingly, the true ^{15}NH chemical shift of $[Leu^*]_n$-2 cannot be determined from this spectrum because of the extremely low S/N ratio, and neither can the ^{14}NH proton chemical shift of $[Leu]_n$-2.

Next, we describe the β-sheet poly(L-leucine). The half-widths of the NH proton signals of β-sheet poly(L-leucines) could not be determined. The two ^{15}NH proton signals of $[Leu^*]_n$-1 are assigned to the β-sheet and α-helix forms. It was impossible to determine the true ^{15}NH proton chemical shift due to the very poor signal resolution. Thus, it may be concluded that (1) the ^{14}N quadrupole effect clearly contributes to NH proton signal broadening and to the asymmetric line shape; and (2) the true ^{15}NH chemical shifts of poly(L-leucines) could not be determined because of the very low S/N ratio. The main cause of ^{15}NH proton signal broadening for the fully ^{15}N-labelled peptides is the $^{15}N-^{1}H$ dipolar interaction, which will be discussed in the next subsection.

3.4.3. The MAS speed dependence on amide ^{1}H signal broadening

If the $^{15}N-^{1}H$ heteronuclear dipole interaction is the main reason for ^{15}NH signal broadening, it should be possible to obtain a sharper NH proton signal by use of a faster MAS speed measurement.[44] To confirm whether the dipolar interaction is the major cause of signal broadening or not, the ^{1}H CRAMPS NMR of fully ^{15}N-labelled polypeptides have been measured at increased MAS speed. The frequency of the best spectral condition empirically obtained for the BR-24 pulse sequence (MAS frequency of 1.5–2.0 kHz) is too slow to obtain the required resolution and a sharper NH signal. So, a different pulse sequence is needed to allow the MAS frequency to be raised to more than 2.0 kHz, because the two averaging techniques (MAS and multi-pulse averaging) interfere with each other and lead to a degradation in resolution.[93] We have measured the ^{1}H CRAMPS NMR spectra of fully ^{15}N-labelled polypeptides using the MREV-8 pulse sequence at the higher MAS speed of 3.5 kHz, which gave the best spectral resolution with this system. It is known that ^{1}H

CRAMPS spectra above 4.0 kHz give poorer resolution than those at 3.5 kHz with the MREV-8 pulse sequence.

Figure 42 shows the ^{1}H CRAMPS NMR spectra of ^{15}N-labelled poly(L-alanines) in the α-helical form: (A) BR-24 pulse sequence at 2.0 kHz MAS speed, (B) MREV-8 pulse sequence at 3.5 kHz MAS speed in the solid state. The intensity of the NH proton signal of poly(L-alanine) was increased when measuring with the MREV-8 pulse sequence at a faster MAS speed (3.5 kHz).

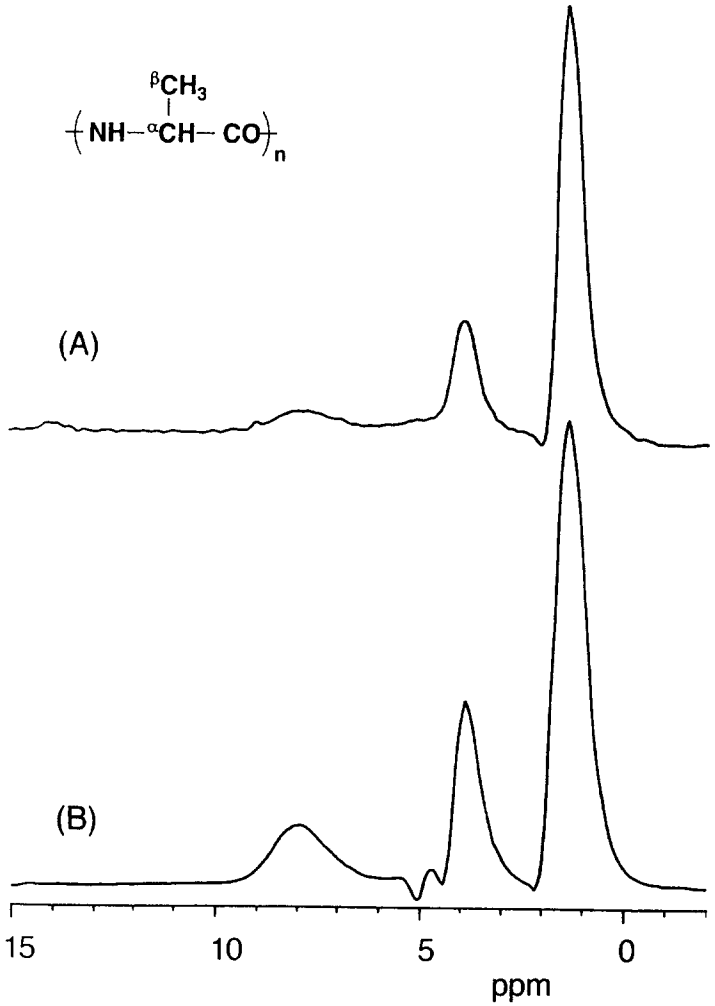

Fig. 42. 300 MHz ^{1}H CRAMPS NMR spectra of ^{15}N-labelled poly(L-alanines) in the α-helical form: (A) the BR-24 pulse sequence at 2.0 kHz MAS speed, and (B) the MREV-8 pulse sequence at 3.5 kHz MAS speed.

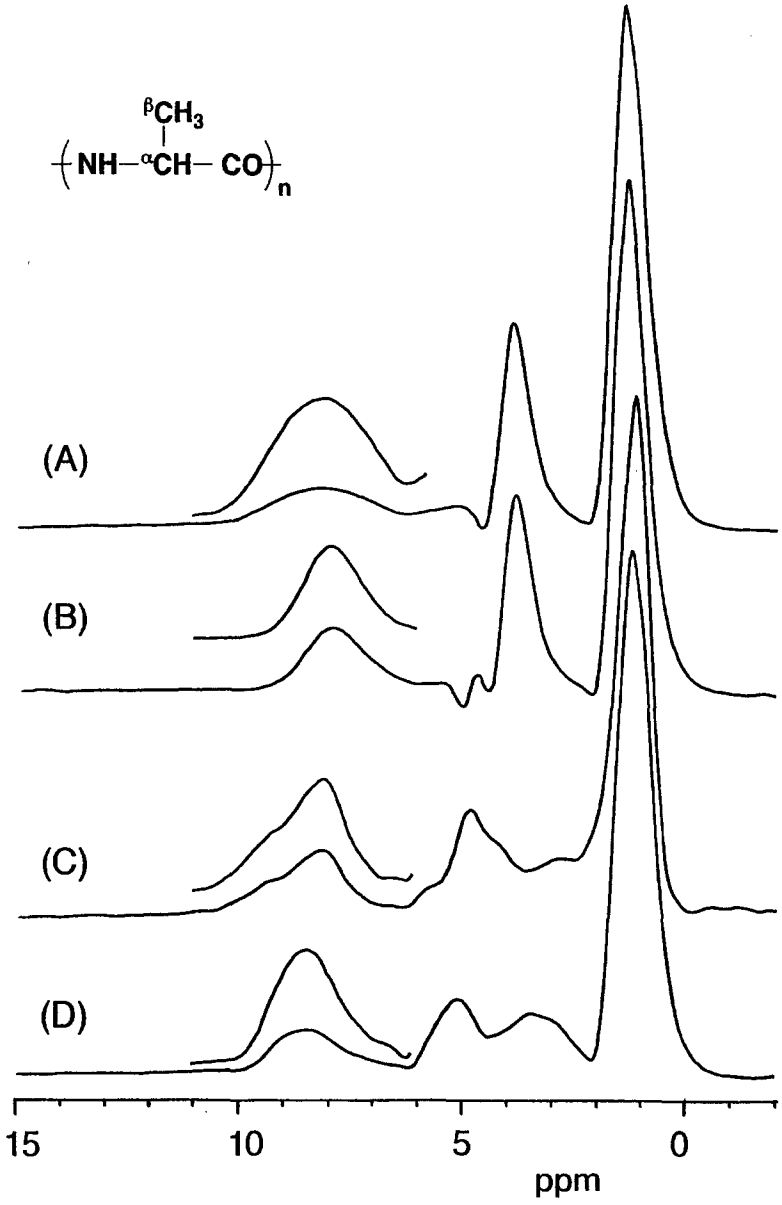

Fig. 43. 300 MHz ^{1}H CRAMPS NMR spectra of α-helical and β-sheet poly(L-alanines) using the MREV-8 pulse sequence at 3.5 kHz MAS speed: (A) $[Ala]_n$-5 (α-helix); (B) $[Ala^*]_n$-2 (^{15}N, α-helix); (C) H-$[Ala]_5$-NHBu (β-sheet); (D) $[Ala^*]_n$-1 (^{15}N, β-sheet). Peak assignment: H^N, 8.6 ppm (β-sheet) and 8.0 ppm (α-helix); H^α, 5.0–5.2 ppm (β-sheet) and 3.9–4.2 ppm (α-helix), H^β, 1.2 ppm (β-sheet) and 1.4 ppm (α-helix). Note that the additional peaks around 4.0–5.0 ppm in spectra (A) and (B) were assigned to carrier noise signal (from ref. 45). Reproduced with permission from the American Chemical Society.

Figure 43 shows the ^{1}H CRAMPS spectra of poly(L-alanines) using the MREV-8 pulse sequence at 3.5 kHz MAS speed: (A) $[Ala]_n$-5 (natural abundance of ^{15}N, α-helix form), (B) $[Ala^*]_n$-2 (99 at.% purity of ^{15}N, α-helix), (C) H-$[Ala]_5$-NHBu (natural abundance of ^{15}N, β-sheet), and (D) $[Ala^*]_n$-1 (99 at.% purity of ^{15}N, β-sheet) in the solid state. The additional peaks around 4.0–5.0 ppm in spectra (A) and (B) are assigned to carrier noise.

From the ^{1}H CRAMPS NMR spectra, therefore, it was possible to determine the ^{15}NH proton chemical shift value for $[Ala^*]_n$-2 (α-helix; $\delta = 8.0$) which is identical with that determined using BR-24 (2.0 kHz). Further, it was possible to determine the ^{14}NH proton chemical shift for $[Ala^*]_n$-1 (β-sheet, $\delta = 8.6$) using the MREV-8 pulse sequence at 3.5 kHz. However, unfortunately, the ^{14}NH proton chemical shift values for $[Ala]_n$-2 and $[Ala]_n$-1 could not be determined because the line shapes of the ^{14}NH signals exhibit an asymmetric doublet pattern in this system also. Thus, it is found that determination of the true NH chemical shift of poly(L-alanines) can be achieved to measure fully ^{15}N-labelled samples at higher MAS speed (3.5 kHz) and that these chemical shifts depend on conformation (α-helix: $\delta = 8.0$; β-sheet: $\delta = 8.6$). This is the first determination of the true NH proton chemical shifts of poly(L-alanines) by ^{1}H CRAMPS NMR.

Figure 44 shows the ^{1}H CRAMPS spectra of poly(L-leucines) using the MREV-8 pulse sequence at 3.5 kHz MAS speed: (A) $[Leu]_n$-2 (natural abundance, α-helix), (B) $[Leu^*]_n$-2 (99 at.%^{15}N, α-helix), (C) $[Leu^*]_n$-1 (99 at.%^{15}N, β-sheet + α-helix) in the solid state. The additional peaks around 4.0–5.0 ppm in spectra (A) and (B) are assigned to carrier noise.

The intensity of the NH proton signals of poly(L-leucines) was increased by measuring with a MREV-8 pulse sequence at the higher MAS frequency (3.5 kHz). From ^{1}H CRAMPS spectra, therefore, it is possible to determine the ^{15}NH proton chemical shift values for $[Leu^*]_n$-2 (α-helix, $\delta = 8.1$) and for $[Leu^*]_n$-1 (β-sheet, $\delta = 9.1$; α-helix, $\delta = 8.2$). However, it was impossible to determine the ^{14}NH proton chemical shift values for $[Leu]_n$-2 from this measurement. Thus, it was found that the true NH proton chemical shift of poly(L-leucines) can be the determined by using fully ^{15}N-labelled samples at the higher MAS frequency (3.5 kHz), and that the chemical shift depends on conformation (α-helix, $\delta = 8.1$–8.2; β-sheet, $\delta = 9.1$).

Therefore, it was proved that a ^{1}H CRAMPS method which combines higher MAS speed (3.5 kHz) with MREV-8 pulse spectroscopy is a very useful tool for the determination of ^{15}NH proton chemical shifts in solid polypeptides.

3.4.4. Correlation between the amide ^{1}H chemical shift and main-chain conformation

The NH proton chemical shifts of some polypeptides were successfully determined using fully ^{15}N-labelled samples at a higher MAS frequency with a MREV-8 pulse sequence. The NH proton chemical shifts determined with the

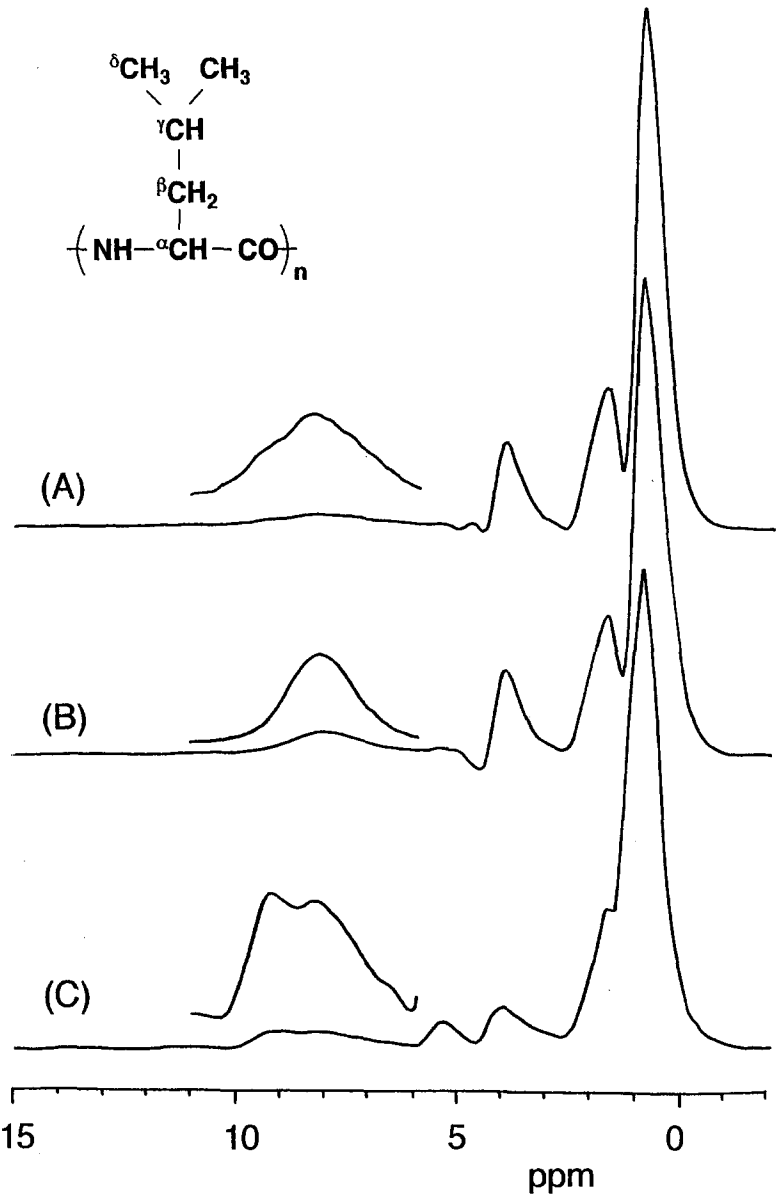

Fig. 44. 300 MHz ^{1}H CRAMPS NMR spectra of α-helical and β-sheet poly(L-leucines) using the MREV-8 pulse sequence at 3.5 kHz MAS speed: (A) $[Leu]_n$-2 (α-helix); (B) $[Leu^*]_n$-2 (^{15}N, α-helix); (C) $[Leu^*]_n$-1 (^{15}N, β-sheet + α-helix). Peak assignment: H^N, 9.1 ppm (β-sheet) and 8.1–8.2 ppm (α-helix); H^α, 5.4 ppm (β-sheet) and 4.0 ppm (α-helix), H^β and H^γ, 1.5–1.7 ppm, H^δ, 0.8–0.9 ppm. The additional peaks around 4.0–5.0 ppm in spectra (A) and (B) were assigned to carrier noise signal (from ref. 45). Reproduced with permission from the American Chemical Society.

fully ^{15}N-labelled homopolypeptides are summarized in Table 5. It is found that the true ^{15}NH proton chemical shifts of the fully ^{15}N-labelled polypeptides are conformation-dependent: [Ala*]$_n$-2 (α-helix, 8.0 ppm); [Leu*]$_n$-2 (α-helix, 8.1 ppm); [Ala*]$_n$-1 (β-sheet, 8.6 ppm); and [Leu*]$_n$-1 (β-sheet, 9.1 ppm; α-helix, 8.2 ppm). Accordingly, the ^{15}NH proton chemical shifts of poly(L-alanines) and poly(L-leucines) adopting the α-helix form appear to low frequency by 0.6–1.0 ppm compared with those of the β-sheet, and it is now possible to distinguish the α-helix and β-sheet conformations readily from their ^{15}NH proton chemical shifts. The NH proton chemical shift differences between the α-helix and β-sheet forms seem to be related to the hydrogen bond lengths as well as their conformations. According to X-ray diffraction studies of poly(L-alanines) by Arnott *et al.*,[94,95] the distance between the nitrogen and oxygen atoms is 2.83 and 2.87 Å for the β-sheet and α-helix forms, respectively. Accordingly, the ^{15}NH proton chemical shifts of [Ala*]$_n$-1 (β-sheet: hydrogen bond distance 2.83 Å) appears to high frequency by comparison with that of [Ala*]$_n$-2 (α-helix: hydrogen bond distance 2.87 Å), which is qualitatively acceptable.

Next, it is interesting to compare the ^{1}H chemical shift results of polypeptides in the solid state with those in solution, attention being given to the dependence of the amide proton chemical shifts on conformation.[83–85] The following results are obtained: (1) the amide proton chemical shifts of the α-helical polypeptides in the solid state (8.0–8.2 ppm from TMS) are identical with those in solution (7.96–8.04 ppm from DSS); and (2) the amide proton chemical shifts of the β-sheet polypeptides in the solid state (8.6–9.1 ppm from TMS) are, in contrast 0.1–0.6 ppm to high frequency from those in solution (8.44–8.52 ppm from DSS). These chemical shift displacements of the ^{15}NH protons are very similar to those of the H$^\alpha$ protons for poly(L-alanines) and poly(L-leucines) as follows: (1) the H$^\alpha$ chemical shifts of α-helical polypeptides in the solid state (3.9–4.0 ppm from TMS) are identical with those in solution (3.94–3.95 ppm from DSS); and (2) the H$^\alpha$ chemical shifts of β-sheet polypeptides in the solid state (5.1–5.5 ppm from TMS) are 0.4–0.8 ppm to high frequency from those in solution (4.70–4.71 ppm from DSS). These results are quite interesting findings and the main reason for the chemical shift difference between solid state and solution can be explained by a solvent effect in the solution.

In conclusion, it is certified that the ^{15}NH proton chemical shift is a useful index for conformational analysis and to distinguish the hydrogen bond characteristics of polypeptides in the solid state.

3.5. Determination of N—H bond length from the dipolar spinning sideband pattern of the amide ^{1}H signals[96]

An accurate determination of the N—H covalent bond length is important for elucidating polypeptide conformations because the N—H bond length directly

mirrors the >N—H · · · O=C< hydrogen bond strength, and is responsible for the long-range order in the system. ^{1}H CRAMPS has great potential for this purpose, and it is necessary to examine whether it is effective.

In a previous section, we showed the relationship between the ^{1}H chemical shifts of the NH proton and the conformation of some solid polypeptides using ^{1}H CRAMPS NMR.[45] In that study, a problem which had to be solved was that the NH proton signal of natural abundant polypeptide is very broad and exhibits asymmetric doublet patterns due to the residual heteronuclear dipolar coupling between the quadrupolar ^{14}N nucleus and the amide proton.[16,44,45] In the ^{1}H CRAMPS experiment on ^{15}N-labelled poly(L-alanines) at 2.0 kHz MAS speed, the $^{15}N-^{1}H$ dipolar sideband patterns of the NH proton signal can be observed. The magnitude of the $^{15}N-^{1}H$ heteronuclear dipolar coupling is proportional to the inverse cube of the distance between the ^{15}N and ^{1}H nuclei.[97] The $^{15}N-^{1}H$ bond length can be measured by observing the dipolar linewidth, which is simulated by the $^{15}N-^{1}H$ dipolar spinning sidebands. The $^{15}N-^{1}H$ dipolar interaction has been measured utilizing ^{15}N SLF (Separated Local Field) spectroscopy,[97–99] in which the $^{15}N-^{1}H$ dipolar interaction can be separated from the ^{15}N chemical shift anisotropy by using a two-dimensional (2D) NMR technique. The $^{15}N-^{1}H$ dipolar interaction can also be estimated directly from the ^{1}H CRAMPS NMR, because the ^{1}H chemical shift anisotropy is averaged to zero during the ^{1}H CRAMPS measurement. It is noteworthy that the N—H bond length of poly(L-alanine) is almost indeterminate by X-ray diffraction. It is also difficult to determine the N—H bond length using neutron diffraction, because this method needs the deuterium-labelled poly(L-alanine) to be in single crystal state.

In this section, we introduce a new methodology to determine the $^{15}N-^{1}H$ bond lengths of fully ^{15}N-labelled poly(L-alanines) adopting the α-helix and β-sheet forms from the $^{15}N-^{1}H$ dipolar sideband patterns observed in the ^{1}H NMR spectra. To observe the full spectral width of the dipolar sideband patterns, quadrature-phase (QD) detection measurements were performed.[47]

The samples used here are fully ^{15}N-labelled poly(L-alanines) (99 at.% of ^{15}N purity; MASSTRACE, Inc.), which is shown in the previous section.

The solid-state ^{1}H CRAMPS NMR measurements were performed on a Chemagnetics CMX 300 spectrometer equipped with a CRAMPS probe with 5 mm rotor. Quadrature-phase detection was carried out according to the phase-cycling technique proposed by Burum *et al.*[47] Here, we used the MREV-8 pulse sequence for homonuclear decoupling. The experimental conditions are the same as those described in the previous section.

A spectral simulation was performed on an NEC 9801 personal computer equipped with a transputer (INMOS, UK) using the SLFDIP program, which is written in FORTRAN 77 language based on the theory described by Naito *et al.*[99]

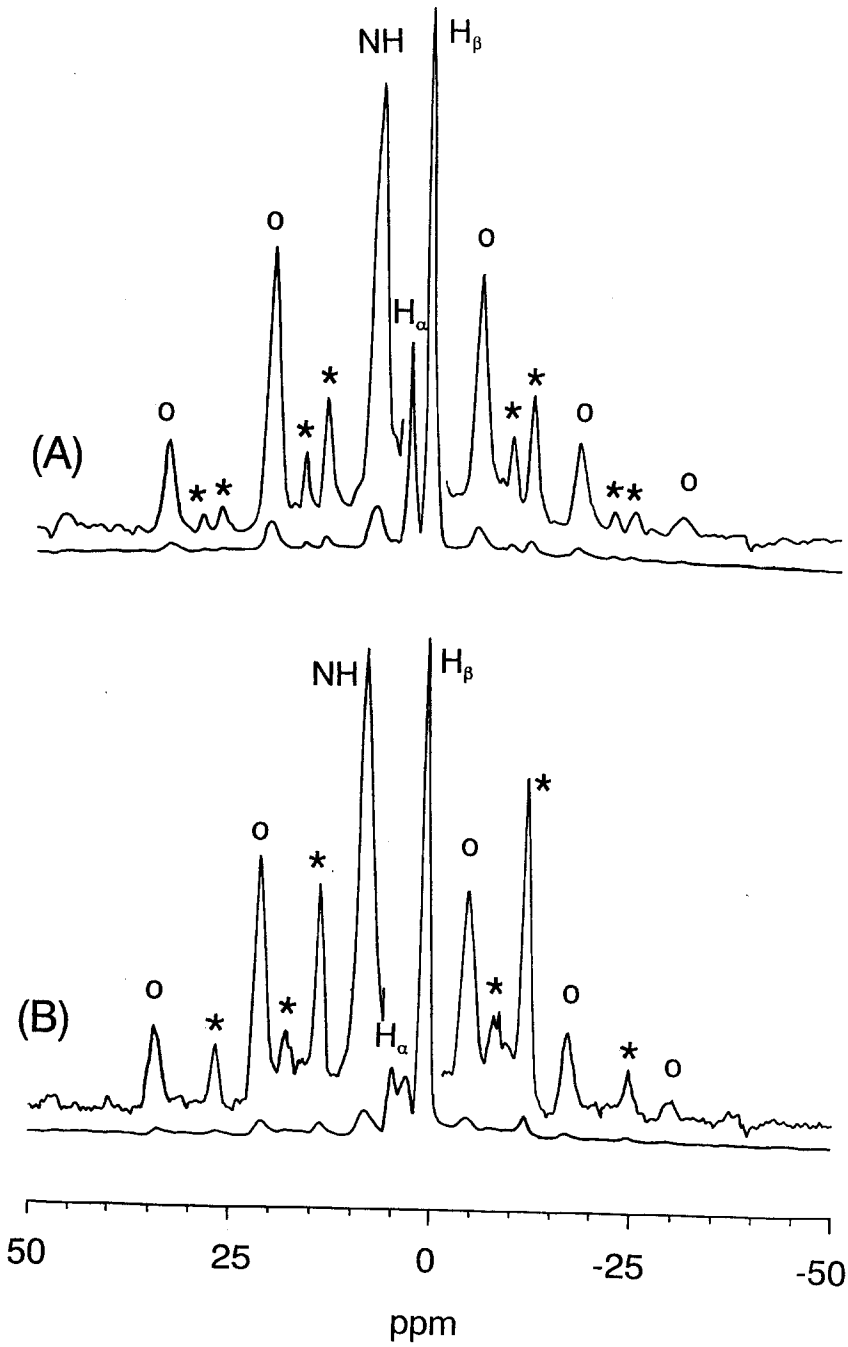

Fig. 45. 300 MHz ^{1}H CRAMPS NMR spectra of fully ^{15}N-labelled poly(L-alanines) taking (A) α-helix and (B) β-sheet conformations in the solid state. Peak assignment: H^N, 10–8 ppm; H^α, 3.9–5.0; H^β, 1.4–1.2 ppm. Note: —N—CH_2— peak (3.2–3.5 ppm) of *n*-butylamide group in spectrum (B). The sign (O) indicates the spinning sidebands (SSB) of H^N signal, and the sign (*) indicates SSB of H^α and H^β signals (from ref. 96). Reproduced with permission from the American Chemical Society.

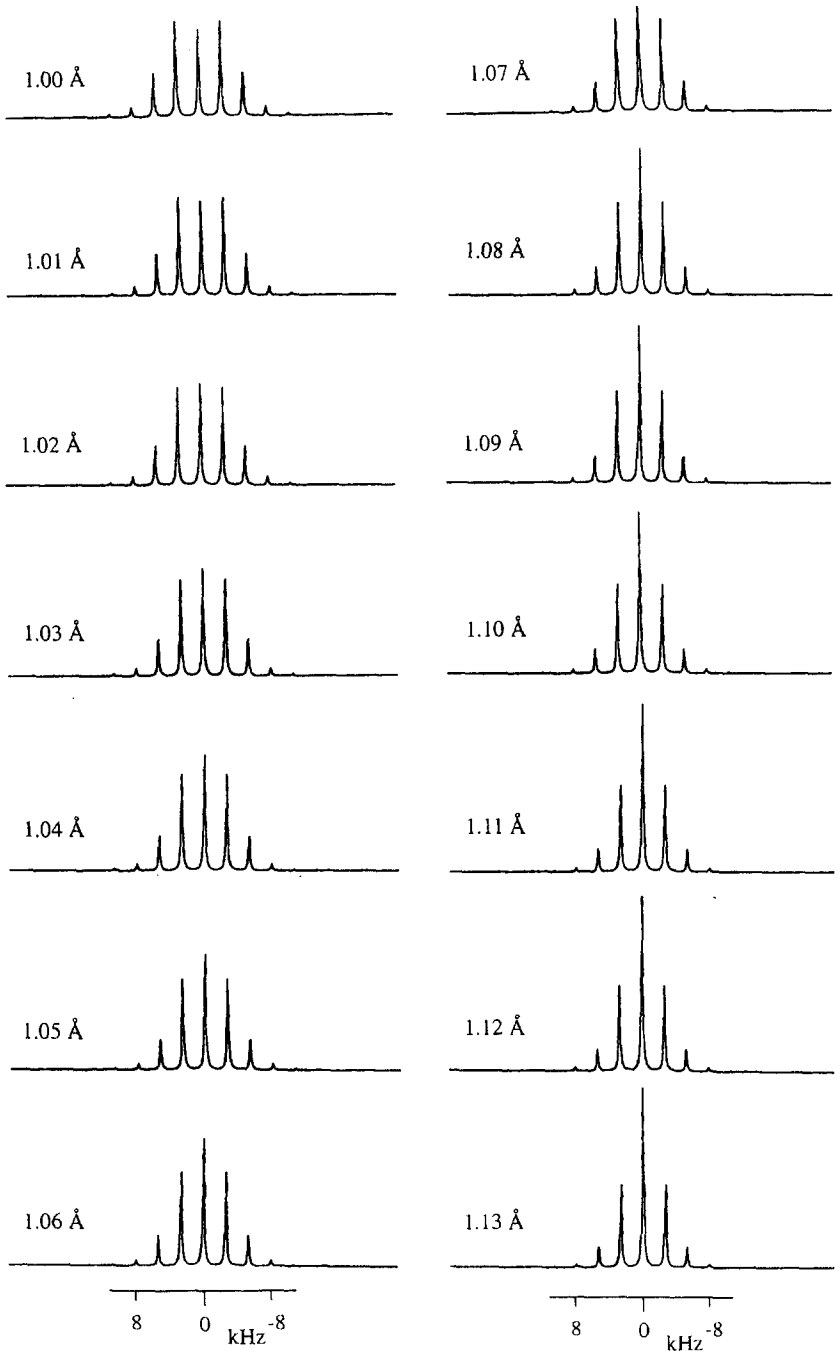

Fig. 46. Simulated spectra of ^{1}H CRAMPS NMR for the ^{1}H dipolar sideband patterns in a series of different N—H bond lengths (scaling factor; 0.53, spinning frequency; 2 kHz, and linewidth; 160 Hz) (from ref. 96). Reproduced with permission from the American Chemical Society.

3.5.1. Determination of N—H bond length

Figure 45 shows the ^{1}H CRAMPS NMR spectra of fully ^{15}N-labelled poly(L-alanines) for (A) α-helix and (B) β-sheet forms in the solid state. The spinning sidebands (SSBs) of the H^{α} proton and H^{β} proton signals of poly(L-alanines) are indicated by asterisks (*), and those of the amide proton (H^N) signal by open circles (O). The SSBs of the H^{α} and H^{β} signals fell off rapidly compared to those of the amide protons, whereas those of the H^N signal gradually decreased due to the large ^{15}N–^{1}H heteronuclear dipolar interaction. It was confirmed that the integral intensities of the SSBs at the left side of the centre (isotropic) signal are almost the same as the corresponding one at the right side, whereas their peak heights are different. The N—H dipolar SSB pattern of

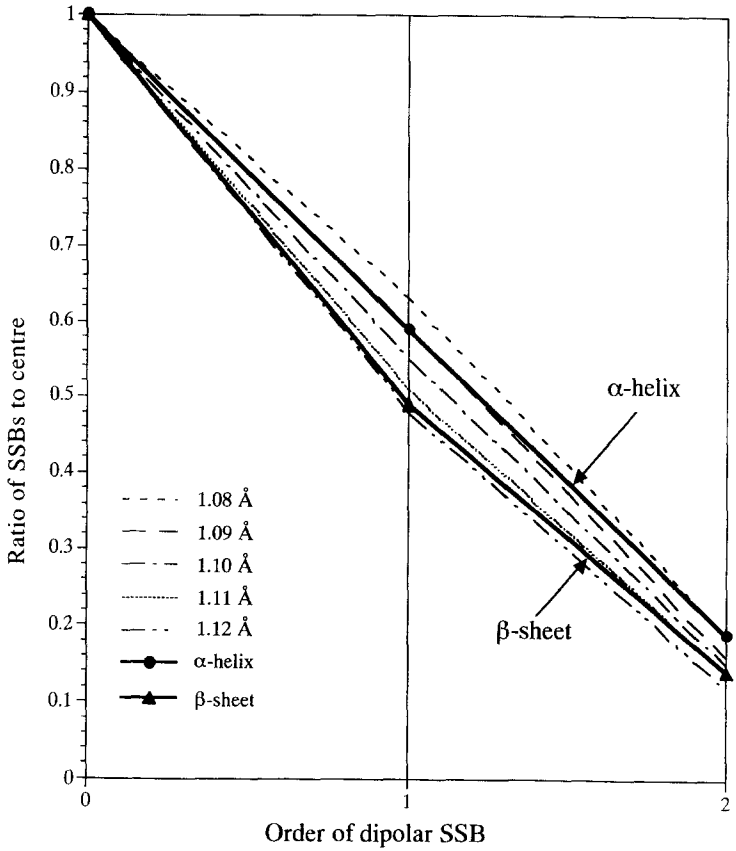

Fig. 47. Plots of the intensity ratio of the first and second-order sideband intensities to the centre signal of the simulated and experimentally obtained ^{15}N–^{1}H dipolar spectra of poly(L-alanines) vs. the order of the sidebands. The experimental results are indicated by the heavy lines (from ref. 96). Reproduced with permission from the American Chemical Society.

α-helical poly(L-alanine) is different from that of β-sheet poly(L-alanine), as can be seen from Fig. 45.

Figure 46 shows the simulated spectra for a series of different N—H bond lengths at a rotor frequency of 2.0 kHz. The sideband pattern is sensitive to the N—H bond length. The relative intensity of SSBs to the centre peak decreases with longer N—H distance. It is therefore possible to determine the N—H bond length within an accuracy of 0.01 Å by careful comparison of the integral ratio of the centre peak to the sideband intensities of the dipolar spectrum obtained experimentally with that of the simulated spectra.

Figure 47 shows plots of the intensity ratio of the first and second sideband peak to the centre peak of the simulated and experimentally obtained $^{15}N-^{1}H$ dipolar spectra vs. the order of the sidebands. Thus, it is successfully determined that the true N—H bond lengths for the poly(L-alanines) were 1.09 and 1.12 Å for the α-helix and β-sheet conformations, respectively, with an accuracy of 0.01 Å. Therefore the N—H distance in the β-sheet was 0.03 Å longer than in the α-helix. This result means that the (>N—)H···O(=C<) hydrogen bond strength (distance) of the β-sheet poly(L-alanine) must be stronger (shorter) than that of the α-helix one.

The above N—H bond length difference between the α-helix and β-sheet forms seems to be related to the hydrogen bond strengths and amide proton chemical shifts. From the X-ray diffraction studies of poly(L-alanines) by

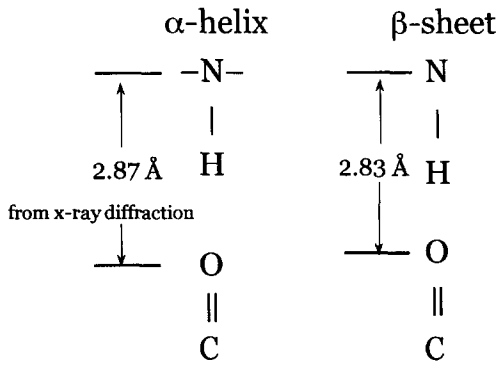

hydrogen bond	weaker	stronger
^{1}H chemical shift	8.0 ppm	8.6 ppm

N–H distance	1.09 Å	1.12 Å

Fig. 48. Schematic diagram of the hydrogen bond characteristic, the N—H bond length, and the amide ^{1}H chemical shifts experimentally determined for α-helical and β-sheet poly(L-alanines).

Arnott *et al.*,[94,95] it is known that the distance between the nitrogen and oxygen atoms is 2.87 and 2.83 Å for the α-helix and β-sheet forms, respectively. Therefore, the N—H distance in the β-sheet is 0.03 Å longer than that in the α-helix for poly(L-alanines), which is of significance. This is consistent with the hydrogen bond distances between nitrogen and oxygen atoms determined from X-ray diffraction and with the ^{1}H chemical shifts of amide proton signals found using the ^{1}H CRAMPS method, which are summarized in Fig. 48.

On the other hand, the amide ^{1}H chemical shift value in the α-helix is 0.6 ppm to high frequency from that of the β-sheet (α-helix, δ = 8.0 ppm; β-sheet, δ = 8.6 ppm).[45] The above ^{1}H chemical shift displacement is consistent with that of the ^{15}N chemical shift data in poly(L-alanines).[56–59] These results suggest that the hydrogen bond strength in the β-sheet is stronger than that in the α-helix for poly(L-alanines). This is consistent with the hydrogen bond distances between the nitrogen and oxygen atoms determined from X-ray diffraction and with the ^{1}H chemical shifts of amide proton signals found using the ^{1}H CRAMPS method. Accordingly, it is reasonable to conclude that the amide proton of the β-sheet poly(L-alanine) is more strongly attracted to the oxygen than the proton of α-helical poly(L-alanine).

ACKNOWLEDGEMENTS

The authors thank Professor B. C. Gerstein for a critical reading of, and suggestions for this chapter. The authors also thank Professor G. A. Webb, the editor of this book.

REFERENCES

1. E. M. Purcell, H. C. Torrey and R. V. Pound, *Phys. Rev.*, 1946, **69**, 37–38.
2. F. Bloch, W. W. Hansen and M. E. Packard, *Phys. Rev.*, 1946, **69**, 127.
3. J. T. Arnold, S. S. Dharmatti and M. E. Packard, *J. Chem. Phys.*, 1951, **19**, 507.
4. E. D. Becker, C. L. Fisk and C. L. Khetrapal, in *Encyclopedia of Nuclear Magnetic Resonance*, D. M. Grant and R. K. Harris (eds), John Wiley & Sons, Chichester 1996, Vol. 1, pp. 1–158.
5. F. Engelke, in *Encyclopedia of Nuclear Magnetic Resonance*, D. M. Grant and R. K. Harris, (eds), John Wiley & Sons; Chichester 1996, Vol. 3, pp. 1529–1535.
6. E. R. Andrew, A. Bradbury and R. G. Eades, *Nature*, 1959, **183**, 1802–1803.
7. A. Samoson and T. Anupold, in *Proceeding of the 15th European Experimental NMR Conference*, University of Leipzig, 2000; p. 5.
8. J. S. Waugh, L. M. Huber and U. Haeberlen, *Phys. Rev. Lett.*, 1968, **20**, 180–182.
9. K. Schmidt-Rohr and H. W. Spiess, in *Multidimensional Solid-State NMR and Polymers*, Academic Press, San Diego, CA, 1994; pp. 70–134.
10. W. K. Rhim, D. D. Elleman and R. W. Vaughan, *J. Chem. Phys.*, 1973, **59**, 3740–3749.
11. D. P. Burum and W. K. Rhim, *J. Chem. Phys.*, 1979, **71**, 944–956.
12. B. C. Gerstein, in *Encyclopedia of Nuclear Magnetic Resonance*, D. M. Grant and R. K. Harris (eds), John Wiley & Sons, Chichester, 1996, Vol. 3, pp. 1501–1509.
13. B. C. Gerstein, R. G. Pembleton, R. C. Wilson and L. M. Ryan, *J. Chem. Phys.*, 1977, **66**, 361–362.

14. R. G. Pembleton, L. M. Ryan and B. C. Gerstein, *Rev. Sci. Instrum.*, 1977, **48**, 1286–1289.
15. B. C. Gerstein and C. R. Dybowski, in *Transient Techniques in NMR of Solids*, Academic Press, London, 1985, pp. 94–95.
16. A. Shoji, H. Kimura, T. Ozaki, H. Sugisawa and K. Deguchi, *J. Am. Chem. Soc.*, 1996, **118**, 7604–7607.
17. D. P. Burum and A. Bielecki, *J. Magn. Reson.*, 1991, **94**, 645–652.
18. K. Saalwaechter, R. Graf and H. W. Spiess, *J. Magn. Reson.*, 1999, **140**, 471–476.
19. C. E. Bronnimann, B. L. Hawkins, M. Zhang and G. E. Maciel, *Anal. Chem.*, 1988, **60**, 1743–1750.
20. G. E. Maciel, C. E. Bronnimann and B. L. Hawkins, in *Advances in Magnetic Resonance*, Academic Press, New York, 1990, Vol. 14, pp. 125–150.
21. D. P. Burum, D. G. Cory, K. K. Gleason, D. Levy and A. Bielecki, *J. Magn. Reson.*, 1993, **A104**, 347–352.
22. K. Yamauchi, S. Kuroki, K. Fujii and I. Ando, *Chem. Phys. Lett.*, 2000, **324**, 435–439.
23. E. Vinogradov, P. K. Madhu and S. Vega, in *Proceeding of the 15th European Experimental NMR Conference*, University of Leipzig, 2000, p. 9.
24. H. Sugisawa, personal communication (unpublished data).
25. H. Kimura, K. Nakamura, A. Eguchi, H. Sugisawa, K. Deguchi, K. Ebisawa, E. Suzuki and A. Shoji, *J. Mol. Struct.*, 1998, **447**, 247–255.
26. G. V. Garskaya, in *The Molecular Structure of Amino Acids*, Consultants Bureau, New York, 1968.
27. N. Nagashima, *J. Cryst. Soc. Jpn.*, 1993, **35**, 381–391.
28. G. Albrecht and R. B. Corey, *J. Am. Chem. Soc.*, 1939, **61**, 1087–1103.
29. R. Marsh, *Acta Cryst.*, 1958, **11**, 654–663.
30. Y. Iitaka, *Acta Cryst.*, 1961, **14**, 1–10.
31. J. J. Madden, E. L. McGandy and N. C. Seeman, *Acta Cryst.*, 1972, **B28**, 2377–2382.
32. J. J. Madden, E. L. McGandy and N. C. Seeman, *Acta Cryst.*, 1972, **B28**, 2382–2389.
33. Y. Iitaka, *Nature*, 1959, **183**, 390–391.
34. Z. Gu, K. Ebisawa and A. McDermott, *Solid State NMR*, 1996, **7**, 161–172.
35. A. McDermott and C. F. Ridenour, in *Encyclopedia of Nuclear Magnetic Resonance*, D. M. Grant and R. K. Harris (eds), John Wiley & Sons, Chichester, 1996, Vol. 6, pp. 3820–3825.
36. R. K. Harris, P. Jackson, L. H. Merwin, B. J. Say and G. Haegele, *J. Chem. Soc., Faraday Trans.*, **1**, 1988 **84**, 3649–3672.
37. G. A. Jeffrey and Y. Yeon, *Acta Cryst.*, 1986, **B42**, 410–413.
38. B. Berglund and R. W. Vaughan, *J. Chem. Phys.*, 1980, 73, 2037–2043.
39. S. Ando, I. Ando, A. Shoji and T. Ozaki, *J. Am. Chem. Soc.*, 1988, **110**, 3380–3386.
40. N. Asakawa, S. Kuroki, H. Kurosu, I. Ando, A. Shoji and T. Ozaki, *J. Am. Chem. Soc.*, 1992, **114**, 3261–3265.
41. D. P. Burum and W. K. Rhim, *J. Chem. Phys.*, 1979, **71**, 944–956.
42. M. Tsuboi, T. Onishi, I. Nakagawa, T. Shimanouchi and S. Mizushima, *Spectrochim. Acta.*, 1958, **12**, 253–261.
43. S. Hayashi and K. Hayamizu, *Bull. Chem. Soc. Jpn.*, 1991, **64**, 685–687.
44. A. Naito, A. Root and C. A. McDowell, *J. Phys. Chem.*, 1991, **95**, 3578–3581.
45. H. Kimura, T. Ozaki, H. Sugisawa, K. Deguchi and A. Shoji, *Macromolecules*, 1998, **31**, 7398–7403.
46. S. Hayashi and K. Hayamizu, *Bull. Chem. Soc. Jpn.*, 1991, **64**, 688–690.
47. D. P. Burum, D. G. Cory, K. K. Gleason, D. Levy and A. Bielecki, *J. Magn. Reson.*, 1993, **A104**, 347–352.
48. M. Kitamura, *J. Soc. Pow. Tech. Jpn.*, 1992, **29**, 118–123.
49. T. Taki, S. Yamashita, M. Satoh, A. Shibata, T. Yamashita, R. Tabeta and H. Saito, *Chem. Lett.*, 1981, 1803–1806.
50. D. Mueller and H. R. Kricheldorf, *Polym. Bull.*, 1981, **6**, 101–108.

51. H. Saito, R. Tabeta, A. Shoji, T. Ozaki and I. Ando, *Macromolecules*, 1983, **16**, 1050–1057.
52. H. R. Kricheldorf and D. Mueller, *Macromolecules*, 1983, **16**, 615–623.
53. A. Shoji, T. Ozaki, H. Saito, R. Tabeta and I. Ando, *Macromolecules*, 1984, **17**, 1472–1479.
54. H. Saito and I. Ando, in *Annual Reports on NMR Spectroscopy*, G. A. Webb (ed.), Academic Press, London, 1989, **22**, pp. 209–290.
55. H. G. Foerster, D. Mueller and H. R. Kricheldorf, *Int. J. Biol. Macromol.*, 1983, **5**, 101–105.
56. A. Shoji, T. Ozaki, T. Fujito, K. Deguchi and I. Ando, *Macromolecules*, 1987, **20**, 2441–2445.
57. A. Shoji, T. Ozaki, T. Fujito, K. Deguchi, S. Ando and I. Ando, *Macromolecules*, 1989, **22**, 2860–2863.
58. A. Shoji, T. Ozaki, T. Fujito, K. Deguchi, S. Ando and I. Ando, *J. Am. Chem. Soc.*, 1990, **112**, 4693–4697.
59. A. Shoji, S. Ando, S. Kuroki, I. Ando and G. A. Webb, in *Annual Reports on NMR Spectroscopy*, G. A. Webb (ed.) Academic Press, London, 1993, **24**, pp. 55–98.
60. A. Shoji, T. Ozaki, T. Fujito, K. Deguchi, I. Ando and J. Magoshi, *J. Mol. Struct.*, 1998, **441**, 251–266.
61. H. Saito, R. Tabeta, T. Asakura, Y. Iwanaga, A. Shoji, T. Ozaki and I. Ando, *Macromolecules*, 1984, **17**, 1405–1412.
62. H. Saito, R. Tabeta, A. Shoji, T. Ozaki, I. Ando and T. Miyata, *Biopolymers*, 1984, **23**, 2279–2297.
63. T. Asakura, M. Demura, T. Date, N. Miyashita, K. Ogawa and M. P. Williamson, *Biopolymers*, 1997, **41**, 193–203.
64. H. Kimura, S. Kishi, A. Shoji, H. Sugisawa and K. Deguchi, *Macromolecules*, 2000, **33**, 9682–9687.
65. T. Ozaki and A. Shoji, *Makromol. Chem., Rapid Commun.*, 1983, **4**, 363–369.
66. A. Shoji, T. Ozaki, H. Saito, R. Tabeta and I. Ando, *Makromol. Chem., Rapid Commun.*, 1984, **5**, 799–804.
67. A. Shoji, *et al.*, unpublished data.
68. S. Kitazawa, T. Hiraoki, T. Hamada and A. Tsutsumi, *Polymer J.*, 1994, **26**, 1213–1226.
69. A. Tsutsumi, S. Anzai and K. Hikichi, *Polymer J.*, 1994, **15**, 355–359.
70. D. P. Burum and A. Bielecki, *J. Magn. Reson.*, 1991, **94**, 645–652.
71. P. Caravatti, L. Braunschweiler and R. R. Ernst, *Chem. Phys. Lett.*, 1983, **100**, 305–310.
72. D. P. Burum, in *Encyclopedia of Nuclear Magnetic Resonance*, D. M. Grant and R. K. Harris (eds), John Wiley & Sons, Chichester, 1996, Vol. 4, pp. 2323–2329.
73. K. Saalwaechter, R. Graf and H. W. Spiess, *J. Magn. Reson.*, 1999, **140**, 471–476.
74. S. Kishi, A. Santos, Jr., O. Ishii, K. Ishikawa, S. Kunieda, H. Kimura and A. Shoji, To be published.
75. A. Shoji and T. Kawai, *Kobunshi Kagaku*, 1971, **28**, 805–809.
76. T. Ozaki, A. Shoji and M. Furukawa, *Makromol. Chem.*, 1982, **183**, 771–780.
77. A. Shoji, T. Kawai and A. Nishioka, *Makromol. Chem.*, 1978, **179**, 611–624.
78. T. Miyazawa, in *Poly-α-Amino Acids*, G. D. Fasman (ed.), Marcel Dekker, New York, **1967**, Chapter 2.
79. K. Ito, H. Katabuchi and T. Shimanouchi, *Nature, New Biol.*, 1972, **239**, 42–43.
80. E. Sletten, *J. Am. Chem. Soc.*, 1970, **92**, 172–177.
81. E. Benedetti, P. Corradini and C. Pedone, *Biopolymers*, 1969, **7**, 751–764.
82. R. D. B. Fraser and T. P. MacRae, in *Conformation in Fibrous Proteins and Related Synthetic Polypeptides*, Academic Press, New York, 1973, Chapter 13.
83. D. S. Wishart and B. D. Sykes, in *Methods in Enzymology*, T. L. James and N. J. Oppenheimer (eds), Academic Press. San Diego, CA, 1994, Vol. 239, pp. 363–392.
84. D. S. Wishart, B. D. Sykes and F. M. Richards, *FEBS Lett.*, 1991, **293**, 72–80.
85. D. S. Wishart, B. D. Sykes and F. M. Richards, *J. Mol. Biol.*, 1991, **222**, 311–333.
86. O. Kratky, E. Schauenstein and A. Seoka, *Nature*, 1950, **165**, 319–320.
87. B. Lotz and H. D. Keith, *J. Mol. Biol.*, 1971, **61**, 201–205.

88. N. D. Lazo and D. T. Downing, *Macromolecules*, 1999, **32**, 4700–4705.
89. J. Kirimura, *Bull. Sericul. Exp. Sta.*, 1962, **17**, 447–515.
90. D. Voet and J. G. Voet, in *Biochemistry*, second edition, John Wiley & Sons, Chichester, 1995, Chapter 7.
91. J. Magoshi, Y. Magoshi and S. Nakamura, *J. Appl. Polym. Sci. Appl. Polym. Symp.*, 1985, **41**, 187–204.
92. W. K. Rhim, D. D. Elleman and R. W. Vaughan, *J. Chem. Phys.*, 1973, **59**, 3740–3749.
93. S. Hafner and H. W. Spiess, *J. Magn. Reson.*, 1996, **A121**, 160–166.
94. S. Arnott and A. L. Wonacott, *J. Mol. Biol.*, 1966, **21**, 371–383.
95. S. Arnott, S. D. Dover and A. Elliot, *J. Mol. Biol.*, 1967, **30**, 201–208.
96. H. Kimura, A. Shoji, H. Sugisawa, K. Deguchi, A. Naito and H. Saito, *Macromolecules*, 2000, **33**, 6627–6629.
97. J. A. Diverdi and S. Opella, *J. Am. Chem. Soc.*, 1982, **104**, 1761–1763.
98. R. G. Griffin, *J. Am. Chem. Soc.*, 1982, **104**, 1761–1763.
99. A. Naito, S. Tuzi and H. Saito, *Bull. Chem. Soc. Jpn.*, 1993, **66**, 3309–3313.

Stray Field (STRAFI) and Single Point (SPI) Magnetic Resonance Imaging

JOHN A. CHUDEK and GEOFFREY HUNTER

Division of Inorganic and Physical Chemistry, School of Life Sciences, University of Dundee, Dundee DD1 4HN

1. Introduction 152
2. STRAFI and SPI methodologies 155
   2.1. Stray field imaging (STRAFI) 155
   2.2. Single point imaging (SPI) and its derivatives 160
   2.3. STRAFI and SPI/SPRITE imaging of nuclei other than ^{1}H 165
3. Applications of STRAFI and SPI/SPRITE imaging 167
   3.1. Unswollen solid synthetic polymers 167
   3.2. Polymerization processes 170
   3.3. Fluid imbibition into homogeneous materials 171
   3.4. Porous materials 175
   3.5. Biological samples 179
   3.6. Soils and sediments 181
4. Concluding remarks 182
   Acknowledgements 183
   References 183

The ability of magnetic resonance imaging (MRI) to examine non-destructively and non-invasively dynamic changes in a vast range of systems has made MRI a major analytical tool in many scientific disciplines. However, one of the main drawbacks to its even wider acceptance, particularly in materials science, has been the difficulty of recording signals from samples containing nuclei with very short spin relaxation times. Stray field imaging (STRAFI) and single point imaging (SPI) not only overcome this difficulty, but can be applied with relatively modest changes to existing, commercially available NMR spectrometers. 'Solid state' MRI is therefore no longer the province solely of specialist NMR laboratories. This chapter contains a brief overview of the theory and methodology of STRAFI and SPI imaging, and reviews the literature to date that describes the already successful applications of the techniques. As with 'liquid' MRI, these emanate from a wide range of disciplines and demonstrate the versatility of these imaging modalities.

ANNUAL REPORTS ON NMR SPECTROSCOPY
VOLUME 45 ISBN 0-12-505445-9

1. INTRODUCTION

It is now almost three decades since the principles of magnetic resonance imaging (MRI) were first enunciated.[1,2] Since then the science has burgeoned and this imaging modality has, of course, found primary application in medicine where it is now often the method of choice for clinical diagnosis. Clinical imagers with horizontal bore magnets up to 1.0 m in diameter, operating at magnetic field strengths up to 2.4 T, can achieve spatial resolutions of the order of 5 mm^3. Rather better resolution ($\sim 10^{-2}$ mm^3) is obtainable with the smaller horizontal bore (diameter 0.40 m), but higher field strength (4.7 T), magnets of the mini-imagers used in small animal biomedical research. The development of magnetic resonance microscopy (or microimaging) (MRM) with image resolution corresponding to a volume element (voxel) of the order of 10^{-5} mm^3 has been somewhat tardy, although for some time suitable hardware has been available from a number of instrument manufacturers as an accessory to a conventional medium–high-field NMR spectrometer with a vertical bore 4.7–17.6 T magnet. Such an accessory consists of an imaging probe with in-built screened or actively-shielded magnetic field gradient coils, a control unit for the gradient coils, and a modulation unit to produce shaped radiofrequency pulses. After a rather long gestation period MRM has moved beyond the exploratory stage and is now established as a non-invasive technique which allows time course experiments, particularly in the life sciences.[3] Contrast the relatively short period of, at most, hours needed to obtain a full three-dimensional MRM data set from a chemically and physically intact specimen with the many man-weeks of effort required by a skilled artist to reconstruct a three-dimensional anatomical picture from the two-dimensional sections obtained by optical microscopy. Such benefits can be regarded as very useful trade-offs against the lower image resolution of MRM, particularly if time-dependent changes in specimen anatomy are being observed. MRM and optical microscopy must therefore be regarded as complementary rather than competing techniques, especially as they may not be imaging the same thing. Where MRM does have a primary advantage over other imaging modalities is that dynamic as well as density parameters can be spatially resolved. This results from the sensitivity of the NMR signal, *via* the spin–lattice (T_1) and spin–spin (T_2) relaxation times, to molecular motion on a broad range of timescales from the submicrosecond to the quasistatic. This is particularly so for the imaging of biological samples and semi-mobile solids/liquids, where differences in the rates of molecular motion are the prime source of image contrast. Conventional MRI images are therefore usually parameter maps and are only very rarely images of true spin density, ρ_H.

Data acquisition is, however, only the first stage in image production. On transformation of the raw imaging data, a two- or three-dimensional array of numbers is produced, these numbers corresponding to voxel intensities. Laying out these intensities using a grey-scale or a colour table gives the image. A

number of different subsequent image manipulations is possible using the same basic raw data set. MRI manufacturers supply imaging manipulation packages with their equipment, commercial packages are available, and many packages are custom designed. Most packages allow the user to select one or more subsets of intensities from the overall range of intensities displayed in the image. The computing routine sorts through the data and where voxels within the subset are contiguous they are clustered together. A 'skin' is finally placed round each cluster to give a *surface reconstruction* or rendering. This skin may be cut to display other cluster sets within an outer one, etc., or to show the shape of the inside of the skin. Images may be rotated and sliced at will. Many packages also allow pseudo three-dimensional images to be reconstructed (*maximum intensity projections*). A range of translucencies replaces the grey levels, opaque white representing maximum voxel intensity, through a range of reducing white translucency to transparent for the darkest grey level. Again these images may be manipulated at will. A third method is to display *contour lines*. Although at first sight this might appear to be a regression when compared to the previous two methods of display, packages allow users to stipulate which contours are required and, by judicious selection, it is possible to display small, intricate structures in three dimensions which would be otherwise hidden or lost in the other reconstructions.

The vast majority of the published applications of conventional or 'liquid' MRM correspond to materials or systems with relatively long-lived MR signals. For Fourier imaging in one dimension, the minimum field gradient $\boldsymbol{G}_x$ required to distinguish two points separated by Δx is given by

$$\Delta x = 2\pi/\gamma \boldsymbol{G}_x T_2 \tag{1}$$

Proton spin–spin relaxation for (say) plant tissue water is usually multi-exponential, with the longest component seldom exceeding a T_2 value of 30 ms. To obtain a spatial resolution of 10 μm with a typical short T_2 of 3 ms requires a field gradient no greater than 0.0235 $\mathrm{T\,m^{-1}}$, well within the usual capabilities of a commercial microscopy accessory.[4] However, there exists a large number of interesting and important systems where the MR lifetimes are significantly shorter than the millisecond range, and therefore not readily visualized with these methods. Far greater technical difficulties need to be overcome for the imaging of rigid solids, polymerization processes, liquids confined in small pores, and the diffusion of liquids through materials. Here, developments have, inevitably, been even slower than with conventional 'liquid' MRM and most equipment used so far has been 'homebuilt' and largely confined to specialist NMR laboratories, although a number of instrument manufacturers now market suitable probes and imaging accessories. The previous lack of commercial instrumentation has particularly handicapped the applications of MRM in the materials and soil sciences and only now are these moving beyond the exploratory phase. The problem is largely the result of the very short (μs)

T_2 s, with concomitant very broad lines in the observed NMR spectrum. An excellent recent review by McDonald and Newling includes a 'very much simplified account' of the general considerations of relaxation phenomena and associated time constants appropriate to an understanding of the MRI techniques presently available to image rigid polymers and liquids confined in the small pores of heterogeneous solids.[5] We do not intend to cover these basic aspects of magnetic resonance phenomena in anything like the same detail as that review. Nevertheless, there are still some important aspects of basic magnetic resonance which need to be retold briefly if the remainder of this article is to be intelligible to readers other than the specialist in broad line MRI.

Spin relaxation arises from transitions between the Zeeman levels induced by fluctuations in local magnetic fields at the corresponding Larmor frequencies, ω_L. Relaxation rates are therefore dependent both on the magnitude of the interactions and the rates of their fluctuations (τ_c^{-1}). Direct dipole–dipole interactions are the primary magnetic interaction responsible for the relaxation of spin-$\frac{1}{2}$ nuclei. In mobile liquids, where rapid molecular tumbling and frequent intermolecular collisions occur, such interactions average to zero (extreme narrowing limit). Both T_1 and T_2 are long and the linewidth ($1/\pi T_2$) is narrow. As the correlation time τ_c increases, both relaxation times decrease but then T_1 passes through a minimum at $\omega_L \tau_c \sim 1$ (i.e. when there is maximum motion at the Larmor frequency) and then starts to increase, whereas T_2 continues to fall. Beyond the minimum, T_1 and T_2 increasingly diverge and this is the situation in rigid solids which therefore have very broad natural linewidths as a result of their very short T_2 values (μs). The very rapid dephasing of the NMR signal (very short T_2), combined with the slow recovery of the magnetization to its equilibrium value (long T_1) make this a particularly difficult regime in which to image. There is the intermediate situation of liquids in the restricted geometries of porous media where broadening occurs due to restricted motion or rapid exchange of mobile nuclei with strongly relaxing pore-surface adsorption sites. In very viscous liquids, molecular tumbling may be sufficiently restricted that temporal averaging is incomplete and there is some residual dipolar line broadening. Both of these two situations can bring T_2 values of a small fraction of a millisecond. Magnetic field inhomogeneity across the sample leads to further line broadening, when the linewidth is given by $1/\pi T_2^*$ ($T_2^* < T_2$). There are particularly large sample-induced magnetic susceptibility differences at the interfaces between pore structures and their liquid contents and the diffusional motion of spins across these regions of variable magnetic susceptibility results in additional transverse relaxation and hence a much more rapid decay of the detected signal.[6] In heterogeneous samples such diffusive broadening is often the dominant contribution to line width, as the pore fluid itself may be quite mobile and have a long natural T_2 value. Another important line broadening mechanism is relaxation by paramagnetic impurities, even small quantities of which decrease both T_1 and, particularly, T_2.

There are two basic approaches to imaging materials with very short T_2 values: either narrow artificially the very wide NMR signals of dipolar broadened solids by magic angle spinning and/or multiple pulse techniques; or accept the natural linewidths and find other means to overcome the problem. For complete averaging the spinning frequency must exceed the frequency of the dipolar interaction, which is very large for $^1H-^1H$ interactions in rigid solids, although somewhat reduced where there is some motional averaging.[5] Some success has been achieved in the imaging of elastomers by the synchronized rotation of the sample and axis of rotation at rates up to 5 kHz.[7] However, as well as being technically very demanding, magic angle spinning is not generally appropriate for liquids confined in the pores of heterogeneous solids, where there is always the risk that the high centripetal forces will express the fluid.[8] Nor is it suitable for irregularly shaped samples that do not spin well. Severe susceptibility broadening cannot be narrowed by multiple pulse techniques. Neither can that caused by the presence of paramagnetic impurities. We therefore consider that the artificial line narrowing approach to imaging is likely to remain of interest only for specialized applications, although combined multiple pulse and high gradient approaches would seem to hold out considerable promise of general applicability.[9]

A number of methods have been developed which do not require artificial line narrowing of samples with very short T_2 s and full reviews of solid-state imaging methodologies can be found in the literature.[10–12] While the frequency encoded oscillating gradient echo methods[13–15] are amongst the most practical for imaging solids and confined liquids, stray field imaging (STRAFI) and single point imaging (SPI) appear to be emerging as the most promising from the viewpoint of practicality, high spatial resolution, and *general* application. They also have the considerable advantage in that only relatively modest additional investment is required to adapt existing, commercially available NMR systems. This article describes recent developments and applications of STRAFI and SPI which should be regarded as complementary techniques, each having its strengths but also some major weaknesses. Both tend to overlap with more conventional MRM with miniature radiofrequency coils and gradient sets for those specimens, such as elastomers and soft solids, which have values of T_2 of the order of a fraction of a millisecond.

2. STRAFI AND SPI METHODOLOGIES

2.1. Stray field imaging (STRAFI)

This section gives a brief outline of the basic principles of stray field imaging in sufficient detail to allow an understanding of the applications of the technique. For more comprehensive descriptions, the reader is referred to two excellent recent

reviews of STRAFI.[5,16] There are also much briefer descriptions of STRAFI[17] and of the potential applications of STRAFI (and SPI) in process analysis.[18] As indicated by Eq. (1), a very short value of T_2 can be compensated for by a proportionately large field gradient, although what is required is up to two orders of magnitude greater than those used in conventional MRM. While such gradients cannot be generated satisfactorily by conventional coils, it was recognized by Samoilenko that they exist in the fringe field surrounding a superconducting magnet.[19,20] For example, a standard Magnex 9.4 T 89 mm bore superconducting magnet (Magnex Scientific Ltd.) gives a suitable fringe field gradient of 58 T m^{-1}, albeit at a reduced field of 5.58T, some 0.2 m below the isocentre;[5] a standard Bruker 9.4 T wide bore magnet has $\boldsymbol{G}$ = 80 T m^{-1} and $\mathbf{B_0}$ = 3.83 T.[21] Although it is not controllable, the fringe field gradient can nevertheless be exploited to provide a method to image samples with very short T_2 s.

In the 58 T m^{-1} gradient the spread of ^1H frequencies approaches 2.5 MHz mm^{-1} and a pulse length of as little as a fraction of a microsecond would be too long to generate a sufficient bandwidth to excite the whole of even a small sample. Therefore even hard pulses are slice selective in the fringe field. An absolute lower limit to the slice thickness results from the requirement that the pulse length cannot be longer than T_2. This is the basis of STRAFI whereby in its simplest form the sample is moved through the gradient and the nuclei in very thin slices orthogonal to the gradient direction are excited by a radiofrequency pulse. A complete one-dimensional profile of the spin density or some other NMR parameter of the sample is thereby obtained. To obtain a three-dimensional data set requires that the sample be manipulated about one or two rotational axes orthogonal to the direction of the sample translational motion, the image being obtained by reconstruction from many one-dimensional profiles. However, such a data set is extremely time consuming to obtain, as well as requiring a complicated and well-engineered probe. Nevertheless, a probe suitable for three-dimensional STRAFI imaging has been offered commercially.[22] While most probes take samples with a maximum diameter of only about 10 mm, a recent report describes the design and construction of a STRAFI probe that can take samples up to 50 mm in diameter and up to 80 mm long and which can be fitted into a 330 mm horizontal bore imaging spectrometer ($\boldsymbol{G}$, 12.1 T m^{-1}; $\mathbf{B}_0$, 2.62 T).[23]

As McDonald has pointed out, one-dimensional STRAFI images can be obtained using a standard broadband NMR spectrometer and rapid data capture system. The most important technical obstacle to be overcome in configuring a conventional spectrometer for use as a STRAFI system lies in determining the optimum position for imaging. It is necessary to locate a sensitive plane of uniform gradient in the axial (z) direction (parallel to $\mathbf{B}_0$) and uniform field in the orthogonal (xy) plane. The location of the optimum plane is that at which the condition

$$\partial \mathbf{B}_0/\partial x = \partial \mathbf{B}_0/\partial y = 0 \tag{2}$$

is most nearly met off axis, and is not usually that at which the gradient is greatest. The frequency selective pulse and gradient select a slice which should be as flat as possible, otherwise resolution is effectively reduced by slice curvature.[5] For two hetero-nuclei at a fixed radiofrequency there are two 'sensitive planes', which are displaced in space because of the difference in the magnetogyric ratios, γ_n. This displacement provides the basis of a method to calibrate the stray field gradient.[24] The separation d depends upon the field profile: a larger $\mathbf{B}_0$ increases d, whereas a larger gradient $\boldsymbol{G}$ decreases it. At a fixed frequency ω for (say) ^{19}F and ^{1}H in a linear gradient, d is given by

$$d = (\gamma_F^{-1} - \gamma_H^{-1})\omega/\boldsymbol{G} \tag{3}$$

A phantom containing both of these nuclei in a single substance gives a STRAFI one-dimensional profile consisting of two images that are displaced by d.[25] All that is required for the calibration of the gradient is an accurate measurement of the displacement of the images.

An X-nucleus probe positioned in the field gradient at a position corresponding to the ^{1}H frequency can be mounted simply on a free screw thread, with either the sample and radiofrequency coil being moved together, or with the radiofrequency coil fixed and only the sample being moved. In either case it is important that some means is provided for levelling the sample so that it is orthogonal to the pseudo plane of the field gradient. The best achievable resolution obtainable from a sample tilted at an angle α to the magnetic field varies as $2r\sin\alpha$ where r is the sample radius. Consequently, the ideal sample shape is a long cylinder of small, constant radius, as it then becomes easier to reduce the tilt angle α.[16]

As well as being difficult to control the tilt angle α, an additional complication arises in the imaging of thin films and coatings. Most coatings start out as liquids and end up as solids only after curing. During the liquid stage, not only must they be kept horizontal but also the sample meniscus prevents the film from being entirely uniform across the sample area. In the conventional STRAFI arrangement $\mathbf{B}_0$ is oriented parallel to the gradient in the vertical direction which requires that, for a planar horizontal sample, the radiofrequency coil generates the $\mathbf{B}_1$ field parallel to the sample plane. Recently the design and construction has been reported of a benchtop instrument based on a low-cost permanent magnet with specially shaped pole pieces in which the magnetic field $\mathbf{B}_0$ (0.8 T) is *horizontal* and has a strong uniform linear field gradient (20 $T\,m^{-1}$) in the *vertical* direction.[26] A forte of this instrument is the profiling of drying and film-forming processes in polymer latex coatings such as paints as little as 200 μm thick. A profile is obtained using a planar-spiral surface coil which has a *vertical* $\mathbf{B}_1$ field, giving transverse localization as well as improved sensitivity.[27] Rather than moving the sample through the gradient, a frequency swept method uses standard pulse sequences to detect magnetization from different slices within the sample, the slice thickness being determined

by the pulse length.[28–30] The latter is the more important controlling factor. The frequency swept method is also applicable to the conventional STRAFI geometry when the radiofrequency bandwidth and the sensitivity of the coil at a distance govern the maximum field of view.[16]

Similar in concept to the frequency swept method is the *field sweep* variant of STRAFI (fs-STRAFI) in which an additional magnetic field sweep coil is used to sweep the region of resonant frequency through a stationary sample.[31] Two methods of field sweep have been described: method I where the magnetic field at the centre of the magnet was varied by the addition of a superconducting field sweep coil within the windings of the magnet; method II which used a short solenoid sweep coil operating at room temperature and positioned such that its centre was coincident with the sensitive plane. Method I required a rather specialized magnet, although such is available commercially and designed primarily for the spectroscopy of very broad line materials. The current through the field sweep coil was increased from zero to its maximum value over a few minutes, during which period the current through the main field coil reduced and the fringe field strength therefore also decreased. As a result the sensitive slice moved towards the centre of the magnet as the sweep current was increased. A short square section of commercial *Perspex*, polymethylmethacrylate, was successfully imaged by this method, although the field of view was limited to only 0.7 ± 0.1 mm. Method II does not require a specialized magnet and is therefore likely to be of more general interest. The sweep coil and the main field coil were only loosely coupled so that the central field of the magnet was virtually unaffected by current in the field sweep coil and the sensitive plane could be moved more rapidly and over a greater sweep distance (up to 9 mm). A cylindrical polytetrafluoroethylene phantom was successfully imaged using a 20 cm horizontal bore magnet (nominal magnetic field strength, 4.7 T; ^{19}F STRAFI frequency, 109.13 MHz). The fs-STRAFI method has the advantage that there are no problems associated with positional reproducibility, backlash, or misalignment in the sample travel. It would therefore appear to be most suited to experiments where it is impractical to move the sample during the timescale of the experiment and/or where the region of interest is of the order of a few millimetres or less.[31]

Fourier transform imaging has also been achieved, but requires the radiofrequency bandwidth to be sufficiently wide to encompass the whole length of the sample. Other than that the field gradient is static rather than dynamic; the method is analogous to conventional MRM. It should be noted that neither frequency swept nor Fourier methods are suitable for samples with effective T_2 s much shorter than about 100 μs. The former fails because the narrow band pulse needed for high resolution becomes longer than T_2; the latter because the delay τ required for high resolution is so long that the signal decays during the course of the pulse sequence (see below).[16]

There is a major subsidiary benefit arising from the application of such large gradients in that strong localized susceptibility-broadening gradients are

overwhelmed and image distortions disappear completely. Indeed, using STRAFI it has been possible to obtain a distortion-free image of a water-filled capillary surrounded by a matrix of paramagnetic nickel sulphate crystals, whereas MRM gave a hopelessly distorted image.[32] A more negative aspect, however, is that the fringe field gradient is static, not dynamic and this leads to problems in diffusion experiments, such as defining precisely the diffusion period and distinguishing between direct and simulated echoes arising from variable flip angle pulses across the excited slice. Moreover, as the fringe field gradient strength cannot be varied, it is the pulse gap parameters which must be varied.[16] It should also be noted that mobile liquids in a strong field gradient have a very short, diffusion limited, T_2^{eff}.

A Fourier method of solving the Bloch equations for nuclear magnetization precession in a strong magnetic field has been developed for the purpose of simulating the increasing number of pulse sequences now used in stray field experiments. The simulation explicitly includes the action of the gradient during radiofrequency pulses and the effects of spin relaxation and diffusion.[33] The method has been used to simulate a multiple diffusion sequence, $(2\tau_1 - \alpha_x)_n - \tau_1 - (90°)_y - \tau_1 - (\text{echo} - 2\tau_1)_n - (\tau_2 - (2n+1)\tau_1) - (90°)_y - \tau_1 - (\text{echo} - 2\tau_1)_n$, where α_x is a low flip angle pulse. This sequence was designed to achieve spatially resolved one-shot measurement of self-diffusion in the stray field and has been successfully tested with liquid water and hexadecane phantoms.[33]

With the very short T_{2*} values characteristic of samples imaged by STRAFI, the magnetization normally decays too quickly to observe a free induction decay following the radiofrequency pulse. It is therefore necessary to observe the signal as an echo or echo train which give signals well clear of the spectrometer dead time. Moreover, by comparing the intensities of early and late echoes, contrast can be obtained which is based on the relaxation parameters. While early STRAFI work usually used conventional 'quadrature echoes' $[(90°)_x - \tau - (90°)_y - \text{echo}]$, more recent developments have tended to use the extended quadrature sequence $[(90°)_x - \tau - ((90°)_y - \tau - \text{echo} - \tau)_n]$ which gives multiple echoes from which a series of spin relaxation weighted profiles can be obtained from a single experiment.[5,16] Contrast information from different components in the system can thereby be obtained. It should be noted that with such a short τ (μs range), a degree of spin locking occurs and the relaxation data arises from a mix of T_2 (spin–spin relaxation) and $T_{1\rho}$ (spin–lattice relaxation in the rotation frame) effects. While the decay constant is therefore neither strictly T_2 nor $T_{1\rho}$ it nonetheless reflects molecular motion, differences in which can be implied from the image contrast. Using such sequences, samples can be imaged with T_2 values as short as a few microseconds. Moreover, as time is not wasted in switching large gradients, the echo time can always be made short compared with T_2 and true spin density maps can be obtained in all but the most severely broadened systems.[5]

As the τ delay is increased the reduction in the intensity of the first echo is governed by T_2 only, but subsequent echoes have contributions from

components which have some T_1 character. This T_1 contribution can help give rise to very long echo trains from the extended quadrature sequence because of large values for T_1. This is quite advantageous since at each spatial location the echoes in each train may be summed to accumulate the signal in the technique of long echo train summation (LETS) which, for large values of n, can give large gains in signal : noise ratio.[34,35] The characteristics of multiple spin echoes observed for sodium chloride in a large magnetic field gradient have been investigated. It was shown that this type of multiple echo could be explained as an extension of Hahn's secondary echoes.[36]

A significant experimental difficulty is to set accurately the 90° pulse length.[37] Benson and McDonald have analysed the echoes produced by the extended quadrature sequence and which are strongly modulated in the stray field gradient. They showed that the largest absolute echo intensities occur for a nominal flip angle of approximately 120°. Thus one means of tuning the 90° pulse length is first to seek maximum signal, and then reduce the pulse length or amplitude to 90/120 that required for maximum signal.[37] Also, in STRAFI work the phase of the initial pulse relative to the subsequent pulse train has a dramatic effect on the echo amplitudes, although both out-of- and in-phase sequences do produce echoes. The echoes are a form of spin or Hahn echoes and Bain and Randall have calculated for spin-$\frac{1}{2}$ nuclei the intensities of such echoes produced by a series of 90° pulses applied to a sample in large static field gradients.[38] In an ('odd') imaging pulse sequence consisting of pulses with phases $(90°)_x - ((90°)_y)_n$, the first seven echoes (in the absence of spin relaxation) have the relative intensities $1:3/2:3/2:11/8:11/8:23/16:23/16$, whereas an 'even' $(90°)_x - ((90°)_x)_n$ pulse sequence produces echoes that oscillate between negative and positive amplitude and which have relative intensities of $-1:-1/2:1/2:3/8:-3/8:-5/16:5/16$. Subsequent experimental work using the constant phase sequence $[(90°)_x - \tau - ((90°)_x - \tau - \text{echo} - \tau -)_n]$ confirmed the relative phase sequence of two up two down, at least up to $n = 2$.[39] The alternative 'Randall' method to calibrate pulse length therefore uses the 'even' sequence, as the hallmark of a 90° pulse is the production of two first echoes which are negative, and two following echoes which are positive.[40]

More conventional CPMG spin echo sequences $[(90°)_x - \tau - ((180°)_y - \tau - \text{echo} - \tau -)_n]$ can also be used with consequent advantages in signal-to-noise ratio.[41] In this case, uniform slice selection is achieved by the use of a 180° pulse of twice the 90° amplitude, rather than twice its length, so that the frequency bandwidth of the pulses is identical.

2.2. Single point imaging (SPI) and its derivatives

Single point (or constant time) imaging (SPI) is a phase encoding MRI method which uses reasonably large, pulsed magnetic field gradients (up to $\sim 0.1\ \text{T m}^{-1}$).[42–44] Band-selective radiofrequency pulses are not used and

uniform excitation of the whole sample is achieved by small angle radiofrequency hard pulses with bandwidths greater than the maximum spectral width ($G_{max} \times$ sample length).[45] Position is encoded in reciprocal space, $S(k)$, where $k = 2\pi\gamma Gt$), by amplitude cycling of the applied phase encoding gradients G. A single point on the free induction decay is sampled at a fixed encoding time $t = t_p$ after the radiofrequency pulse. The full FID can be obtained by incrementing the detection time. Relaxation time contrast for T_{2*} can be generated by systematically changing t_p.[44] Figure 1 shows a one-dimensional SPI sequence. Applying additional secondary and tertiary phase encoding gradients gives, respectively, two- and three-dimensional image data sets. Therefore, unlike three-dimensional STRAFI, SPI is not a projection reconstruction technique. SPI images are free from distortions due to $\mathbf{B}_0$ inhomogeneity, susceptibility variations, and chemical shift and their resolution is limited only by the maximum gradient which can be applied to the sample, and is independent of T_{2*}.[43,44] Even the presence of non-ferromagnetic) metallic components included in the sample, which cause distortions in $\mathbf{B}_0$ homogeneity, do not cause artefacts in SPI images.[46] Moreover, a further major advantage of SPI is that it can be implemented on existing NMR imaging equipment by simple pulse sequence programming.

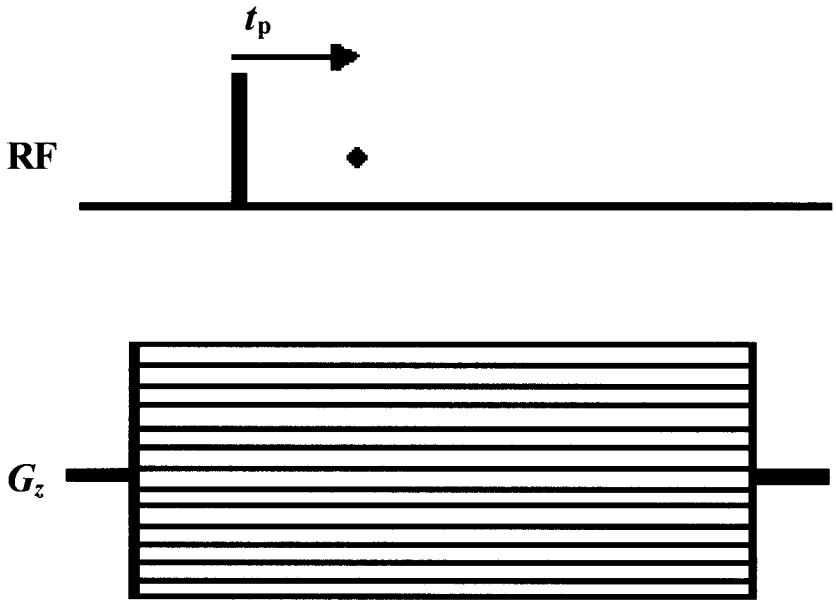

Fig. 1. One-dimensional SPI sequence. Note the broadband radiofrequency pulse applied in the presence of the phase encode gradient: k-space is sampled, point by point, by amplitude cycling the phase encode gradient with repetitive radiofrequency excitation pulses. The encoding time is t_p, the repetition time is TR. After Balcom. [48])

The principal instrumental limitations are gradient heating and restrictions on gradient amplifier duty cycle. Many modern gradient coils are, however, actively cooled by either water or cold air and driven by amplifiers that can approach a 100% duty cycle for extended periods.[45]

Assuming that the transverse magnetization is completely dephased prior to the excitation, the signal amplitude in the longitudinal steady state following a radiofrequency pulse of length θ from any point in the image is given by

$$S(\boldsymbol{k}) = \rho \exp(-t_p/T_2*)\{[1 - \exp(-TR/T_1)]/[1 - \cos\theta \,.\, \exp(-TR/T_1)]\}\sin\theta \tag{4}$$

where ρ is the spin density and TR is the repetition time between successive pulses.[47]

Despite the promise of SPI, it is inherently time inefficient since one gradient switch and radiofrequency pulse is associated with each experimental point. It is necessary to wait for T_1 recovery after each sampled point, making it particularly time consuming for materials with long T_1 values. Also, intense, rapidly switched gradient pulses can lead to excessive gradient vibration.[45] Balcom's group at the University of New Brunswick has been most active in finding means by which the limitations of basic SPI can be circumvented. In particular, they have developed the single point ramped imaging with T_1 enhancement (SPRITE) and TurboSPI sequences, and have already described a number of applications of these imaging techniques to materials science. In the SPRITE sequence, the gradients are not switched on/off for each acquisition. Instead, as originally suggested by Heid,[48] the primary phase encoding gradient is ramped in discrete steps with a radiofrequency pulse applied and a single data point collected at each gradient step (Fig. 2). Typically, each step length is less than 5 ms for each of 64 gradient steps so that the overall gradient duration is brief and the mechanical force on the gradients is minimal.[45,49] A dramatic time improvement over basic SPI is obtained with samples where T_1 is of the order of, or shorter than, the magnetic field gradient switching time. As longitudinal magnetization evolves during sampling, the SPRITE technique is a 'transient state' imaging method, but with short T_2* samples, unwanted and deleterious transverse magnetization is eliminated. Moreover, the ramped gradient enables the introduction of quantitative T_1 contrast into the images. While short T_2* values allow for natural dephasing, spin–echo artefacts may arise when longer T_2 species are also present. However, such artefacts can be eliminated by the introduction of a rapidly switched spoiling gradient, G_{spoil}, into the SPRITE sequence.[44]

Imaging times are greatly reduced and magnetization preparation is easily introduced into the SPRITE sequence by sampling a single k-space point after each magnetization filter is applied.[50] Therefore, as with 'liquid' MRM, contrast based on quantitative T_1-, T_2-, T_2*-, $T_{1\rho}$-, or ρ_H-mapping can be applied to the images. Appropriate preparation sequences to allow SPRITE T_1,

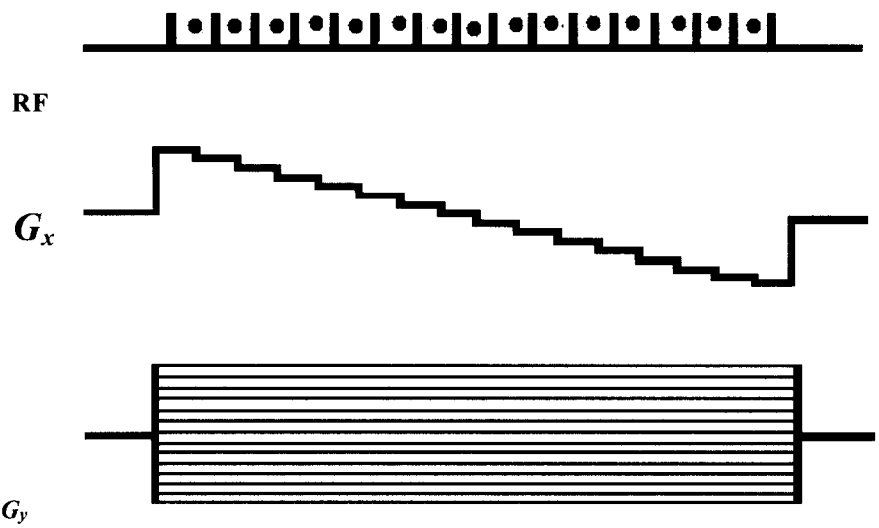

Fig. 2. Two-dimensional SPRITE sequence. The primary phase encode gradient is stepped between discrete values as a function of the secondary phase encode gradients (one shown). The encoding time is t_p, the repetition time is TR. A single point is acquired at each gradient value. (After Balcom.[49])

T_2, and T_{2*} mapping have been developed already.[46] With actively cooled gradient coils and modern amplifiers which support 100% gradient duty cycles the SPRITE acquisition time limitation is the experimental sensitivity. For example, a 1 ms TR 64^3 SPRITE acquisition, with no signal averaging, typically requires less than 5 minutes to acquire.[49] With quadrature probes a significant increase (approximately $2\times$) in sensitivity can be achieved by multiple-point averaging in which, for each gradient step, a series of data points (typically four) is collected rather than just a unique value.[51,52] These points are collected over the brief interval $[t_p, t_p + 3\Delta t_p]$ where Δt_p (typically 3 μs) is much shorter than t_p. After the separated images are produced, the data points are interpolated to a common grid and a single image is obtained by intensity averaging.[52] Although SPRITE permits shorter TR times than SPI, there are still restrictions on the overall image acquisition time due to gradient rise times as well as gradient coil and amplifier duty cycles, restricting its applicability to materials with T_1 longer than 10 ms. For shorter T_1 s it is necessary to use a simple SPI sequence with rapidly switched gradients and apply a spin preparation of each $\boldsymbol{k}$-space point.[50]

Total acquisition time has been further reduced with the development of *half-ramp* SPRITE.[50] During a conventional SPRITE acquisition, phase encode gradients vary from $-\boldsymbol{G}$ to $\boldsymbol{G}$ and a full line of $\boldsymbol{k}$-space is sampled during each magnetization cycle. As $\boldsymbol{k}$-space data is assembled point by point,

the zero-phase point can be identified exactly. Therefore, in half-ramp SPRITE, the trajectory begins at the *origin* and only one half of $\boldsymbol{k}$-space is collected, the missing half being reconstructed by exploiting the inherent symmetry of $\boldsymbol{k}$-space. While half $\boldsymbol{k}$-space acquisitions do have a lower S/N ($\times 1/\sqrt{2}$) because of fewer independent data points, such *centric order* sampling is so advantageous that it can easily produce a S/N increase of more than a factor of 2 for the same overall acquisition time.

When an image, matrix size N^2, is acquired with a field of view (FOV), and maximum phase encoding gradient, $\boldsymbol{G}$,

$$\gamma \boldsymbol{G} t_{\mathrm{p}}(FOV) = \pi N \tag{5}$$

the nominal pixel resolution, Δx, for the phase encoding time, t_{p}, will be

$$\Delta x = (FOV)/N = \pi/\gamma \boldsymbol{G} t_{\mathrm{p}} \tag{6}$$

The sampling point spread function pixel resolution is 21% more coarse than the nominal resolution.[50] While it is not possible in the SPRITE experiment to introduce slice selection with radiofrequency pulses, *physical* slice selection with good edge definition is possible by using a moveable, metallic radiofrequency shield to restrict excitation/detection to a defined region of the sample.[45]

SPRITE has been extended to the imaging of gases containing either ^{1}H or ^{19}F.[49,51] Gas phase MRI is technically challenging due to the inherently low spin concentration, signal attenuation caused by rapid molecular diffusion through magnetic field gradients, and very short relaxation times caused by rapid molecular rotation. Nevertheless, one- and three-dimensional gas phase SPRITE imaging is perfectly feasible and is not restricted to spin-hyperpolarized noble gases with long T_1 values, as is the case with more conventional MRI techniques. Indeed, SPRITE is able to exploit the short T_1 relaxation times that are common due to spin rotation relaxation in gases and benefit from enhanced relaxation due to surface interactions.[51] The S/N and spin relaxation times associated with conventional ^{1}H gas phase NMR are sufficient to readily enable the measurement of methane gas flow down a cylindrical pipe, with flow measurement sensitive to its direction, rate, and its spatial position. A velocity encoded SPI imaging sequence has been developed for spatially resolved flow measurements on gases.[53]

In the quest to further reduce acquisition time, Balcom has developed the turbo spin echo single-point imaging (turboSPI) sequence to image porous materials, in particular.[54] This is based on the RARE[55,56] and turboFLASH[57,58] imaging methods and can achieve image resolution in the range of several hundred microns. Once again, pure phase encoding is used on all axes and broadband excitation and 180° refocusing pulses are combined with RARE-type bipolar phase encoding gradients to give a train of eight or sixteen echoes. With a gradient switching time of 100 μs, a minimum phase encoding time t_{p} of about 200 μs is required. However, encoding times as short as possible are desirable to

minimize the signal loss due to molecular diffusion in the field gradient. A number of rasters, including spiral trajectories, are available for sampling ***k***-space, although only those segmented in one dimension have been employed so far.

2.3. STRAFI and SPI/SPRITE imaging of nuclei other than ^{1}H

The relative sensitivity and almost 100% natural abundance of the ^{1}H nucleus, combined with the ubiquity of hydrogen, makes it the obvious choice for most imaging studies. As with conventional MRM, it is the active nucleus probed for the great majority of reported STRAFI/SPI work. However, there are systems when other magnetically-active nuclei would be more appropriate for imaging purposes. The only published report of non-^{1}H SPI imaging involves the SPRITE ^{19}F imaging of gaseous SF_6 in a balloon phantom and occupying the pores of coral rock, *Diploria labyrinthiformis*.[49,51] While actual imaging studies still remain few, there is a significant number of reports (largely by Randall and co-workers) on the behaviour of quadrupolar ($I > \frac{1}{2}$) and non-^{1}H dipolar nuclei ($I = \frac{1}{2}$) in the large fringe field gradient required for STRAFI.

Many half-integral quadrupolar nuclei are of high sensitivity and naturally relax quickly. Their solid-state NMR spectra are usually dominated by the quadrupolar term arising from the interaction of the non-spherically symmetrical nuclear charge with an electrostatic field generated by the surrounding electrons. The product of the principal component of the field gradient and the quadrupolar moment eQ describes the quadrupolar coupling constant C_Q, which may be of the order of megahertz. Dipolar interactions and chemical shift anisotropy are normally very small by comparison. Quadrupolar nuclei in low symmetry (less than cubic) environments therefore usually have very broad NMR signals which may be much greater than the radiofrequency excitation bandwidth. Fortunately, for half-integral quadrupolar nuclei the central transition ($m_I = +\frac{1}{2} \leftrightarrow m_I = -\frac{1}{2}$) is least affected by first-order quadrupolar effects and there has been significant success in interrogating it selectively in STRAFI experiments.[40] The relative intensities of Hahn (spin) echoes obtained using both 'odd' and 'even' pulse sequences (see 2.1, above) have been observed and compared with those calculated for samples containing ^{7}Li, ^{23}Na, ^{11}B, ^{65}Cu,[40] ^{75}As [59] ($I = 3/2$), ^{27}Al($I = 5/2$), ^{51}V, ^{59}Co [40] ($I = 7/2$), and ^{93}Nb,[59] ^{115}In [40] ($I = 9/2$) nuclei. ^{11}B observations for a number of ionic crystalline solids and glasses showed that both trigonal and tetrahedral boron environments can be imaged.[60] The ^{11}B echo trains of sodium borohydride ($NaBH_4$) and sodium fluoroborate ($NaBF_4$) decayed more rapidly than that of borax ($Na_2B_4O_7 . 10H_2O$), even though the latter has a larger value for C_Q, indicating that it is the dipole–dipole rather than the electric–quadrupole interaction which dominates the relaxation behaviour of the first two species. The signal of a quadrupolar nucleus is the sum of $2I$ signals provided by the $2I$ transitions, the evolution of each of which depends distinctively on the

quadrupolar interaction. Therefore the determination of 90° pulses is usually even more difficult for quadrupolar nuclei than it is for a dipolar nucleus such as ^{1}H.[40] However, solid sodium chloride has cubic symmetry, its ^{23}Na signal is therefore not quadrupolar broadened ($C_Q \approx 0$ MHz) and its three transitions occur at the same frequency. Non-selective pulses can therefore be used to excite all the transitions where the bandwidth (typically 50 kHz) is so much greater than the quadrupolar coupling constant. For crystalline sodium chloride there is good agreement between the calculated and experimental amplitudes of the first nine echoes resulting from the application of both 'odd' and 'even' pulse sequences, using a 90° tip angle previously determined with a precision of better than ± 0.5 μs for NaCl in aqueous solution. For solid sodium sulphate with its lower symmetry, C_Q (2.6 MHz) is much greater than the bandwidth and only the central transition (40% of the total signal intensity) was selectively excited. Using the same pulse length the echo intensities were comparable to those of NaCl, allowing for the proportion of overall signal attributable to the central transition, although one effect of the large C_Q was that the alternation of down and up echoes was no longer observed.

A cylinder of solid lithium fluoride has been readily imaged and even the paramagnetic oxovanadium(IV) complex VO(*acac*)$_2$ gave an easily detected ^{51}V signal. Notwithstanding the decrease in the proportion of the overall signal arising from the central transition as I increases ($I = 5/2$, 26%; $I = 7/2$, 19%; $I = 9/2$, 15%), imaging on a realistic timescale appears to be feasible for any half-integral nucleus with a receptivity down to 2×10^{-2} that of ^{1}H.[40] There is already a report of a one-dimensional ^{27}Al image of a hollow alumina tube obtained using a magnet with the very high nominal field of 19.6 T ($\boldsymbol{G} = 76$ T m^{-1}; $\mathbf{B}_0 = 11.2$ T). The experimental and calculated profiles were in good agreement and it was deduced that the linewidth of the ^{27}Al resonance was quite narrow, indicating a highly symmetric aluminium atom site.[61] Calculations based on the density matrix formalism indicate that for quadrupolar nuclei with $I = 3/2$ the attainable image spatial resolution becomes poorer (i.e. slice thickness becomes greater) as C_Q increases, although some compensation can be obtained by using smaller pulse angles.[62]

For quadrupolar nuclei with *integral* spins STRAFI studies have been reported for ^{2}H [34] and ^{14}N [62] (both $I = 1$). In this case there is no central transition and the full effects of quadrupolar broadening should be expected when solids are imaged. Deuterium has only a relatively low quadrupolar coupling constant (e.g. $C_Q < \sim 200$ kHz in heavy water ice) and there was little appreciable effect on the echo shapes produced by either the 'odd' or 'even' pulse sequences. Heavy ice was produced by freezing and maintaining heavy water samples (^{2}H enriched to 99.8%) at 268 K, while deuteriated samples of copper sulphate and silica gel were obtained by the addition of heavy water to the anhydrous samples. The echo trains for the last two samples decayed relatively rapidly and only about 16 echoes could be obtained for each train. In contrast, very long echo trains (up to 9000 echoes) were obtained for both

heavy water and heavy ice, both decays being fitted to a double exponential (time constants: water, 12 ± 7 and 141 ± 1 ms; ice, 20 ± 7 and 194 ± 10 ms). The initial signal from the heavy ice was three times greater in intensity than that from the heavy water sample under the same experimental conditions.[34]

For ^{14}N C_Q can cover a wide range from virtually zero (e.g. quasi terahedrally-symmetric NH_4^+ in $NH_4H_2PO_4$, 0.03 MHz) to as high as 5 MHz (e.g. $NaNO_2$, 4.93 MHz). Nevertheless, by judicious choice of pulse length and τ for the 'odd' pulse sequence it proved possible to observe long echo trains from a variety of nitrogen-containing species, including solid sodium nitrite, with a high field spectrometer ($\boldsymbol{G}$, 52.9 $T\,m^{-1}$; $\mathbf{B}_0$, 10.8 T).[63] Using long echo-train summation (LETS) accumulated over a train of 16 echoes, a one-dimensional image was obtained of crystalline ammonium nitrate in a vial of square cross section.

STRAFI imaging has already been demonstrated for samples containing the dipolar nuclei ^{19}F [24,25,64,65] and ^{31}P.[35,59] Even strongly paramagnetic solids can be imaged, provided that the electronic relaxation time is so short that the nuclear linewidths are governed mostly by nuclear dipole–dipole interactions.[64] As already alluded to, ^1H and ^{19}F can be imaged simultaneously in the same sample at a fixed radiofrequency with the two sensitive planes displaced in space because of the difference in their magnetogyric ratios.[25] This has been exploited in the STRAFI imaging of dental restorative materials which release fluoride ion (long T_2 component) into the adjacent tooth.[65,66] For the spectrometer used in these studies ($\boldsymbol{G}$, 58 $T\,m^{-1}$; $\mathbf{B}_0$, 5.58 T) the ^{19}F sensitive plane was offset by 6 mm from that of ^1H. STRAFI ^{31}P studies of a variety of diamagnetic and paramagnetic materials containing phosphate, including chicken bone, bone meal, calcium hydroxyapatite, ammonium hexafluorophosphate, and cobaltous phosphate have been reported.[35] In these materials the ^{31}P T_2 s are of the order of a few hundred microseconds so that signal loss between the first two pulses was not a major difficulty. Moreover, for the diamagnetic materials the relatively long T_1 s were actually advantageous as very long echo trains were observed which could be summed using LETS to increase the S/N. Trains extending over several thousand echoes were obtained, whereas that for paramagnetic cobaltous phosphate had decayed to a negligible value after only 32 echoes. An attempt was made to obtain further enhancement of S/N for ammonium hexafluorophosphate by $^{31}P-\{^{19}F\}$ double resonance but only a 26% increase in the level of the ^{31}P initial echo-signal was observed.

3. APPLICATIONS OF STRAFI AND SPI/SPRITE IMAGING

3.1. Unswollen solid synthetic polymers

Chemically homogeneous solid polymers are often *physically* inhomogeneous as they are complex multiphase materials whose exact composition depends on

the conditions of their manufacture. Important properties such as impact strength, yield strength, tensile strength, craze, and fracture behaviour are dependent on the relative number, type, and distribution of the structural and morphological entities. It is the nature and extent of the molecular mobility of each component which have a profound influence on the overall physical, mechanical, and deformation properties of the polymer. As relaxation times reflect polymer chain mobility, the range of T_2 values for a single material, even under ambient conditions, may therefore span two to three orders of magnitude. For example, semicrystalline thermoplastic plastics crystallized from the melt usually consist of lamellar crystalline regions (T_2, ~5–10 μs) separated by non-crystalline interzonal regions (T_2, up to several hundred μs). There are also diffuse and ill-defined interfacial (transition) regions with intermediate T_2 values. The ability to provide spatial distribution information for these relaxation times opens up many new possibilities for product development, quality control, equipment design, process development, failure analysis, and the modelling of deformation processes.[44,67] Many rubbery polymers with low glass transition temperatures and high chain segmental mobility can be imaged successfully using conventional 'liquid' MRM techniques and there are numerous examples whereby the absorption of organic solvents by rigid glassy polymers increases the chain mobility of a swollen polymer.[44,68,69] However, without enhanced chain mobility the T_2 s of both rigid thermoplastic and thermosett materials are usually so low that solid MRI imaging techniques are required to image the complete material. Both STRAFI and SPI/SPRITE have the demonstrated ability to image in three dimensions, and without distortion, objects manufactured from rigid thermoplastic and thermosett polymers which are irregularly shaped and which, moreover, have non-ferromagnetic metal inserts.

An early report illustrated 3-D STRAFI images of polycarbonate objects inside which the manufacturing process had left air bubbles, a microswitch, a polyethene tube with inhomogeneities, and an Andrew type MAS rotor made of Delrin and which showed inhomogeneity of the material.[22] However, perhaps because the accumulation of 2-D and 3-D STRAFI data sets is extremely time consuming, as well as requiring a complicated and well-engineered probe, there have been only a few such images subsequently reported. These include 3-D images of the inhomogeneous distribution of polyethylene glycol and polyvinyl alcohol binders in unsintered ceramics,[70] and 2-D images of materials with potential uses in aerospace applications such as a solid rocket motor bondline analogue, a polyphenylene sulphide/carbon fibre composite, and a conducting polymer coating used in a novel nylon welding technique.[71]

It is much more time efficient to design the experiment to allow the use of 1-D STRAFI profiles to give the required information. A number of such studies of both pure and composite rigid polymers have been reported, virtually all as precursors to solvent imbibition and/or diffusion. However, a very few have been intended to obtain information about the relationships between the molecular

chain dynamics and the mechanical properties of the polymer. The latter category include the cured commercial epoxy adhesives *Ciba–2015*, *2011*, *2005* (Ciba Geigy), *FD808* (Formulated Resins), *Sikadur 31* (Sika), and *Epofix* (Struers), and glass fibre reinforced plastic (grp) sandwiches bonded together with *Ciba–2015*;[72] the fluoride releasing dental restorative materials, *Fuji IX* (GC Corporation) and *Vitremer* (3M Healthcare) glass polyalkenoates, *Dytract* compomer (Dentsply GmbH), and *Z100* composite (3M Healthcare);[65,66] *Athpol 90* High Impact Polystyrene (Athlone Extrusions Ltd.).[73,74] The last material is a thermoplastic composite with a rubbery polybutadiene (PB) dispersed phase which reduces both the tensile and compressive yield stress of the brittle polystyrene (PS) matrix to give much improved impact properties to the material.[75] The mechanisms of yielding in HIPS are distinctly different in compression from those operating in tension.[76] Changes in the STRAFI images subjected to compressive stress were monitored for both PS and PB phases; conventional MRM was able to monitor the behaviour of only the rubber disperse phase.[73,74]

An early report indicated the ability of SPI to image the protons of the rigid polymer *Delrin*.[43] Other workers reported on the ability of the technique to distinguish regions of different T_{2*} within a semicrystalline polypropylene polymeric sample. A 2-D surface plot of T_{2*} was obtained at 150 °C of the crystalline component of the sample.[44] One advantage with SPI/SPRITE is that, to a first approximation, sample size is not a serious limitation. Large and irregularly shaped parts of industrial relevance can be imaged, although there are limitations to the quality of the images acquired due to the large field of view, decreased digital resolution resulting from limitations on matrix size, excessively long acquisition times, and decreased maximum gradient strengths. With large gradient sets, the minimum achievable detection time is too long to allow imaging of the crystalline components with very short T_2 values, only the interfacial and amorphous phases being detectable. The point has been made, however, that even low (>1 mm) pixel resolution may suffice to characterize adequately large samples and fabricated parts if the information content of the detected components still reflects relevant process and product histories. Imaging of large parts can be used as a preliminary scouting tool for selection of relevant pieces at higher resolution.[67] A large, irregularly shaped 'chunk' of polyethylene which essentially filled the 120 mm (i.d.) probe has been imaged as a 2-D projection. Also reported in this paper are SPI images of photodegraded polyethylene films, and oxidized bromobutyl rubbers, as well as of some polyolefin blends.[67] Three-dimensional SPRITE images of both phantoms and commercially manufactured objects made from polyvinyl chloride, polyethylene, cross-linked *cis*-polybutadiene, and *Plexiglas* polymethylmethacrylate have been reported. In the undistorted image of a plastic stop-valve, all the rigid polymeric components, which comprised valve handle and T-joint, threaded shaft, and washer (made from chlorinated-PVC), and two elastomeric O-rings, were observed despite the presence of two brass screws in the assembly. Contrast between the rigid polymer and elastomer was due primarily to the difference

in their T_{2*} values. The 3-D image of a solid-core, multi-layer golf ball distinguished the two outer layers and the cross-linked *cis*-polybutadiene core. Regions of the core where the NMR signal decayed more rapidly relative to their surroundings were attributed to an inhomogeneous distribution of additives.[46] Phantoms made from cross-linked polybutadiene, from PVC, and from polyethylene have been imaged by half-ramp SPRITE. The signal due to PVC was easily nulled by inversion recovery preparation, when the image from the PVC/polyethylene sample arose only from the polyethylene.[50]

3.2. Polymerization processes

As monomers are polymerized one effect is to reduce the value of T_2 as mobility is restricted with the growth in molecular chain length. Conventional 'liquid' MRM techniques are usually quite adequate to image the monomer phase(s), whereas STRAFI and SPI/SPRITE are capable of imaging both mobile monomer and the formed solid polymer, providing a means of studying both polymerization mechanism and kinetics. To our knowledge, there are no published reports of the study of polymerization processes involving the latter technique. This section therefore describes only STRAFI studies, including the imaging of drying 'thin' films, paints, other protective coatings, and adhesives, where T_2 shortening occurs from oxidative coupling as well as by solvent loss.

In medical and dental applications which require *in situ* polymerization, control of the polymerization process is not nearly as practicable as in laboratory or industrial practice and, consequently, the reaction may proceed with spatially dependent rates. The hardening process following a free-radical polymerization (initiator, 3 wt% *Lucidol* CH50, a 50 : 50 master batch of benzoyl peroxide and dicyclohexylphthalate) of *n*-butylmethacrylate (BMA), in a 2 : 1 blend of polyethylmethacrylate (PEMA) and BMA used for hip bone prosthesis has been investigated using pastes prepared in cylindrical glass vials. It was found that there was a significant increase in the reaction rate along the axis of the cylindrical reactor from the surface to the bottom of the vial. Also, the degree of polymerization increased in the opposite direction, thus increasing the residual unsaturation in the final product, and giving concern about deleterious effects on the mechanical properties of the polymer blend.[77] Similar concerns about the possibility of incomplete curing occurring in visible light cured (VLC) dental restorative materials have been addressed in other studies.[65,78] A reduction in the degree of polymerization with depth is inherent to the chemistry of VLC materials and has clinical implications, not only with regard to the physical properties of the cured resins, but also from the possible toxic effects of eluted uncured monomer. Visible light curing of a number of different shades of the posterior composite *Occlusin* (ICI Dental plc) was followed by one-dimensional STRAFI which was able to observe simultaneously the formation of the polymer and the disappearance of the uncured monomer. Previous studies using 'liquid'

MRM to determine the time-dependent depth of cure had been able to observe only the disappearance of the monomer.[79,80]

'Thin' film technology is important for many applications such as adhesives, binders, coatings and paint. STRAFI has been shown to be highly suited to study dynamic processes such as drying and polymerization occurring in thin films. Gradients of concentration and/or structure exist across developing thin films and the measurement of average properties by standard NMR spectrometry or relaxometry is often insufficient to fully characterize the system.[81] The first such STRAFI study was of the temperature-dependent drying (temperature range, 22 to 62 °C) of sodium silicate films from aqueous solution. Such solutions are widely used as paper adhesives. The films showed a strong dependence of T_2 on hydration ranging from tens of microseconds in the glassy state to a few milliseconds in the highly viscous 'rubbery' state. One-dimensional imaging with a resolution better than 25 μm was by a modified Bruker X nucleus probe operating with a Bruker MSL 300 spectrometer. It was concluded that the local water mobility in the films depended primarily on the local hydration and was independent of the drying conditions.[81]

The high resolution imaging of thin films has been made much more convenient by two developments: a surface coil which is static in the fringe field of a superconducting magnet and can be used with either frequency-swept or Fourier STRAFI;[82] and a benchtop instrument based on a low-cost permanent magnet with specially shaped pole pieces.[26] The surface coil has been used to study the evaporative drying of a latex paint film in which a colloidal dispersion is transformed to a continuous polymer film.[82] The benchtop instrument has been used to study the solvent loss and cross-linking of spin-cast alkyl coating with a cobalt catalyst for which it appeared that spatially non-uniform auto-oxidative cross-linking occurred across the thickness of the film.[26] There is also a very recent report of its use to study the film formation of a latex/water dispersion undergoing photo-initiated cross-linking. The latex was based on a vinyl acetate/ethylene copolymer with reactive aceto-acetoxy functionality and the cross-linker was poly(ethyleneglycol) diacrylate. The depth-resolved composition and mobility profiles were compared with numerical simulations and a model developed combining the principles of water evaporation, mutual diffusion of various components, photo-initiated free radical polymerization, and oxygen ingress. The model was able to explain the observed highly non-uniform drying and cross-linking in the depth of the latex films and it was concluded that both oxygen inhibition and latex turbidity are obstacles to obtaining uniformly cross-linked, waterborne coatings.[83]

3.3. Fluid imbibition into homogeneous materials

For the purposes of this section a material will be regarded as homogeneous even if, although a 'chemically pure' polymer, it is complex multiphase (see

above), or it is a composite comprising two or more distinct materials. As the industrial applications of polymeric materials have increased it has become increasingly important to understand the adverse effects on their physical and mechanical properties caused by liquid and vapour imbibition and the rate(s) of such imbibition. This is particularly so for those applications where polymers are exposed intentionally to contact with aggressive organic liquids, such as in fuel and chemical storage tanks and associated pipework. Incidental exposure to aggressive organic solvent attack may be anticipated for any application, and water is, of course, ubiquitous.

In Case I (Fickian) diffusion fluid ingress proceeds as the square root of time and there is a smooth concentration profile; in Case II diffusion the fluid ingress proceeds linearly with time and there is a sharp concentration front at the furthest point of ingress. Behind the front, the penetrant concentration is approximately constant and the polymer is usually swollen and softened (i.e. rubbery). A critical solvent concentration is required to induce the glass-to-rubber transition, but behind the solvent front diffusion is very rapid. Diffusion of the solvent is slow into regions of the polymer where there is less than this critical concentration, so that ahead of the front, a Fickian precursor is observed, the characteristics of which vary according to the system. Prior to the front formation there is an induction period, during which the diffusion of the penetrant is Fickian in nature and also during which its surface concentration builds up to the concentration threshold which is required for front formation.[84] Case I diffusion can be expected for polymers above their glass transition temperature, T_g, when the diffusion rate is slow compared with polymer segmental relaxation rate. Case II diffusion can be expected to occur for polymers below their T_g, when the diffusion rate is fast compared with the polymer segmental relaxation rate. For Case II, the rate limiting step to ingress is the visco-elastic response of the polymer at the solvent front.[85] Most traditional methods of determining the kinetics, and hence elucidating the mechanism, of fluid uptake cannot allow for any anisotropic effects which might be anticipated for complex multiphase materials. Nor can they give reliable information about any changes in mechanism as fluid uptake proceeds. Under favourable circumstances 'liquid' MRM can provide partial information when the swollen polymer has chain mobility sufficient to give a relatively long T_2 value.[69] However, methods which allow imaging of both rigid and swollen polymer are required for most situations.

To our knowledge, there have been no SPI/SPRITE systematic studies reported for fluid ingress into homogeneous polymers. There is, however, already a substantial body of knowledge derived from STRAFI studies, much of which has emerged from work done by MacDonald and his co-workers using the high-field STRAFI facility at the University of Surrey ($\boldsymbol{G}$, 58 T m^{-1}; $\mathbf{B}_0$, 5.58 T). Polymer samples have been normally prepared so as to minimize any anisotropic effects and of an appropriate geometry such that measurement in one dimension alone was needed to investigate solvent diffusion. For pure

single component solvents, Case II behaviour has been reported for: the diffusion of acetone vapour into the commercial polyvinyl chloride (PVC) thermoplastic *Simona* (Aquarius Plastics Ltd.,) over the temperature range 20 to 50 °C;[37,84] and the diffusion of deuteriated methanol vapour into polymethylmethacrylate (prepared by pressing uncrosslinked PMMA powder; T_g, 109 °C).[86] However, some polymers can exhibit Case II behaviour for solvent vapour ingress, but Fickian behaviour for the same solvent as a liquid and at the same temperature. This apparent paradox has now been resolved by the Surrey group in a very recent paper describing complementary MRM (liquid solvent) and STRAFI (solvent vapour) studies of the diffusion of toluene into polystyrene samples prepared by pressing polystyrene powder. They have determined that there are circumstances other than just the normal (Thomas and Windle) description of Case II diffusion by which a linear advance of the solvent front can be modelled. It was found that the visco-elastic swelling at the solvent front need not in fact limit the speed of solvent ingress, but rather that it is limited by the *flux* of solvent impinging on the surface of the polymer. The general case situation has been dubbed 'surface flux limited Case II diffusion' and this will be observed whenever the flux of solvent on the surface is reduced. This most readily occurs as a consequence of the solvent being provided in vapour form. However, Case II diffusion is a transitory phenomenon and left long enough, in a sufficiently large system, the diffusion will always revert to Fickian behaviour.[87]

Combined MRM and STRAFI studies have shown that strongly anisotropic organic solvent imbibition can occur in a chemically homogeneous, but physically inhomogeneous, polymer sample. Extruded *isotactic* polypropylene imbibes much more rapidly *via* damaged surfaces than through intact moulded surfaces and this has been attributed to the formation during the extrusion process of a highly oriented skin layer, resistant to penetration by normally good solvents.[68] Just as the progressive ingress of the solvent affects the polymer chain dynamics, there may be also a significant time-dependent effect on the mobility of the *solvent* molecules. This has been shown by a ^{19}F STRAFI study of the ingress of solvent hexafluoro-benzene into a polymer blend (2 : 1) of PMMA and poly(*n*-butyl)methacrylate. When the solvent first enters the glassy polymer it is 'solid-like'; i.e. it has a short T_2 value, presumably because of restricted rotation. Thereafter, at any one position, T_2 lengthens when the solvent starts to rotate as the polymer swells.[25]

Virtually all polymeric materials, not just those designed to function in an aqueous environment, will be exposed to environmental water at some stage of their service lives, and water imbibition can have adverse effects on their physical and mechanical properties.[88] Although the polymer itself may be able to tolerate such degradation, if water is absorbed at the interfaces of high moduli materials, substantial swelling pressures and the generation of unwanted stresses can be anticipated.[89] Combined STRAFI and MRM studies of some commercial thermoset adhesives used in the construction industry have

shown that water absorption was a two-stage, anisotropic process, occurring through the cut ends of samples rather than through intact or set surfaces. Fillers present in the adhesive significantly affected the chain dynamics of the epoxy resin matrix, and their role was crucial in the sorption of water, with uptake strongly coupled to the local dynamics of the adhesive polymer chains. Moreover, water penetration into soaked GRP structures bonded by these adhesives was, initially, *via* the adhesive despite the much greater exposed surface area of the GRP.[72] Water uptake by sodium polyacrylate has been studied by low-field STRAFI ($\boldsymbol{G}$, 37.5 $\mathrm{T\,m^{-1}}$; $\mathbf{B}_0$, 2.9T) when it was shown that the diffusion was Case I (Fickian) and that the swelling of the polymer was about twice as rapid as the progress of the water front, whose position was defined as the interpolated value at half-maximum of each of the time-dependent one-dimensional profiles.[90]

The ingress of water into starch is of interest because it has relevance to the storage, drying, and processing of starch-containing materials of importance to the food industry. Amylose is a linear, amorphous polysaccharide found in starch and can serve as a model for multi-component food systems. STRAFI one-dimensional profiles have been used to study the ingress of water into pellets of corn starch amylose prepared by compression moulding at 100 °C. As prepared, the samples were clear and transparent and therefore considered as a homogeneous glassy polymer. It was found that ingress of water vapour into the amylose pellets behaved in a Fickian manner, whereas the ingress of liquid water was non-Fickian and approximated to Case II diffusion behaviour.[91]

In everyday situations polymers are often exposed to *mixtures*, rather than single-component solvents. At present the ingress of even binary mixtures of solvents into glassy polymers is far from being well understood, there being too little data available to make modelling worthwhile for such processes. It is particularly unclear whether a 'bad' solvent will diffuse ahead of, alongside, or behind a 'good' solvent with which it is miscible.[92] One disadvantage of solid-state MRI to study such situations is that chemical shift selective imaging is not possible so that individual components of solvent mixtures, and the polymer itself, can be differentiated only by their different spin relaxation properties. Nevertheless, STRAFI has been used to study the ingress of methanol–acetone mixtures into PMMA samples, methanol being the 'bad', and acetone the 'good' solvent for this polymer. Both solvents were deuteriated and the solvent mixtures ranged in composition from 80 wt% methanol–20 wt% acetone (methanol, 0.76 mole fraction) to 94% methanol–6% acetone. Polymer spin relaxation time and the solvent diffusion coefficient gradients were observed and there was also a small gradient in the polymer fraction across the swollen region. The gradients generally increased with the proportion of acetone in the solvent mixture.[86] A subsequent study of methanol/acetone ingress into polymethylmethacrylate provided further evidence of the synergistic effects of two or more mixed solvents acting together and of residual solvent left over in the polymer from manufacture. Samples were prepared by dissolving polymer

powder in acetone that was then allowed to evaporate over a period of weeks to produce pre-swollen samples containing between 0 and 8 weight % acetone. As long as the drying process was sufficiently slow, the preparation procedure produced homogeneous samples. Frequency swept STRAFI one-dimensional profiles showed the ingress of methanol, when it was found that methanol ingressed far more rapidly into those samples pre-swollen with acetone than into pure PMMA. The solvent front advanced linearly with time into the pure PMMA sample, but with the square root of time into most pre-swollen samples, indicating a clear transition from Case II to Fickian diffusion with pre-swelling. Lowering the temperature of the sample reversed the transition. Pre-swelling lowered T_g for the PMMA samples, as shown by differential scanning calorimetry and dynamical mechanical thermal analysis measurements. The results were analysed using the Thomas and Windle model of solvent diffusion in polymers.[93] A very recent study by *MRM* cyclic cross-polarization methods, which allow ^{13}C-edited chemically resolved images,[94] has provided some information on the ingress of miscible mixtures of a good and a bad solvent (methyl ethyl ketone and ethanol) into polystyrene. The two solvents were found to ingress together, although their spatial concentration profiles were markedly different: the methyl ethyl ketone profile showed a sharp solvent front at the interface between the swollen rubber and the non-invaded glass phases and had a high solvent fraction throughout the rubber; the ethanol profile showed that that fraction decreased smoothly across the rubber and approached zero at the front. The results were explained in terms of a simple model of multi-component diffusion, wherein the diffusion of the bad solvent is enabled by the presence of the good solvent.[92] It is known that the composite restorative materials used in modern dentistry absorb solvent mixtures from saliva and food, affecting some of the properties that influence clinical performance. Frequency-swept STRAFI has been used to study the diffusion of water–ethanol mixtures into 500 μm thick sheets of the VLC diacrylate dental resin which is the base for the commercial composite *Occlusin* (ICI Dental plc). There was no sharp front to the solvent concentration profiles and therefore the distance travelled by the diffusion front was measured to the mid-intensity level. With ethanol concentrations of less than 55% the solvent front advanced initially with the square root of time, then slowed significantly after a few hours. This phenomenon was considered to be due to the ethanol concentration dependence of the diffusion coefficient. At 65% ethanol the diffusion was straightforwardly Fickian and there was no change in the diffusion coefficient as the solvent ingressed the sample.[66,95]

3.4. Porous materials

The ability to study non-invasively the mobility and diffusion behaviour of liquids in porous materials is of crucial importance in a wide range of industrial

applications. Consequently, there is a long history of the application of NMR to investigate the microstructure of porous media, fully- or partially-filled with a liquid. The NMR relaxation times of the contained liquid(s) decrease as pore size is reduced and are sensitive to pore structure. There is general agreement that collision/interaction with the pore walls controls the relaxation behaviour, and that therefore the overall relaxation rate will increase with the surface : volume ratio in a pore. Also, there are particularly large sample-induced magnetic susceptibility differences at the interfaces between pore structures and their liquid contents and susceptibility broadening cannot be artificially narrowed. With their ability to deal with the imaging of systems with very broad lines, STRAFI and SPI/SPRITE are now being employed to resolve the spatial distribution of both spin density and relaxation times in many otherwise intractable systems.

Amongst the most active areas of study are the hydration, curing, and drying of cements and concretes. The apparently simple hydration of cement powders is in fact a highly complex process which involves the formation of a gel of tricalcium silicate around the cement grains. Due to the various sizes and random packing of unhydrated cement grains, air trapped during mixing, and to the amorphous structure of the gel, pores vary in size over many orders of magnitude.[96] Therefore, in cement pastes and concretes, pores have to be broadly defined because they span such a wide variety of shapes, length scales, and sizes. The hardening of Portland cement at different water : cement ratios has been studied by STRAFI, when it was found that the magnetization decays, obtained from different points of the one-dimensional profiles, could be fitted to single mono-exponential functions.[97] A subsequent report by the same authors indicated that the first 30 hours of the hydration reaction follow a mono-exponential decay but after that initial period, the magnetization decays with a time constant an order of magnitude higher. It was suggested that the water molecules were in two different environments, which could be correlated with water in open gel pores and in capillary (micron-scale) pores.[77]

Although reinforced concrete is the most successful and widely used construction material, there are major problems with its durability. These largely arise because both gaseous and dissolved chemical species in the environment migrate into concrete and affect markedly the mechanisms and rates of corrosion of embedded reinforcing steel.[98] The most rapid diffusions in concrete matrices use the pore network as a pathway. The frictional forces in nanoscale pores (10^{-9} m), which are not much larger than a water molecule, impede flow and cannot therefore be regarded as an important diffusion pathway. The permeability of the material therefore arises from the interactions of the density, size, shapes, and interconnectivity of larger pores on the micron-scale. Its porosity and moisture content is also of crucial importance in the development of the ultimate compressive and tensile strengths of concrete, its insulating value, and its ability to withstand damage from frost and fire.

Due to the sample size restrictions of most STRAFI instrumentation its use has been restricted to studying cement pastes. SPI/SPRITE therefore has a significant advantage in that it can also handle real concrete samples that contain stone aggregates, which are known to differ in some important properties from those of cement pastes.[49] One-dimensional STRAFI imaging of cylindrical samples has shown that the ^1H signal from Portland cement pastes at a number of different water : cement ratios originates from water in three broad categories; chemically combined water (shortest T_2), tightly bound gel water (intermediate T_2), and more mobile water in capillary pores (longest T_2). The spatial distribution of the different types of water could be determined.[99] STRAFI studies of water absorption and transport in fibrous cement roofing tiles were able to reveal pores with three characteristic sizes in the different layers resulting from the manufacturing process in which the raw material was pressed through rollers in three stages followed by appropriate curing. When the tiles were exposed to liquid water it was found that the water concentration was greatest within the layer with significantly the greatest pore volume, irrespective of whether the water entered from the inner or outer surface (upper surface in a roofing application).[100] One method to control the imbibition of water, and water-borne degrading agents into concrete structures is to block off the pore structure completely with a hydrophobic polysiloxane surface treatment. The absorption and curing of such a polymeric coating into cement pastes has been followed by STRAFI, when it was found that the treatment reached a depth of 1.5 mm and then ingressed no further. The application of a second polymer coating 24 hours after the first also did not penetrate any further.[101] The NMR group at the University of Kent has modelled successfully the kinetics of capillary imbibition in Portland cement to fit data derived from STRAFI ($\boldsymbol{G}$, 18 $T\,m^{-1}$; $\mathbf{B}_0$, 2.42 T) water concentration profiles. The profiles followed a $t^{1/2}$ law and allowed a master curve to be formed using the Boltzmann transformation. The distribution of pore sizes within the sample, as measured by NMR cryoporometry,[102] showed a prominent peak at 100 Å and the model of the pore structure consisted of a lattice of interconnecting pore sizes with a size distribution consistent with the cryoporometry results.[96]

A series of papers describing SPI/SPRITE imaging of cement paste and *concrete* samples containing aggregates has appeared recently from the New Brunswick group. All samples studied were prepared using 'white' Portland cement of low iron content, for which the T_2 values of its water contents are longer than in 'ordinary' Portland cement with its uncontrolled paramagnetic centres. The moisture content of drying concrete samples,[103] and the influence of shrinkage-cracking on the drying behaviour of cement pastes,[104] have been determined from one-dimensional SPRITE profiles. Cracks in the cement matrix fundamentally alter the permeability of the material and therefore directly affect the drying behaviour. It was also found that the drying behaviour of the cement pastes was distinctly different from the drying

behaviour of related concrete materials containing aggregates.[104] The spatially-resolved T_1, T_2, and T_{2*} distributions in intact concrete and mortar samples were determined successfully from one-dimensional SPRITE profiles.[47,105] As a consequence of the additional inhomogeneity introduced by the coarse aggregates, magnetization decay for concrete was found to be systematically faster than the decay for mortar. Evolution of the one-dimensional profiles as a function of temperature was qualitatively compared with a series of differential scanning calorimetry experiments for cement pastes conditioned under controlled humidity. A localized occupied pore size distribution was calculated, based on the percentage of water freezing in determined regions of the sample, and T_{2*} relaxation time map evolution as a function of the sample temperature. It was considered that such an assessment can help in identifying regions of low frost resistance in mortars and concretes.[105] Concrete structures exposed to frost conditions are susceptible to deterioration caused by ice formation, whose dynamics are driven by the chemical and structural properties of the material. For water-saturated hydrated cement cooled from room temperature, the first phase transition occurs at about 0 °C, when the water freezes in the capillary pores.[106] Freeze/thaw in concrete (from −50 to 11 °C) has been studied by SPRITE one- and two-dimensional imaging, the latter images being acquired in under 3 minutes. An analysis of the images permitted quantification of the non-frozen water distribution, showing that the technique can successfully follow position-based thermal changes as they take place in materials with short relaxation times.[51,106,107] Pore sizes in a drying cylinder of concrete were obtained from the freezing point depression of pore water over a temperature range of 0 to −40 °C. Unlike freshly cured concrete, where all of the pores are completely filled with water, once the concrete is exposed to ambient conditions, drying begins from the exposed surfaces, when water is evaporated more quickly from the larger pores than from the smaller pores. Therefore moisture content in the air-dried experimental sample was greatest at the sample centre, and progressively decreased towards the ends of the cylinder. SPRITE imaging showed that freezing of the pore water started at the centre of the cylinder, and then spread with progressively lower temperatures toward the sample ends. This clearly demonstrated that in the wet regime water existed in pores of various dimensions, but in proximity to the exposed surfaces the upper limit of water occupied pore sizes became smaller. The lowest temperature freezing occurred equally along the entire cylinder, indicating that the smallest pore size range were all occupied throughout the concrete sample.[108]

Microporous zeolites are industrially very important, being used as catalysts, drying agents, and in separation processes. *Zeolite 4A* is an efficient drying agent for natural gas, liquid paraffins, and organic solvents, its water capacity being 22 wt%. SPI/SPRITE relaxometry has been used to investigate the water adsorption process in *Zeolite 4A*, when relaxation time mapping (T_1, T_2, and T_{2*}) showed that water mobility at the sorption front, characterised by a long T_1 recovery, was clearly different from that of the hydration region.[109]

3.5. Biological samples

'Liquid' MRM is unable to image those parts of plant materials with very short T_2 values, such as the cellulose and lignins of cell walls and the water content of small cells whose NMR signal is strongly broadened by magnetic susceptibility differences at their interfaces with intercellular air spaces.[3] STRAFI and SPI/SPRITE have the potential to be able to image *all* of the protic content of plant materials, although little has so far been published. SPI/SPRITE has been used to image the short relaxation time components of processed tobacco leaves in cigarettes, complementing conventional spin-echo imaging of the wax and water contents. In the manufacture of cigarettes it is the custom to pack the tobacco tightest at the end to stop the fibres falling out, leading to disproportional drying. It was possible to obtain detailed information on the distribution of moisture and the drying effects on the tobacco, as well as the distribution of the tobacco fibres.[110]

The T_2 values for bone and teeth are of the order of 100 μs, too short for conventional spin- and gradient-echo imaging. However, both STRAFI and SPI/SPRITE are well able to image mineralized tissues, with ^{1}H signals arising from collagen and ^{31}P signals from the mineral content. Imaging the latter nucleus is likely to become of clinical significance as knowledge of bone mineral density is of crucial importance in the diagnosis of osteoporosis, predicting the risk of fracture and monitoring healing.[49] A SPRITE ^{1}H image of a bovine femur[49] and constant time (i.e. SPI) ^{1}H images of an extracted human anterior tooth, and rabbit and bovine bone have been reported.[111] Both trabecular and cortical bone were imaged, as well as tissue within the marrow. SPI not only allows the imaging of enamel and dentine in teeth, but also the detection, without image distortion, of caries which are filled with amalgam (Fig. 3). STRAFI has also been used to examine extracted human teeth when post-processed images can give insights into the detailed dental anatomy of extracted teeth.[113,114] While 'liquid' MRM can image root canals and caries in considerable detail,[115] with three-dimensional STRAFI and SPI/SPRITE it has also now become possible to image, for example, channels in the dentine, arborization, the formation of branching channels in the root canals, and a detailed topography of the tooth surface.

An early SPI report suggested the potential significance to the food industry of imaging semi-crystalline food materials. A goal in the molecular science of food is to characterize the structure and dynamics of structural components, since food mechanical and rheological properties depend entirely on the flexibility of molecular networks. Solid-state imaging can therefore open a valuable window into macroscopic deformation, swelling, melting, and crystallization phenomena in complex food materials. As an illustration, these authors report the two-dimensional spatial distribution determined by SPI of crystalline material in a sample of starch.[44] SPRITE has also been used to examine a number of food-related systems as diverse as the uptake of milk into cereals, and the distribution of caramel in confectioneries.[116]

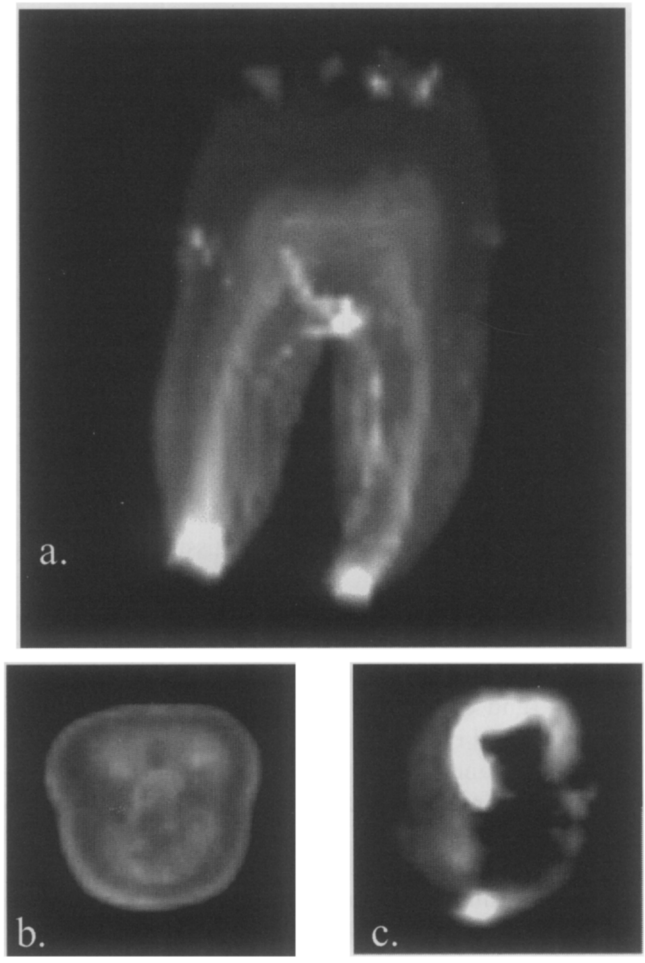

Fig. 3. ^{1}H SPI images of human teeth: **a**. shows a three-dimensional maximum intensity image of a 64^3 data set, *TR*, 100 ms; **b**. is a slice from the same tooth, taken just below the cusp; **c**. shows another tooth with an amalgam-filled caries. The bright areas are caries under the amalgam filling, the grey areas are healthy tooth material, and the black area the filling. Note that there is no apparent image distortion caused by the metal amalgam filling.[112]

Creaming is the gravimetric separation of a dispersed phase from the continuous phase of an emulsion and can be either an advantage to be exploited in industrial separation processes, or a disadvantage as a destabilizing process that can reduce product shelf life. A good understanding of the creaming of oil-in-water emulsions is important to the production of cosmetics and pharmaceuticals, as well as to food science. The traditional method for its study is simply to observe directly the movement of the interface between the cream layer and

the continuous phase, giving the so-called creaming velocity, but affording no information about the concentration profiles as they develop in the creaming emulsion. However, STRAFI has been able to determine the concentration profiles of submillimetre thick layers in sunflower oil–water coarse emulsions, thickened with gum xanthan, undergoing creaming. Further, it was shown that the individual layers, which previously had been assumed to be of uniform concentration, have concentration gradients running through them. By use of a probe specifically constructed to study films of emulsion, and tuning it in such a way as to only excite the oil nuclei, layers less than 600 μm thick were analysed, with a best resolution of about 5 μm. The concentration profiles determined by STRAFI were compared with those predicted by a numerical model.[27]

Bacteria, to confer a competitive advantage to their growth and survival in hostile environments, generate exopolysaccharides, which strongly interact with, and bind, large amounts of water. With the aim of understanding how these systems might be 'engineered' to improve the survival of beneficial bacteria in water-stressed environments, STRAFI has been used to study the diffusion of water into a series of model substances related to bacterial exopolysaccharides. The water self-diffusion coefficients were determined for the commercially available bacterial exopolysaccharide xanthan and a chemically derived deacylated form. The removal of acetyl groups from xanthan resulted in a reduction in D_{self} at any given polymer concentration. Additionally, STRAFI measurements gave the rate at which water diffused through a polysaccharide gel at a range of polymer concentrations in xanthan, deacylated xanthan, and polymers produced by the soil bacteria *Enterobacter cloacae* and *Azobacter chroococcum*.[117] Follow-up STRAFI studies of water ingress into xanthan provided data which enabled the development of an analytical model which successfully described the coupling of water vapour transport through the pore space, and liquid water transport through the progressively swelling gel which gradually occluded the vapour path.[118] Others have used STRAFI to image colonies of bacteria in water, when one of the main objectives was to differentiate the water inside the bacteria from that outside. This was achieved by using the diffusion sensitivity inherent in STRAFI. The sample was moved in the *transverse* direction and, by using a long copper strip as resonator, a diffusion-weighted one-dimensional profile was obtained across the sensitive slice. The in-plane resolution achieved was of the order of 1 mm and it was possible to detect bacteria in concentrations down to approximately 4×10^9 cells mm^{-1}, even in the presence of significant quantities of paramagnetic impurities.[119]

3.6. Soils and sediments

Describing the use of STRAFI and SPI/SPRITE in studies of soil and sediment samples separately from those of other porous and heterogeneous

materials may seem somewhat arbitrary, but soil science has long been treated as a separate discipline. The distributions of liquids and root growth in soils are of fundamental significance to their fertility and physical structure. However, their highly heterogeneous nature and the common occurrence of paramagnetic species usually render 'liquid' MRM imaging of soils very difficult, although not impossible under favourable circumstances.[120] Many of these problems can be circumvented by the use of solid-state MRI. It has been demonstrated already that STRAFI can be used to image roots and other protic materials in soils with at least 2% Fe content.[121] The recent development of a large (50 mm diameter) STRAFI probe means that the technique can now be extended to monitor water movement in soil and sandstones using more realistically sized samples.[23,122] Turbo-SPI has been used to image the water in the interstices of a water-saturated quartz sand. For an acquisition time of 8 hours, it was possible to achieve an in-plane resolution of 150 μm × 150 μm, with a slice thickness of 220 μm. The study was extended to image the structure of a water-saturated *Tepexil* aggregate (a highly porous rock of volcanic origin). An acquisition time of only two hours was needed for a three-dimensional image with a resolution of approximately 0.05 mm on a voxel side.[52] SPRITE images of lake sediments, with a resolution on the millimetre scale, successfully showed changes in porosity resulting from the transition from Lake Agassiz to Lake Winnipeg.[123]

4. CONCLUDING REMARKS

Given that both STRAFI and SPI/SPRITE imaging can be performed on most standard MRI equipment with only modest investments in new equipment, we consider it likely that, notwithstanding the merits of other solid-state MRI methodologies, these two techniques will become the most favoured for general use. Both techniques can reach the parts of samples untouched by 'liquid' MRM, although neither is capable of the chemical shift selective imaging of MRM. Moreover, both can give undistorted images in the presence of strongly paramagnetic centres, or even when non-ferromagnetic metal components are present. It would seem that STRAFI can image materials with shorter T_2 values than SPI/SPRITE, and also has the potential for better spatial resolution. However, its forte is those applications where the sample geometry is such that the required information can be obtained from one-dimensional profiles. It would also seem to be ideally suited to studying 'thin' film materials; it is extremely inefficient in obtaining data sets for three-dimensional imaging. SPI/SPRITE is much better suited to three-dimensional imaging, particularly of relatively large, heterogeneous samples. Both techniques are maturing and have now moved out of the exploratory phases of their development. Over the next few years we shall see many more 'real' applications appearing in the literature. The techniques are complementary, both to each other and to 'liquid' MRM, and in combination offer materials scientists, in particular, the

exciting ability to carry out time-dependent, non-invasive studies of a wide range of systems of scientific, industrial, and economic importance.

ACKNOWLEDGEMENTS

We thank those authors who have kindly supplied reprints of their papers, and particularly thank Professors Balcom, McDonald and Randall for giving us sight of the manuscripts of papers, accepted but yet to appear in print.

REFERENCES

1. P. C. Lauterbur, *Nature*, 1973, **242**, 242.
2. P. Mansfield and P. K. Grannell, *J. Phys. C*, 1973, **6**, L422.
3. J. A. Chudek and G. Hunter, *Progr. Nucl. Magn. Reson. Spect.*, 1997, **31**, 43.
4. W. Kuhn, *Angew. Chem., Int. Ed. Engl.*, 1990, **29**, 1.
5. P. J. McDonald and B. Newling, *Rep. Prog. Phys.*, 1998, **61**, 1441.
6. K. J. Packer, *J. Magn. Reson.*, 1973, **9**, 438.
7. D. G. Cory, A. M. Reichwein, J. W. M. Vanos and W. S. Veeman, *Chem. Phys. Lett.*, 1988, **143**, 466.
8. J. A. Chudek, G. Hunter, M. R. Jones, S. N. Scrimgeour, P. C. Hewlet and A. B. Kudryavtsev. *J. Mater. Sci.*, 2000, **35**, 4275.
9. R. E. Botto, G. D. Cody, S. L. Dieckmann, D. C. French, N. Gopalsami and P. Rizo, *Solid State Nucl. Magn. Reson.*, 1996, **6**, 389.
10. P. Jezzard, J. J. Attard, T. A. Carpenter and L. D. Hall, *Prog. Nucl. Magn. Reson. Spect.*, 1991, **23**, 1.
11. P. Blümler and B. Blümich, in *NMR Basic Principles and Progress* (eds P. Diehl, E. Flock and R. Kosfeld) Springer, Berlin, 1994.
12. M. E. Smith and J. H. Smith, *Meas. Sci. Technol.*, 1996, **7**, 449.
13. S. P. Cottrell, M. R. Halse and J. H. Strange, *Meas. Sci. Technol.*, 1990, **1**, 624.
14. Y. Mat Daud and M. R. Halse, *Physica B.*, 1992, **176**, 167.
15. P. J. McDonald, K. L. Perry and S. P. Roberts, *Meas. Sci. Technol.*, 1993, **4**, 896.
16. P. J. McDonald, *Progr. Nucl. Magn. Reson.*, 1997, **30**, 69.
17. E. W. Randall, Magnetic resonance: MRI Using Stray Fields, in *Encyclopaedia of Spectroscopy and Spectrometry* (ed. J. C. Lindon), Academic Press, 1999, p. 1396.
18. P. J. Prado, B. Blümich and B. J. Balcom, Magnetic resonance techniques, in *Spectroscopy in Process Analysis* (ed. J. Chalmers) Sheffield, Academic Press Ltd., Sheffield, 2000.
19. A. A. Samoilenko, D. U. Artemov and A. L. Sibel'dina, *JETP Lett.*, 1988, **47**, 348.
20. A. A. Samoilenko, D. U. Artemov and A. L. Sibel'dina, *Bruker Rep.*, 1987, **2**, 30.
21. A. A. Samoilenko and K. Zick, *Bruker Rep.*, 1990, **1**, 40.
22. K. Zick, STRAFI solids imaging, Technical Report NMR/B353/393, BRUKER Analytische Messtechnik GmbH, D-7512 Rheinstettin, 4/Karlsruhe, 1993.
23. P. Kinchesh, A. A. Samoilenko, A. R. Preston and E. W. Randall, *J. Environ. Quality*, in press.
24. A. R. Preston, P. Kinchesh and E. W. Randall, *J. Magn. Reson.*, 2000, **146**, 359.
25. E. W. Randall, A. A. Samoilenko and T. G. Nunes, *J. Magn. Reson., Series A*, 1995, **117**, 317.
26. P. M. Glover, P. S. Aptaker, J. R. Bowler, E. Ciampi and P. J. McDonald, *J. Magn. Reson.*, 1999, **139**, 90.

27. B. Newling, P. M. Glover, J. L. Keddie, D. M. Lane and P. J. McDonald, *Langmuir*, 1997, **13**, 3621.
28. J. B. Miller and A. N. Garroway, US Patent 5 126 674, 1992.
29. J. B. Miller, *Proc. 28th Congress Ampere*, Canterbury, UK, 1996, p. 113.
30. P. Glover and P. J. McDonald, *Proc. 28th Congress Ampere*, Canterbury, UK, 1996, p. 141.
31. M. J. D. Mallett, M. R. Halse and J. H. Strange, *J. Magn. Reson.*, 1998, **132**, 172.
32. P. Kinchesh, E. W. Randall and K. Zick, *J. Magn. Reson.*, 1992, **100**, 411.
33. A. J. Bohris, D. A. Faux, D. G. Gillies and P. J. McDonald, The analysis and development of pulse sequences for self-diffusion weighted stray field imaging, in *Spatially Resolved Magnetic Resonance: Methods, Materials, Medicine, Biology, Rheology, Geology, Ecology, Hardware*, (eds P. Blümler, B. Blümich, R. Botto and E. Fukushima), Wiley-VCH, Weinheim, 1998, Ch. 7, p. 95.
34. E. W. Randall, T. G. Nunes, G. Guillot and P. R. Bodart, *Solid State Nucl. Magn. Reson.*, 1999, **14**, 165.
35. D. G. Gillies, B. Newling and E. W. Randall, *J. Magn. Reson.*, 2001, **151**, 235.
36. N. Okubo, T. Suzuki and T. Aoki, *Phys. Lett, A*, 1998, **248**, 463.
37. T. B. Benson and P. J. McDonald, *J. Magn. Reson., Series A*, 1995, **112**, 17.
38. A. D. Bain and E. W. Randall, *J. Magn. Reson., Series A*, 1996, **123**, 49.
39. E. W. Randall, *Solid State Nucl. Magn. Reson.*, 1997, **8**, 179.
40. P. R. Bodart, T. G. Nunes and E. W. Randall, *Solid State Nucl. Magn. Reson.*, 1997, **8**, 257.
41. T. B. Benson and P. J. McDonald, *J. Magn. Reson., Series B*, 1995, **109**, 1995.
42. S. Emid and J. H. N. Creyghton, *Physica*, 1985, **128B**, 81.
43. S. Gravina and D. G. Cory, *J. Magn. Reson., Series B*, 1994, **104**, 53.
44. D. E. Axelson, A. Kantzas and T. Eads, *Can. J. Appl. Spectrosc.*, 1995, **40**, 16.
45. B. J. Balcom, R. P. MacGregor, S. D. Beyea, D. P. Green, R. L. Armstrong and T. W. Bremner, *J. Magn. Reson., Series A*, 1996, **123**, 131.
46. C. B. Kennedy, B. J. Balcom and I. V. Mastikhin, *Can. J. Chem.*, 1998, **76**, 1753.
47. S. B. Beyea, B. J. Balcom, P. J. Prado, A. R. Cross, C. B. Kennedy, R. L. Armstrong and T. W. Bremner, *J. Magn. Reson.*, 1998, **135**, 156.
48. O. Heid and M. Deimling, *Abs. Soc. Magn. Reson., 3rd Ann. Meeting*, 1995, p. 684.
49. B. J. Balcom, SPRITE imaging of short relaxation time nuclei, in *Spatially Resolved Magnetic Resonance: Methods, Materials, Medicine, Biology, Rheology, Geology, Ecology, Hardware* (eds P. Blümler, B. Blümich, R. Botto and E. Fukushima), Wiley-VCH, Weinheim, 1998, Ch. 5, p. 75.
50. I. V. Mastikhin, B. J. Balcom, P. J. Prado and C. B. Kennedy, *J. Magn. Reson.*, 1999, **136**, 159.
51. P. J. Prado, B. J. Balcom, S. D. Beyea, R. L. Armstrong and T. W. Bremner, *Solid State. Nucl. Magn. Reson.*, 1997, **10**, 1.
52. P. J. Prado, B. J. Balcom, I. V. Mastikhin, A. R. Cross, R. L. Armstrong and A. Logan, *J. Magn. Reson.*, 1999, **137**, 324.
53. P. J. McDonald, personal communication.
54. S. D. Beyea, B. J. Balcom, I. V. Mastikhin, T. W. Bremner, R. L. Armstrong and P. E. Grattan-Bellew, *J. Magn. Reson.*, 2000, **144**, 255.
55. J. Hennig, A. Nauerth and H. Friedburg, *Magn. Reson. Med.*, 1986, **3**, 823.
56. J. Hennig, *J. Magn. Reson.*, 1988, **78**, 397.
57. A. Haase, J. Frahm, D. Matthaei, W. Haenicke and K.-D. Merboldt, *J. Magn. Reson.*, 1986, **67**, 258.
58. A. Haase, *Magn. Reson. Med.*, 1990, **13**, 77.
59. A. A. Samoilenko, *Proc. 28th Congress Ampere*, Canterbury, UK, 1996, p. 139.
60. E. W. Randall and D. G. Gillies, *J. Magn. Reson., Series A*, 1996, **121**, 217.
61. A. A. Samoilenko, E. W. Randall and V. Soghomonian, *Ann. Rep. Nat. High Magn. Field Lab.*, 1997 p. 184.

62. P. R. Bodart, T. G. Nunes and E. W. Randall, *Appl. Magn. Reson.*, 1997, **12**, 269.
63. E. W. Randall, A. A. Samoilenko and R. Fu, *Solid State Nucl. Magn. Reson.*, 1999, **14**, 173.
64. E. W. Randall, *Solid State Nucl. Magn. Reson.*, 1997, **8**, 173.
65. C. H. Lloyd, S. N. Scrimgeour, G. Hunter, J. A. Chudek, D. M. Lane and P. J. McDonald, *J. Mater. Sci.: Mater. Med.*, 1999, **10**, 369.
66. S. N. Scrimgeour, C. H. Lloyd, G. Hunter, D. M. Lane and P. J. McDonald, Applications of stray field imaging to dental materials science, in *Spatially Resolved Magnetic Resonance: Methods, Materials, Medicine, Biology, Rheology, Geology, Ecology, Hardware* (eds P. Blümler, B. Blümich, R. Botto and E. Fukushima), Wiley-VCH, Weinheim, 1998, Ch. 26, p. 293.
67. D. E. Axelson, A. Kantzas and A. Nauerth, *Solid State Nucl. Magn. Reson.*, 1996, **6**, 309.
68. R. J. Abbott, J. A. Chudek, G. Hunter, R. L. MacKay, P. J. McDonald and L. Squires, Stray field imaging and magnetic resonance microimaging studies of the anisotropic absorption of solvents by extruded polypropylene, in *Spatially Resolved Magnetic Resonance: Methods, Materials, Medicine, Biology, Rheology, Geology, Ecology, Hardware* (eds P. Blümler, B. Blümich, R. Botto and E. Fukushima), Wiley-VCH, Weinheim, 1998, Ch. 20, p. 253.
69. R. J. Abbott, J. A. Chudek, G. Hunter and L. Squires, *J. Mater. Sci. Lett.*, 1996, **15**, 1108.
70. P. S. Wang, D. B. Minor and S. G. Malghan, *J. Mater. Sci.*, 1993, **28**, 4940.
71. J. H. Iwamiya and S. W. Sinton, *Solid State Nucl. Magn. Reson.*, 1996, **6**, 333.
72. S. N. Scrimgeour, G. Hunter, W. J. Harvey, C. H. Lloyd, D. M. Lane and P. J. McDonald, Stray field imaging and magnetic resonance microimaging studies of water intrusion/stress mobilisation in dense polymer systems used in construction, in *Spatially Resolved Magnetic Resonance: Methods, Materials, Medicine, Biology, Rheology, Geology, Ecology, Hardware* (eds P. Blümler, B. Blümich, R. Botto and E. Fukushima), Wiley-VCH, Weinheim, 1998, Ch. 24, p. 281.
73. F. Mohd. Som, J. A. Chudek and G. Hunter, *J. Rubber Res.*, 1999, **2**, 169.
74. J. A. Chudek, G. Hunter, F. Mohd. Som, P. J. McDonald and B. J. Newling, Stray field imaging and magnetic resonance microimaging studies of high impact polystyrene, an elastomer-toughened material, in *Spatially Resolved Magnetic Resonance: Methods, Materials, Medicine, Biology, Rheology, Geology, Ecology, Hardware*, (eds P. Blümler, B. Blümich, R. Botto and E. Fukushima), Wiley-VCH, Weinheim, 1998, Ch. 18, p. 235.
75. J. L. Amos, *Polym. Eng. Sci.*, 1984, **14**, 1.
76. C. B. Bucknall, P. Davies and I. K. Partridge, *J. Mater. Sci.*, 1987, **22**, 1341.
77. T. G. Nunes, P. R. Bodart and E. W. Randall, Stray field magnetic resonance imaging of hardening materials, in *Spatially Resolved Magnetic Resonance: Methods, Materials, Medicine, Biology, Rheology, Geology, Ecology, Hardware* (eds P. Blümler, B. Blümich, R. Botto and E. Fukushima), Wiley-VCH, Weinheim, 1998, Ch. 25, p. 287.
78. C. H. Lloyd, S. N. Scrimgeour, D. M. Lane, G. Hunter and P. J. McDonald, *Dent. Mater.*, 2001, **17**, 381.
79. C. H. Lloyd, S. N. Scrimgeour, J. A. Chudek, G. Hunter, R. L. MacKay, D. Pananakis and E. W. Abel, *Dent. Mater.*, 1994, **10**, 128.
80. C. H. Lloyd, S. N. Scrimgeour, J. A. Chudek, G. Hunter and R. L. MacKay, *Dent. Mater.*, 2000, **17**, 170.
81. P. D. M. Hughes, P. J. McDonald, N. P. Rhodes, J. W. Rockcliffe, E. G. Smith and J. Wills, *J. Colloid. Interface Sci.*, 1996, **177**, 208.
82. P. M. Glover, P. J. McDonald and B. Newling, *J. Magn. Reson.*, 1997, **126**, 207.
83. M. Wallin, P. M. Glover, A. C. Hellgren, J. L. Keddie and P. J. McDonald, *Macromol.*, 2000, **33**, 8443.
84. K. L. Perry, P. J. McDonald, E. W. Randall and K. Zick, *Polymer*, 1994, **13**, 2744.
85. N. L. Thomas and A. H. Windle, *Polymer*, 1982, **25**, 529.
86. D. M. Lane and P. J. McDonald, *Polymer*, 1997, **38**, 2329.
87. P. J. McDonald, J. Godward, R. Sackin and R. P. Sear, *Macromol.*, 2001, **34**, 1048.

88. R. C. L. Tai and Z. Szklarska-Smialowska, *J. Mater. Sci.*, 1993, **28**, 6199.
89. J. Comyn (ed.), *Polymer Permeability*, Elsevier, London, 1985, p. 177.
90. T. G. Nunes, G. Guillot and J. M. Bordado, *Polymer*, 2000, **41**, 4643.
91. I. Hopkinson, R. A. L. Jones, S. Black, D. M. Lane and P. J. McDonald, *Carbohydrate Polymers*, 1997, **34**, 39.
92. R. Sackin, E. Campi, J. Godward, J. L. Keddie and P. J. McDonald, *Macromol.*, 2001, **34**, 890.
93. D. M. Lane, P. J. McDonald and J. L. Keddie, Mixed solvent ingress into PMMA measured by stray field magnetic resonance imaging, in *Spatially Resolved Magnetic Resonance: Methods, Materials, Medicine, Biology, Rheology, Geology, Ecology, Hardware* (eds P. Blümler, B. Blümich, R. Botto, and E. Fukushima), Wiley-VCH, Weinheim, 1998, Ch. 19, p. 241.
94. M. Heidenreich, W. Köckenberger, R. Kimmich, N. Chandrakumar and R. Bowtell, *J. Magn. Reson.*, 1998, **132**, 109.
95. C. H. Lloyd, D. M. Lane, S. N. Scrimgeour, P. J. McDonald and G. Hunter, submitted to *Dent. Mater.*
96. A. Leventis, D. A. Verganelakis, M. R. Halse, J. B. Webber and J. H. Strange, *Transport in Porous Media*, 2000, **39**, 143.
97. T. G. Nunes, P. Bodart and E. W. Randall, The hardening of Portland cement studied by ^{1}H stray field imaging: influence of concentration and evaporation rate of water. *Proc. Second Int. Conf. NMR Spect. of Cement Based Mater.* (eds P. Colombat and H. Zanni), Springer Verlag, Weinheim, 1997, p. 411.
98. P. C. Hewlet, G. Hunter and M. R. Jones, *Chem. Brit.*, 1999, **35**, 40.
99. A. J. Bohris, U. Görke, P. J. McDonald, M. Mulheron, B. Newling and B. le Page, *Magn. Reson. Imaging*, 1998, **16**, 455.
100. A. J. Bohris, B. Newling, P. J. McDonald, A. Raoof and N. L. Tran, *J. Mater. Sci.*, 1998, **33**, 859.
101. S. Black, D. M. Lane, P. J. McDonald, D. J. Hannant, M. Mulheron, G. Hunter and M. R. Jones, *J. Mater. Sci. Lett.*, 1995, **14**, 1175.
102. J. H. Strange, M. Rahman and E. G. Smith, *Phys. Rev. Lett.*, 1993, **71**, 3589.
103. S. D. Beyea, B. J. Balcom, T. W. Bremner, P. J. Prado, D. P. Green, R. L. Armstrong and P. E. Grattan-Bellew, *Cement Concrete Res.*, 1998, **28**, 453.
104. S. D. Beyea, B. J. Balcom, T. W. Bremner, P. J. Prado, A. R. Cross, R. L. Armstrong and P. E. Grattan-Bellew, *Solid State Nucl. Magn. Reson.*, 1998, **13**, 93.
105. P. J. Prado, B. J. Balcom, S. D. Beyea, T. W. Bremner, R. L. Armstrong, R. Pishe and P. E. Gratten-Bellew, *J. Phys. D: Appl. Phys.*, 1998, **31**, 2040.
106. P. J. Prado, B. J. Balcom, S. D. Beyea, T. W. Bremner, R. L. Armstrong and P. E. Grattan-Bellew, *Cement Concrete Res.*, 1998, **28**, 261.
107. P. J. Prado, B. J. Balcom, S. D. Beyea, R. L. Armstrong, T. W. Bremner and P. E. Grattan-Bellew, *Magn. Reson. Imaging*, 1998, **16**, 521.
108. C. Choi, B. J. Balcom, S. D. Beyea, T. W. Bremner, P. E. Grattan-Bellew and R. L. Armstrong, *J. Appl. Phys.*, 2000, **88**, 3578.
109. P. J. Prado, B. J. Balcom and M. Jama, *J. Magn. Reson.*, 1999, **137**, 59.
110. D. E. Axelson and J. B. Wooten, *J. Agric. Food. Chem.*, 2000, **48**, 2199.
111. Y. Seo, H. Takamiya, H. Ishikawa, T. Nakashima, Y. Sharfand and G. Navon, NMR imaging of rigid biological tissues, in *Spatially Resolved Magnetic Resonance: Methods, Materials, Medicine, Biology, Rheology, Geology, Ecology, Hardware* (eds P. Blümler, B. Blümich, R. Botto and E. Fukushima), Wiley-VCH, Weinheim, 1998, Ch. 42, p. 445.
112. J. A. Chudek, G. Hunter, C. H. Lloyd and S. N. Scrimgeour, submitted to *J. Dental. Res.*
113. M. A. Baumann, G. M. Doll and K. Zick, *Oral Surg. Oral Med. Oral Pathol.*, 1993, **75**, 517.
114. M. A. Baumann, T. Schwebel and A. Kriete, *Comput. Med. Imaging Graphics*, 1993, **17**, 221.

115. C. H. Lloyd, S. N. Scrimgeour, J. A. Chudek, G. Hunter and R. L. MacKay, *Quintessence Int.*, 1997, **28**, 349.
116. P. Cornillon and L. C. Salim, *Magn. Reson. Imaging*, 2000, **18**, 335.
117. T. D. Hart, A. H. L. Chamberlain, J. M. Lynch, B. Newling and P. J. McDonald, *Enzyme Microb. Technol.*, 1999, **24**, 339.
118. U. Görke, A. H. L. Chamberlain, E. A. Crilly and P. J. McDonald, *Phys. Rev. E*, 2000, **62**, 5353.
119. K. J. Carlton, M. R. Halse and J. H. Strange, *J. Magn. Reson.*, 2000, **143**, 24.
120. M. H. G. Amin, L. D. Hall, R. J. Chorley and K. S. Richards, *Prog. Phys. Geography*, 1998, **22**, 135.
121. E. W. Randall, N. Mahieu and G. I. Ivanova, *Geoderma*, 1997, **80**, 307.
122. P. Kinchesh, A. A. Samoilenko, A. R. Preston and E. W. Randall, *Proc. 2nd Europ. Symp. NMR Soil Science*, Freising, Germany, 2000, p. 65.
123. F. R. Rack, B. J. Balcom, R. P. MacGregor and R. L. Armstrong, *J. Paleolimnology*, 1998, **19**, 255.

rate, its NMR signal is resolved outside the protein envelope, 0–10 ppm. These signals are highly sensitive to electronic structure and microenvironments of His residues and unequivocally describe the tautomerism and the protonation behaviour of the side-chains. NMR parameters of hydrogen-bonded His imidazole ring NH proton signals reflect the strength of the hydrogen bond and the local tertiary structure of the protein and therefore provide unique structural information that cannot be obtained by other techniques.

1. INTRODUCTION

The concept of hydrogen bonds was first introduced as an important principle in structural chemistry to researchers in a variety of fields by a chapter on hydrogen bonding in Pauling's *The Nature of the Chemical Bond*[1] in 1939. Subsequently, hydrogen bond was accepted as a major cohesive force between molecules. In general, a hydrogen bond may be represented as A–H—B, where A–H is a weakly acidic 'donor group', B is a lone pair electron bearing and hence weakly basic 'acceptor atom', and — represents a hydrogen bond. Thus, the A–H—B interaction involves the sharing of a hydrogen atom by a weakly acidic donor atom and a weakly basic acceptor atom. The essential requirement of a hydrogen atom in the A–H—B interaction arises from the fact that, since its size is the smallest, only a hydrogen nucleus can approach the lone pair electron cloud of an acceptor atom close enough to permit an electrostatic association of significant magnitude.[2]

Besides their importance in the structural organization of biological macromolecules,[3–6] hydrogen bonds exhibit functional properties that are essential to regulate biological systems. Since they are weak interactions, fast intermolecular recognition and reaction can easily occur with energies that are within the range of thermal fluctuations of interacting molecules at biological temperatures.[7] Furthermore, the strong hydrogen bond between bases of similar proton affinity has been proposed to account for most of the stabilization energy in enzyme-bound intermediates and transition states, relative to the initial enzyme–substrate complex, in many enzyme-catalysed reactions,[8–16] although the importance of the strength of hydrogen bonds in enzymatic catalysis has been under debate.[13,17–19]

A number of books and reviews on hydrogen bonds have already appeared, some comprehensive[7,20,21] and others more focused.[22–24] The present chapter focuses on, NMR signals arising from His imidazole ring NH hydrogens that are involved in internal hydrogen bonds in metalloproteins, and the usefulness of these signals as spectroscopic probes in studies of protein folding and function are reviewed. In 1969, Glickson *et al.*[25] reported the first ^{1}H NMR spectrum of a protein in H_2O and demonstrated the observation of the Trp indole NH proton signal of hen egg white lysozyme in the high-frequency

shifted region of the spectra. This report showed the significance of observing ^{1}H NMR spectra of biological molecules in H_2O for study of their structure. Since the observation of high-frequency shifted NMR signals arising from hydrogen-bonded His imidazole ring NH protons in the spectra of myoglobin (Mb) and hemoglobin (Hb) by Shulman and his associates[26] in the early 1970s, similarly resolved exchangeable proton signals have been detected in the spectra of various proteins[27–35] and nucleic acids[36–41] in H_2O. These signals can be interpreted in terms of the hydrogen bond length and linearity, the nature of its microenvironment, and the p*K*a values of the conjugate acids, provided that they are unambiguously assigned, and facilitate a wealth of information about structural and functional aspects of proteins. His is often found as an active site residue in a variety of enzymes and metalloproteins and as a proton-donor or proton-acceptor residue in forming an internal hydrogen bond which contributes to the stabilization of protein structure. Since a His imidazole ring NH hydrogen involved in an internal hydrogen bond in a protein matrix is magnetically deshielded and exhibits a moderate hydrogen exchange rate, its NMR signal is resolved outside the protein envelope, 0–10 ppm. These signals are highly sensitive to the electronic structure and microenvironment of the His imidazole ring.

2. HYDROGEN BONDS

Hydrogen bonds not only provide a three-dimensional conformational basis for the native folding pattern of biomolecules such as proteins and nucleic acids, but also play a crucial role in the stabilization of their structures. Despite the significance of the bonds, experimental techniques for detecting them in a direct and unambiguous manner were not available until the reported observation of spin–spin (*J*) couplings transmitted through hydrogen-bonded donor and acceptor atoms.[42] We obviously knew that hydrogen bonds are present in various molecules, but the existence of the bonds was generally inferred from the spatial proximity of donor and acceptor groups in X-ray and NMR structures or from other indirect evidence, such as deshielding of NMR signals or reduced hydrogen-exchange rates for protons involved in putative hydrogen bonds. The observation of the *J* couplings through hydrogen bonds not only proved the idea proposed by Linus Pauling, that there is substantial orbital overlap in the hydrogen bonds,[1] but also provides an important clue to reveal the nature of the bonds. The theory of *J* coupling is not straightforward, but the couplings are related to the extent of orbital overlap between atoms. Observation of *J* couplings demonstrates the covalency of the bonds, although they have been considered to be purely electrostatic interactions.

2.1. Properties of hydrogen bonds

The strength of a hydrogen bond depends on its length and linearity, the nature of its microenvironment, and the degree to which the pK_a values of the conjugate acids of the heavy atoms sharing the proton are matched.[8] In water, the nearest-neighbour oxygen atoms are separated by ~0.28 nm, and the ΔH for formation was reported to be -15 ± 2 kJ mol^{-1}.[20] The relatively weak hydrogen bonds in water are proposed to be due to a large difference in the pK_a value between the participating oxygen atoms. Since the pK_a values of H_3O^+ and H_2O are -1.7 and 15.7, respectively, the proton between the oxygen atoms in the structure, H_2O—H—OH, is tightly associated with OH^- as a water molecule.[8] In the gas phase, where the dielectric constant is low, hydrogen bonds with matched pK_a values can be very short and strong, and the bond energy is reported to be as large as that of a covalent bond, i.e. 60–165 kJ mol^{-1}.[8] The O—O distance in gas-phase H_2O dimer was reported to be slightly elongated (0.298 nm), compared with the distance in water.[43,44] But the ΔE for formation of a hydrogen bond was reported to be -32 kJ mol^{-1} (ΔE and ΔH are related by a work term ΔPV (ideally RT)). In crystals, hydrogen bonds can be very strong. The O—O distance in ice is known to be 0.275 nm[45] and the distance could be much smaller in crystals of other compounds. In organic solvents, hydrogen bonds can also form and their strength depends on the polarity of the solvent. Theoretical considerations suggest that the strength of hydrogen bonds levels off dramatically when the dielectric constant of the solvent reaches a certain value.[46,47] As far as the effects of microenvironments on hydrogen bonds are concerned, characterization of the bonds in organic solvents is important for an understanding of the nature of the bonds formed in biological macromolecules.

2.2. Potential energy diagram for hydrogen bond

When an A—H bond participates in a hydrogen bond, a second potential energy minimum develops as illustrated in Fig. 1(a). Thus, in the case of moderate hydrogen bonds, an unsymmetrical double minimum potential energy curve is established (Fig. 1(b)). Hence, the hydrogen is firmly attached to either A or B and is more loosely bonded to the other one (in Fig. 1(b), the hydrogen is attached to A). Therefore, a measure of the vibration of the A—H bonds has been used as a sensitive criterion for both the formation and strength of hydrogen bonds. There is an energy barrier between the two possible positions of the hydrogen, with the zero point energy levels shown in Fig. 1(b) and (d). The hydrogen bond of this type is essentially electrostatic. If the pK_a values of A—H and B—H happen to be the same as in water, the two minima exhibit equal potential energy (Fig. 1(c)). As the bond strength increases, the energy barrier drops until it reaches the zero point energy level. Hydrogen

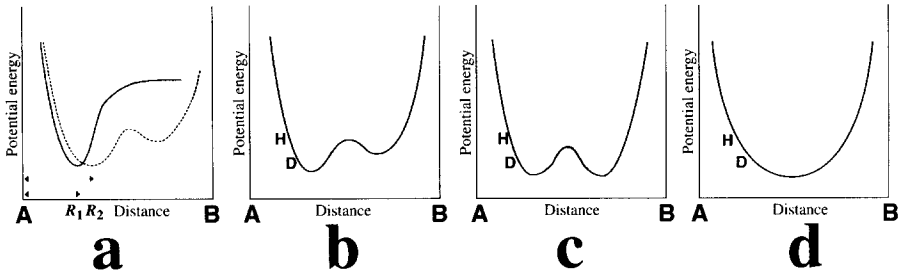

Fig. 1. Qualitative potential energy diagrams for a hydrogen bond, A–H—B. (a) Potential energy curves for a free A–H group (–) and a hydrogen-bonded A–H group with B (---). (b) Potential energy curve for an A–H—B hydrogen bond. This curve is essentially same as the one indicated by --- in (a). (c) Potential energy curve for an A–H—B hydrogen bond with the identical p*K*a values for A–H and B–H. (d) Potential energy curve for a very strong A–H—B hydrogen bond with the identical p*K*a values for A–H and B–H. The horizontal lines in (b)–(d) represent zero point energy levels for hydrogen (H) and deuterium (D).

bonds of this type are called low-barrier hydrogen bonds (LBHB (see below)). In crystals containing LBHBs, neutron diffraction shows the hydrogen to be diffusely distributed with its average position in the centre.[48] LBHBs are believed to be largely covalent.[49,50] There are number of possible structures between Fig. 1(b) and (c); as the hydrogen bond becomes stronger, the A–H bond becomes longer and, on the other hand, the covalency of the H–B hydrogen bond increases. In a few extremes with very short A–B distance, there is a single potential energy minimum and the hydrogen occupies a position exactly midway between A and B (Fig. 1(d)).

2.3. Low-barrier hydrogen bonds

There has been a great deal of interest in LBHBs, since they were proposed to play a key role in catalysis of enzymatic reactions.[8–16,51–55] Although the existence of LBHBs has been well known among organic chemists,[22] the presence of LBHBs in proteins was only recently recognized and their roles in enzymatic catalysis were then proposed.[10–12] In the proposed roles of LBHBs in enzymatic reactions,[8] a weak hydrogen bond formed upon the initial enzyme–substrate complexation is believed to be converted to an LBHB in the transition state of an enzymatic process by changing the pK_a value of the substrate to reduce the difference in the pK_a value between the donor and acceptor atoms in the hydrogen bond. For example, the pK_a values for protonated ketones are approximately −5, whereas the pK_a values of the corresponding enols are 10–14. If the ketone moiety of substrates is hydrogen-

bonded to a neutral imidazole side-chain of a histidine ($pK_a \sim 14$ for imidazolide formation), there will be a good pK_a match between the enolate and histidine (not between the ketone and histidine). The increased strength of the LBHB between the enolate and neutral histidine was proposed to provide most of the energy needed for enolization of the substrate.[8]

The effects of pK_a mismatching (ΔpK_a) on the strength of hydrogen bonds has been analysed theoretically. Shan and Herschalg showed that the variation in ΔG for formation with ΔpK_a depends on the solvent.[14,56] Although the slope for a plot of the log of the formation constant (K) as a function of ΔpK_a is only 0.05 in water, it is 0.73 in dimethyl sulfoxide for a series of salicylate monoanions and 0.65 in tetrahydrofuran for complexes between phenoles of varying pK_a value. Enzyme active sites are non-aqueous, and obviously the effective dielectric constants resemble those in organic solvents rather than that in water. Although a linear relationship between the $\log(K)$ and ΔpK_a cannot be assumed over the entire range of pK_a values, a weakening of the hydrogen bond by a factor of 5 for each unit of ΔpK_a is estimated with the assumption of a slope of 0.7 for the $\log(K) - \Delta pK_a$ correlation. This consideration qualitatively provides the stabilization energy potentially available to a transition state of the enzyme–substrate complex by LBHBs, which contributes to reduce the activation energy for enzymatic reactions.

3. NMR CHARACTERIZATION OF HYDROGEN BONDS

In macromolecules, the presence of hydrogen bonds is indicated by the spatial proximity and relative arrangement of the atoms involved, after the structure has been solved by either crystallography or NMR. A variety of NMR spectroscopic parameters have been used for characterizing these important interactions.

3.1. Observation of spin–spin couplings through hydrogen bonds

The J coupling transmitted via a hydrogen bond was first observed in proteins between a backbone amide proton and ^{113}Cd through a Cys sulphur atom coordinated to the metal ion,[57,58] i.e., $^{2h}J_{NCd}$ for NH—S⟶Cd, where — and ⟶ represent hydrogen- and ligand-bonds, respectively, and the superscript, h, to the J indicates the coupling through a hydrogen bond. Dingley and Grzesiek[42] have shown that the existence of hydrogen bonds can be established in ^{15}N-labelled nucleic acid base pairs by the observation of $^{2h}J_{NN}$, the coupling constant between the nitrogen atoms in the N–H—N interaction. These J coupling constants seem to correlate well with hydrogen bond length and can be used to identify the coupling partner directly.[59,60] $^{2h}J_{NN}$ values of 6–7 Hz for the Watson–Crick base pairs of RNA were detected[42] and these values are

almost comparable to the $^{2}J_{NN}$ values, generally <10 Hz. In certain cases, anomalously large coupling constants are observed for nuclei many bonds apart, but physically close in space. This occurs particularly for $^{n}J_{FF}$, particularly $n > 4$.[61] There appears to be a direct electron spin correlation between electrons of fluorine atoms close in space. Hence, observation of the relatively large $^{2h}J_{NN}$ values[42] provides direct evidence for the covalency of the hydrogen bond in the N–H—N interaction. Generally, the $^{2h}J_{NN}$ value of the adenosine–uridine (A—U) base pair is slightly larger than that of the guanosine-cytidine (G—C) base pair. This result has been interpreted on the basis of a shorter N—N distance in the former base pair observed in crystal structures. Since the first report on the observation of the $^{2h}J_{NN}$ value for Watson–Crick base pairs in ^{15}N-labelled RNA,[42] the $^{2h}J_{NN}$ ($6.0 \pm 0.1 - 7.0 \pm 0.1$ Hz) and $^{1h}J_{NH}$ ($1.8 \pm 0.2 - 3.7 \pm 0.3$ Hz) for Watson–Crick base pairs in ^{15}N-labelled DNA have been demonstrated.[62] The mean values of the $^{2h}J_{NN}$ were reported to be 10.1 ± 0.3 Hz for Hoogsteen G—C^{+}(protonated cytidine), 8.5 ± 0.4 Hz for Watson–Crick A—T, 7.2 ± 0.7 Hz for Hoogsteen A—T, and 6.6 ± 0.6 Hz for Watson–Crick G—C base pairs.[59] In addition, there is a distinct decrease of about 1–6.6 Hz in the $^{2h}J_{NN}$ values for the Watson–Crick and Hoogsteen T—A base pairs located at each end of the DNA triplex. Since the observed couplings represent a time and ensemble average over the states of the molecule, such a reduction in the $^{2h}J_{NN}$ value could be attributed to an increase in the distance between the donor and acceptor groups or to a shift of the dynamic equilibrium between closed and open states of the base pair toward the latter.[59]

The observations of other J couplings such as $^{3h}J_{C'N}$,[63–65] $^{2h}J_{C'H}$,[65,66] $^{2h}J_{NN}$,[67] $^{2h}J_{HP}$,[68] $^{3h}J_{NP}$,[68] $^{3h}J_{CH}$,[69] $^{4h}J_{NN}$,[70] have been reported. Theoretical studies demonstrated that the J coupling through a hydrogen bond is interpreted within the framework of ordinary quantum chemical calculations, as in the case of the usual J couplings, and is closely related to the hydrogen bond geometry.[59,71–73] Thus observation of the J coupling through a hydrogen bond not only allows the identification of the pair of donor and acceptor atoms sharing the same hydrogen atom, but also provides important information for structural chemical characterization of hydrogen bonds.

3.2. ^{1}H NMR probe for hydrogen bond of distal residue to bound ligand in haemoprotein

Heme electronic structures can depend sensitively and selectively on molecular structure details, that very subtle aspects of the heme environment may be elucidated by their influences on hyperfine shifts.[74–78] Myoglobin (Mb) is a monomeric b-type haemoprotein of ~17k Da and its protein moiety consists of eight helices, A–H, that are linked by short polypeptide segments to form an oblate spheroid molecule (Fig. 2). Lecomte and La Mar[79] reported that

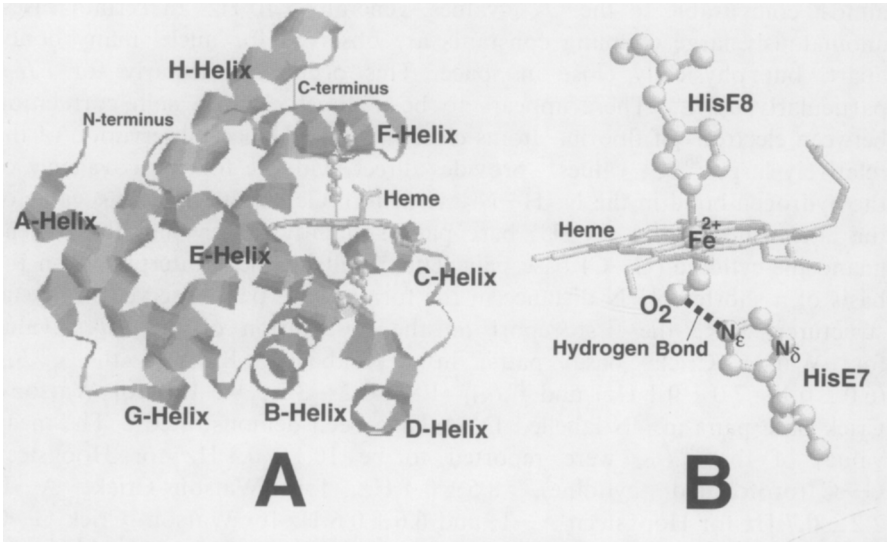

Fig. 2. (A) The myoglobin molecule is built up from eight stretches of α helices, A–H, that form a cavity for the heme group, represented by stick model. Two histidine residues, HisE7 and HisF8, which are relevant to the function of myoglobin are indicated by a ball-and-stick model. PDB file, 4MBN, was used to draw this picture. (B) Schematic representation of interactions among the heme group, HisE7, HisF8, and Fe-bound O_2. A broken line represents the hydrogen bond between HisE7 and Fe-bound O_2.

differences in the heme hyperfine shift which depend only on whether the ligated cyanide ion in met-cyano Mb (metMb(CN^-)) (see Fig. 3) is stabilized by a hydrogen bond with the participation of ^1H or ^2H, to the distal HisE7 (E7 is the alphanumeric code referring to the position of the residue in the primary structure of Mb and represents the 7th residue in the E helix) side-chain can be detected through the observation of paramagnetically shifted signals. The ligand-binding properties of hemoproteins depend crucially on the specific interaction of the axial ligands with the protein matrix. Hydrogen bonding can involve either the HisF8 imidazole or a direct interaction between the HisE7 imidazole and a bound ligand. The influence of such hydrogen bond on the active site structure of hemoproteins has been primarily detected by the observation of the solvent isotope effects on vibrational frequency[80] or EPR spectral change.[78] Although these techniques clearly detect localized effects due to hydrogen bonds, they seldom provide identification of the participating proton. Hydrogen bonds by an axial histidyl imidazole or a bound ligand are detected by crystallographic techniques,[81–83] but in the presence of several such interactions, their functional consequences cannot be inferred from crystal structures. The increased resolution for heme cavity residues in paramagnetic

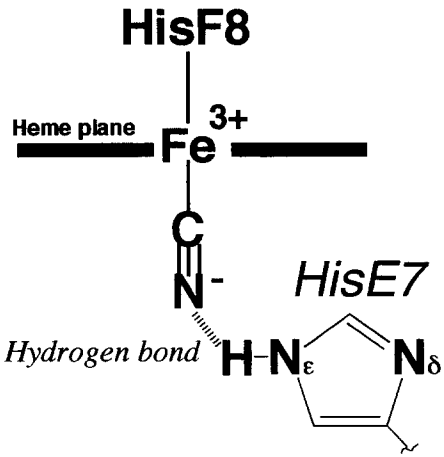

Fig. 3. The coordination of CN^- to heme iron in metMb(CN^-). The ligation of CN^- to the heme is stabilized by a hydrogen bond with HisE7.

complexes and the high sensitivity of the hyperfine shift to small structural perturbations allow ready elucidation of the hydrogen bond.

The high-frequency shifted portions of the 500 MHz ^1H NMR spectra of sperm whale metMb(CN^-) in 90 : 10 and 50 : 50 mixtures of H_2O and ^2H_2O are illustrated in traces A and B of Fig. 4, respectively. The signals resolved in this region of the spectra have been characterized exhaustively.[75,77] Comparison of the traces revealed that the trace 4B corresponds to the spectrum of a 1 : 1 superposition of the subspectra observed in the isotopically pure solvents. As indicated in the inset of the trace B, the relative splitting of the heme methyl proton signals are about 20–30 Hz. Thus isotope composition of the solvents exerts an influence on the electronic structure of the heme and the two species differentiated by the solvent isotopes are in slow exchange on the NMR timescale under these experimental conditions. The response of the two 12-methyl signal intensities to variable solvent isotope composition is illustrated in Fig. 5. In any solvent mixture, there are two signals per heme methyl proton and their relative intensity is identical with the bulk ^1H:^2H solvent composition, indicating that the isotope perturbation on the heme electronic structure is attributed exclusively to a single $^1H/^2H$ exchange site in the protein. The high-frequency shifted component for each heme methyl signal corresponds to the '^1H' form, while the low-frequency shifted component arises from the '^2H' form in each case. Splitting for other resonances was not observed. The effect of pH displayed in traces D—G of Fig. 5 demonstrates that the dynamic collapse of the two 12-methyl signals is acid-catalysed. Furthermore, the lines remain well resolved and sharp up to pH 10.4. HisE7 imidazole ring NH proton exhibits a compatible exchange behaviour.[84,85]

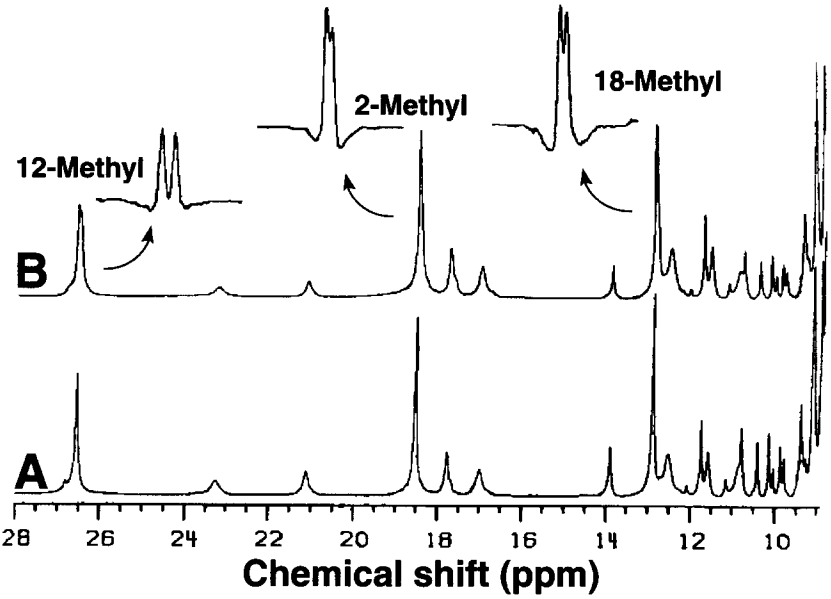

Fig. 4. High-frequency shifted portions of the 500 MHz ^1H NMR spectra of sperm whale metMb(CN^-) at pH 9.2, 30 °C. (A) In 90:10 = H_2O:^2H_2O. (B) In 49:51 = H_2O:^2H_2O. The expanded plots show the three resolved heme methyl signals after resolution enhancement by sine-bell function; the vertical scale is arbitrary, frequency scale magnified by a factor of 5. Asymmetry in the expanded peaks is due to overlapping lines of different width. (From ref. 79, © 1987, with permission from the publishers.)

The relative magnitude of the isotope splitting and the fact that only heme resonances exhibit such splitting demand that the contact contribution to the paramagnetic shift be sensitive to the $^1H/^2H$ replacement. The resolved '^1H' heme methyl proton signals are all high-frequency shifted relative to the corresponding signals for the '^2H' component and this result has been interpreted as being due to the larger heme in-plane asymmetry in ^1H_2O than in ^2H_2O.[79] This can be rationalized by the observation that the CN^- is tilted from the heme normal and suggests that the differential hydrogen bond with ^1H or ^2H either induces an electronic perturbation in the Fe—CN^- bond or causes a small change in the tilt angle. Although the absence of an isotope effect on the bound cyanide ion stretching frequencies in metMb(CN^-) favours the latter interpretation, the isotopic effect on a direct electronic interaction between the heme and the HisE7 side-chain through the hydrogen bond cannot be ruled out. A similar isotope perturbation on the heme electronic structure has been observed for a mollusc Mb.[86]

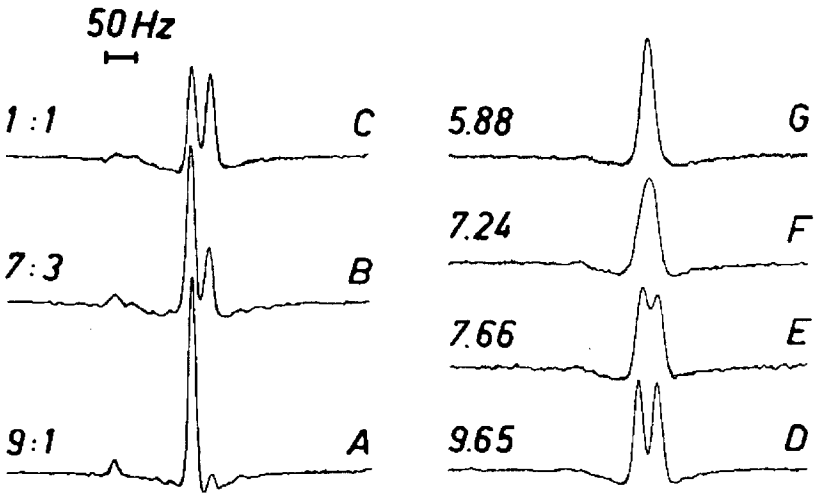

Fig. 5. Heme 12-methyl signal(s) of sperm whale metMb(CN^-) at 30 °C. (A–C) At pH 9.2 as a function of solvent composition (H_2O:^2H_2O): (A) 9 : 1, (B) 7 : 3, (C) 1 : 1. (D–G) In 1 : 1 H_2O:^2H_2O as a function of pH: (D) pH 9.65, (E) pH 7.66, (F) pH 7.24, (G) pH 5.88. (From ref. 79, © 1987, with permission from the publishers.)

Furthermore, the observed shift of the HisE7 $N_\varepsilon H$ proton signal of sperm whale metMb(CN^-) demonstrates the existence of unpaired electron delocalization from heme iron to this proton through the hydrogen bond.[87] The observed shift (δ_{obs}) of a signal for paramagnetic metMb(CN^-) is the sum of diamagnetic (δ_{dia}) and paramagnetic (δ_{para}) shifts. δ_{dia} is the shift that would have been observed if the molecule contained no unpaired electron and δ_{para} is the shift due to the permanent magnetic moment of the unpaired electron. δ_{para} is expressed by the sum of contact (δ_c) and pseudo-contact (δ_{pc}) shifts.[75] The former is related to delocalization of the unpaired electron and the latter is due to the magnetic dipolar field arising from the unpaired electron at the heme iron. The δ_{obs} value is 23.67 ppm for HisE7 $N_\varepsilon H$ proton signal of metMb(CN^-), pH 8.6, at 25 °C.[88] The value of 3.88 ppm is estimated for its δ_{dia} from the consideration of porphyrin ring-current shift.[89] Hence the δ_{para} contribution is calculated to be 19.79 ppm. This δ_{para} value cannot be solely accounted for by δ_{pc} that is determined to be 25.59 ppm for this proton.[90] Consequently, the value of −5.80 ppm is attributed to the δ_c contribution. This result indicates that the unpaired electron is delocalized to the HisE7 $N_\varepsilon H$ proton through the hydrogen bond. The unpaired electron density at the nitrogen atom of the Fe-bound ligand in metMb(CN^-) cannot be determined quantitatively due to the lack of the knowledge of δ_{dia} for this nitrogen signal. But the fact that its δ_{obs} is >1000 ppm relative to the signal of free CN^-[85,87,91]

suggests that there is a considerable high-frequency contribution of δ_c to its shift, i.e. δ_c of the Fe-bound CN^- nitrogen signal is positive. The difference in the sign between the δ_c values for HisE7 $N_\varepsilon H$ proton and Fe-bound CN^- nitrogen dictates that the delocalization of unpaired electron is through the spin polarization mechanism. Although the pattern of this hydrogen bond is different from those generally found in biological macromolecules, the spin polarization mechanism in the delocalization of an unpaired electron through the hydrogen bond in metMb(CN^-) is consistent with the observation of positive $^{1h}J_{NH}$ couplings in nucleic acids.[62]

The interaction of HisE7 side-chain with Fe-bound oxygen in Hb has been characterized through a multidimensional multinuclear NMR study of subunit-selectively labelled Hb.[92–95] Determination of the tautomeric state of the HisE7 imidazole ring[96] and analysis of the exchange of HisE7 $N_\varepsilon H$ hydrogen, together with structural determination based on the analysis of ^1H NMR shifts, have been utilized to prove the formation of a hydrogen bond between HisE7 imidazole NH hydrogen and Fe-bound oxygen in each subunit of Hb in solution.[95]

3.3. Conventional methods

Various NMR observations give indirect evidence for the existence of hydrogen bonds in macromolecules: (i) the reduced hydrogen-exchange rates with the solvent;[97,98] (ii) the interatomic distances estimated from the measurements of nuclear Overhauser effect (NOE);[99] (iii) the primary isotope shifts for substitution of the hydrogen-bonded proton by ^2H or/and ^3H;[100, 101] (iv) the isotropic proton chemical shift;[102] (v) the isotropic nitrogen chemical shift;[103] (vi) the magnitude of the electric field gradient at the site of the proton as observed by the ^2H quadrupolar coupling constant;[104, 105] (vii) the magnitude of the proton chemical shift anisotropy;[106, 107] (viii) the measurements of the sequential one bond $^1J_{CN}$ coupling constants in proteins;[108] and (ix) low deuterium atom fraction factor.[22, 109–112]

Within the same well of the potential energy curve, the zero-point energy of the deuterium atom is lower than that of the hydrogen atom because of the difference in their masses (Fig. 1). Deuterium becomes enriched in more stiffly bonded positions, and the fractionation factor measures the degree of discrimination against deuterium in a given bond relative to the OH bonds in water. Because the covalent O—H distance increases from ~0.10 to ~0.12 nm as a weak hydrogen bond is converted to a LBHB, the bond order decreases and thus the discrimination against deuterium increases. Fractionation factors as low as 0.3 have been observed for the nitrophenolate ion in organic solvents.[113] The fractionation factor of the hydrogen in a LBHB in a protein can be measured by integrating the high-frequency shifted ^1H NMR signals in $H_2O/^2H_2O$ mixtures.

4. INTERNAL HYDROGEN BONDS IN METALLOPROTEINS

Crystallographic studies of Mbs,[81–83,114–116] cytochromes c[117,118] (cyt-c), and superoxide dismutase[119] revealed many internal hydrogen bonds between the side-chains of hydrophilic amino acid residues, that are proposed to stabilize the tertiary structure of the proteins. In particular, His residues are often involved in hydrogen bonds in the interfaces between helical and loop regions, which contribute to stabilize protein folding. These internal hydrogen bonds can be used as sensitive probes for characterizing the local structure of a protein.[75,101,109–113,120–137]

4.1. His imidazole ring NH hydrogen atoms at the interfaces between helix and loop regions in myoglobin

^{1}H signal assignments in the diamagnetic carbonmonoxy form of sperm whale Mb (Mb(CO)) have been investigated extensively by Wright and co-workers,[99,138–144] and ~95% of the signals of the Mb have been assigned by an NOE-based sequential assignment procedure using uniformly ^{15}N-labelled protein.[139] There are twelve His residues in the Mb. The site-specific titration behaviours of all the His residues in the Mb have been characterized in detail

Table 1. Histidine residues in sperm whale and horse myoglobins

Histidine	Solvent exposure (nm^2)		Contacts in myoglobin	pKa [c]
	Sperm whale[a]	Horse[b]		
12(A10)	1.14	—	Myoglobin solvent	6.4
24(B5)	0.03	0.07	N_ε—His119 N_ε, N_δH—Asp20(B1) peptide O hydrogen bond	<4.8
36(C1)	0.46	0.48	G Helix [Phe106(G7)]	8.2
48(CD6)	1.18	1.03	Solvent	5.5
64(E7)	0.03	0.09	Fe-bound ligand	<5
81(EF4)	1.34	1.37	Solvent	6.7
82(EF5)	0.06	0.06	N_εH—Asp141(H18)O_δ hydrogen bond	<4.8
93(F8)	~0	0.01	N_ε—Fe coordinate bond, N_δH—Leu89(F4) peptide O hydrogen bond	<5
97(FG3)	0.33	0.25	N_εH—Heme 17-propionate carboxyl O salt bridge	5.6
113(G14)	0.72	0.82	Solvent	5.4
116(G17)	1.04	0.66	Solvent	6.6
119(GH1)	0.21	0.27	N_εH—His24(B5) N_ε hydrogen bond	6.1

[a] From ref. 114. PDB file: 4MBN.
[b] From ref. 117. PDB file: 1YMB.
[c] From ref. 145.

from the analysis of pH dependence of the shifts for His imidazole ring CH proton signals in order to investigate electronic environments around the individual residues.[144–148] However, a His imidazole ring NH proton signal, except HisF8 $N_\delta H$ proton signal, has not been located. In general, these labile proton resonances are quite elusive and not always observable due to rapid hydrogen exchange. However, in cases where it is buried in the protein matrix and involved in an internal hydrogen bond, its moderate hydrogen exchange and magnetically deshielded environment enable one to observe their NMR resonances in the high-frequency shifted region of the spectra.[30–34]

According to the X-ray structure of Mb,[83,114–116] five His residues, i.e. 24(B5), 82(EF5), 93(F8), 97(FG3), and 119(GH1), are proposed to be involved in internal hydrogen bonds through their side-chains (Table 1). As shown in Figs 6 and 7, HisB5 and HisGH1 are involved in a unique internal hydrogen bond such that the $N_\varepsilon H$ proton of HisGH1 is hydrogen-bonded to the N_ε atom of HisB5 and the $N_\delta H$ proton of HisB5 interacts with the peptide carbonyl oxygen of Asp 20(B1).[81–83,114–116] This internal hydrogen bond is believed to stabilize the interface between the B helix and the GH loop. On the other hand, the $N_\varepsilon H$ proton of HisEF5 is hydrogen-bonded to the O_δ of Asp 141(H18) and this internal hydrogen bond stabilizes the interface between the EF loop and

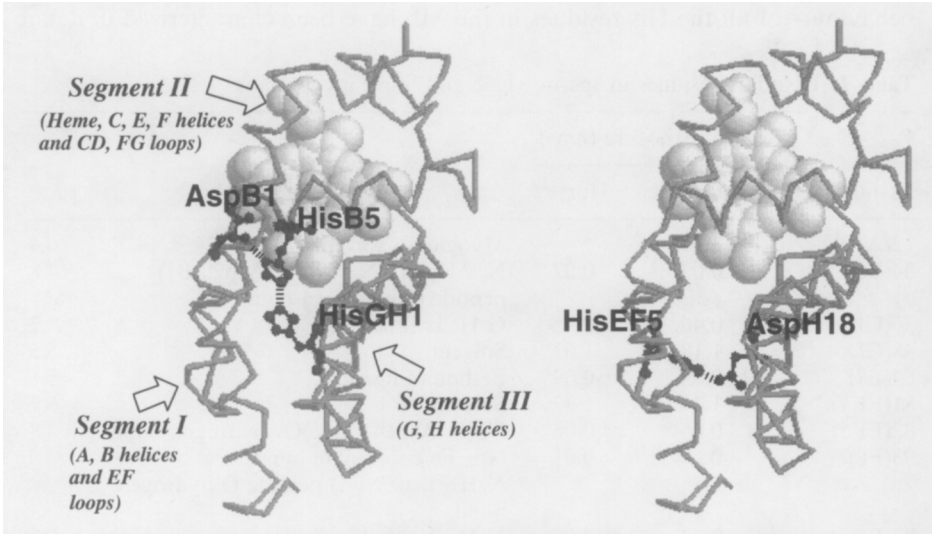

Fig. 6. The inter-segmental hydrogen bonds of AspB1—HisB5—HisGH1 (left) and HisFE5—AspH18 (right). PBD file, 4MBN, was used to draw the structure of sperm whale Mb. Except for the residues involved in the inter-segmental hydrogen bonds, only back-bone folding is drawn and heme is indicated by a space-filling model. The structure of Mb is roughly divided into three segments I–III as indicated by arrows, i.e. I (A and B helices and EF loop), II (Heme and C, E, F helices and CD and FG loops) and *III* (G and H helices). Hydrogen bonds are indicated by thick broken lines. (From ref. 121, © 1997, with permission from the publishers.)

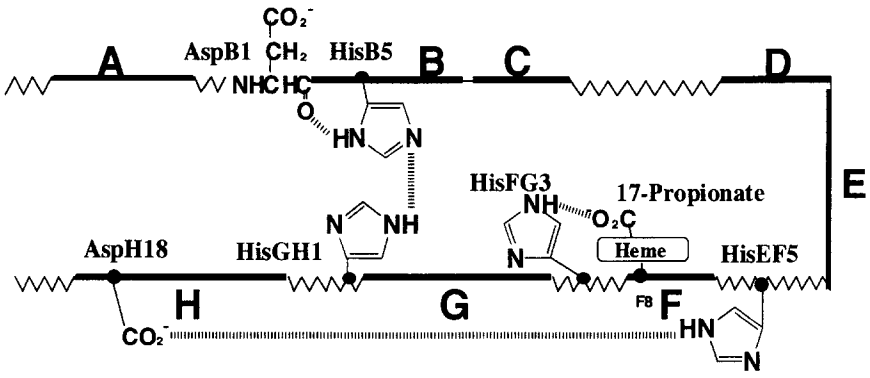

Fig. 7. Schematic representation of the AspB1—HisB5—HisGH1 and HisEF5—AspH18 hydrogen bonds in Mb. A–H helices are represented by thick lines and loops, non-helical regions, are indicated by zigzag lines. Internal hydrogen bonds are indicated by broken lines. (From ref. 122, © 1997, with permission from the publishers.)

the H helix.[81–83,114–116] Conformational alterations at these interfaces are expected to be sensitively manifested in NMR spectral parameters of these His NH proton signals.

4.2. Observation of high-frequency shifted His imidazole ring NH proton signals

The 400 MHz ^{1}H NMR spectrum of sperm whale met-hydroxyl Mb (metMb(OH^-)) in 90%H_2O/10%^2H_2O, pH 9.47, at 5 °C is illustrated in Fig. 8. Three peaks are resolved in the high-frequency shifted region (>11.5 ppm). The disappearance of these peaks in the spectrum of ~100% ^2H_2O samples confirms that they arise from exchangeable protons. The difference in the resonance frequency between these signals and the bulk water signal dictates that their hydrogen exchange rates should be $\ll 3\times10^3$ s^{-1}. Their shifts and hydrogen exchange rates resemble those of His imidazole ring NH or Trp indole $N_\varepsilon H$ hydrogen, which is buried in the protein matrix and possibly involved in an internal hydrogen bond.[30,98,125,126] The reported assignments for the HisF8 $N_\delta H$ proton signal and the indole $N_\varepsilon H$ proton signals for all the Trp residues in sperm whale Mb[139] preclude these protons from being candidates for the assignments of these peaks. Signal assignments are obtained from observation of the NOE connectivities. The high-frequency shifted portion of the 400 MHz ^{1}H NMR spectrum of metMb(OH^-) in 90%H_2O/10%^2H_2O, pH 9.47, at 5 °C is illustrated in trace A of Fig. 9. The NOE difference spectra recorded with the selective saturation of each peak are illustrated in traces 9B–9D. Peak **a** can be observed under the limited experimental conditions of low temperature and pH ~10 (see below). The saturation of peak **a** yielded

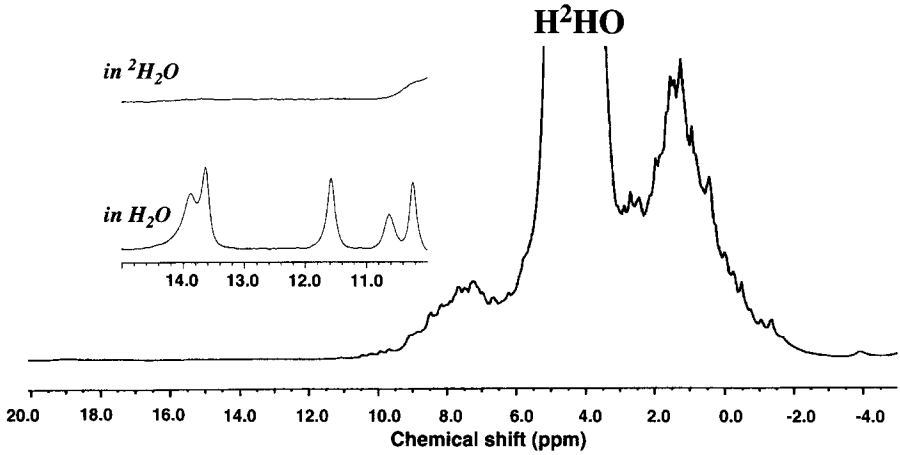

Fig. 8. The 400 MHz ^1H NMR spectrum of sperm whale metMb(OH^-) in 90%H_2O/10%^2H_2O, pH 9.47, at 5 °C. In the inset, the high-frequency shifted portion, 10–15 ppm, of the spectrum (lower) is expanded, together with the corresponding portion of the spectrum in ~100%^2H_2O (upper).

NOEs to peaks at 6.71 and 7.79 ppm. Both the NOE connectivities and their shifts strongly suggest that peak **a** arises from a His side-chain imidazole ring $N_\varepsilon H$ proton that is involved in an internal hydrogen bond and that peaks at 6.71 and 7.79 ppm due to $C_\delta H$ and $C_\varepsilon H$ protons, respectively, of the same residue. Peak **b** also exhibits similar NOE connectivities (trace 9C) to those in trace 9B. Furthermore, the NOE difference spectra observed in the pH range 6.5–9 indicated that their shifts are essentially independent of pH. There are two His residues that are buried in the protein matrix and participate in intramolecular hydrogen bonds through $N_\varepsilon H$ hydrogen (Table 1). As mentioned above, one is HisEF5 of which $N_\varepsilon H$ hydrogen is accepted by the carboxyl oxygen of the AspH18 side-chain to form a hydrogen bond and the other is HisGH1 of which $N_\varepsilon H$ hydrogen is donated to N_ε of HisB5 to form a hydrogen bond. According to the X-ray structure of sperm whale Mb,[83,114–116] solvent-exposure surface areas of HisEF5 and HisGH1 are estimated to be 0.06 and 0.21 nm^2, respectively (Table 1). Since the p*K*a value of HisEF5 is <4.8 (Table 1),[145] the absence of pH-dependent shift for the signals in trace 9B supports their arising from HisEF5 imidazole ring protons. Their shifts are close to those reported previously.[139] Hence, the signals observed in trace 9B can be attributed to side-chain imidazole ring protons of HisGH1. The saturation of peak **c** exhibits NOEs to peaks at 7.57 and 7.71 ppm (trace 9D). The intensity of the signal at 7.57 ppm is influenced by the solvent composition ($H_2O/^2H_2O$), indicating that this signal arises from an exchangeable proton. Additionally, these signals exhibit no significant pH-dependent shift change in the pH range 6.5–9. Their shifts are similar to the values reported for HisB5

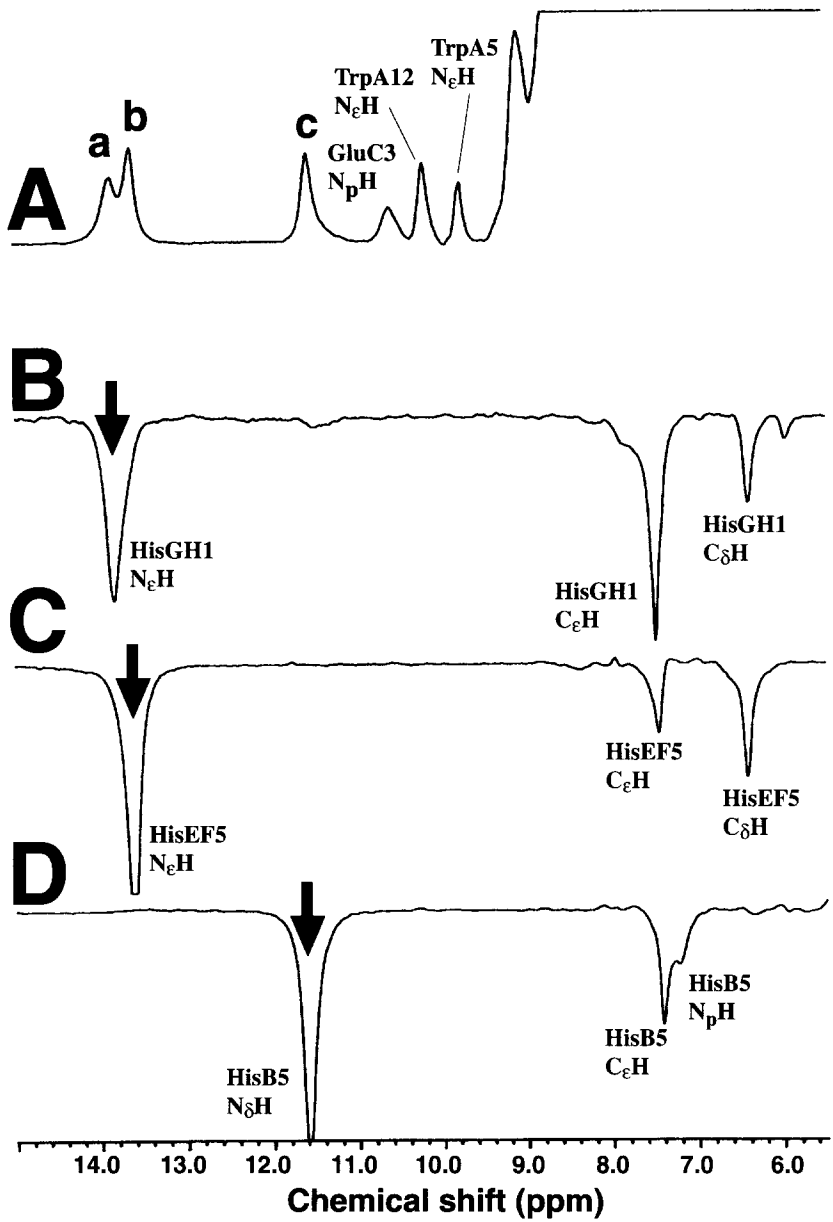

Fig. 9. (A) The high-frequency shifted portion of the 400 MHz ^{1}H NMR spectrum of sperm whale metMb(OH^-) in 90%H_2O/10%^2H_2O, pH 9.47, at 5 °C. Three peaks, **a**–**c**, are resolved below 11.5 ppm. (B) The NOE difference spectrum resulting from saturation of peak **a**. The peaks at 6.71 and 7.79 ppm exhibit NOEs. (C) The NOE difference spectrum resulting from saturation of peak **b**. The peaks at 6.72 and 7.76 ppm exhibit NOEs. (D) The NOE difference spectrum resulting from saturation of peak **c**. The peaks at 7.51 and 7.71 ppm exhibit NOEs. The signal assignments are indicated in traces B—D. The signals at 9.5–11.5 ppm have been assigned previously.[139] (From ref. 187, with permission from Elsevier Science.)

main-chain amide NH (N_pH) and imidazole ring $C_\varepsilon H$ hydrogens,[139] which are located at 0.25 and 0.27 nm, respectively, away from HisB5 $N_\varepsilon H$ hydrogen. Besides HisF8, HisB5 is the only residue whose $N_\delta H$ proton participates in an internal hydrogen bond and is buried in protein matrix (its solvent exposure is 0.03 nm^2 (Table 1)). Hence, the signals in trace 9D can be attributed to protons of HisB5. The observation of these His imidazole ring NH proton signals in the high-frequency shifted region provides clear evidence that they participate in internal hydrogen bonds in the protein in solution. NOESY can also be used to identify NOE connectivities among these His proton signals (Fig. 10) and double-quantum spectroscopy is used to locate His $C_\delta H$ and $C_\varepsilon H$ proton signals.[144,145] Furthermore, peaks at 9.5–11.5 ppm have been assigned to GluC3 N_pH, TrpA12 $N_\varepsilon H$, and TrpA5 $N_\varepsilon H$ protons as indicated in trace 9A.[139]

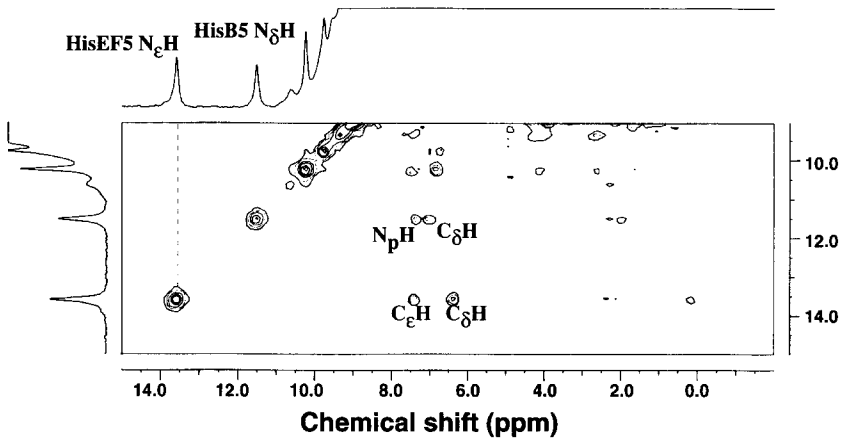

Fig. 10. A portion of NOESY spectrum of sperm whale metMb(OH^-) in 90%H_2O/10%^2H_2O, pH 9.47, at 25 °C. The NOE connectivities of HisB5 and HisEF5 proton signals are indicated. A mixing time of 10 ms was used.

4.2.1. Effects of temperature on the His imidazole ring NH proton signals

The temperature dependence of the high-frequency shifted portions of the 400 MHz ^1H NMR spectra of sperm whale metMb(OH^-) is illustrated in Fig. 11. Slight low-frequency shift and considerable exchange broadening are observed for all signals with increasing temperature. These results are in sharp contrast with the temperature dependence of paramagnetically high-frequency shifted signals, which generally exhibit narrowing and large low-frequency shift with increasing temperature. Since these His imidazole ring NH protons are at least 1.5 nm away from heme iron, the paramagnetic contribution of unpaired electron(s) to their NMR parameters is essentially negligible. The plots of their

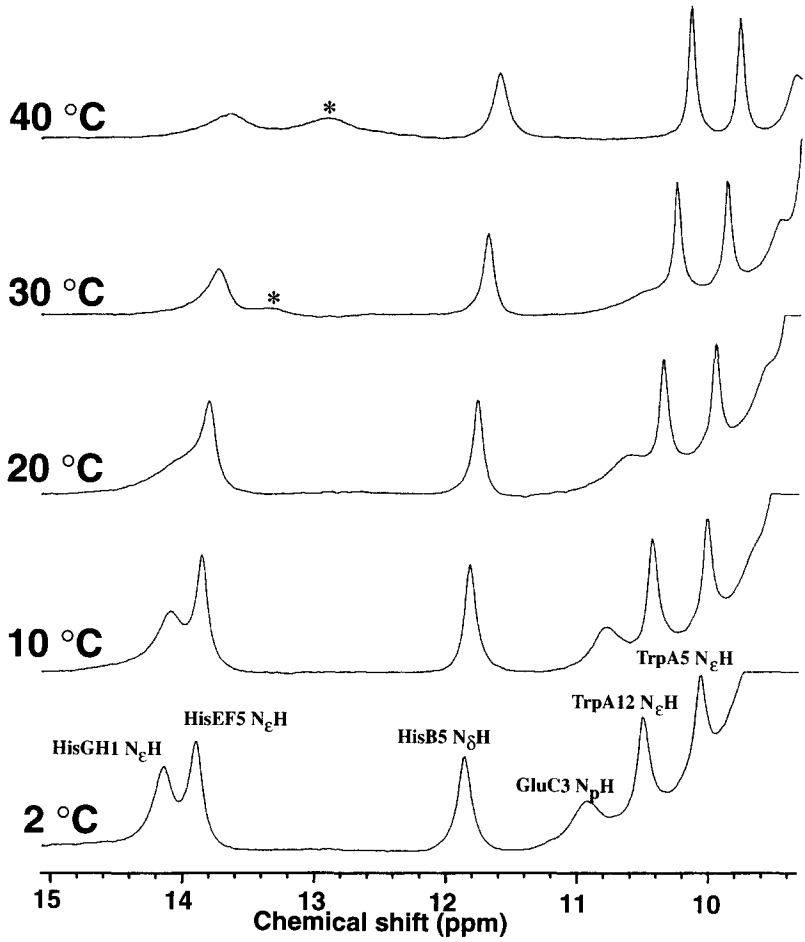

Fig. 11. The high-frequency shifted portions of the 400 MHz ^{1}H NMR spectra of sperm whale metMb(OH^-) in 90%H_2O/10%^2H_2O at pH 9.47 and the indicated temperatures. A paramagnetically shifted signal is labelled by an asterisk.

shifts against temperature exhibit straight lines in the temperature range examined, 2–45 °C.

4.2.2. Effects of pH on the His imidazole ring NH proton signals

The pH dependence of the high-frequency shifted portions of the 400 MHz ^{1}H NMR spectra of sperm whale metMb(OH^-) is illustrated in Fig. 12A. The

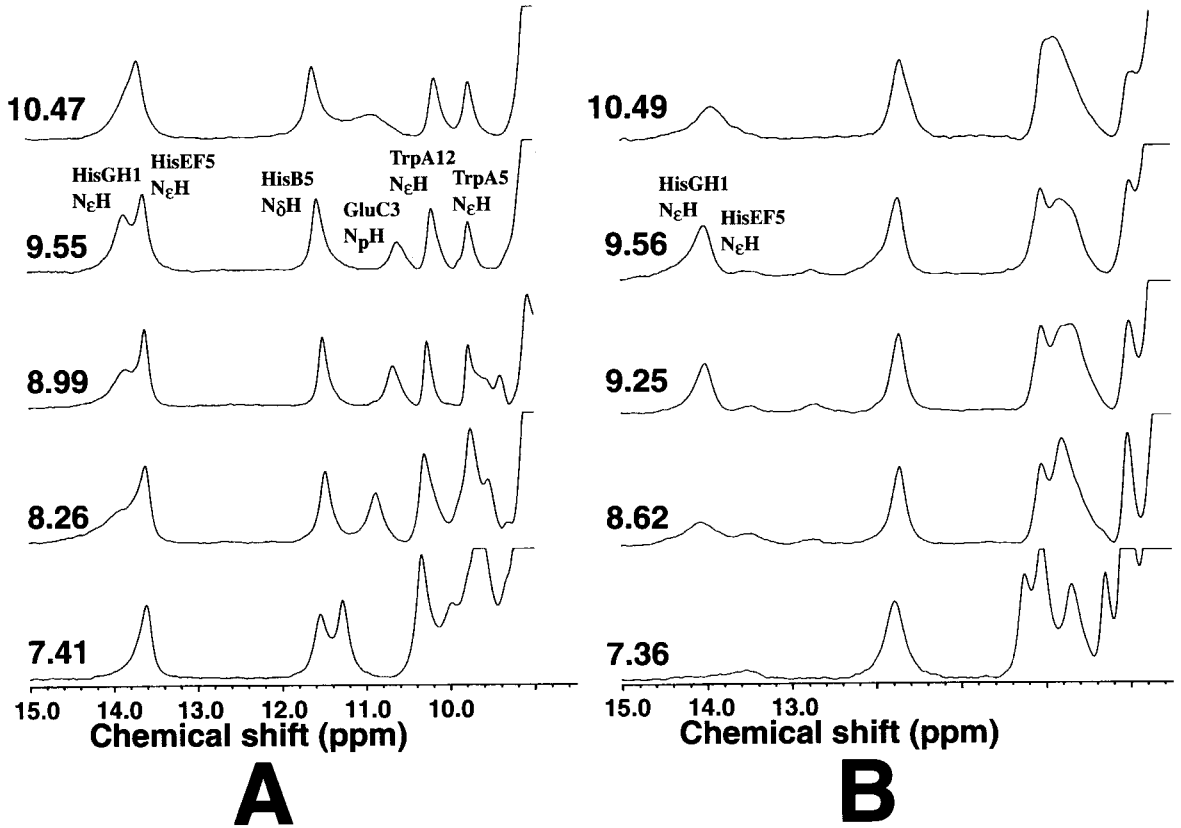

Fig. 12. The high-frequency shifted portions of the 400 MHz ^1H NMR spectra of sperm 90%H_2O/10%^2H_2O at 5 °C and the indicated pH values. (From ref. 187)

signals exhibit their characteristic pH-dependent hydrogen exchange behaviours. In a slow exchange regime such as observed in the present case, the linewidth of a labile proton signal increases with increasing exchange rate. These His NH proton signals exhibit intrinsic spin–lattice relaxation rates of 15–25 s^{-1} at pH ~9.5 and 5 °C, and saturation transfer experiments yielded saturation transfer factors of 0–0.62 for these signals in the pH range 7–11. The pH profiles of the calculated hydrogen exchange rates for these protons are illustrated in Fig. 13. The plots show both acid and base catalyses in their exchange, with the minimum rate at pH ~9.5.

The hydrogen exchange rate (k_{ex}) is usually expressed as,[149]

$$k_{ex} = k_a[H^+]^n + k_b[OH^-]^m + k_W$$

where k_a, k_b, and k_W are the rate constants for H^+, OH^- and H_2O catalyses,

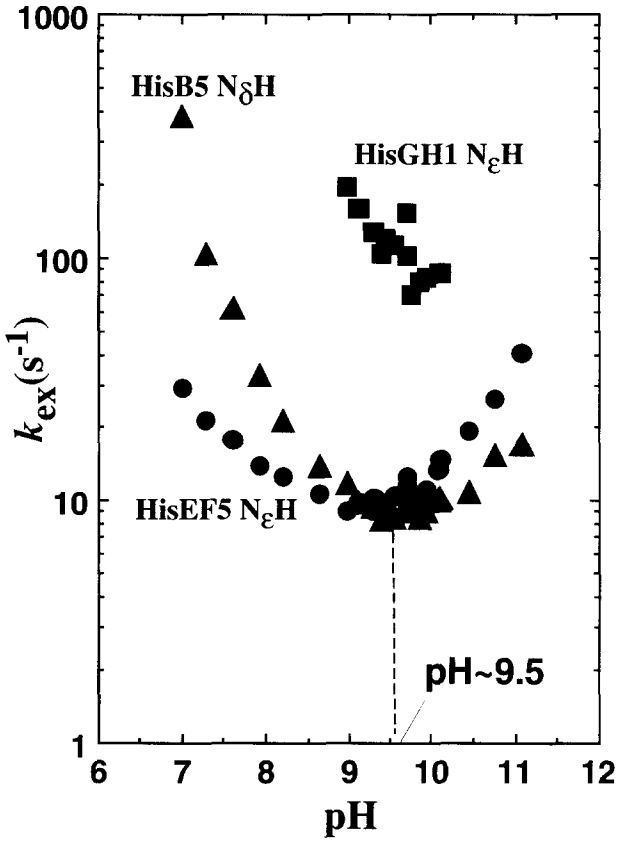

Fig. 13. Plots of hydrogen exchange rate of HisB5 $N_\delta H$ (▲), HisEF5 $N_\varepsilon H$ (●), and His GH1 $N_\varepsilon H$ (■) at 5 °C as a function of pH.

respectively. k_a and k_b depend on the local environment of the labile proton. In the extreme case where the labile proton is fully exposed to the bulk water, the exponents n and m are expected to be unity with k_a and k_b values close to those observed for a model compound or denatured protein.[150,151] Thus the pH value at the minimum rate reflects the relative contribution of the first two terms, i.e. acid- and base-catalyses, in the above equation to k_{ex}. In the present case, the observed increase in the pH value at the minimum rate for HisGH1 can be interpreted as the increased contribution of acid-catalysis, relative to that of base-catalysis, to k_{ex} at a given pH value. Such an alteration in acid-catalysis in the His imidazole ring NH hydrogen exchange may be ascribed to the increase of the p*K*a value for the HisGH1 imidazole ring. In fact, the p*K*a value of HisGH1 is larger than those of HisB5 and HisEF5.[144,146]

4.2.3. Effects of ionic strength on the His imidazole ring NH proton signals

The high-frequency shifted portions of the 400 MHz ^{1}H NMR spectra of sperm whale metMb(OH^-) in the presence of various concentrations of NaCl are illustrated in Fig. 14. As seen in the spectra, the high-frequency shifted His imidazole ring NH proton signals are highly sensitive to the salt concentration. Two different mechanisms would account for the effects of ionic strength on these His signals. Mb structure may be entirely or locally influenced through the modulation of electrostatic interaction, which contributes to the stabilization protein folding, by an increase in salt concentration. Moreover, the addition of salt could lead to alterations of microenvironments of these hydrogen bonds, which in turn affect the electrostatic interaction between donor and acceptor and/or their p*K*a values.[148]

4.2.4. Other myoglobins

The high-frequency shifted portions of the 400 MHz ^{1}H NMR spectra of horse and bovine metMb(OH^-)s are compared with that of sperm whale metMb(OH^-) in Fig. 15. The pH value of each Mb sample was adjusted to observe the HisGH1 $N_\varepsilon H$ proton signal with minimum linewidth. Horse and bovine Mbs possess a high sequence homology of over 80% with sperm whale Mb, and the His residues that exhibit the side-chain NH proton signals in the region >11.5 ppm are all conserved in these Mbs. Consequently, the assignments of the signals in traces 15B and 15C can be simply obtained from spectral comparison. Similarly to the case of sperm whale Mb,[81–83,114–116] crystallographic study of horse Mb revealed that HisEF5 $N_\varepsilon H$ hydrogen is donated to O_δ of AspH18 to form a hydrogen bond.[152,153] The spectral similarity between horse and sperm whale metMb(OH^-)s indicates that this internal hydrogen bond is also formed in the former Mb in solution. The difference in the shift of the HisEF5 $N_\varepsilon H$ proton signal between the proteins

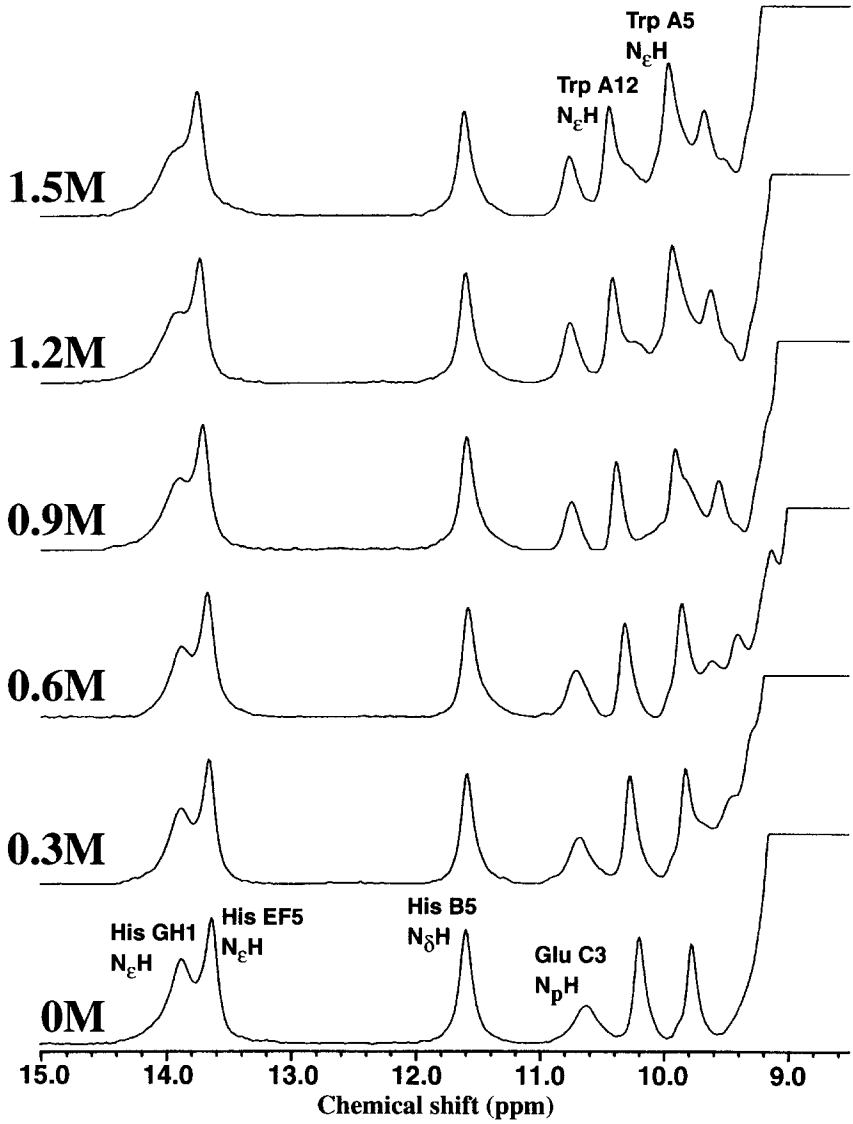

Fig. 14. The high-frequency shifted portions of the 400 MHz ^1H NMR spectra of sperm whale metMb(OH^-) in 90%H_2O/10%^2H_2O, pH 9.5, at 5 °C in the presence of the indicated concentrations of NaCl.

suggests a possible difference in the hydrogen-bonding interaction between HisEF5 and AspH18, although X-ray comparative studies indicated a structural similarity at the EF—H interface in these two Mbs.[152,153] On the other hand, the fact that the shifts of HisEF5 $N_\varepsilon H$ proton signals for bovine and sperm whale Mbs are similar to each other suggests a conformational

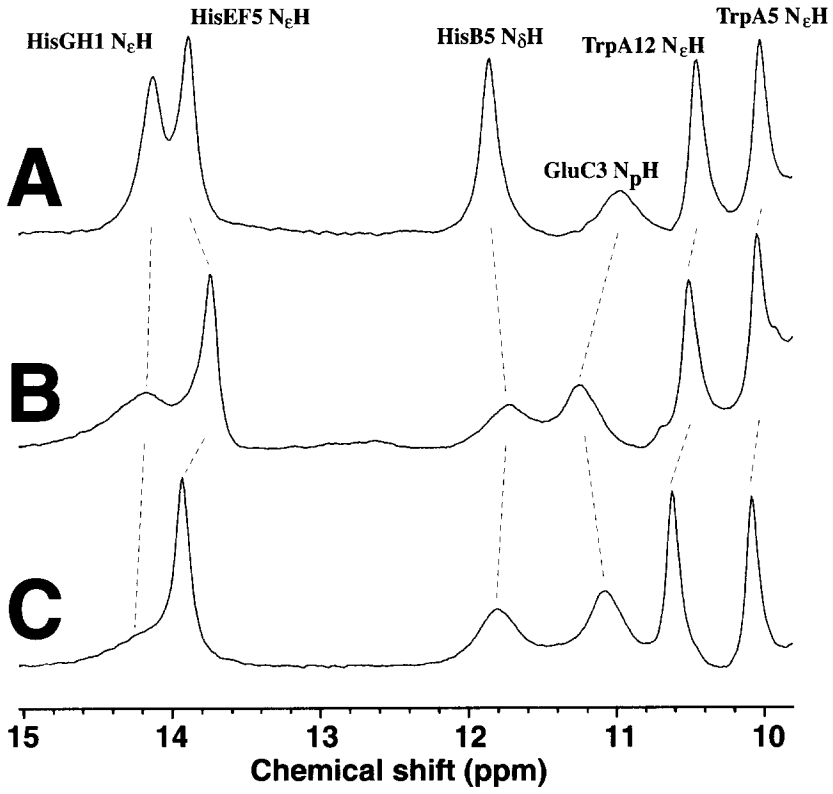

Fig. 15. The high-frequency shifted portions of the 400 MHz ^1H NMR spectra of metMb(OH^-)s in 90%H_2O/10%^2H_2O at 2 °C: (A) sperm whale Mb, pH9.47; (B) horse Mb, pH 10.01; (C) bovine Mb, pH 9.81. The pH of each sample was adjusted to observe HisGH1 $N_\varepsilon H$ proton signal with the minimum line width. The signal assignment is indicated in A. The corresponding signals are connected by broken lines.

resemblance of their EF—H interfaces. Compared with the spectrum of sperm whale metMb(OH^-) (trace 15A), the HisGH1 $N_\varepsilon H$ proton signal exhibits considerable exchange line broadening in the spectrum of horse metMb(OH^-) (trace 15B) and is barely observed in the spectrum of bovine metMb(OH^-) (trace 15C). The X-ray structures of sperm whale and horse Mbs show sizeable deviations in α-carbon positions in the regions at the end of the A helix, A13—A15, at the end of the G helix and the GH corner, G19—GH5, and at the N- and C-termini.[152, 153] In addition, the HisB5 $N_\delta H$ proton signal is broader in traces 15B and 15C. These results reflect a relatively large difference in the chemical environment of the B—GH interface among these Mbs. The fact that linewidths of His B5 and His GH1 imidazole ring NH proton signals in horse and bovine Mbs are larger than those of the corresponding signals in sperm

whale Mb at a given temperature suggests that the AspB1—HisB5—HisGH1 hydrogen bond is weaker in the former Mbs.

4.3. Effect of heme ligation on the structures of B—GH and EF—H interfaces in myoglobin

Structural changes of Mb have been examined from both the experimental[81–83,114–116,154–156] and theoretical points of view.[157–159] The dynamic structure of the heme active site has attracted primary interest because of the biological activity of this molecule. But other parts of the molecule also exhibit conformational alterations that are closely correlated with structural change at the active site.[81,82,114–116] Crystallographic study has provided a powerful tool for elucidating the three-dimensional structure of the Mb molecule[81–83,114–116,154,160,161] and has revealed tertiary structural differences among different ligation states of the protein from least-square superpositioning of the molecular coordinates.[81,83,114–116] In such studies, however, it is difficult to make a detailed comparison of portions of the molecule, which exhibit high temperature factors and concomitant positional errors, and crystal lattice packing effects may also complicate data interpretation. On the other hand, NMR provides a simple, but highly refined, structural comparison between molecules in solution, because NMR shifts generally reflect an equilibrium structure of a molecule exhibiting a wide range of structural fluctuations. Hence these His imidazole ring NH proton signals of Mb can be used to provide information about the local tertiary structure change of the critical packing interfaces, induced by change in heme ligation. Upon oxygenation[81,159] or CO binding[116] of Mb, a large displacement is suggested to occur at the region from the F helix to the beginning of the G helix. Such structural change of the heme pocket would affect the structure of the EF loop, and hence the EF—H interface is possibly influenced. Furthermore, the hydrogen bond between HisE7 and the Fe-bound ligand was found to be largely different among the proteins with various exogenous ligands. In met-aquo Mb (metMb(H_2O)), the N_ε atom of HisE7 acts as a proton-acceptor for Fe-bound H_2O.[115] In met-azido Mb (metMb(N_3^-)), the $N_\varepsilon H$ proton of HisE7 is hydrogen-bonded to the N atom of the ligand directly coordinated to the iron.[160] In met-imidazole Mb (metMb(Im)), free NH hydrogen of the Fe-bound imidazole is accepted by the N_δ atom of HisE7 and substantial rotation of the HisE7 imidazole ring around the C_α—C_β bond, relative to its orientation in metMb(H_2O), occurs.[161] These structural differences of the distal pocket could also influence the structure of the EF loop at the hinge between the heme binding E and F helices.

The high-frequency shifted His imidazole ring NH proton signals in a variety of oxidation/ligation states of Mb are compared in Fig. 16. Observations of

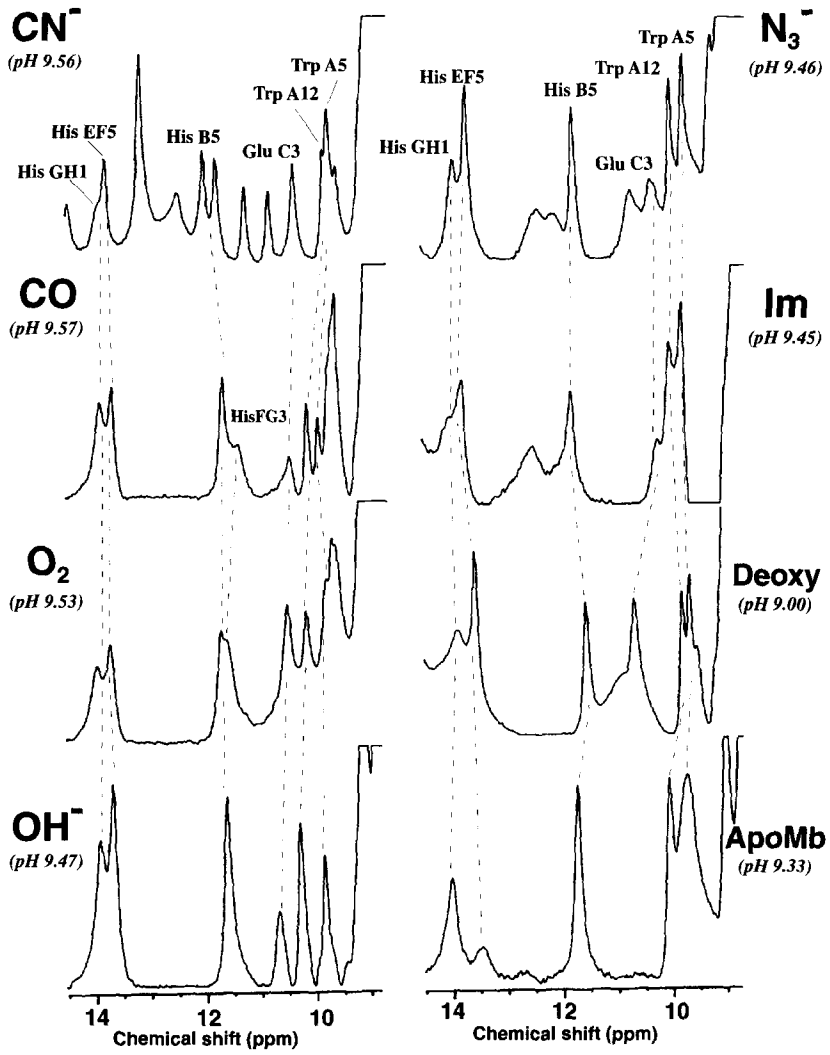

Fig. 16. The high-frequency shifted portions of the 400 MHz ^{1}H NMR spectra of sperm whale Mb in a variety of oxidation/ligation states at 5 °C. CN^-; metMb(CN^-), CO; Mb(CO), O_2; Mb(O_2), OH^-; metMb(OH^-), N_3^-; metMb(N_3^-), Im; metMb(Im), Deoxy; Deoxy Mb. The number in parentheses indicates the pH value. The corresponding signals are connected by broken lines.

NOE connectivities provided the shifts of non-exchangeable proton signals of these His imidazole rings. Their shifts are summarized in Table 2. The similarity in the shifts between metMb(OH^-) and diamagnetic Mbs, i.e. Mb(CO) and oxy-Mb (Mb(O_2)), demonstrates that paramagnetic contribution to these resonances is quite small. Semiquantitative analysis of δ_{pc}, due to

Table 2. Chemical shifts (ppm) of HisB5, HisGH1 and HisEF5 imidazole ring proton signals at 5°C

		HisB5		HisGH1			HisEF5		
Ligand	pH	$N_\delta H$	$C_\varepsilon H$	$N_\varepsilon H$	$C_\varepsilon H$	$C_\delta H$	$N_\varepsilon H$	$C_\varepsilon H$	$C_\delta H$
CN^-	9.56	12.07	n.d.	14.23	n.d.	n.d.	14.10	n.d.	n.d.
CO	9.57	11.96	7.72	14.17	7.82	6.79	13.94	7.71	6.83
O_2	9.53	11.97	7.77	14.22	7.83	6.72	13.95	7.75	6.74
OH^-	9.47	11.87	7.71	14.17	7.79	6.71	13.92	7.76	6.72
N_3^-	9.46	12.05	7.83	14.23	7.86	6.77	13.99	7.71	6.78
Im	9.45	12.09	n.d.	14.30	n.d.	n.d.	14.09	n.d.	n.d.
Deoxy	9.00	11.86	7.63	14.21	7.77	6.58	13.87	7.65	6.80
ApoMb	9.33	12.03	7.76	14.34	7.83	6.66	13.80	7.68[a]	6.81[a]

[a] At pH 8.55. n.d.; Not detected.

magnetic anisotropy, in deoxy Mb[162] yielded a value of $< |0.03|$ ppm for these signals. In the absence of knowledge about the δ_{pc} contribution to these shifts in metMb(OH^-), metMb(N_3^-), and metMb(Im), their shifts cannot be interpreted solely in terms of the strength of the hydrogen bonding interaction, although magnetic anisotropy in these paramagnetic Mbs is relatively small.[163] But the similarity in the shifts of the corresponding signals and their temperature dependence among not only paramagnetic Mbs, but also diamagnetic Mbs strongly suggests that the paramagnetic contribution to these shifts is negligible and hence the shift differences among the Mb complexes are largely attributable to diamagnetic contributions.

4.3.1. B—GH interface

The N_ε atoms of HisB5 and HisGH1 imidazole rings in various ligation states of the protein are located within a hydrogen bond distance of about 0.280 nm. In addition, the values of 0.260–0.290 nm for the distance between the HisB5 N_δ atom and AspB1 peptide carbonyl oxygen also suggests the presence of a hydrogen bond between these atoms. Solution NMR studies[99,164] confirmed the presence of the N_ε—N_ε hydrogen bond between HisB5 and HisGH1. Observation of the HisB5 $N_\delta H$ proton signal in the high-frequency shifted region of >11 ppm, together with its relatively slow hydrogen exchange, confirms formation of the AspB1—HisB5 hydrogen bond in these Mb complexes in solution. Consequently, the triad hydrogen bond, AspB1—HisB5—HisGH1, is formed in each one of the Mb complexes.

HisB5 $N_\delta H$ proton shift spans 0.33 ppm at 5 °C among the Mb complexes (Table 2), indicating that the AspB1—HisB5 hydrogen bond depends on the heme ligation state. Since the alteration of the electronic structure of either a hydrogen-donor or -acceptor influences the NH proton signal, the HisB5 $N_\delta H$

proton shift cannot be simply interpreted in terms of the strength of the AspB1—HisB5 hydrogen bond. But the fact that the HisB5 $N_\delta H$ and $C_\varepsilon H$ proton shifts correlate well with each other (Table 2) suggests that the electronic structure of this imidazole ring depends upon the heme ligation state. Since the B helix is known to be one of the most stable helices in Mb,[165,166] the AspB1—HisB5 hydrogen bond in this helix would not be greatly affected by structural change at the heme active site. Therefore the electronic structure of the HisB5 imidazole ring is most likely to be influenced through the HisB5—HisGH1 hydrogen bond. Small changes in the orientation of the GH loop relative to the B helix, which in turn alters the HisB5—HisGH1 hydrogen bond, would induce changes in electronic structure and conformation of the HisB5 side-chain. In fact, X-ray structures[81–83,114–116,154–156] of these Mb complexes demonstrated that, among the Mb complexes, the angle between the vectors of the HisB5 N_δ—AspB1 peptide carbonyl oxygen and the HisB5 N_ε—HisGH1 N_ε varies between 123° and 147°, although the variation of the distance between the N_ε atoms of HisB5 and HisGH1 is only 0.01 nm.

A detailed comparison between the crystal structures of sperm whale Mb(CO) and deoxy Mb has revealed the presence of large displacements in the CD and GH loops upon the ligation of the protein.[116] The displacement of the CD loop is attributed to a conformational transition of ArgCD3 side-chain relative to the heme between the two states. Since the CD loop of one molecule packs, with several intervening ordered water molecule, close to the GH loop of another molecule in the crystal, the possibility that the water transmits the effect of structural alteration of the CD loop of one molecule to the GH loop of another in the crystal has been suggested.[116] But the differences in HisGH1 proton shifts between deoxy Mb and Mb(CO) strongly suggest that the tertiary structure of the B—GH interface is influenced by CO binding.

4.3.2. EF—H interface

The HisEF5 $N_\varepsilon H$ proton shift spans 0.23 ppm among the Mb complexes. The high-frequency shift bias for the HisEF5 $N_\varepsilon H$ proton signal with increasing size of the ligand might suggest the presence of a correlation between the heme ligation state and the structure of the EF—H interface.

4.4. Protein folding in apomyoglobin

It has been well-documented that the prosthetic heme group in Mb not only plays a functional role, but also allows the protein to adopt and maintain the correct native protein folding.[165] In contrast with the detailed information available for the three-dimensional structure of Mb,[81–83,114–116,154–156] the apomyoglobin (apoMb) structure has not been fully described. Since removal of heme from Mb renders the apoMb less stable than the holoprotein and

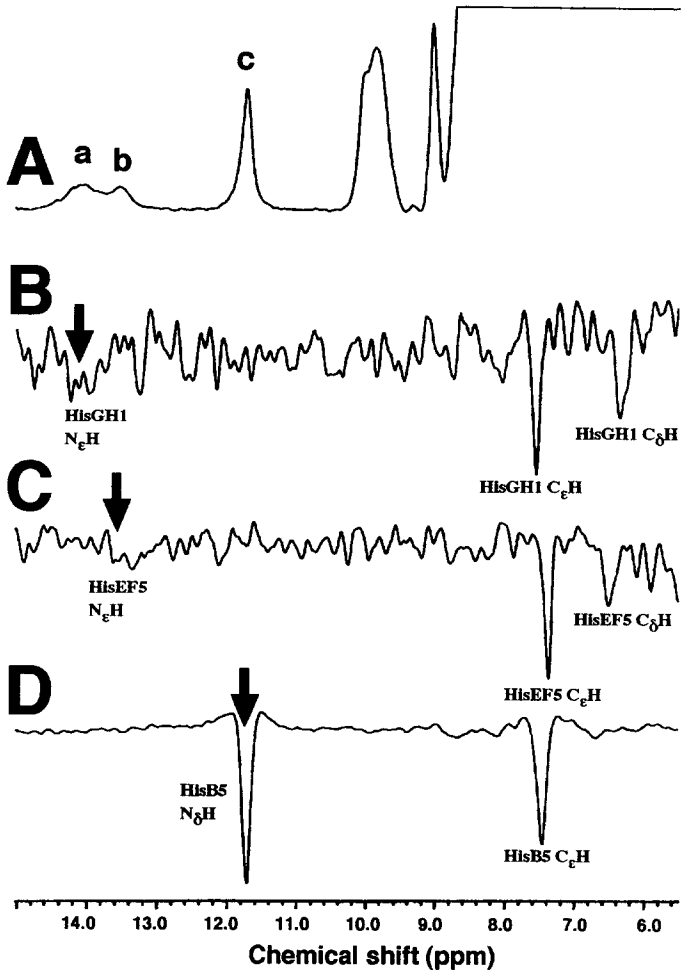

Fig. 17. (A) The high-frequency shifted portion of the 400 MHz ^1H NMR spectrum of sperm whale apoMb in 90%H_2O/10%^2H_2O, pH 8.55, at 5 °C. Peaks a–c are resolved below 11 ppm. (B) The NOE difference spectrum resulting from saturation of peak a. The peaks at 6.66 and 7.83 ppm exhibit NOEs. (C) The NOE difference spectrum resulting from saturation of peak b. The peaks at 6.81 and 7.68 ppm exhibit NOEs. (D) The NOE difference spectrum resulting from saturation of peak c. The peak at 7.76 ppm exhibits an NOE. The signal assignments are indicated in traces B—D. (From ref. 187, with permission from Elsevier Science.)

reduces its helical content, apoMb has been thought to be a valuable protein for analysing the folding mechanism and thermodynamic stability of water-soluble globular protein.[165–169] Although it has often been assumed for simplicity that native apoMb is structurally the same as the holoprotein, this view is not supported by various experimental data such as the measurements of circular

dichroism,[170] hydrogen exchange kinetics,[167,171] dynamic light scattering,[172] and small angle X-ray scattering,[172] which all report a significant loss in the compactness of the Mb molecule when the heme is removed from the protein matrix. On the other hand, fluorescence depolarization and lifetime measurements of sperm whale apoMb have shown that the environments of the two Trp residues located in the A helix is practically unchanged by heme extraction.[173] Solution NMR studies have revealed that the amphiphilic A, B, G and H helices in apoMb maintain the same packing as they do in Mb.[148,167,174–179]

The high-frequency shifted portion of the 400 MHz ^{1}H NMR spectrum of apoMb in 90%H_2O/10%^2H_2O, pH 8.55, at 5 °C is illustrated in trace A of Fig. 17. Three exchangeable proton signals, peaks a–c, are observed at >11 ppm in the spectrum. The NOE difference spectra with the saturation of the individual peak are illustrated in traces 17B–17D. Similarly to the case of holoMb (Fig. 9), the observed NOE connectivities facilitate signal assignments of HisB5, HisEF5, and HisGH1 protons. Their shifts are listed in Table 2. The similarity in the chemical shift of HisB5 $C_\varepsilon H$ proton signal between holo- and apoMbs indicates that the removal of heme does not affect the structure of the B—GH interface.

The high-frequency shifted portions of the 400 MHz ^{1}H NMR spectra of apoMb and metMb(OH^-) at two different pH values are compared in Fig. 18. Upon the removal of heme, the HisEF5 $N_\varepsilon H$ proton signal broadens considerably, whereas the HisB5 $N_\delta H$ and HisGH1 $N_\varepsilon H$ proton signals are only slightly influenced. Formation of the hydrogen bond between the side-chains of HisB5 and HisGH1 in ^{15}N-labelled apoMb has been confirmed by the detection of the spin–spin coupling constant between $^{15}N_\varepsilon$ nuclei of the two residues through the intervening hydrogen bond.[67] The observation of HisB5 $N_\delta H$ proton signal shifted to >13 ppm demonstrates the formation of the AspB1—HisB5 hydrogen bond in apoMb. Consequently, the unique triad hydrogen bond, AspB1—HisB5—HisGH1, is formed in apoMb. The fact that the shifts of HisB5 $N_\delta H$ and HisGH1 $N_\varepsilon H$ proton signals are only slightly influenced by heme removal (Table 2) dictates that the AspB1—HisB5—HisGH1 hydrogen bond in Mb is independently stabilized within a hydrophobic core composed of A, B, G, and H helices.[166,167]

4.4.1 B—GH interface in apoMb

X-ray studies suggested that a unique triad AspB1—HisB5—HisGH1 hydrogen bond stabilizes the docking of the B helix on the GH corner in sperm whale and horse Mbs.[81–83,114–116,152,153] Refined neutron diffraction data confirmed the presence of this hydrogen bond in the solid-state[81–83] and NMR study demonstrated that the imidazole rings of HisB5 and HisGH1 in Mb are within hydrogen-bonding distance in solution.[99] The presence of similar signals in the spectrum of sperm whale apoMb confirmed that the AspB1—HisB5 hydrogen bond is retained in this protein in solution. The

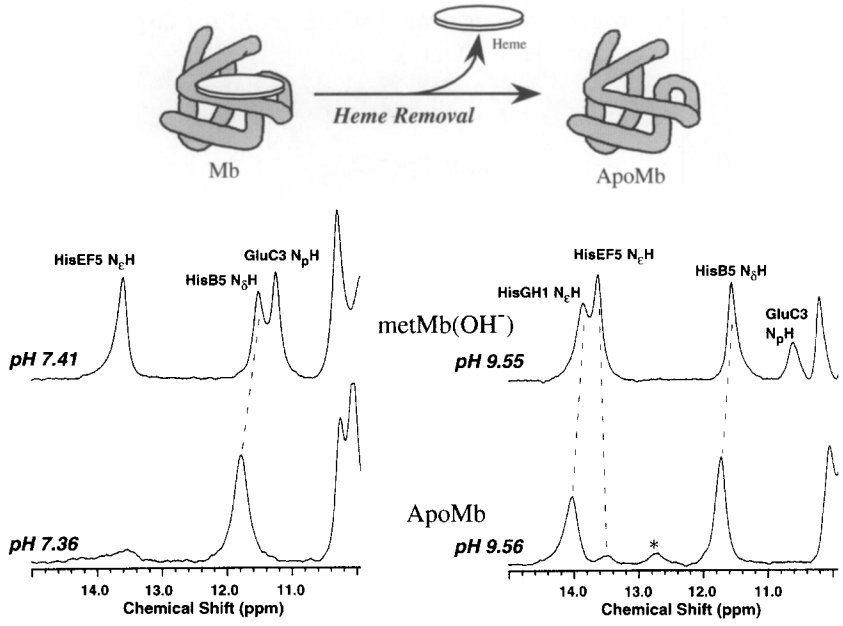

Fig. 18. The high-frequency shifted portions of the 400 MHz ^{1}H NMR spectra of sperm whale metMb(OH^-) and apoMb in 90%H_2O/10%^2H_2O at 5 °C and neutral (left) and basic (right) pH values. Peak indicated by an asterisk is due to impurity. The preparation of apoMb from Mb is schematically represented in the inset.

similarity in the electronic structure of the HisB5 imidazole ring between various Mb complexes and apoMb, as manifested by the observed shifts of HisB5 imidazole ring proton signals, strongly suggests that the AspB1—HisB5—HisGH1 hydrogen bond is formed in apoMb in solution. Since HisB5 is located at the centre of this unique triad hydrogen bond, ionization of its side-chain is quite different from that of an ordinary His side-chain in a protein. The p*K*a values of HisB5 in holoMb as well as apoMb has not been determined because this residue does not titrate between pH 5.5 and pH 10.[145] The similarity in both the pH and temperature dependence of HisB5 $N_\delta H$ proton signal between holoMb and apoMb provides further confirmation that the strength of the AspB1—HisB5 hydrogen bond is essentially unchanged for the two different states of the protein. Thus it is concluded that the B—GH interface is one of the regions within Mb, that are not significantly affected by the heme extraction. In fact, the importance of the HisB5—HisGH1 hydrogen-bonding interaction in the stabilization of apoMb structure has been demonstrated by mutation study.[179]

Furthermore, the pH dependence of the high-frequency shifted His imidazole NH proton signals of apoMb are essentially similar to those of the corresponding signals of metMb(OH^-) (see Fig. 12), except that the pH value

at the minimum hydrogen exchange rate for the apoMb is larger by about a half pH unit than that for metMb(OH^-).

4.4.2. EF—H interface and C helix in apoMb

Although the shift of HisEF5 $N_\varepsilon H$ proton signal is affected only slightly by the heme removal, its linewidth is significantly increased. The increased linewidth of HisEF5 $N_\varepsilon H$ proton signal for apoMb indicates that the hydrogen bond between HisEF5 and AspH18 is influenced significantly by heme removal. This could be attributed to conformational averaging of the F helix in the absence of heme.[180] A detailed NMR structural analysis of sperm whale apoMb has suggested that the structure of the region from the beginning of the EF loop to the beginning of the G helix is disordered in solution. Based on the analysis of the NMR spectra of sperm whale apoMb, together with the results of mass spectrometry[181] and mutation[182] studies, Eliezer and Wright[180] proposed that this region undergoes an interexchange reaction between holoMb-like folded form and one or more largely unfolded forms with a timescale of milliseconds.

Upon heme extraction, the GluC3 N_pH proton signal disappears completely in the high-frequency shifted region of the spectra and resonates at 10.51 ppm (at 25 °C and pH 5.7).[176] This result suggests that a significant structural alteration in the C helix is induced upon heme removal.

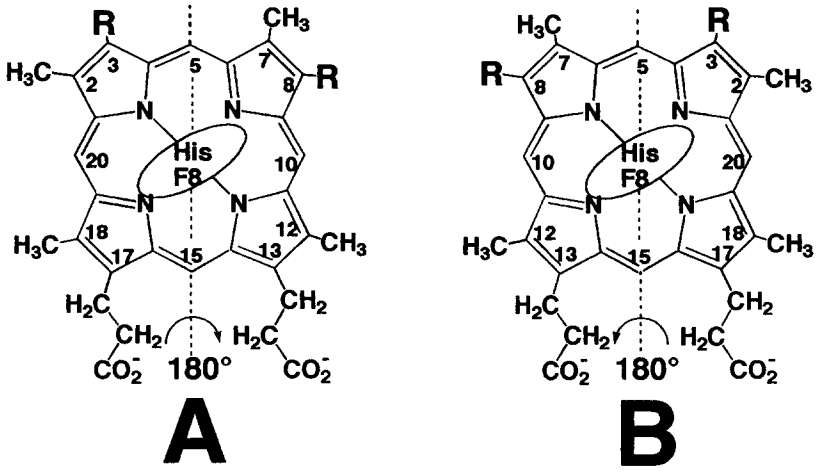

Fig. 19. Structure and numbering system of hemins. R is —CH=CH_2 for protohemin, —CH_2CH_3 for mesohemin, and —H for deuterohemin. Two possible orientations of hemin relative to HisF8; (A) that found in the crystal structure of sperm whale Mb[114] and (B) that with the hemin rotated by 180° about the 5, 15-*meso* proton axis from that of (A).

4.5. Long-range structural correlation in myoglobin

The active site of an enzyme is usually formed from about 10–15% of all the constituent amino acid residues. The function of the remaining residues is thought to be to maintain the structure of the active site, to recognize other molecules, and/or to transmit structural information between the active site and remote sites within a protein complex as seen in allosteric proteins. Hemoglobin (Hb), tetrameric oxygen transport hemoprotein, is one of the best, albeit incompletely, understood allosteric proteins in terms of its structure and function. The molecular basis of cooperative oxygen binding of Hb has been proposed to involve transmission of structural information between the two types of subunits by altering specific contacts between heme and amino acid side-chains. Hb is thought to be evolved from Mb, monomeric oxygen-binding hemoprotein. Hence, although Mb does not exhibit allostery in its function, it may be worthwhile to find the origin of a long-range structural correlation between the active site and other portions of Mb.

NMR study of Mb revealed that there are two interconverting protein forms in solution at equilibrium, which differ in the orientation of the heme by a 180° rotation about the 5,15-*meso* axis (Fig. 19).[183,184] The dominant form possesses the same heme orientation as found in the single crystal (A of Fig. 19) and is called the major form. The protein with the reversed heme orientation (B of Fig. 19) is called the minor form. Although the concentration of the minor form relative to the major form is small in native Mb, it can be raised using the reconstitution technique. The reconstitution of apoprotein with heme initially

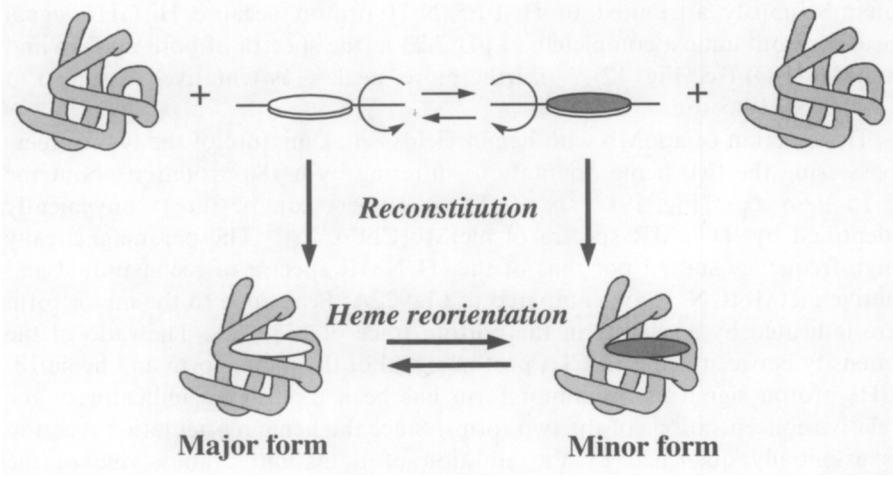

Fig. 20. Schematic representation of the reconstitution of apoMb with heme and the heme reorientation reaction. The reconstitution of apoMb with heme initially results in ~1 : 1 mixture of the two forms[183,184] and the minor form is converted to the major form with time to reach the equilibrium ratio found in native Mb.[85,185,186]

results in ~1 : 1 mixture of the two forms[183,184] and the minor form is converted to the major form with time to reach the equilibrium ratio found in native Mb (Fig. 20).[85,185,186] This phenomenon is known as heme disorder and the interconversion between the two forms is called the heme reorientation reaction. As shown in Fig. 16 and Table 2, comparison of the His imidazole ring NH proton signals among Mbs in various ligation states revealed the transmission of structural interaction between the active site and these interfaces, which are at least 1.1.nm away from the heme.[122] Differential heme–protein contacts due to the difference in the orientation of heme relative to the protein are expected to influence the structure of these interfaces through a long-range structural correlation within the molecule.

4.5.1. Titration of apoMb with hemin

The high-frequency shifted portions of the 400 MHz ^{1}H NMR spectra of apoMb in the presence of various concentrations of hemin, together with that of metMb(OH^-), for comparison, at 5 °C and pH 7.23 are illustrated in Fig. 21. With the addition of hemin, the signals arising from reconstituted Mb increase at the expense of those due to apoMb. Among the hemin concentration-dependent peaks, x_1–x_5, peaks x_2, x_3, and x_5 can be unambiguously assigned to HisEF5 $N_\varepsilon H$, HisB5 $N_\delta H$, and GluC3 $N_p H$ protons, respectively, of reconstituted Mb, based on the similarity in the shifts to those of the corresponding signals in the spectrum of metMb(OH^-). Peaks x_1 and x_4 are not observed in the spectrum of metMb(OH^-). Although the $N_\varepsilon H$ proton signals of HisEF5 and HisGH1 resonate at ~13.5 ppm, peak x_1 is unambiguously attributed to HisEF5 $N_\varepsilon H$ proton because HisGH1 signal broadens out almost completely at pH 7.23 in the spectra of both apoMb and metMb(H_2O) (see Fig. 12).[187] Furthermore, peak x_4 is tentatively assigned to GluC3 $N_p H$ proton.

The reaction of apoMb with hemin yields ~1 : 1 mixture of the two isomers possessing the two heme orientations differing by a 180° rotation about the 5, 15-*meso* axis (Fig. 19).[85,183–186] These isomers can be most conveniently identified by ^{1}H NMR spectra of metMb(CN^-).[183,184] The paramagnetically high-frequency shifted portions of the ^{1}H NMR spectra of reconstituted and native metMb(CN^-)s are compared in Fig. 22A. Peaks due to the minor form are indicated by an arrow in the bottom trace of Fig. 22A. The ratio of the intensity between heme 12-CH_3 proton signal of the major form and heme 18-CH_3 proton signal of the minor form has been used as an indicator of the relative concentrations of the two forms. Since the heme reorientation reaction is essentially quenched by the addition of potassium cyanide due to the extremely slow reaction in metMb(CN^-),[185,186] the time-evolution of the heme reorientation reaction can be monitored through the analysis of the signals at ~27 ppm. The high-frequency shifted portion of the ^{1}H NMR spectrum of freshly reconstituted metMb(OH^-) is illustrated in the bottom trace of

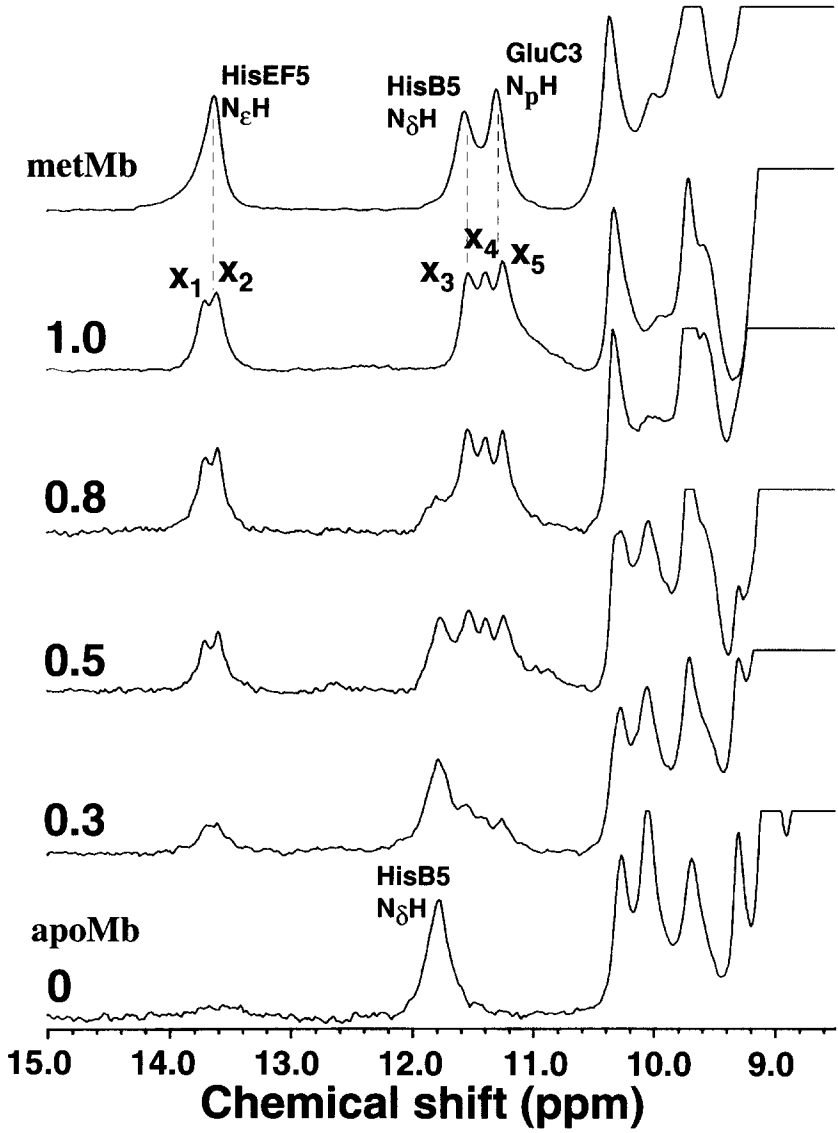

Fig. 21. The high-frequency shifted portions of the 400 MHz ^1H NMR spectra of sperm whale apoMb in 90%H_2O/10%^2H_2O, pH 7.23, at 5 °C in the presence of the indicated stoichiometric ratio of protohemin. The spectrum of sperm whale metMb in 90%H_2O/10%^2H_2O, pH 7.22, at 5 °C is illustrated in the top trace for comparison. Peaks $x_1 - x_5$ emerge with the addition of the hemin. (From ref. 187, with permission from Elsevier Science.)

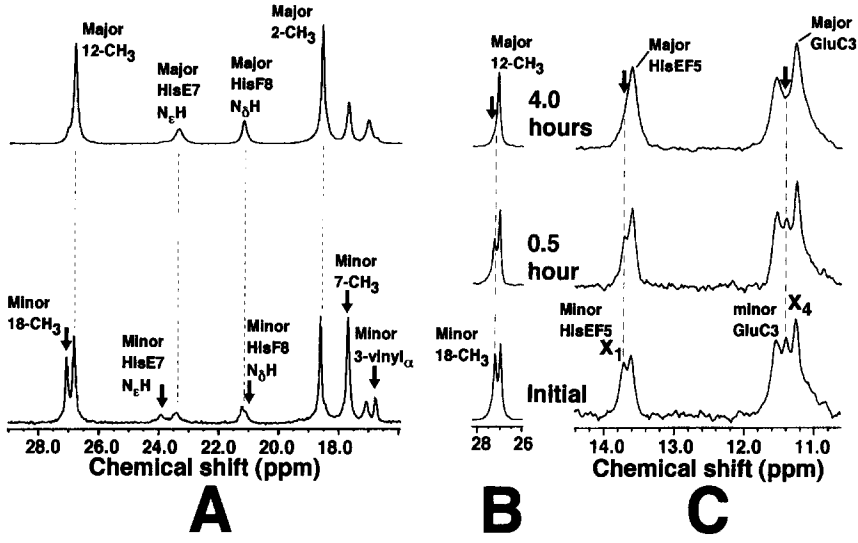

Fig. 22. (A) The high-frequency shifted portions, 16–29 ppm, of the 400 MHz ^{1}H NMR spectra of freshly reconstituted sperm whale metMb(CN^-) with protohemin (bottom trace) and native metMb(CN^-) (top trace) in 90%H_2O/10%^2H_2O, pH 9.57, at 25 °C. The signal assignments are given with the spectra. Peaks indicated by an arrow arise from the minor form (B of Fig. 19). (B) and (C) the time evolution of the spectra of freshly reconstituted sperm whale metMb with protohemin in 90%H_2O/10%^2H_2O, pH 7.32, at 5 °C. (B) shows the heme 12- and 18-methyl proton signals of the metMb(CN^-) converted from the reconstituted metMb(OH^-), of which the spectrum is illustrated in (C), immediately after the measurement. (C) shows the high-frequency shifted portions, 10–15 ppm, of the 400 MHz ^{1}H NMR spectra of freshly reconstituted sperm whale metMb with protohemin in 90%H_2O/10%^2H_2O, pH 7.32, at 5 °C, recorded at the elapsed times indicated. The time evolution of the intensity of peak x_1 in (C) resembles that of heme 18-methyl proton signal of the minor form in (B). (From ref. 187, with permission from Elsevier Science.)

Fig. 22C and those of the spectra recorded 0.5 and 4 hours after the reconstitution are shown in the centre and top traces in Fig. 22C, respectively. The samples were converted to metMb(CN^-) by the addition of a 10-fold molar excess of potassium cyanide immediately after the measurements of the spectra shown in Fig. 22C and the portions 26–28.5 ppm of the spectra recorded on the resulting metMb(CN^-)s are illustrated in Fig. 22B. As shown in Fig. 22C, peaks x_1 and x_4 decrease with time and their decay rate is closely related to the equilibration rate of the heme reorientation reaction as reflected in the time evolution of the spectra shown in Fig. 22B. Thus, peaks x_1 and x_4 are assigned to HisEF5 $N_\varepsilon H$ and GluC3 $N_p H$ protons of the minor form, respectively.[187] The splitting of these signals strongly suggests that the tertiary structure of Mb is influenced by the orientation of heme. The shift difference of 0.08 ppm between HisEF5 $N_\varepsilon H$ proton signals of the major and minor forms

dictates that the timescale of heme reorientation reaction is $\ll 3\ s^{-1}$. This rate is consistent with the apparent first-order rate constant of $5 \times 10^{-6}\ s^{-1}$ for the heme reorientation reaction in metMb(OH^-) reconstituted with protohemin.[185]

The high-frequency shifted portions of the 400 MHz ^1H NMR spectra of apoMb in the presence of various concentrations of protohemin, together with that of metMb(OH^-), for comparison, at 5 °C and pH 8.24 or 9.55 are illustrated in Fig. 23. A broad signal arising from HisGH1 $N_\varepsilon H$ proton is observed at pH 8.24 (Fig. 23A) and this signal is more apparent at pH 9.55 (Fig. 23B).[187]

The high-frequency shifted portions of the 400 MHz ^1H NMR spectra of apoMb in the presence of various concentrations of mesohemin and deuterohemin (see the structures in Fig. 19) at 5 °C and neutral and alkaline pH values are compared in Fig. 24. As has been observed in the spectra of Figs. 21, 22C, and 23, a similar splitting of the HisEF5 $N_\varepsilon H$ proton signals is observed for Mb reconstituted with mesohemin at pH 9.47 and hence the splitting of the HisEF5 signal is attributed to the heme disorder.[187] The shift difference of the HisEF5 $N_\varepsilon H$ proton signal between the two different heme

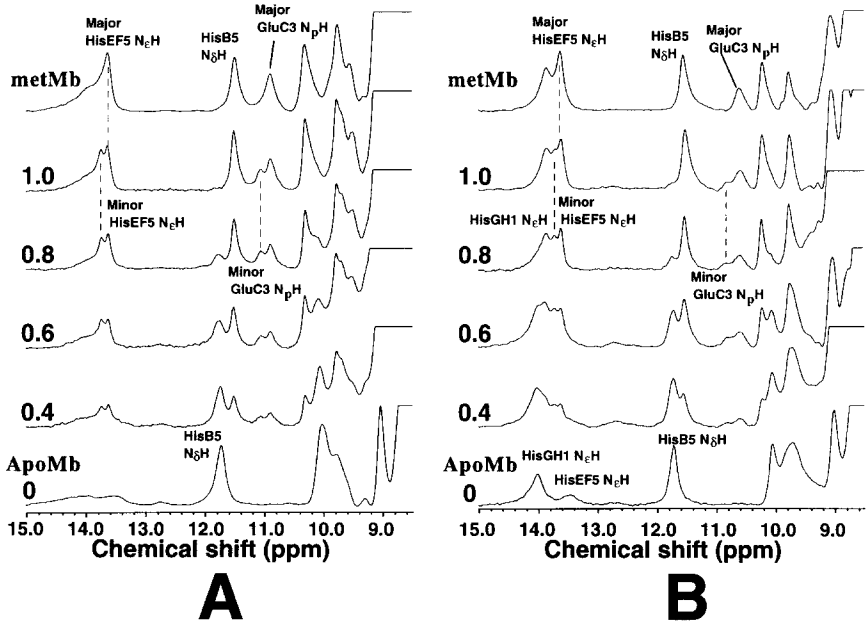

Fig. 23. The high-frequency shifted portions of the 400 MHz ^1H NMR spectrum of sperm whale apoMb in 90%H_2O/10%^2H_2O at 5 °C, pH 8.24 (A) and pH 9.55 (B) in the presence of the indicated stoichiometric ratio of protohemin. The spectra of sperm whale metMb(OH^-) in 90%H_2O/10%^2H_2O at 5 °C and the corresponding pH values are illustrated in the top traces for comparison. The signal assignments are indicated with the spectra. (From ref. 187, with permission from Elsevier Science.)

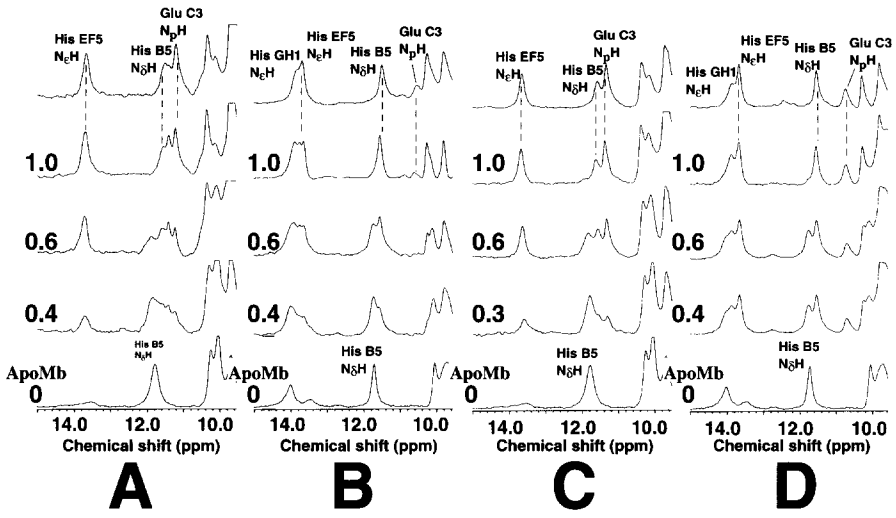

Fig. 24. The high-frequency shifted portions of the 400 MHz ^1H NMR spectra of sperm whale apoMb in 90%H_2O/10%^2H_2O at 5 °C, pH 7.24 (A) and pH 9.47 (B) in the presence of the indicated stoichiometric ratio of mesohemin, and pH 7.20 (C) and pH 9.32 (D) in the presence of the indicated stoichiometric ratio of deuterohemin. The spectra of the reconstituted metMb with the corresponding hemin in 90%H_2O/10%^2H_2O at 5 °C and the corresponding pH values are illustrated in the top traces. (From ref. 187, with permission from Elsevier Science.)

orientational forms dictates that the heme reorientation reaction for mesohemin is $\ll 40\ s^{-1}$ and this rate is consistent with the reported apparent first-order rate constant of $5 \times 10^{-4}\ s^{-1}$.[185] On the other hand, splitting of the HisEF5 $N_\varepsilon H$ proton signal due to the heme disorder was not observed for Mb reconstituted with deuterohemin.[187] The absence of the HisEF5 $N_\varepsilon H$ proton signal of the minor form in Figs. 24C and 24D is not due to fast equilibration for deuterohemin, because signals for the heme disorder are clearly observed in the spectrum of metMb(CN^-) converted, by the addition of potassium cyanide, immediately after the measurement of the spectra of Figs. 24C and 24D.[187]

4.5.2. His imidazole ring NH proton signals of various reconstituted Mbs

The temperature dependence of the high-frequency shifted His NH proton signals of native metMb is compared with those of metMbs reconstituted with mesohemin and deuterohemin in Fig. 25. Although the corresponding signals among the spectra of three different Mbs are quite similar in the shifts and their temperature dependence, they are slightly different in the temperature dependence of the linewidth, suggesting that the structure of the EF—H and B—GH interfaces in Mb is affected by the heme–protein contacts.[187]

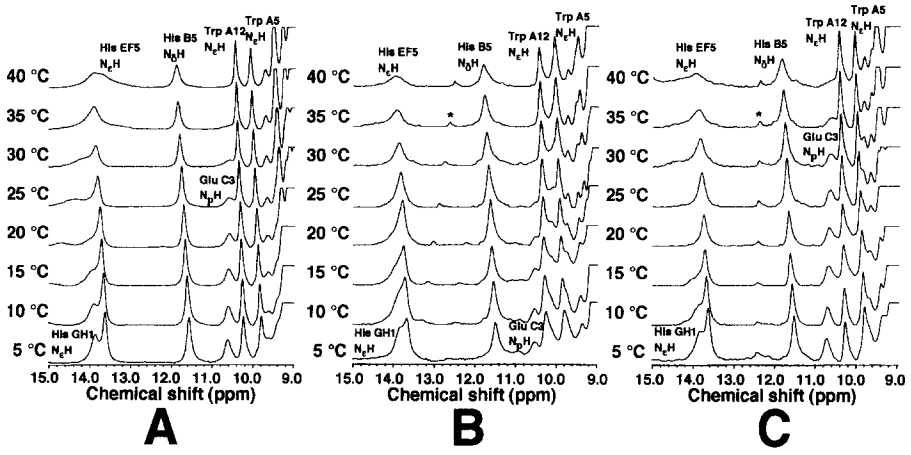

Fig. 25. Temperature dependence of the high-frequency shifted portions of the 400 MHz ^1H NMR spectra of native sperm whale metMb at pH 9.51 (A), metMb reconstituted with mesohemin at pH 9.53 (B), and metMb reconstituted with deuterohemin at pH 9.52 (C). Peaks indicated by * are due to impurity. (From ref. 187, with permission from Elsevier Science.)

4.5.3. Effects of the heme orientation on the structure of the B—GH and EF—H interfaces

The HisEF5 $N_\varepsilon H$ proton signal appears to be sensitive to the heme orientation at the active Mb site. The emergence of a HisEF5 $N_\varepsilon H$ proton signal with the addition of heme, as shown in the spectra in Figs. 21, 22, and 23, indicates that the EF—H interface is stabilized by the incorporation of heme into apoMb. In addition, two signals observed at ~13.5 ppm in the spectra of freshly reconstituted metMb(H_2O) at pH 7.23, (peaks x_1 and x_2 in Fig. 21), are assigned to HisEF5 $N_\varepsilon H$ proton and the splitting of its signal is attributed to the presence of two different heme orientational forms (A and B in Fig. 19).[187] The splitting of the HisEF5 signal can be interpreted as indicative of the influence of the difference in the heme-protein contacts, due to the two different orientations of heme relative to the protein, on the structure of the EF—H interface. A similar splitting is also observed for the spectra of Mb reconstituted with mesohemin, but no such splitting is observed for the Mb reconstituted with deuterohemin. These results suggest that the contact between the protein and the heme side-chains at the 2-, 3-, 7-, and 8-positions are transmitted to the EF—H interface.

Roughly speaking, the shift of the HisEF5 $N_\varepsilon H$ proton signal is categorized into three groups. ApoMb, which has the value of 13.80 ppm, is considered an independent group and the other two groups are the major and minor forms of Mb, which have the values 13.91–13.95 and 1401–14.05 ppm at pH ~9.5,

Table 3. Chemical shifts (ppm) of HisEF5 imidazole ring NH proton signals of sperm whale apoMb and reconstituted Mbs at 5°C

	Ligand	pH	HisEF5 $N_\varepsilon H$	
			Major	Minor
ApoMb[a]		9.33	13.80	
Protohemin				
	H_2O	7.34	13.90	14.00
	OH^-	9.53	13.91	14.01
Mesohemin				
	H_2O	7.16	13.96	13.96
	OH^-	9.53	13.94	14.05
Deuterohemin[b]				
	H_2O	7.37	13.92	13.92
	OH^-	9.32	13.95	13.95

[a] ApoMb does not possess heme.
[b] Signals for major and minor forms are degenerate.

respectively (Table 3).[187] The fact that the shift of the major form is essentially independent of the heme used for the reconstitution strongly suggests that the contacts between the protein and the heme side-chains at the 2- and 7-positions in the major form are responsible for the transmission of a structural alteration at the active site, exerted by the differential heme–protein contacts, to the EF—H interface.[187] Furthermore, if we assume that the shift of the HisEF5 signal is determined solely by deshielding of the nucleus due to polarization of the N—H bond by the formation of a hydrogen bond, the strength of the hydrogen bond can be correlated to the high-frequency shift of the signal. Hence, the strength of the HisEF5—AspH18 hydrogen bond at the EF—H interface is aligned apoMb < major form < minor form in order of increasing strength of the bond. In fact, the lowest-frequency shifted HisEF5 $N_\varepsilon H$ proton signal observed for apoMb exhibits the largest exchange broadening. The HisEF5 $N_\varepsilon H$ proton signals for the major and minor forms exhibit almost the same linewidth.

4.5.4. Long-range structural correlation between the heme active site and the EF—H interface

Structural characterization of the interfaces from analysis of the high-frequency shifted His imidazole ring NH proton signals has revealed that there is a path for the transmission of structural information between the heme active site and the EF—H interface.[187] The presence of a similar structural correlation between the heme active site and the EF—H interface has been

observed in a mutation study. Cocco *et al.*[188] reported that the replacement of HisEF5 by Gln affects both dynamic and thermodynamic properties of the heme reorientation reaction. The activation energy for the reaction was found to be smaller by 11 kJ mol^{-1} for the mutant relative to that for the wild type and the minor form in the mutant is destabilized by 1.5 kJ mol^{-1} relative to that in the wild type. These results have been interpreted on the basis of the structural stability of the EF—H interface.

Structural change of the EF—H interface is sharply manifested in the NMR parameters of the HisEF5 $N_\varepsilon H$ proton signal through the alteration of the HisEF5—AsH18 hydrogen bond. Although the change in the spectral parameters cannot be quantitatively interpreted in terms of the geometric factors of the hydrogen bond such as the bond length and the bond angle at the present, the linewidth of the HisEF5 $N_\varepsilon H$ proton signal is roughly related to the strength of the HisEF5—AspH18 hydrogen bond. As has been mentioned above, splitting of the HisEF5 $N_\varepsilon H$ proton signals observed for the two heme orientational forms of the Mbs reconstituted with protohemin and mesohemin, and the degeneracy of these signals for the Mb reconstituted with deuterohemin suggest that the protein–heme contacts at 2- and/or 7-positions in the major form play a crucial role for structural coupling between the heme active site and the EF—H interface. The H helix docking against A and G helices in the hydrophobic core of the protein is one of the most stable helices in Mb. Hence it is unlikely that the structure of this helix is influenced by the heme–protein contacts. It is therefore assumed that the structural information between the heme active site and the EF—H interface is transmitted through E- and/or F-helices. The heme side-chain at the 2-position packs against ThrE10, AlaE14, and LeuF4. According to X-ray crystal structure,[114] both N_pH and $N_\varepsilon H$ protons of HisF8 are hydrogen-bonded to carbonyl oxygen of LeuF4. Carbonyl oxygen of HisEF5 accepts the N_pH proton of LeuF1 to form a hydrogen bond, and carbonyl oxygen of LeuF1 accepts the N_pH proton of AlaF5 to form another hydrogen bond. Therefore, if the contact between the heme side-chain at the 2-position and LeuF4 affects the orientation of AlaF5 with respect to the heme, the differential contacts between the heme side-chain at the 2-position and LeuF4 would be transmitted to HisEF5 through the hydrogen bond network AlaF5—LeuF1—HisEF5.[187] Of course, it is also possible that the structural information is transmitted via the E-helix, although more intervening residues are involved, compared with the mechanism via the F-helix.

4.6. Protein folding in cytochrome *c*

Cytochrome *c* (cyt-*c*) is a heme-containing electron carrier of the mitochondorial respiratory chain. Two His residues are conserved in most cyt-*c*:[189] one is His 18 whose side-chain imidazole ring is coordinated to heme iron as an axial

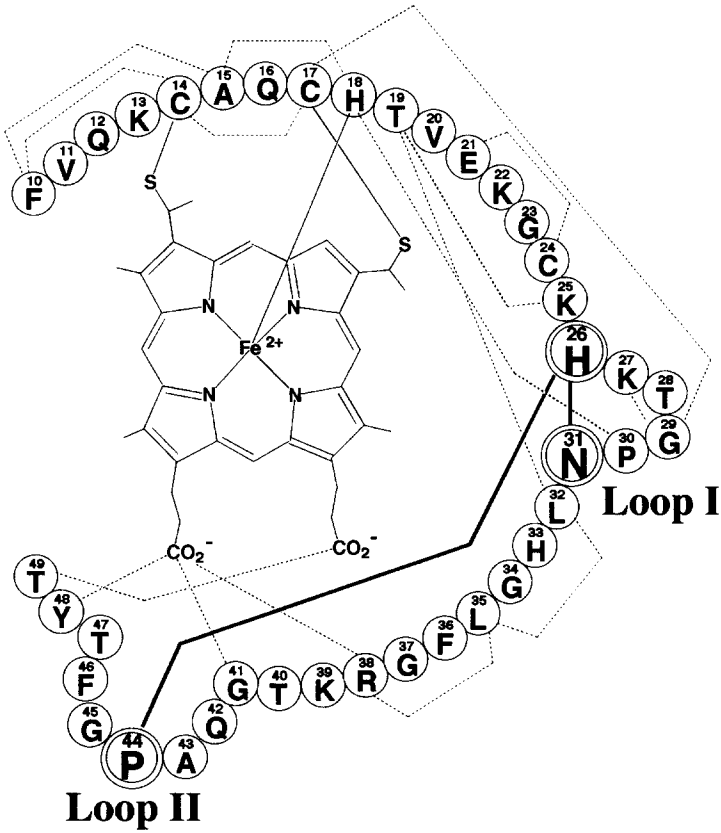

Fig. 26. Schematic representation of the internal hydrogen bond network in horse cytochrome *c*.[117,118] Amino acid residues are indicated by single letter representation in circles. A unique hydrogen bond network of Asn 31—His 26—Pro 44 is indicated by thick solid lines and other hydrogen bonds are represented by broken lines. The residues of 26–31 and 41–47 form loop structures and there is no helical region in the indicated segment of the polypeptide chain. (From ref. 123, © 1997, with permission from the publisher.)

ligand at the active site. The other is His 26 whose side-chain is involved in a unique triad hydrogen bond network with residues at 31 and 44.[117,118,190–192] In this hydrogen bond network, the $N_\varepsilon H$ hydrogen of His 26 is accepted by the carbonyl oxygen of the residue at 44 and the main-chain NH hydrogen of the residue at 31 is hydrogen-bonded to the N_δ atom of His 26 (see Fig. 26). These hydrogen bonds have been proposed to stabilize protein folding of the non-helical region that spans two loop regions, i.e., Loops I and II in Fig. 26. In fact, the substitution of His 26 by Val in rat cyt-*c* leads to a considerable decrease in not only the strength of the coordination bond between heme iron

and Met 80 sulphur, but also globular stability of the protein.[193] The NMR parameters of hydrogen-bonded His imidazole ring NH proton signals reflect the strength of the hydrogen bond as well as the local tertiary structure of the protein and therefore provide unique structural information that cannot be obtained by other techniques.

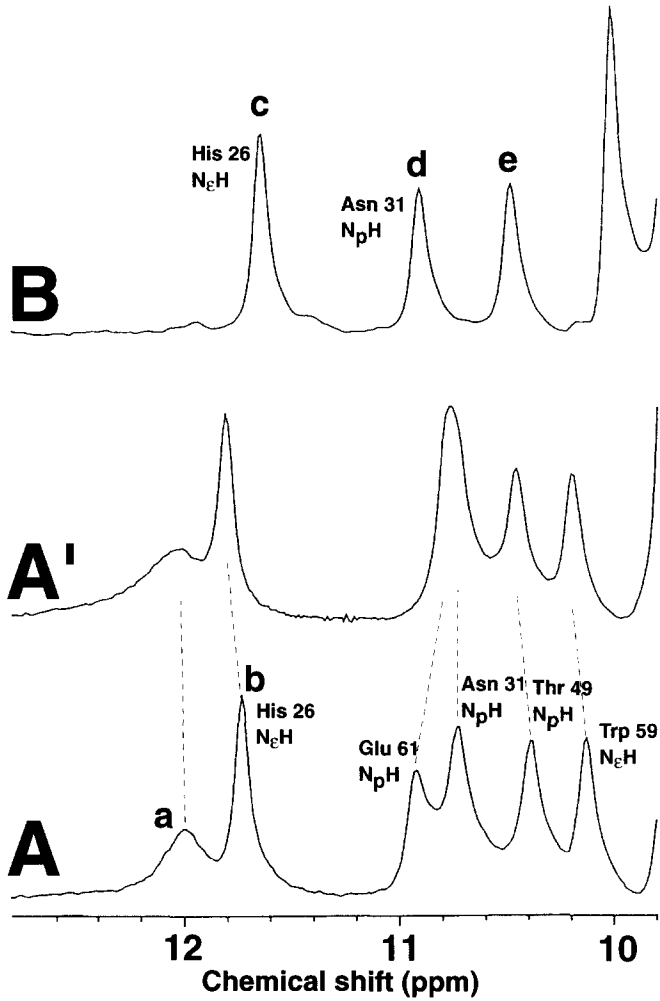

Fig. 27. The high-frequency shifted portions of the 400 MHz ^1H NMR spectra of ferrocytochromes *c* in 90%H_2O/10%^2H_2O at 5 °C. (A) Horse cyt-*c*, pH 8.75. (A′) Same as (A), but in the presence of 400 mM NaCl. (B) Tuna cyt-*c*, pH 8.68. Peaks resolved in the region 10–11 ppm of trace A have been assigned.[194] (From ref. 123, © 1997, with permission from the publisher.)

4.6.1. High-frequency shifted His imidazole NH proton signals

The high-frequency shifted portion of the 400 MHz ^1H NMR spectrum of horse ferro cyt-*c* in 90%H_2O/10%^2H_2O, pH 8.68, at 5 °C is illustrated in Fig. 27A. Six peaks are resolved below 9.6 ppm.[35,123] As indicated with the spectrum, the signals in 9.6–11 ppm have been assigned to the N_pH protons of Glu 61, Asn 31, and Thr 49 and $N_\varepsilon H$ proton of Trp 59.[194] Glu 61 is located at the N terminal of the α helical region composed of residues at 60–69. Glu 61 N_pH hydrogen is relatively isolated from the solvent by the side-chains of Lys 60, Glu 61, and Glu 62, although X-ray crystallographic studies have indicated that this N_pH hydrogen is not involved in a hydrogen bond.[117,118] Asn 31 N_pH proton has been proposed to be hydrogen-bonded to the N_δ atom of His 26 in various cyt-*c*.[117,118,190–192] Thr 49 N_pH and Trp 59 $N_\varepsilon H$ protons were proposed to interact with carboxyl oxygen atoms of heme peripheral propionate side-chains through salt bridges.[117,118] NOE difference spectra recorded with the selective saturation of peak **b** and the Asn 31 N_pH proton signal are shown in traces B and C of Fig. 28(a), respectively. The saturation of peak **b** yields

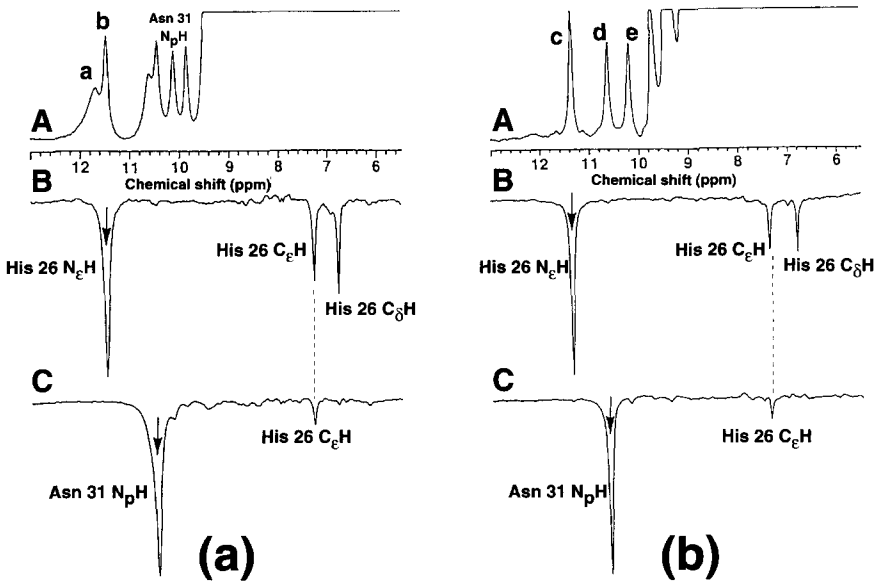

Fig. 28. (a) The high-frequency shifted portion of 400 MHz ^1H NMR spectrum and NOE difference spectra recorded on horse ferrocytochrome *c* in 90%H_2O/10%^2H_2O, pH 8.68, at 5 °C. Reference spectrum (A); NOE difference spectra resulting from saturation of peak b (B); and Asn 31 N_pH proton signal (C). (b) The high-frequency shifted portion of 400 MHz ^1H NMR spectrum and NOE difference spectra recorded on tuna ferrocytochrome *c* in 90%H_2O/10%^2H_2O, pH 8.75, at 5 °C. Reference spectrum (A); NOE difference spectra resulting from saturation of peak **c** (B); and peak **d** (C). (From ref. 123, © 1997, with permission from the publisher.)

almost equivalent NOEs to two peaks at 6.74 and 7.23 ppm. The observed NOE connectivity pattern is similar to that observed for the imidazole ring $C_\varepsilon H$ and $C_\delta H$ proton signals for saturation of the $N_\varepsilon H$ proton signal of a His side-chain involved in an internal hydrogen bond in the Mbs (see Figs. 9, 10, and 17).[120-122] Hence peak **b** is assigned to the $N_\varepsilon H$ proton of a His residue in horse cyt-*c* and peaks at 6.74 and 7.23 ppm are assigned to $C_\varepsilon H$ and $C_\varepsilon H$ protons, respectively, of the same residue on the basis of their shifts. The $C_\delta H$ and $C_\varepsilon H$ proton shifts of this His residue at 35 °C and pH 9.42 are 7.15 and 7.62 ppm, respectively. Horse cyt-*c* contains three His residues, His 18, 26, and 33.[195] The side-chain of His 18 is one of the axial ligands to heme iron and its $C_\delta H$ and $C_\varepsilon H$ proton signals are low-frequency shifted to 0.13 and 0.41 ppm at 40 °C and pH 5.75, respectively, due to the ring-current effects of porphyrin.[194] The $C_\delta H$ and $C_\varepsilon H$ proton resonances of His 26 at 40 °C and pH 5.75 are reported to be 7.05 and 7.51 ppm, respectively, and those of His 33 are 7.46 and 8.37 ppm, respectively.[194] Consequently the similarity in the shifts indicates that the signals in trace B of Fig. 28(a) are attributed to imidazole ring protons of His 26.[123] This assignment is confirmed by the observation of an NOE connectivity between Asn 31 N_pH proton and His 26 $C_\varepsilon H$ proton signals, as illustrated in trace C of Fig. 28(a). The fact that the Asn 31 N_pH and His 26 $C_\varepsilon H$ protons are located in close proximity strongly suggests the presence of a hydrogen bond between these two residues in this protein in solution.[123]

The spectrum of tuna ferro cyt-*c* in 90%H_2O/10%^2H_2O, pH 8.75, at 5 °C is illustrated in Fig. 27B. Three exchangeable proton signals, peaks c–e, are resolved below 10 ppm. NOE difference spectra of tuna ferro cyt-*c* are illustrated in Fig. 28(b). Saturation of the signal at 11.35 ppm, peak **c** in trace B of Fig. 27, yields NOEs to two peaks at 6.79 and 7.36 ppm. In tuna cyt-*c*, His residue at 33 is replaced by Trp, whereas His 18 and 26 are conserved.[196,197] Although the signal assignments of this protein was only partly reported,[198] the similarity in the NOE connectivity pattern between traces B of Figs. 28(a) and 28(b) strongly suggests that the three resonances in trace B of Fig. 28(b) can be assigned to His 26 imidazole ring protons. Furthermore, the fact that the saturation of peak **d** yields an NOE to the His 26 $C_\varepsilon H$ proton signal not only indicates that this signal arises from the Asn 31 N_pH proton, but also confirms formation of the hydrogen bond between His 26 and Asn 31 in tuna cyt-*c* in solution.[123]

4.6.2. Temperature dependence of exchangeable proton signals

The high-frequency shifted portions of the 400 MHz ^1H NMR spectra of horse and tuna ferro cyt-*c* in 90%H_2O/10%^2H_2O at various temperatures are illustrated in Figs. 29A and B, respectively. In the spectra of horse cyt-*c*, peak **a** and His 26 $N_\varepsilon H$ and Glu 61 amide N_pH proton signals exhibit exchange broadening with increasing temperature and almost completely disappear

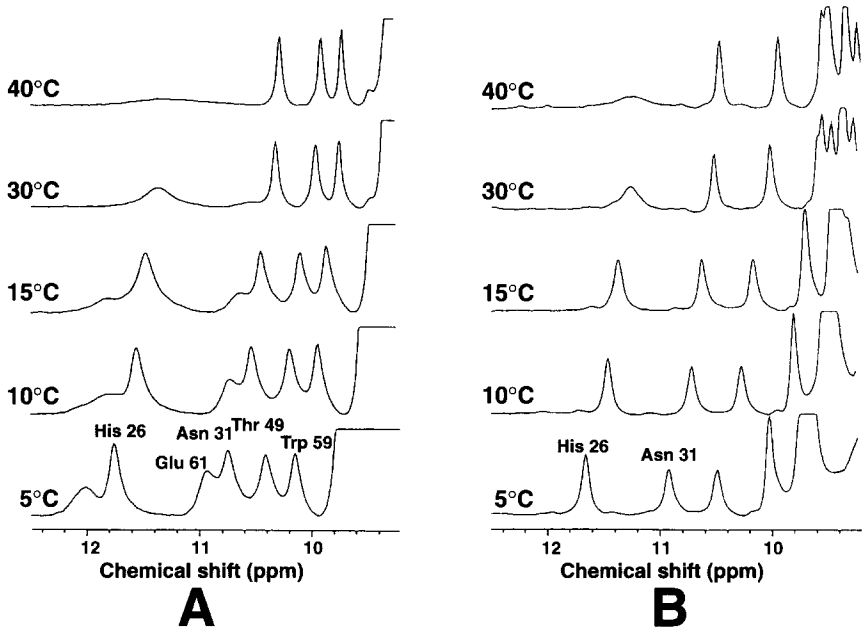

Fig. 29. The high-frequency shifted portion, 9.2–13.0 ppm, of the 400 MHz ^{1}H NMR spectra of horse, pH 8.68, (A) and tuna, pH 8.75, (B) ferrocytochromes *c* in 90%H_2O/10%^2H_2O at the indicated temperatures. (From ref. 123, © 1997, with permission from the publisher.)

at 40 °C. His 26 $N_\varepsilon H$ proton signal of tuna cyt-*c* also exhibits a similar temperature dependence. NOE difference spectra with the saturation of His 26 $N_\varepsilon H$ proton signal at various temperatures yield temperature-dependent shifts of the $C_\delta H$ and $C_\varepsilon H$ proton signals. They exhibit low-frequency shift with increasing temperature and the plots of their shifts as a function of temperature are satisfactorily represented by a straight line.[123]

4.6.3. pH dependence of exchangeable proton signals

The high-frequency shifted portions of the 400 MHz ^{1}H NMR spectra of horse and tuna ferro cyt-*c* in 90%H_2O/10%^2H_2O at 5 °C and the indicated pH values are illustrated in Figs. 30A and B, respectively. The plots of the linewidth of the His 26 $N_\varepsilon H$ proton signal of the two cyt-*c* as a function of pH, together with similar plots for the HisEF5 $N_\varepsilon H$ proton signal of horse Mb(CO),[120] for comparison, are shown in Fig. 31. The linewidth of the His 26 $N_\varepsilon H$ proton signal of cyt-*c* broadens in both acidic and alkaline pH conditions with the minimum at pH ~9, and this signal exhibits essentially no shift change over the pH range examined.[123] The slopes of the pH profiles in Fig. 31 vary among

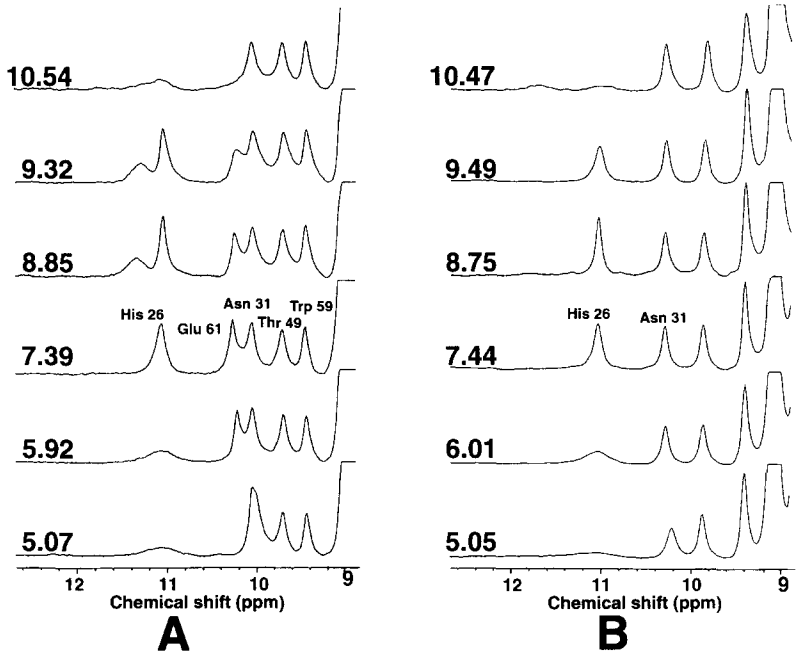

Fig. 30. The high-frequency shifted portion, 9.2–13.0 ppm, of the 400 MHz ^{1}H NMR spectra of horse (A) and tuna (B) ferrocytochromes *c* in 90%H_2O/10%^2H_2O at 5 °C and the indicated pH values. (From ref. 123, © 1997, with permission from the publisher.)

the proteins, reflecting differences in their chemical environments. The absence of pH-dependent shift for the His 26 $N_\varepsilon H$ proton signal in the pH range examined indicates that the pK_a value of His 26 is <5.

*4.6.4. Chemical environment of His 26 in horse and tuna cyt-*c

X-ray crystallographic studies of various cyt-*c* indicate that the His 26 side-chain imidazole ring participates in a unique triad hydrogen bond network formed with residues at 31 and 44.[117,118,190–192] Asn occupies residue 31 in both horse[195] and tuna[196,197] proteins and Pro and Asp are located at residue 44 in the former and the latter, respectively. In this hydrogen bond network, the Asn 31 $N_\delta H$ proton is accepted by the His 26 N_δ atom and the His 26 $N_\varepsilon H$ proton is hydrogen-bonded to the carbonyl oxygen atom of Pro 44 in horse cyt-*c* (or Asp 44 in tuna cyt-*c*). Polarization of the N–H bonds of His 26 and Asn 31 by these hydrogen bonds results in relatively large high-frequency shifts for these NH proton signals. The NOE connectivity between His 26 and Asn 31 signals (see Fig. 28) confirms the formation of this triad hydrogen bond in these proteins in solution.[123]

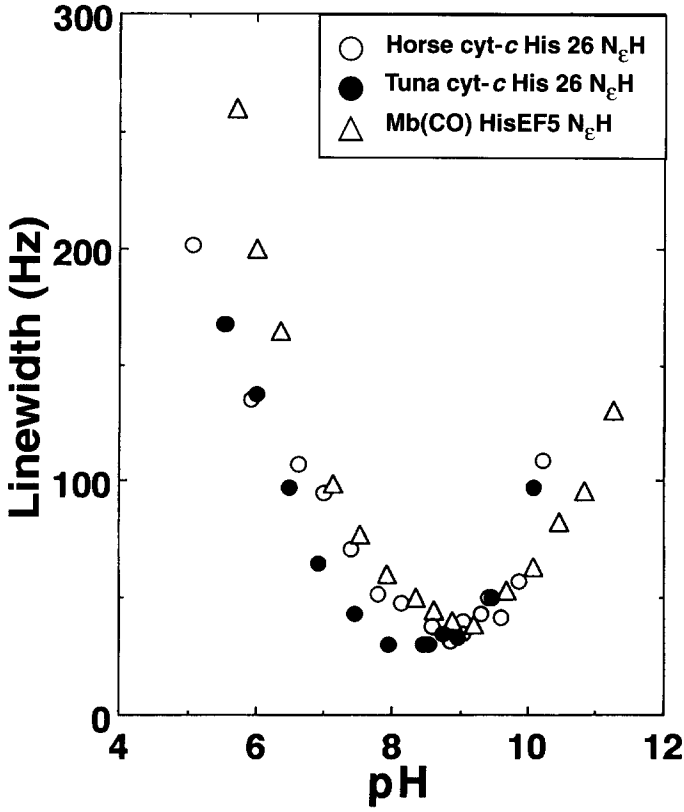

Fig. 31. Plots of the linewidth of His 26 $N_{\varepsilon}H$ proton signal in horse (open circles) and tuna (filled circles) ferrocytochromes *c* in 90%H_2O/10%^2H_2O at 5 °C as a function of pH. Similar plots for HisEF5 $N_{\varepsilon}H$ proton signal in horse Mb(CO)[120] are indicated by triangles, for comparison. (From ref. 123, © 1997, with permission from the publisher.)

Comparison of the shifts of the corresponding resonances between horse and tuna cyt-*c* indicates that the effects of the substitution at residue 44 on this hydrogen bond network is not significant. But the shifts of His 26 $N_{\varepsilon}H$ and Asn 31 N_pH proton signals appear to be correlated with each other in such a manner that the polarization of one N–H bond is influenced by that of the other via the His 26 imidazole ring. Hence the low- and high-frequency shifts for His 26 $N_{\varepsilon}H$ and Asn 31 N_pH proton signals, respectively, in tuna cyt-*c*, relative to the corresponding signals in horse cyt-*c*, would indicate that the His 26 N_{ε}–H bond is less polarized in tuna cyt-*c* than in horse cyt-*c* and, on the other hand, the magnitude of the polarization of the Asn 31 N–H bond is larger in the former.

4.6.5. *Comparison of protein conformation between horse and tuna cyt-c*

The similarity in Asn 31 and Thr 49 amide N_pH proton shifts between the two proteins clearly demonstrates the homologous active site structures in these proteins in solution,[123] as suggested by an X-ray study.[117,118] Since there is no helical region from residue 14 to residue 48, the internal hydrogen bonds, Asn 31—His 26—Pro 44 and Asn 31—His 26—Asp 44 in horse and tuna cyt-*c*, respectively, are thought to contribute to stabilize the protein conformation in this region. The importance of His 26 in the stability of protein folding has been demonstrated by a mutation study.[193]

As mentioned above, Glu 61 N_pH hydrogen is relatively isolated from solvent by the side-chains of Lys 60, Glu 61, and Glu 62. The conformation of Glu 61 side-chain is fixed by the formation of a hydrogen bond between the Glu 61 O_ε atom and $N_\eta H$ hydrogen of Lys 99.[117,118] Lys 60, Glu 61 and Glu 62 in horse cyt-*c* are replaced by Asn 60, Asn 61 and Asp 62, respectively, in tuna protein.[196,197] Asn 61 N_pH proton signal in tuna protein is not resolved below 10 ppm. Comparison of the crystal structures between the two proteins indicates that the chemical environment of Asn 61 N_pH hydrogen in tuna protein is more exposed to the solvent than Glu 61 N_pH hydrogen in horse cyt-*c*[117,118] because of these amino acid substitutions.

4.6.6. *Effects of salt concentration on high-frequency shifted exchangeable proton signals*

The effects of ionic strength on protein folding of cyt-*c* have been investigated using a variety of physicochemical measurements. Small-angle X-ray scattering measurements of horse cyt-*c* suggested that the radius of gyration of the oxidized protein increases with decreasing ionic strength.[199] On the other hand, comparison of X-ray structures determined for the crystals grown under two different salt conditions indicated the absence of a significant influence of ionic strength on the conformation of the protein.[117,118] ^1H NMR study of horse cyt-*c* demonstrated the presence of relatively large salt-dependent shifts on the signals of the residues at 61, 83, and 87–89.[200]

The addition of 400 mM NaCl affects both the shift and linewidth of high-frequency shifted exchangeable proton signals of horse cyt-*c* (A′ of Fig. 27). Peak a becomes slightly broader in the presence of high salt concentration, whereas its shift is not influenced. The His 26 $N_\varepsilon H$ proton signal (peak b) shifts slightly towards high frequency in the presence of high salt concentration.[123] The Glu 61 N_pH proton signal exhibits low-frequency shift of 0.17 ppm. The relatively large low-frequency shift of the Glu 61 N_pH proton signal in the presence of high salt concentration is consistent with a previous report.[200] High-frequency shift and narrowing of the signals for both Thr 49 N_pH and Trp 59 $N_\varepsilon H$ protons are induced by the addition of 400 mM NaCl. The relatively large salt-induced shift observed for the Glu 61 N_pH proton signal

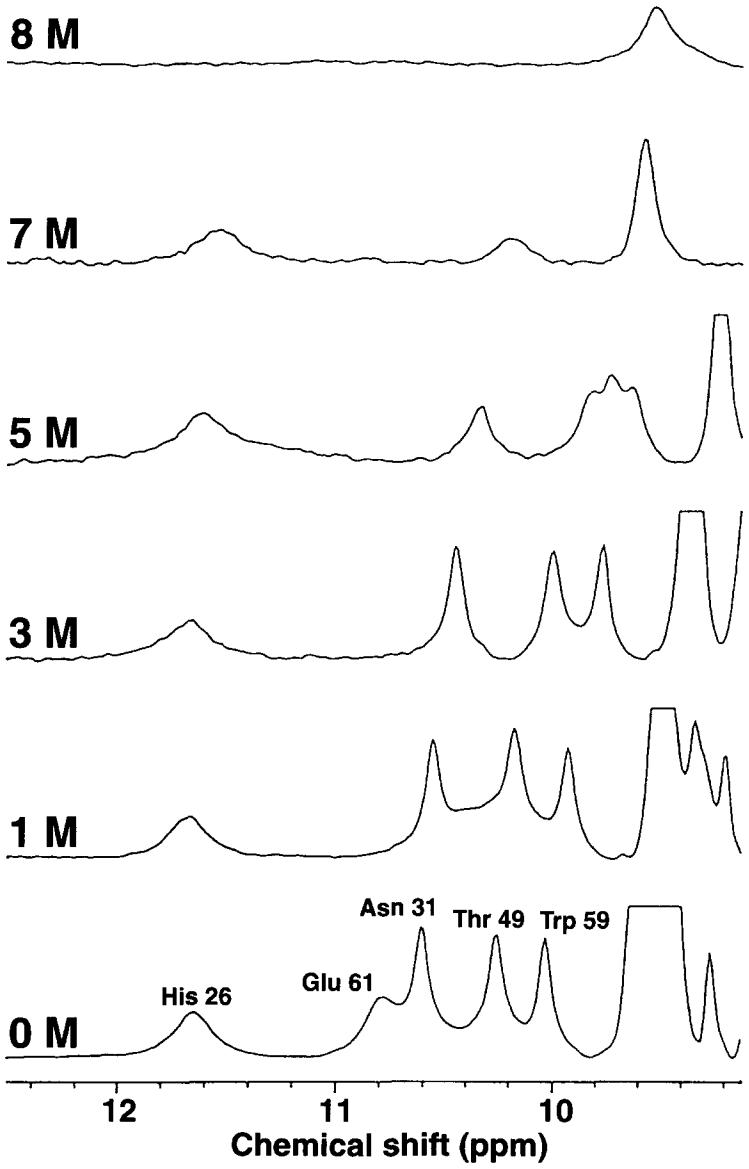

Fig. 32. The high-frequency shifted portions, 9.15–12.5 ppm, of 400 MHz ^{1}H NMR spectra of horse ferrocytochrome *c* in 90%H_2O/10%$^{2}H_2O$, pH 8.85, at 25 °C in the presence of the indicated concentrations of Gdn-HCl. (From ref. 123, © 1997, with permission from the publisher.)

could be attributed to the fact that this proton is surrounded by charged side-chains on the surface of the molecule, as described above. On the other hand, the relatively small salt-induced shift for the other signals indicates that the hydrogen bond network, Asn 31—His 26—Pro 44, and the heme–protein salt bridges via the Thr 49 N_pH and the Trp 59 $N_\varepsilon H$ protons are nearly intact in the presence of 400 mM NaCl.

4.6.7. Effect of denaturant on the exchangeable proton signals

The high-frequency shifted portions of the 400 MHz ^1H NMR spectra of horse cyt-*c* in the presence of various concentrations of the denaturant guanidine hydrochloride (Gdn—HCl) are illustrated in Fig. 32. The high-frequency shifted exchangeable proton signals are influenced by the addition of Gdn—HCl. AUV—VIS study of the effect of the Gdn—HCl addition on the structure of ferric cyt-*c* at pH 8.80 indicated that the coordination bond between heme iron and Met 80 sulphur is completely broken in the presence of 6M Gdn—HCl. Complete unfolding of horse cyt-*c* in the presence of 6M Gdn—HCl is consistent with the results of fluorescence[201,202] and far-UV CD studies.[203] The Glu 61 N_pH proton signal considerably broadens and shifts towards low-frequency with increasing denaturant concentration. But the other NH proton signals are observable even in the presence of 7M Gdn—HCl.[123]

Trp 59 $N_\varepsilon H$ proton signal is observable in the presence of 5M Gdn—HCl, strongly suggesting that the hydrogen bond between Trp 59 $N_\varepsilon H$ hydrogen and heme propionate carboxyl oxygen atom is retained under these experimental conditions. A single Trp residue in horse cyt-*c* has been characterized exhaustively by fluorescence spectroscopy.[201,202] Fluorescence study of Gdn—HCl denaturation of horse ferri cyt-*c* demonstrated that more than 80% fluorescence is influenced by the addition of 5M Gdn—HCl. Since the fluorescence intensity of this residue in the protein has shown to be quenched largely by energy transfer to the heme,[204] it could be extremely sensitive to the distance between these two chromophores.

Although, in the absence of the denaturant, the linewidth of the His 26 $N_\varepsilon H$ proton signal is larger than that of the Asn 31 N_pH proton signal at a given temperature and pH value, the linewidth of the latter signal is more significantly affected by the addition of the denaturant than that of the former and they simultaneously disappear in the presence of 8M Gdn—HCl. Since the signals exhibit low-frequency shifts with increasing concentration of the denaturant, the structural changes upon Gdn—HCl denaturation could be related to conformational changes induced by thermal motion. These results indicate that the triad hydrogen bond network, Asn 31—His 26—Pro 44 in horse cyt-*c*, is formed even in 7M Gdn—HCl, although the measurements of CD[201] and absorption spectra indicated that the protein is completely unfolded in the presence of 7M Gdn—HCl. Since the intensities of the CD band at 222

nm and the absorption at 695 nm reflect the helical contents and the coordination bond between heme iron and the Met 80 sulphur atom, respectively, conformation of the loop regions composed of residues at 26–44 may not be inferred from these spectroscopic data.[123]

4.7. Active site of Cu, Zn superoxide dismutase

When metalloproteins are investigated by NMR, the primary interest at the very beginning of the study focuses quite often on structural features in the vicinity of the metal ion(s). Because of this consideration, the way the NMR approach is used for studies of metalloproteins is different from that for characterizing other biological macromolecules. Cu, Zn superoxide dismutases (SOD) are ubiquitous enzymes that play a key role in the mechanisms of cell protection against the toxic effects of reactive oxygen species by catalysing the disproportionation of superoxide ion.[205] SOD is a homodimeric enzyme and each subunit consists of about 150 amino acid residues. The structure of SOD is characterized by a flattened β-barrel with a dimetallic active site of copper and zinc ions, which are linked together by the side-chain imidazole ring of a His residue (His 63 for human SOD) in the crystalline state (see the inset of

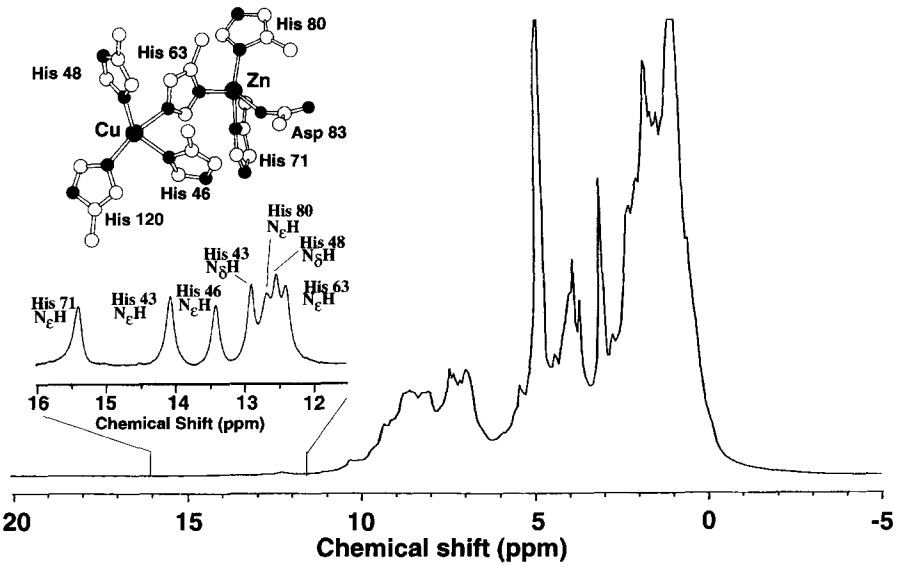

Fig. 33. The 400 MHz ^{1}H NMR spectrum of human SOD in 90%H_2O/10%^2H_2O, pH 5.15, at 25 °C. The high-frequency shifted portion, 11.5–16 ppm, of the spectrum is expanded in the inset and the signal assignments are given.[207] The structure of the catalytic dimetallic core in the enzyme is also given in the inset.

Fig. 33).[119] In the case of human SOD, three other His residues (His 43, 46, and 120) coordinate to the copper ion and His 71, His 80, and Asp 83 bind to the zinc ion. According to the X-ray structure,[119] the side-chain NH hydrogen atoms of these His residues participate in internal hydrogen bonds.

NMR has been used exhaustively to characterize the structure–function relationship in various SODs in diamagnetic as well as paramagnetic forms.[206, 207] NMR can unequivocally describe the tautomerism and the protonation behaviour of His side-chains. Similarly to the cases of Mb and cyt-*c*, His imidazole NH proton signals are resolved in the high-frequency shifted portion of ^{1}H NMR spectrum of human reduced SOD (Cu^+, Zn^{2+}) in 90%H_2O/10%^2H_2O,[208, 209] as illustrated in Fig. 33. Using the techniques described above, these signals have been assigned as indicated with the spectrum.[208] Observation of the signal for His 63 $N_\varepsilon H$ proton argued against the result from crystallographic study, that the imidazolate side-chain of this His bridges the two metal ions at the active site of the protein. Later, it was confirmed that the Cu—His 63—Zn bridge is intact in the solid state and that the bridge is broken in solution to produce a protonated neutral His 63

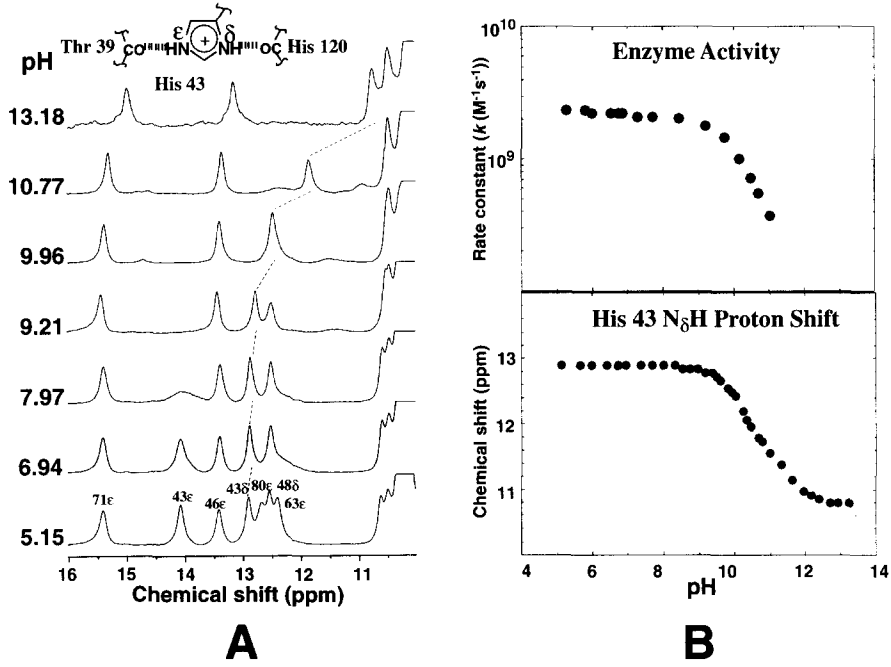

Fig. 34. (A) pH dependence of high-frequency shifted His imidazole NH proton signals of human SOD in 90%H_2O/10%^2H_2O at 25 °C. (B) pH profiles of the enzyme activity[211] (upper) and His 43 $N_\delta H$ proton shift (lower). The pH-dependent His 43 $N_\delta H$ proton shift exhibits a p*K*a value of 10.7.[212]

imidazole ring coordinated to Zn.[210] The details of the electron and proton transfer in conjunction with the role of the imidazolate-bridged dimetallic centre and the functional properties of this enzyme require further investigation.

The pH dependence of high-frequency shifted His imidazole NH proton signals are shown in Fig. 34A. The His 43 $N_\delta H$ and $N_\varepsilon H$ proton signals are largely influenced by pH changes. His 43 possesses an imidazolonium side-chain with $N_\delta H$ and $N_\varepsilon H$ hydrogen-bonded to carbonyl oxygen atoms of His 120 and Thr 39, respectively. The pH-dependent shift of the His 43 $N_\delta H$ proton signal correlates well with the reported pH-dependence of the enzyme activity[211] (Fig. 34B), indicating the importance of this residue in the structure–function relationship of human SOD.[212]

5. CONCLUDING REMARKS

This chapter has described the characterization of the structure–function relationship in metalloproteins through the analysis of high-frequency shifted His imidazole ring NH proton signals as spectroscopic probes. These His signals sharply reflect the microenvironments of their side-chains within a macromolecule and hence subtle structural alterations can be detected through observation of changes in their NMR spectral parameters. Thus characterization of these signals possibly provides not only local structural information complementary to structural features of the whole macromolecule, determined by crystallography or NMR, but also an opportunity for a simple, but highly refined, structural comparison at specific sites of the molecules in solution.

REFERENCES

1. L. Pauling, *The Nature of the Chemical Bond*, Cornell University Press, Ithaca, New York, 1939.
2. D. Voet and J. G. Voet, *Biochemistry*, Chapter 2, John Wiley & Sons, New York, 1990.
3. R. E. Dickerson, *Meth. Enzymol.*, 1992, **211**, 67.
4. B. Alberts, D. Bray, J. Lewis, M. Raff, K. Roberts and J. D. Watson, *Molecular Biology of the Cell*, Third Edition, Chapter 3, Garland Publishing, New York, 1994.
5. L. Stryer, Biochemistry, Fourth Edition, Parts I, II and V, W. H. Freeman and Company, New York, 1995.
6. C. Branden and J. Tooze, *Introduction to Protein Structure*, Second Edition, Garland Publishing, New York, 1999.
7. G. A. Jeffrey and W. Sanger, *Hydrogen Bonding in Biological Structures*, Springer-Verlag, Berlin, 1994.
8. W. W. Cleland, P. A. Frey and J. A. Gerlt, *J. Biol. Chem.*, 1998, **273**, 25529.
9. W. W. Cleland and D. B. Northrop, *Meth. Enzymol.*, 1999, **308**, 3.
10. P. A. Frey, S. A. Whitt and J. B. Tobin, *Science*, 1994, **264**, 1927.
11. P. A. Frey, *Science*, 1995, **268**, 189.
12. W. W. Cleland and M. M. Kreevoy, *Science*, 1994, **264**, 1887.

13. W. W. Cleland and M. M. Kreevoy, *Science*, 1995, **269**, 104.
14. S. Shan and D. Herschlag, *Meth. Enzymol.*, 1999, **308**, 246.
15. J. A. Gerlt, M. M. Kreevoy, W. W. Cleland and P. A. Frey, *Chem. Biol.*, 1997, **4**, 259.
16. W. W. Cleland, *Arch. Biochem. Biophys.*, 2000, **382**, 1.
17. A. Warshel, A. Papazyan and P. A. Kollman, *Science*, 1995, **269** 102.
18. J. P. Guthrie, *Chem. Biol.*, 1996, **3**, 163.
19. E. L. Ash, J. L. Sudmeier, E. C. De Fabo and W. W. Bachovchin, *Science*, 1997, **278**, 1128.
20. G. A. Jeffrey, *An Introduction to Hydrogen Bonding*, Oxford University Press, Oxford, 1997.
21. G. R. Desiraju and T. Steiner, *The Weak Hydrogen Bond in Structural Chemistry and Biology*, Oxford Science Publications, Oxford, 1999.
22. F. Hibbert and J. Emsley, *Adv. Phys. Org. Chem.*, 1990, **26**, 255.
23. D. Hádzi, *Theoretical Treatments of Hydrogen Bonding*, John Wiley & Sons, Chichester 1997.
24. C. L. Perrin and J. B. Nielson, *Annu. Rev. Phys. Chem.*, 1997, **48**, 511.
25. J. D. Glickson, C. C. McDonald and W. D. Phillips, *Biochem. Biophys. Res. Commun.*, 1969, **35**, 492.
26. D. J. Patel, L. Kampa, R. G. Shulman, T. Yamane and M. Fujiwara, *Biochem. Biophys. Res. Commun.*, 1970, **40**, 1224.
27. D. J. Patel, L. Kampa, R. G. Shulman, T. Yamane and B. J. Wyluda, *Proc. Natl. Acad. Sci. USA*, 1970, **67**, 1109.
28. J. D. Glickson, W. D. Phillips and J. A. Rupley, *J. Am. Chem. Soc.*, 1971, **93**, 4031.
29. D. J. Patel, C. K. Woodward and F. A. Bovey, *Proc. Natl. Acad. Sci. USA*, 1972, **69**, 599.
30. G. Robillard and R. G. Shulman, *J. Mol. Biol.*, 1972, **71**, 507.
31. G. Robillard and R. G. Shulman, *Ann. N. Y. Acad. Sci.*, 1973, **222**, 220.
32. J. H. Griffin, J. S. Cohen and A. N. Schechter, *Biochemistry*, 1973, **12**, 2096.
33. G. Robillard and R. G. Shulman, *J. Mol. Biol.*, 1974, **86**, 519.
34. G. Robillard and R. G. Shulman, *J. Mol. Biol.*, 1974, **86**, 541.
35. E. Stellwagen and R. G. Shulman, *J. Mol. Biol.*, 1973, **75**, 683.
36. D. M. Crothers, C. W. Hilbers and R. G. Shulman, *Proc. Natl. Acad. Sci. USA*, 1973, **70**, 2899.
37. D. M. Crothers, P. E. Cole, C. W. Hilbers and R. G. Shulman, *J. Mol. Biol.*, 1974, **87**, 63.
38. R. G. Shulman, C. W. Hilbers, D. Söll and S. K. Yang, *J. Mol. Biol.*, 1974, **90**, 601.
39. R. G. Shulman, C. W. Hilbers, D. Söll and S. K. Yang, *J. Mol. Biol.*, 1974, **90**, 609.
40. D. R. Kearns, D. J. Patel and R. G. Shulman, *Nature*, 1971, **229**, 338.
41. C. W. Hilbers and R. G. Shulman, *Proc. Natl. Acad. Sci. USA*, 1974, **71**, 3239.
42. A. J. Dingley and S. Grzesiek, *J. Am. Chem. Soc.*, 1998, **120**, 8293.
43. T. R. Dyke, K. M. Mack and J. S. Muenter, *J. Chem. Phys.*, 1977, **66**, 498.
44. J. A. Odutola and T. R. Dyke, *J. Chem. Phys.*, 1982, **72**, 5062.
45. W. F. Kuhs and M. S. Lehmann, *J. Phys. Chem.*, 1983, **87**, 4312.
46. Y. Pan and M. A. McAllister, *J. Am. Chem. Soc.*, 1998, **120**, 166.
47. Y. Pan and M. A. McAllister, *Can. J. Chem.*, 1997, **75**, 1195.
48. T. Steiner and W. Sanger, *Acta Crystallogr. Sect. B, Struct. Sci.*, 1994, **50**, 348.
49. P. Gilli, V. Bertolase, V. Ferretti and G. Gilli, *J. Am. Chem. Soc.*, 1994, **116**, 909.
50. T. K. Ghanty, V. N. Staroverov, P. R. Koren and E. R. Davidson, *J. Am. Chem. Soc.*, 2000, **122**, 1210.
51. J. A. Gerlt and P. G. Gassman, *Biochemistry*, 1993, **32**, 11934.
52. J. A. Gerlt and P. G. Gassman, *J. Am Chem. Soc.*, 1993, **115**, 11552.
53. A. Kahyaoglu, K. Haghjoo, F. Gau, F. Jordan, C. Kettner, F. Felföldi and L. Polgár, *J. Biol. Chem.*, 1997, **272**, 25547.
54. R. D. Kidd, P. Sears, D. H. Huand, K. Witte, C. H. Wong and G. K. Farber, *Protein Sci.*, 1999, **8**, 410.
55. K. S. Kim, K. S. Oh and J. Y. Lee, *Proc. Natl. Acad. Sci. USA*, 2000, **97**, 6373.
56. S. Shan and D. Herschlag, *Proc. Natl. Acad. Sci. USA*, 1996, **93**, 14474.

57. P. R. Blake, J.-B. Park, M. W. W. Adams and M. F. Summers, *J. Am. Chem. Soc.*, 1992, **114**, 4931.
58. P. R. Blake, M. F. Summers, M. W. W. Adams, J.-B. Park, Z.-H. Zhou and A. Bax, *J. Biomol. NMR*, 1992, **2**, 527.
59. A. J. Dingley, J. E. Masse, R. D. Peterson, M. Barfield, J. Feigon and S. Grzesiek, *J. Am. Chem. Soc.*, 1999, **121**, 6019.
60. G. Cornilescu, B. E. Ramirez, M. K. Frank, G. M. Clore, A. M. Gronenborn and A. Bax, *J. Am. Chem. Soc.*, 1999, **121**, 6275.
61. R. K. Harris, *Nuclear Magnetic Resonance Spectroscopy*, Chapter 8, Longman, Harlow, Essex, 1986.
62. K. Pervushin, A. Ono, C. Fernández, T. Szyperski, M. Kainosho and K. Wüthrich, *Proc. Natl. Acad. Sci. USA*, 1998, **95**, 14147.
63. F. Cordier and S. Grzesiek, *J. Am. Chem. Soc.*, 1999, **121**, 1601.
64. G. Cornilescu, J.-S. Hu and A. Bax, *J. Am. Chem. Soc.*, 1999, **121**, 2949.
65. A. Meissner and O. W. Sørensen, *J. Magn. Reson.*, 2000, **143**, 387.
66. F. Cordier, M. Rogowski, S. Grzesiek and A. Bax, *J. Magn. Reson.*, 1999, **140**, 510.
67. M. Hennig and B. H. Geierstanger, *J. Am. Chem. Soc.*, 1999, **121**, 5123.
68. M. Mishima, M. Hatanaka, S. Yokoyama, T. Ikegami, M. Wälchili, Y. Ito and M. Shirakawa, *J. Am. Chem. Soc.*, 2000, **122**, 5883.
69. A. Meissner and O. W. Sørensen, *J. Magn. Reson.*, 2000, **143**, 431.
70. A. Liu, A. Majumdar, W. Hu, A. Kettani, E. Skripkin and D. J. Patel, *J. Am. Chem. Soc.*, 2000, **122**, 3206.
71. C. Scheurer and R. Brüschweiler, *J. Am. Chem. Soc.*, 1999, **121**, 8661.
72. H. Benedict, I. G. Shenderovich, O. L. Malkina, V. G. Malkin, G. S. Denisov, N. F. Goloubev and H.-H. Kimbach, *J. Am. Chem. Soc.*, 2000, **122**, 1979.
73. J. E. Del Bene, S. A. Perera and R. J. Bartlett, *J. Am. Chem. Soc.*, 2000, **122**, 3560.
74. J. D. Satterlee, *Annu. Rep. NMR Spectrosc.*, 1986, **17**, 79.
75. Y. Yamamoto, *Annu. Rep. NMR Spectrosc.*, 1998, **30**, 1.
76. I. Bertini and C. Luchinat, *Coord. Chem. Rev.*, 1996, **150**, 1.
77. G. N. La Mar, J. D. Satterlee and J. S. De Ropp, *The Porphyrin Handbook*, Vol. 5 (eds K. M. Kadish, K. M. Smith and R. Guilard), Academic Press, New York, 2000, p. 185.
78. F. A. Walker, *The Porphyrin Handbook*, Vol. 5 (eds K. M. Kadish, K. M. Smith and R. Guilard), Academic Press, New York, 2000, p. 81.
79. J. T. J. Lecomte and G. N. La Mar, *J. Am. Chem. Soc.*, 1987, **109**, 7219.
80. S. Yoshikawa, D. H. O'Keeffe and W. S. Caughey, *J. Biol. Chem.*, 1985, **260**, 3518.
81. S. E. V. Phillips, *J. Mol. Biol.*, 1980, **142**, 531.
82. X. Cheng and B. P. Schoenborn, *J. Mol. Biol.*, 1980, **142**, 133.
83. F. Shu, V. Ramakrishnan and B. P. Schoenborn, *Proc. Natl. Acad. Sci. USA*, 2000, **97**, 3872.
84. J. T. J. Lecomte and G. N. La Mar, *Biochemistry*, 1985, **24**, 7388.
85. Y. Yamamoto, T. Nakashima, E. Kawano and R. Chûjô, *Biochim. Biophys. Acta*, 1998, **1388**, 349.
86. Y. Yamamoto, K. Iwafune, R. Chûjô, Y. Inoue, K. Imai and T. Suzuki, *J. Mol. Biol.*, 1992, **228**, 343.
87. Y. Yamamoto and T. Suzuki, *Biochim. Biophys. Acta*, 1996, **1293**, 129.
88. S. D. Emerson and G. N. La Mar, *Biochemistry*, 1990, **29**, 1545.
89. K. J. Cross and P. E. Wright, *J. Magn. Reson.*, 1985, **64**, 220.
90. S. D. Emerson and G. N. La Mar, *Biochemistry*, 1990, **29**, 1556.
91. I. Morishima and T. Inubushi, *J. Am. Chem. Soc.*, 1987, **110**, 3568.
92. T. J. Shen, N. T. Ho, V. Simplaceanu, M. Zou, B. N. Green, M. F. Tam and C. Ho, *Proc. Natl. Acad. Sci. USA*, 1993, **90**, 8108.
93. T. J. Shen, N. T. Ho, M. Zou, D. P. Sun, P. E. Cottam, V. Simplaceanu, M. F. Tam, D. A. Bell, Jr. and C. Ho, *Protein Eng.*, 1997, **10**, 1085.

94. V. Simplaceanu, J. A. Lukin, T.-Y. Fang, M. Zou, N. Ho and C. Ho, *Biophys. J.*, 2000, **79**, 1146.
95. J. A. Lukin, V. Simplaceanu, M. Zou, N. Ho and C. Ho, *Proc. Natl. Acad. Sci. USA*, 2000, **97**, 10354.
96. B. Geierstanger, M. Jamin, B. F. Volkman and R. L. Baldwin, *Biochemistry*, 1998, **37**, 4254.
97. G. Wagner, *Quart. Rev. Biophys.*, 1983, **16**, 1.
98. K. Wüthrich, *NMR of Proteins and Nucleic Acids*, Chapter 2, John Wiley & Sons, New York, 1986.
99. C. Dalvit and P. E. Wright, *J. Mol. Biol.*, 1987, **194**, 313.
100. L. J. Altman, D. Laungani, G. Gunnarsson, H. Wennerström, W. Ega and S. Forsen, *J. Am. Chem. Soc.*, 1978, **100**, 8264.
101. C. S. Cassidy, J. Lin and P. A. Frey, *Biochem. Biophys. Res. Commun.*, 2000, **273**, 789.
102. R. R. Shoup, H. T. Miles and E. D. Becker, *Biochem. Biophys. Res. Commun.*, 1966, **23**, 194.
103. V. Markowski, G. R. Sullivan and J. D. Roberts, *J. Am. Chem. Soc.*, 1977, **99**, 714.
104. J. Boyd, T. K. Mal, N. Soffe and I. D. Campbell, *J. Magn. Reson.*, 1997, **124**, 61.
105. A. C. Li Wang and A. Bax, *J. Magn. Reson.*, 1997, **127**, 54.
106. N. Tjandra and A. Bax, *J. Am. Chem. Soc.*, 1997, **119**, 8076.
107. M. Tessari, H. Vis, R. Boelens, R. Kaptein and G. W. Vuister, *J. Am. Chem. Soc.*, 1997, **119**, 8985.
108. N. Juranic, V. A. Likic, R. G. Prendergast and S. J. Macura, *J. Am. Chem. Soc.*, 1996, **118**, 7859.
109. W. W. Cleland, *Biochemistry*, 1992, **31**, 317.
110. J. Lin, M. W. Westler, W. W. Cleland, J. L. Markley and P. A. Frey, *Proc. Natl. Acad. Sci. USA*, 1998, **95**, 14664.
111. J. L. Markley and W. M. Westler, *Biochemistry*, 1996, **35**, 11092.
112. A. S. Mildvan, T. K. Harris and C. Abeygunawardana, *Meth. Enzymol.*, 1999, **308**, 219.
113. M. M. Kreevoy and T. M. Liand, *J. Am. Chem. Soc.*, 1980, **102**, 3315.
114. T. Takano, *J. Mol. Biol.*, 1977, **110**, 537.
115. T. Takano, *J. Mol. Biol.*, 1977, **110**, 569.
116. J. Kuriyan, S. Wiltz, M. Karplus and G. A. Petsko, *J. Mol. Biol.*, 1986, **192**, 133.
117. G. W. Bushnell, G. V. Louie and G. D. Brayer, *J. Mol. Biol.*, 1990, **214**, 585.
118. R. G. Sanishvili, K. W. Volz, E. M. Westbrook and E. Margoliash, *Structure*, 1995, **3**, 707.
119. H. E. Parge, R. A. Hallewell and J. Tainer, *Proc. Natl. Acad. Sci. USA*, 1992, **89**, 6109.
120. Y. Yamamoto, *J. Biochem.*, 1996, **120**, 126.
121. Y. Yamamoto, *Eur. J. Biochem.*, 1997, **243**, 292.
122. Y. Yamamoto, *Biochim. Biophys. Acta*, 1997, **1343**, 59.
123. Y. Yamamoto, *Biochim. Biophys. Acta*, 1997, **1343**, 193.
124. Y. Yamamoto, N. Kurihara, T. Egawa, H. Shimada and Y. Ishimura, *Biochim. Biophys. Acta*, 1999, **1433**, 27.
125. J. L. Markley, *Acc. Chem. Res.*, 1975, **8**, 70.
126. J. L. Markley, in *Biological Applications of Magnetic Resonance* (ed. R. G. Shulman), Academic Press, New York, 1979, p. 397.
127. W. W. Bachovchin, *Proc. Natl. Acad. Sci. USA*, 1985, **82**, 7948.
128. A. Kintanar, C. M. Metzler, D. E. Metzler and R. D. Scott, *J. Biol. Chem.*, 1991, **266**, 17222.
129. K. L. House, A. R. Garber, R. B. Dunlap, J. D. Odom and D. Hilvert, *Biochemistry*, 1993, **32**, 3468.
130. D. E. Metzler, C. M. Metzler, T. E. Mollova, R. D. Scott, S. Tanase, K. Koga, T. Higaki and Y. Morino, *J. Biol. Chem.*, 1994, **269**, 28017.
131. D. E. Metzler, C. M. Metzler, T. E. Mollova, H. Kagamiyama, T. Yano, S. Kuramitsu, H. Hayashi, H. Hirotsu and I. Miyahara, *J. Biol. Chem.*, 1994, **269**, 28027.
132. J. Tobin, S. A. Whitt, C. S. Cassidy and P. A. Frey, *Biochemistry*, 1995, **34**, 6919.

133. C. J. Halkides, Y. Q. Wu and C. J. Murray, *Biochemistry*, 1996, **35**, 15941.
134. Q. Zhao, C. Abeygunawardana, P. Talalay and A. S. Mildvan, *Proc. Natl. Acad. Sci. USA*, 1996, **93**, 8220.
135. C. S. Cassidy, J. Lin and P. A. Frey, *Biochemistry*, 1997, **36**, 4576.
136. T. K. Harris, C. Abeygunawardana and A. S. Mildvan, *Biochemistry*, 1997, **36**, 14661.
137. J. Lin, C. S. Cassidy and P. A. Frey, *Biochemistry*, 1998, **37**, 11940.
138. B. C. Mabutt and P. E. Wright, *Biochim. Biophys. Acta*, 1985, **832**, 175.
139. Y. Thériault, T. C. Pochapsky, C. Dalvit, M. L. Chiu, S. G. Sligar and P. E. Wright, *J. Biomol. NMR*, 1994, **4**, 491.
140. H. J. Dyson and P. E. Wright, *Annu. Rev. Phys. Chem.*, 1996, **47**, 369.
141. D. Eliezer, J. Yao, H. J. Dyson and P. E. Wright, *FEBS Lett.*, 1997, **419**, 285.
142. J. Yao, H. J. Dyson and P. E. Wright, *Nature Struct. Biol.*, 1998, **5**, 148.
143. S. Cavagnero, H. J. Dyson and P. E. Wright, *J. Mol. Biol.*, 1999, **285**, 269.
144. D. Bashford, D. A. Case, C. Dalvit, L. Tennant and P. E. Wright, *Biochemistry*, 1993, **32**, 8045.
145. M. Cocco, Y.-H. Kao, A. T. Phillips and J. T. J. Lecomte, *Biochemistry*, 1992, **31**, 6481.
146. S. Bhattacharya, S. F. Sukits, K. L. MacLaughlin and J. T. J. Lecomte, *Biophys. J.*, 1997, **73**, 3230.
147. S. Bhattacharya and J. T. J. Lecomte, *Biophys. J.*, 1997, **73**, 3241.
148. Y.-H. Kao, C. A. Fitch, S. Bhattacharya, C. J. Sarkisian, J. T. J. Lecomte and E. B. Garcia-Moreno, *Biophys. J.*, 2000, **79**, 1637.
149. C. Woodward, E. Simon and E. Tuchsen, *Mol. Cell. Biochem.*, 1982, **48**, 135.
150. A. Hvidt and S. Nielsen, *Adv. Protein Chem.*, 1966, **21**, 287.
151. C. K. Woodward and B. D. Hilton, *Annu. Rev. Biophys. Bioeng.*, 1979, **8**, 99.
152. S. V. Evans and G. D. Brayer, *J. Biol. Chem.*, 1988, **263**, 4263.
153. S. V. Evans and G. D. Brayer, *J. Mol. Biol.*, 1990, **213**, 885.
154. V. Srajer, T.-Y. Teng, T. Ursby, C. Pradervand, Z. Ren, S. Adachi, W. Schildkamp, D. Bourgeois, M. Wulff and K. Moffat, *Science*, 1996, **274**, 1726.
155. B. Giardina, P. Ascenzi, M. E. Clementi, G. De Sanctis, M. Rizzi and M. Coletta, *J. Biol. Chem.*, 1996, **271**, 16999.
156. A. Ansari, C. M. Jones, E. R. Henry, J. Hofrichter and W. A. Eaton, *Biochemistry*, 1994, **33**, 5128.
157. R. F. Tilton, Jr., U. C. Singh, I. D. Kuntz, Jr. and P. A. Kollman, *J. Mol. Biol.*, 1988, **199**, 195.
158. K. Kuczera, J. Kuriyan and M. Karplus, *J. Mol. Biol.*, 1990, **213**, 351.
159. Y. Seno and N. Go, *J. Mol. Biol.*, 1990, **216**, 111.
160. L. Stryer, J. C. Kendrew and H. C. Watson, *J. Mol. Biol.*, 1964, **8**, 96.
161. C. Lionetti, M. G. Guanziroli, F. Fregerio, P. Ascenzi and M. Bolognesi, *J. Mol. Biol.*, 1991, **217**, 409.
162. Y. Yamamoto, K. Iwafune, R. Chûjô, Y. Inoue, K. Imai and T. Suzuki, *J. Biochem.*, 1992, **112**, 414.
163. H. Hori, *Biochim. Biophys. Acta*, 1971, **251**, 227.
164. Y.-H. Kao and J. T. J. Lecomte, *J. Am. Chem. Soc.*, 1993, **115**, 9764.
165. Y. V. Griko, P. L. Privalov, S. Y. Venyaminov and V. P. Kutyshenko, *J. Mol. Biol.*, 1988, **202**, 127.
166. F. M. Hughson and R. L. Baldwin, *Biochemistry*, 1989, **28**, 4415.
167. F. M. Hughson, P. E. Wright and R. L. Baldwin, *Science*, 1990, **249**, 1544.
168. D. Barrick, F. M. Hughson and R. L. Baldwin, *J. Mol. Biol.*, 1994, **237**, 588.
169. S. N. Loh, M. S. Kay and R. L. Baldwin, *Proc. Natl. Acad. Sci. USA*, 1995, **92**, 5446.
170. T. T. Herskovits and N. J. Solli, *Biopolymers*, 1975, **14**, 319.
171. P. A. Jennings and P. E. Wright, *Science*, 1993, **262**, 892.

172. M. Kataoka, I. Nishi, T. Fujisawa, T. Ueki, F. Tokunaga and Y. Goto, *J. Mol. Biol.*, 1995, **249**, 215.
173. S. R. Anderson, M. Brunori and G. Weber, *Biochemistry*, 1970, **9**, 4723.
174. J. T. J. Lecomte and M. J. Cocco, *Biochemistry*, 1990, **29**, 11057.
175. M. J. Cocco and J. T. J. Lecomte, *Biochemistry*, 1990, **29**, 11067.
176. M. J. Cocco and J. T. J. Lecomte, *Protein Sci.*, 1994, **3**, 267.
177. J. N. S. Evans, *Biomolecular NMR Spectroscopy*, Oxford University Press, New York, 1995, p. 223.
178. J. T. J. Lecomte, S. F. Sukits, S. Bhattacharya and C. J. Falzone, *Protein Sci.*, 1999, **8**, 1484.
179. D. Barrick and R. L. Baldwin, *Biochemistry*, 1993, **32**, 3790.
180. D. Eliezer and P. E. Wright, *J. Mol. Biol.*, 1996, **263**, 531.
181. F. Wang and X. Tang, *Biochemistry*, 1996, **35**, 4069.
182. L. Lin, R. J. Pinker, K. Forde, G. D. Rose and N. R. Kallenbach, *Nature Struc. Biol.*, 1994, **1**, 447.
183. G. N. La Mar, D. L. Budd, D. B. Viscio, K. M. Smith and K. C. Langry, *Proc. Natl. Acad. Sci. USA*, 1978, **75**, 5755.
184. G. N. La Mar, N. L. Davis, D. W. Parish and K. M. Smith, *J. Mol. Biol.*, 1983, **168**, 887.
185. G. N. La Mar, H. Toi and R. Krishnamoorthi, *J. Am. Chem. Soc.*, 1984, **106**, 6395.
186. Y. Yamamoto and G. N. La Mar, *Biochemistry*, 1986, **25**, 5288.
187. Y. Yamamoto, K. Takemoto and H. Matsuo, *J. Mol. Struct.*, in press.
188. M. J. Cocco, D. Barrick, S. V. Taylor and J. T. J. Lecomte, *J. Am. Chem. Soc.*, 1992, **114**, 11000.
189. G. R. Moore and G. W. Pettigrew, *Cytochromes c: Evolutionary, Structural and Physicochemical Aspects*, Springer, Berlin, 1990.
190. T. Takano and R. E. Dickerson, *J. Mol. Biol.*, 1981, **153**, 74.
191. T. Takano and R. E. Dickerson, *J. Mol. Biol.*, 1981, **153**, 95.
192. G. V. Louie and G. D. Brayer, *J. Mol. Biol.*, 1990, **214**, 527.
193. W. Qin, R. Sanishvili, B. Plotkin, A. Schejter and E. Margoliash, *Biochim. Biophys. Acta*, 1995, **1252**, 87.
194. A. J. Wand, D. L. Di Stefano, Y. Feng, H. Roder and S. W. Englander, *Biochemistry*, 1989, **28**, 186.
195. E. Margoliash, E. L. Smith, G. Kreil and H. Tuppy, *Nature*, 1961, **192**, 1125.
196. G. Kreil, *Hoppe-Seyler's Z. Physiol. Chem.*, 1963, **334**, 153.
197. G. Kreil, *Hoppe-Seyler's Z. Physiol. Chem.*, 1965, **340**, 86.
198. A. P. Boswell, C. G. S. Eley, G. R. Moore, M. N. Robinson, G. Williams, R. J. P. Williams, W. J. Neupert and B. Hennig, *Eur. J. Biochem.*, 1982, **124**, 289.
199. J. Trewhella, V. Carlson, E. H. Curtis and D. B. Heidorn, *Biochemistry*, 1988, **27**, 1121.
200. Y. Feng and S. W. Englander, *Biochemistry*, 1990, **29**, 3505.
201. T. Y. Tsong, *Biochemistry*, 1975, **14**, 1542.
202. G. A. Elöve, A. K. Bhuyan and H. Roder, *Biochemistry*, 1994, **33**, 6925.
203. D. Hamada, Y. Kuroda, M. Kataoka, S. Aimoto, T. Yoshimura and Y. Goto, *J. Mol. Biol.*, 1996, **256**, 172.
204. D. Hamada, M. Hoshino, M. Kataoka, A. L. Fink and Y. Goto, *Biochemistry*, 1993, **32**, 10351.
205. J. V. Bannister, W. H. Bannister and G. Rotilio, *CRC Cri. Rev. Biochem.*, 1987, **22**, 111.
206. I. Bertini, C. Luchinat and M. Piccioli, *Prog. NMR Spectrosc.*, 1994, **26**, 91.
207. I. Bertini, S. Mangani and M. S. Viezzoli, *Adv. Inorg. Chem.*, 1998, **45**, 127.
208. I. Bertini, F. Capozzi, C. Luchinat, M. Piccioli and M. S. Viezzoli, *Eur. J. Biochem.*, 1991, **197**, 691.
209. L. Banci, M. Benedetto, I. Bertini, R. Del Conte, M. Piccioli and M. S. Viezzoli, *Biochemistry*, 1998, **37**, 11780.

210. L. Banci, I. Bertini, B. Bruni, P. Carloni, C. Luchinat, S. Mangani, P. L. Orioli, M. Piccioli, W. Ripniewski and K. S. Wilson, *Biochem. Biophys. Res. Commun.*, 1994, **202**, 1088.
211. E. D. Getzoff, D. E. Cabelli, C. L. Fisher, H. E. Parge, M. S. Viezzoli, L. Banci and R. A. Hallewell, *Science*, 1992, **358**, 347.
212. Y. Yamamoto and F. Yamakura, manuscript in preparation.

Index

Note — Page numbers in *italic* type refer to figures and tables.

Acetic acid, 5
Acetone, 18
Adhesives, 169
Adipic acid, ^{1}H CRAMPS NMR spectra, 77, 83–4
A–H bond, 190, 192
A–H—B bond, 190, 193
A–H—B interaction, 190
Amide ^{1}H chemical shift
  and main-chain conformation, 139–41
  poly(L-alanines), 146
Amide ^{1}H signal
  ^{15}N-labelled poly(L-alanines), 132–4
  ^{15}N-labelled poly(L-leucines), 134–6
Amide ^{1}H signal broadening, MAS speed dependence, 136–9
Amide proton chemical shift, 128–41
α-Amino acid crystals, ^{1}H CRAMPS NMR, 84–97
Amino acid residues, ^{1}H chemical shift data, 109
Antiferromagnetic-paraelectric phase transition, 31
apoMb
  B—GH interface in, 218–20
  C helix in, 220
  EF—H interface in, 220
  protein folding in, 216–20
  reconstitution with heme, 221
  titration with hemin, 222–6
Azobacter chroococcum, 181

Bacteria, STRAFI imaging, 181
Benzoic acid, 5
  ^{1}H CRAMPS spectra, 77
B—GH interface, 215–16, 227
  in apoMb, 218–20
B—H bond, 192
Bidentate acetate ligands, 32
Biological samples, STRAFI and SPI/SPRITE imaging, 179–81
Bipolar gradients, 14
Bloch equations, 159
Boltzmann constant, 3
Bombyx mori-I, 114–15
  ^{1}H CRAMPS NMR, 115–20, 122–4
  two-dimensional ^{1}H–^{13}C HETCOR NMR spectra, 120–2
Bombyx mori-II, 114–15
  ^{1}H CRAMPS NMR, 115–20, 122–4
  two-dimensional ^{1}H–^{13}C HETCOR NMR spectra, 120–2
BR-24
  pulse sequence, 73, 130
  scaling factor of, 80–3
Bruker DSX, 79

C helix in apoMb, 220
^{13}C chemical shift
  A-histidine, 95
  B-histidine, 95
  polypeptides, 98
^{13}C CP-MAS NMR measurements, 84–5
^{13}C CP-MAS NMR spectra
  L-histidine polymorphic crystals, 94
  L-histidine polymorphs, 92
  poly(L-alanines), 129
  poly(L-leucines), 129
$C_2H_5(C_6H_5)_2P$, 25
C_6F_6, 17
$(C_6H_5)_3P$, 21
$(C_6H_5)_3PO$, 21
Cadmium complexes, 27
Capillary electrophoresis (CE), 8
Carbon, 16–19
Carbon 2, 18
Carbon 6, 18
Carbon, chemical shifts, 32–3
CCl_4, 17
CD_2H, 6
$(CD_3)CO_2$, 17
$CDCl_3$, 24

CE-NMR thermometry, 8
Cement paste, 177
Cesium complexes, 27
$CF_3CF_2Cl_2$, 20
$CF_3CF_2CO_2H$, 20
$CFC3_3$, 19–20
CH_2, 6
CH_2Br_2, 12
CH_3, 6
CH_3 resonance, 8
$CH_3C^{15}N$, 22
Chemagnetics CMX, 79
Chemical shift, 3, 4
Chemical shift anisotropy (CSA), 4
Chemical shift imaging (CSI), 15
$CHFCl_2$, 17
Cl-Pt-Cl, 26
Cobalt(III) complexes, 22–6
Collagen fibrils, two-dimensional ^1H–^{13}C HETCOR NMR, 124–8
Combined Rotation And Multiple Pulse Spectroscopy. *See* CRAMPS
Concrete, 177
Contour lines, 153
Convection, 13, 14
Copper complexes, 26
CP-MAS method, 29, 35, 70, 72
^{13}CP-MAS NMR spectra, glycine crystals, 86–96
CP-MAS NMR temperature calibration experiments, 31
CPMG spin echo sequences, 160
CRAMPS, 74, 78
  see also ^{1}H CRAMPS NMR spectra
Creaming, 180
Cross-polarization magic angle spinning. *See* CP-MAS method
Cryoablation, 43
CSA, 20–1
Cu, Zn superoxide dismutase (SOD) active site, 240–2
Curie law, 33
Cyclo(L-alanyl-D-alanyl, ^{1}H CRAMPS NMR, 109–11
Cyclo(L-alanyl-D-analyl), ^{1}H CRAMPS NMR, 109–11
Cytochrome *c*, protein folding in, 229–40

D_2O, 13
DABCO, 30
DBTFB, 19–20
Decanoic acid, 5
Decoupling, 7
Delrin, 169
Deuterium, 21–2
Deuterohemin, 220
Diffusion coefficient, 46
Diffusion encoding gradient, 46
Difluoroethylenes, 20
4,4′-Dimethylbenzophenone, 75
Diploria labyrinthiformis, 165
Dipolar coupling constants, 4
DMPD, 32
DOTMA, 11
DTFMB, 19–20
Durene, ^{1}H CRAMPS NMR spectra, 77

Echo-planar imaging (EPI), 48
Eddy-current delay, 14
EENC 2000, 72
EF—H interface, 216, 227–9
  in apoMb, 220
Electric field gradient, 200
ENC 2000, 72
Enterobacter cloacae, 181
Ethyl alcohol, nuclear induction signal, 71
Ethylene glycol, temperature calibrations, 6
EU^{3+} complexes, 9
Exchangeable proton signals
  effect of denaturant, 239–40
  pH dependence, 234–5
  temperature dependence, 233–4

^{19}F CRAMPS spectra of KEL-F, 74
Fast-exchange two-state (FETS) model, 42
Ferrocytochrome *c*, 231, 232
FID, 21, 80
  response of protons, 80
FLASH, 44, 45, 53
Fluid imbibition into homogeneous materials, STRAFI and SPI/SPRITE
  imaging, 171–5
Fluorine, 19–21

2-Fluorobenzotrifluorides, 20
FTBA, 20–1
FTPA, 20–1
FUS heating experiment, 56

Gas phase MRI, 164
Gd-DTPA, 11
Glycine crystals
  ^{13}CP-MAS NMR spectra, 86–96
  ^{1}H CRAMPS NMR, 85–90
  ^{1}H electrostatic potential (ESP) charge calculation, 90–2, 96
  ^{15}N CP-MAS NMR spectra, 86–96
GOESY, 14
Gradient compensation, 14
Gradient-recalled acquisition in the steady state (GRASS), 44, 45
GROESY, 14
GRP, 174
Guanidine hydrochloride, 239–40

^{1}H chemical shift data of α-amino acid residues, 109
^{1}H CRAMPS NMR, 69–150
  adjustment for, 78–80
  α-amino acid crystals, 84–97
  carrier signal, 78
  chemical shift error, 81
  chemical shift scaling, 77
  confirmation of modulation, 83–4
  features of, 75–8
  glycine crystals, 85–90
  image signal, 78
  interference of multiple pulse with MAS, 77–8
  L-histidine crystals, 92–4
  measurement conditions, 83
  polypeptides, 97–113
^{1}H CRAMPS NMR spectra
  A-histidine, 94–7
  adipic acid, 77, 83–4
  B-histidine, 94–7
  benzoic acid, 77
  durene, 77
  L-histidine polymorphs, 96
  malonic acid, 77
  poly(γ-benzyl-L-glutamates), 102, 111–13
  poly(butanediol terephthalate), 77
  poly(L-alanines), 76, 100
  poly(L-leucines), 101
  polystyrene, 77
^{1}H electrostatic potential (ESP) charge calculation of glycine crystals, 90–2, 96
^{1}H NMR, history, high-resolution solid-state, 70–5
^{1}H chemical shift
  A-histidine, 95
  B-histidine, 95
  polypeptides, 98
^{2}H quadrupolar coupling constant, 200
Haemoprotein, hydrogen bond of distal residue to bound ligand in, 195–200
Heme
  active site, 228–9
  apoMb reconstitution with, 221
  electronic structures, 195
  ligation effect on structures of B—GH and EF—H interfaces in myoglobin, 213–16
Heme orientation
  effects on structure of B—GH and EF—H interfaces, 227–8
  reaction, 221
Hemins, 220
  apoMb titration with, 222–6
Heteronuclei, 16–29
Hexafluorobenzene, 19
^{1}H–H homonuclear dipolar interaction, 76
^{1}H–^{1}H interactions, 155
High-frequency shifted exchangeable proton signals, effects of salt concentration, 237–9
High-resolution NMR, thermal gradients in, 12–15
High-resolution NMR spectroscopy, 6, 12
High-resolution solid-state NMR studies, 70–5
HisE7 imidazole, 196
HisE7 imidazole ring NH proton, 197
HisE7 side-chain, 200
HisEF5 imidazole ring protons, 204

HisF8 imidazole, 196
HisF8 $N_\delta H$ proton signal, 202
His imidazole NH proton signals, high-frequency shifted, 232–3, 241
His imidazole ring NH hydrogen atoms, 201–3
His imidazole ring NH proton signals
  effects of ionic strength, 210
  effects of pH, 207–10
  effects of temperatures, 206–7
  high-frequency shifted, 203–14
  reconstituted Mbs, 226
His imidazole ring NH protons, 191
His residues, 202
A-Histidine, 86, 92–4
  ^{13}C chemical shift, 95
  ^{1}H chemical shift, 95
  ^{1}H CRAMPS NMR spectra, 94–7
  ^{15}N chemical shift, 95
B-Histidine, 86, 92–4
  ^{13}C chemical shift, 95
  ^{15}N chemical shift, 95
  ^{1}H chemical shift, 95
  ^{1}H CRAMPS NMR spectra, 94–7
L-Histidine crystals, ^{1}H CRAMPS NMR, 92–4
L-Histidine polymorphs
  ^{13}C CP-MAS NMR spectra, 94
  ^{13}CP-MAS NMR spectra, 92
  ^{1}H CRAMPS NMR spectra, 96
Histidine residues in sperm whale and horse myoglobins, 201
H_2O, 7, 15
Hoogsteen T—A base pairs, 195
Horse cytochrome *c*, 230
Horse ferrocytochrome *c*, 233–8
Horse myoglobin, 212
H_3PO_4, 21
Hydrocarbons, 17
Hydrogen bonds, 5
  concept, 190
  conventional observation methods, 200
  distal residue to bound ligand in haemoprotein, 195–200
  functional properties, 190
  inter-segmental, 202
  low-barrier (LBHBs), 193–4, 200
  NMR characterization, 194
  observation of spin–spin couplings through, 194–5
  potential energy diagram, 192–3
  principal features, 191–4
  properties, 192
Hydrogen exchange rate, 209
Hyperthermia, monitoring, 57

Internal hydrogen bonds in metalloproteins, 201–42
In vivo temperature mapping, using magnetic resonance imaging (MRI), 40–59
Isotropic nitrogen chemical shift, 200
Isotropic proton chemical shift, 200

J couplings, 3, 194–5
Joule-Thompson effects, 30
Joule-Thompson heating or cooling, 2

$K_3Co(CN)_6$, 13, 24
KEL-F, ^{19}F CRAMPS spectra, 74
Krytox, 15

Lanthanide complexes, proton chemical shifts in, 9–11
Lanthanide induced shift (LIS), 9
Lanthanides, 33
Larmor frequency, 26, 154
Laser-induced interstitial thermotherapy (LITT), 53–4
Laser tissue ablation, 53–4
Lead chemical shifts, 38–40
Lead complexes, 29
Liquid crystals, 12
Long echo train summation (LETS), 160
Low barrier hydrogen bonds (LBHBs), 193–4, 200
Low deuterium atom fraction factor, 200

Magic angle spinning (MAS). *See* CP-MAS method
Magnetic field inhomogeneity, 154
Magnetic resonance imaging (MRI), 1, 2, 6, 57
  applications, 152
  development, 152
  heating studies, 59

in vivo temperature mapping using, 40–59
monitoring of ultrasonic heating, 58
see also Single point imaging (SPI); SPRITE; STRAFI
Magnetic resonance microscopy (MRM), 152, 182
and STRAFI combined, 173
applications, 153
Malonic acid, ^{1}H CRAMPS spectra, 77
Manganese complexes, 26
MAS
discovery, 72
interference of multiple pulse with, 77–8
speed dependence on amide ^{1}H signal broadening, 136–9
see also CP-MAS
MAS probes, 39
MASSTRACE, 142
Maximum intensity projections, 153
Mercury complexes, 27
Mesohemin, 220
Metalloproteins, internal hydrogen bonds in, 201–42
Methanol, temperature calibrations, 6
MgATP, 21
$MgCl_2$, 21
Microwave heating, 24
Microwave tissue heating, 57
MNDO method, 91
Molecular diffusion based techniques and applications, 46–8
Molecular diffusion coefficient, 3, 4
Morse parameter, 23
MREV-8, 83
pulse sequence, 73, 130–2
Myoglobin, 195, 201–3, 210–13
heme ligation effect on structures of B—GH and EF—H interfaces in, 213–16
long-range structural correlation, 221–9
Myoglobin molecule, 196

N4 liquid crystal, 12
^{15}N chemical shift
A-histidine, 95
B-histidine, 95
^{15}N CP-MAS NMR measurements, 84–5
^{15}N CP-MAS NMR spectra
A-histidine, 94
B-histidine, 94
glycine crystals, 86–96
L-histidine polymorphs, 93
poly(L-alanines), 131
poly(L-leucines), 131
N-acetylaspartate (NNA), 8
^{15}N-labelled poly(L-alanines)
amide ^{1}H signal of, 132–4
^{1}H CRAMPS NMR spectra, 137, 143
^{15}N-labelled poly(L-leucines), amide ^{1}H signal of, 134–6
$Na_4HTm[DOTP]$, 21
NaCl, 8
Natural fibrous proteins
^{1}H CRAMPS NMR, 113–15
synthetic conditions, conformational characteristics, and ^{1}H and ^{13}C chemical shifts, 116
Nd:YAG laser, 43, 53
Net equilibrium magnetization, 3
Net polarization, 3
N—H bond length, 141–7
Niobium complexes, 27
Nitrogen, 21–2
chemical shifts, 33–4
NMR parameters, temperature-dependent, 3–4
NMR temperature measurements, 1–67
liquid state, 4–29
solid state, 29–40
NOESY, 206
Non-transition metals, 28–9
Nuclear magnetic resonance. *See* NMR
Nuclear Overhauser effect (NOE), 200, 205, 206, 213–14, 232–3

Occlusin, 170, 175
OH proton, 5, 6

^{207}Pb MAS spectra, 40
Percutaneous hot saline injection therapy (PSIT), 58
Perfluorotoluene, 20
PFOB, 20–1
pH dependence, exchangeable proton signals, 234–5

pH effects on His imidazole ring NH proton signals, 207–10
Phase-transition calibration materials, 30–1
Phase-transition compounds, 12, 37
Phosphonous acids, 21
Phosphorus, 21–2
  chemical shifts, 35
Planck's constant, 3
Plexiglas, 169
PMMA, 173–5
Polarization, 3
Poly(γ-benzyl-L-glutamates), 99–103
  ^{1}H CRAMPS NMR spectra, 102, 111–13
Poly(butanediol terephthalate), ^{1}H CRAMPS NMR spectra, 77
Polyglycines, ^{1}H CRAMPS NMR spectra, 104–9
Poly(L-alanines), 99–103
  amide ^{1}H chemical shifts, 146
  ^{13}C CP-MAS NMR spectra, 129
  ^{1}H CRAMPS NMR spectra, 76, 100, 133, 138
  ^{15}N CP-MAS NMR spectra, 131
  ^{15}N–^{1}H dipolar spectra, 145
Poly(L-leucines), 99–103
  ^{13}C CP-MAS NMR spectra, 129
  ^{1}H CRAMPS NMR spectra, 101, 135, 140
  ^{15}N CP-MAS NMR spectra, 131
Poly(L-proline), ^{1}H CRAMPS NMR spectra, 105–9
Poly(L-valines)
  chain-length dependence of ^{1}H chemical shifts, 103–5
  ^{1}H CRAMPS NMR spectra, 103
Polymerization processes, STRAFI and SPI/SPRITE imaging, 170–1
Polypeptides
  ^{13}C chemical shifts, 98
  conformational study, 97–113
  deuterium-labelled, 111–13
  ^{1}H CRAMPS NMR, 97–113
  ^{1}H chemical shifts, 98
  NH proton chemical shifts, 139–41
  α-proton chemical shifts, 99–109
  synthetic conditions, conformational characteristics and ^{1}H chemical shifts, 132
Polystyrene, ^{1}H CRAMPS NMR spectra, 77
Porous materials, STRAFI and SPI/SPRITE imaging, 175–8
Pr-MOE-DO3A, 11, 41
  chemical structure, 11
Protein folding
  in apomyoglobin, 216–20
  in cytochrome *c*, 229–40
Protohemin, 220
Proton, 4–15
Proton chemical shift anisotropy, 200
Proton chemical shifts, 5–8, 32
  lanthanide complexes, 9–11
  polypeptides, 99–109
Proton CRAMPS, 78
Proton nuclei, 70
Proton reference frequency (PRF) method
  applications, 52–9
  imaging methodologies, 49–52
  in vivo applications, 58–9
  sample independence studies, 49–52
Proton spin–spin relaxation, 153
Proton temperature sensitivities and association shifts, 5
Protons, response to FID, 80
Pt—P scalar coupling, 25
Pt—Pt bonds, 26
Pulse tuning cycle, 80

Rapid-acquisition-with-relaxation-enhancement (RARE), 43, 164
Rayleigh number, 13
Relaxation rates, 154
Relaxation times, 3
RF tissue heating, 57
Rhodium complexes, 26

Samarium acetate tetrahydrate, 32
Scalar couplings, 3, 4
Scaling factor of BR-24, 80–2
Sediments, STRAFI and SPI/SPRITE imaging, 181–2
Selenium complexes, 26–7
Sequential one bond $^{1}J_{CN}$ coupling constants, 200

Shielding constant, 3
Si-rubber, CRAMPS measurement, 81
Signal intensity (S), 14
Signal-to-noise (S/N) ratio, 2, 4
Silk fibroin model polypeptide, ^{1}H CRAMPS NMR, 122–4
Silk fibroins, two-dimensional ^{1}H–^{13}C HETCOR NMR, 120–2
Simona, 173
Single point imaging (SPI), 151–87
  basic principles, 160–5
  emergence, 155
  instrumental limitations, 162
  one-dimensional sequence, 161
  see also SPI/SPRITE
Sodium, 21–2
Soils, STRAFI and SPI/SPRITE imaging, 181–2
Solid-state 2D HETCOR, 75
Sperm whale apoMb, 217, 219, 223, 225, 226, 228
Sperm whale metMb, 223, 227
Sperm whale metMb(CN^-), 197–9, 224
Sperm whale metMb(OH^-), 204–7, 210–13, 218, 219
SPI/SPRITE imaging
  applications, 167–82
  nuclei other than ^{1}H, 165–7
Spin relaxation, 154
Spin-rotation, 4
Spin-rotational relaxation, 26
Spin–spin couplings, 194
SPRITE, 162–5
  acquisition, 163
  half-ramp, 163–4
  one-dimensional, 178
  two-dimensional, 163
  see also SPI/SPRITE imaging
Squaric acid, 30–2
Stokes–Einstein equation, 4
STRAFI, 151–87
  and MRM combined, 173
  applications, 167–82
  basic principles, 155–60
  emergence, 155
  field sweep variant, 158
  frequency swept method, 157–8
  frequency-swept, 175
  nuclei other than ^{1}H, 165–7
Stray field imaging. *See* STRAFI; SPI/STRAFI
Surface reconstruction, 153

T_1-based techniques and applications, 41–6
Tellurium complexes, 28
Temperature calibration experiments, CP-MAS NMR, 31
Temperature-dependent NMR parameters, 3–4
Temperature dependence, exchangeable proton signals, 233–4
Temperature mapping, non-medical applications, 59
Temperature measurements
  non-invasive, 59
  using NMR. *See* NMR temperature measurements
1,1,4,4-tetrafluoro-1,3-alkadienes, 20
Tetrakis(trimethylsilyl)silane (TTMSS), 32
Tetramethylsilane (TMS), 16, 17
Thallium, 21
Thallium complexes, 28
Thermal gradients in high-resolution NMR, 12–15
Thin film technology, 171
Tin chemical shifts, 35
Tin complexes, 28–9
$TmDOTP^{5-}$, 9–10, 15
  chemical shift temperature dependence and relaxation times, 10
  molecular structure, 10
Transition metal complexes, 22–8
Trp 59 N_εH proton signal, 239
TTAA, 33–4
Tuna ferrocytochrome *c*, 233–7
Tungsten complexes, 28
Turbo spin echo single-point imaging (turboSPI) sequence, 164
TurboFLASH, 45, 164
Tussah Antheraea pernyi, 114–15
  ^{1}H CRAMPS NMR, 115–20
  two-dimensional ^{1}H–^{13}C HETCOR NMR spectra, 120–2

Two-dimensional $^{1}H-^{13}C$ HETCOR NMR, 109, 113, 114
collagen fibrils, 124–8
silk fibroins, 120–2

'Ultrahigh'-resolution NMR, 18
Ultrasonic heating, MRI monitoring, 58
Ultrasound-mediated hyperthermia and tissue ablation, 54–7
United States Food and Drug Administration (FDA), 59
Unswollen solid synthetic polymers, STRAFI and SPI/SPRITE imaging, 167–70

Van Geet equation, 6, 32
Vanadium complexes, 27
Variable temperature (VT) units, 2
$V(CO)_6^-$, 23
Volume susceptibility, 5

WAHUHA-4
multiple-pulse sequences, 73
pulse sequence, 72
WALTZ-4, 58
WALTZ-16 decoupling, 7
Watson–Crick base pairs, 194–5

$Yb(fod)_3$, 16

Zeeman perturbations, 36
Zeolite 4A, 178
Zinc complexes, 26
ZLI-1132 liquid crystal, 12